Italian Chapter of the
European Society of Biomechanics
(ESB-ITA)

ESB-ITA 2014 Meeting

In conjunction with the Italian National

Bioengineering Group (GNB) Congress 2014

Università di Pavia, Pavia – June 27, 2014

Organizing Committee: F Boschetti, M Conti, L Cristofolini, D Gallo

Book of Abstracts

Gruppo Nazionale Bioingegneria
IV Congresso
Università degli Studi di Pavia
Pavia, 25-27 giugno 2014

Menu Principale

Home
Presentazione - Premi
Programma
Iscrizione - Dove alloggiare - Sede
Organizzazione
Sponsor
Sottomissione dei contributi

Città di Pavia

Benvenuti a Pavia
Pavia
Comune di Pavia
Foto di Pavia
Castello Visconteo
Certosa di Pavia
Einstein a Pavia
Università di Pavia
Storia dell'Università di Pavia
Collegi universitari
Oltrepò Pavese

Programma definitivo

Mercoledì 25 giugno 2014

08.30 - Apertura registrazioni

09.30 - Inizio dei lavori, saluto del Magnifico Rettore dell'Università di Pavia, Fabio Rugge, e degli organizzatori del Convegno

09.45 - Relazione invitata "Mario Stefanelli" - *Clinical Prediction Models: from bench to bedside* - Ameen Abu-Hanna - Head of the Department of Medical Informatics, Academic Medical Center, University of Amsterdam

10.30 - Coffee break e Sessioni Poster - Temi: ***Riabilitazione, Analisi del movimento, Ambient-assisted living***; ***Horizon 2020***

12.15 - Lettura Horizon 2020 - *Hyperscanning: a new approach to the study of the physiological basis of human social interaction* - Laura Astolfi, Università "Sapienza" di Roma

12.45 - Premi Giovani Ricercatori - Letture selezionate (*abstract R-11, R-35, R-42*)

13.15 - Pranzo

14.15 - Relazione invitata - *La sfida di Human Brain Project: i modelli matematici del cervello* - Egidio D'Angelo - Università di Pavia, Direttore del Brain Connectivity Center (BCC), IRCCS C. Mondino, Pavia

15.00 - Lettura Horizon 2020 - *Artificial Pancreas for Everyday Life* - Simone Del Favero, Università di Padova

15.30 - Premi Giovani Ricercatori - Letture selezionate (*abstract T-10, T-24, T-31*)

16.00 - Coffee break e Sessioni Poster - Temi: ***Ingegneria delle cellule e tessuti, Biomateriali, Neuroingegneria***; ***Horizon 2020***

17.45 - Assemblea del Gruppo Nazionale di Bioingegneria

20.00 - Chiusura dei Lavori

Giovedì 26 giugno 2014

09.00 - Lettura Horizon 2020 - *How to play an active role and interact with biological microsystems* - Annalisa Tirella, CNR, Pisa

09.30 - Lettura Horizon 2020 - *Towards Next Generation Decision Support: Personalizing Guideline-Based Systems, Clinical Decision Analysis and Data Mining* - Lucia Sacchi, Università di Pavia

10.00 - Premi Giovani Ricercatori - Letture selezionate (*abstract I-2, I-4, I-22*)

10.30 - Coffee break e Sessioni Poster - Temi: ***Informatica biomedica, Bioinformatica e Ingegneria Clinica***; ***Horizon 2020***

12.15 - Relazione invitata - *Il sistema della ricerca pubblica in Italia: proposte per una riforma costruttiva in vista di una nuova politica economica* - Maria Chiara Carrozza, Scuola Superiore S. Anna di Pisa

13.00 - Pranzo

14.00 - Lettura Horizon 2020 - *The use of in silico and in vitro models to study the computational properties of neuronal systems: a neuroengineering approach to design new-generation neuroprostheses* - Paolo Massobrio, Università di Genova

14.30 - Premi Giovani Ricercatori - Letture selezionate (*abstract M-40, M-61, M-79*)

15.00 - Coffee break e Sessioni Poster - Temi: ***Modelli dei sistemi biologici, Elaborazione di dati, segnali e immagini biomediche***; ***Horizon 2020***

16.45 - Tavola Rotonda - *Il futuro della Bioingegneria nello sviluppo economico del* paese. Moderatore: Riccardo Pietrabissa (Politecnico di Milano e Università degli Studi di Brescia). Partecipanti: Umberto Ferri (Medas), Emanuele Gatti (Fresenius Medical Care), Bruno Murari (ST Microelectronics), Italo Poggesi (Jansenn Cilag)

18.45 - Fine dei lavori

20.00 - Cena sociale presso il Collegio Borromeo in piazza Borromeo

Venerdì 27 giugno 2014

09.00 - Relazione invitata - *Emergent challenges in bringing Cardiovascular Mathematics to the Bedside: Cost reduction, Data Assimilation, Uncertainty Quantification* - Alessandro Veneziani, Emory Center for Mathematics and Computing in Medicine, Department of Mathematics and Computer Science, Emory University, USA

09.45 - Relazione invitata - *Strutturazione di modelli biomeccanici-neurologici* - Paolo Pascolo - Università di Udine, Direttore del Dipartimento di Ingegneria Biomedica dell'International Centre of Mechanical Sciences CISM

10.15 - Premi Giovani Ricercatori - Letture selezionate (*abstract B-5, B-43, B-49*)

10.45 - Coffee break e Sessioni Poster - Temi: ***Biomeccanica e Biorobotica; Horizon 2020***

12.30 - Premiazioni Giovani Ricercatori

12.45 - Cerimonia di chiusura GNB 2014

Convegno European Society of Biomechanics, Italian National Chapter

14.30 - Francesco De Gaetano - *Fluid Dynamic Performance of New Polymeric Heart Valves Prototypes tested under Continuous and Pulsatile Flow Condition*

14.45 - Luigi La Barbera - *Preclinical evaluation of posterior spinal fixators: a parametric FEA on international standards*

15.00 - Giuseppe Criscenti - *Biomechanics of Medial patello-femoral ligament: Quasilinear viscoelastic properties*

15.15 - Mauro Ferraro - *Isogeometric Analysis: a novel computational approach to evaluate the performance of endovascular stents*

15.30 - Mara Terzini - *Experimental set-up for the study of dental implant retrieval*

15.45 - Coffee break

16.15 - Grazia Spatafora - *Optical, mechanical and biochemical characterization of trabecular bone*

16.30 - Annalisa Dimasi - *Multiscale CFD and hemodynamic shearing device to support design of blood contact devices*

16.45 - Michele Marino - *Upscaling biochemical and biophysical effects in tissue mechanical modelling*

17.00 - Giuseppe Isu - *A virtual test bench for the assessment of the flow dynamics in hemodialysis catheters*

17.15 - Annamaria Guiotto - *2-dimensional foot FE models for clinical application in gain analysis*

17.30 - Premi

17.45 - Saluti finali

Istruzioni varie

La dimensione massima dei poster è 90 cm x 120 cm (poster verticale).

Ogni giorno i poster di entrambe le sessioni (mattina e pomeriggio) devono essere appesi entro le ore 10.00 e rimossi entro le ore 19.00.

Le Letture Horizon 2020 devono essere di 20' seguite da 10' di domande.

Le presentazioni orali degli abstract che concorrono per i Premi Giovani Ricercatori devono avere una durata massima di 9'. Non sono previste domande al termine della presentazione. In ogni sessione una giuria selezionerà un vincitore tra i tre abstract candidati.

Le presentazioni orali saranno effettuate generalmente in lingua italiana. È prevista la possibilità di proiettare diapositive ppt, pptx o pdf. Per altri speciali esigenze è necessario fare un'esplicita richiesta per tempo.

Lista dei Contributi

Bianchi *et al.*	Development of a two-pool virtual simulator of fluid and mass transfer in a dialysis patient
Carniel *et al.*	Mechanical behaviour of the heel pad in healthy and degenerative conditions
Casaroli *et al.*	Comparative evaluation of the effect of implant length and crown height in edentulous patients: a Finite Element study
Cremonesi *et al.*	Biomechanical characteristics of the swine knee menisci
Criscenti *et al.*	Biomechanics of medial patello-femoral ligament: mechanical and structural properties
Cristofanelli *et al.*	Influence of boundary conditions in an image-based model of left coronary tree
Danesi *et al.*	Stiffness, strength and strain distribution in the augmented vertebrae
De Gaetano *et al.*	Fluid dynamic performance of new polymeric heart valves prototypes tested under continuous and pulsatile flow condition
Dimasi *et al.*	Multiscale CFD and hemodynamic shearing device to support design of blood contact devices
Dordoni *et al.*	Nitinol peripheral stents: experimental validation of fatigue computational analyses
Etenzi *et al.*	Model of a stable passive bipedal walker provided with spring-damping legs
Ferraro *et al.*	Isogeometric Analysis: a novel computational approach to evaluate the performance of endovascular stents
Ferroni *et al.*	Fluid dynamics in porous scaffolds stimulated with cyclic squeeze pressure in the S2PR bioreactor
Fontanella *et al.*	Numerical analysis of the biomechanical behaviour of the forefoot
Forestiero *et al.*	Biomechanical behaviour of the foot ankle ligaments
Frigo *et al.*	Investigation of gastrointestinal tissues and structures biomechanical response
Guiotto *et al.*	Identification of diabetic neuropathic patients at risk of foot ulceration through finite element models and cluster analysis
Isu *et al.*	A virtual test bench for the assessment of the flow dynamics in hemodialysis catheters
La Barbera *et al.*	Preclinical evaluation of posterior spinal fixators: a parametric FEA on international standards
Marino *et al.*	Upscaling biochemical and biophysical effects in tissue mechanical modelling
Mazzoleni *et al.*	Effects of initial exposure to upper limb robot-assisted therapy in stroke patients
Meoli *et al.*	Cardiac biomechanics in patient-specific multi-scale models of single ventricle circulation
Morganti *et al.*	Investigation of TAVI outcomes through patient-specific finite element analysis: two clinical cases
Nava *et al.*	Synthetic three-dimensional niches to control mesenchymal stromal cell colonization in vitro
Scarton *et al.*	2-Dimensional foot FE models for clinical application in gait analysis
Serrani *et al.*	The influence of cardiac trabeculae on ventricular mechanics
Spatafora *et al.*	Optical, mechanical and biochemical characterization of trabecular bone
Terzini *et al.*	Influence of cell removal treatment on dermis mechanical behaviour

Terzini *et al.* Experimental set-up for the study of dental implant retrieval

Tunesi *et al.* Neuroprotective effect of mesenchymal stromal cells in a 3D model of Parkinson's disease

Venturato *et al.* Biomechanical behaviour of tibio-talar joint in stance and push-off configuration with degraded articular cartilage

Development of a Two-pool Virtual Simulator of fluid and mass transfer in a dialysis patient

C. Bianchi[1], G. Casagrande[1], and M.L. Costantino[1]

[1]*Dipartimento di Chimica, Materiali ed Ingegneria Chimica "Giulio Natta", Politecnico di Milano, Milan, Italy*

***Abstract*—This work aims at developing a Two-pool Virtual Patient Simulator able to predict the intra-corporeal mass and fluid transport occurring during the dialysis treatment of uremic patients. The optimisation of this device enables its use as a test bench for the evaluation of commercial or newly-developed dialysers and of the response of the patient to different dialyser membranes and therapy techniques.**

***Keywords*—Hemodialysis, In-vitro simulator, Test bench, Mass and fluid transport, Dialyser.**

INTRODUCTION

HEMODIALYSIS is the most commonly used therapy to replace renal function in uremic patients. Despite the technological improvements in the whole dialysis equipment and automatic control of the machine, this therapy is still associated with a significant rate of co-morbidity and mortality [1]. Indeed dialysis induces deep imbalances of the hydro-electrolyte equilibrium and fast changes in fluid volumes and electrolyte concentrations in the body compartments of the patients. The wide variability of the patients' response to the treatment demands a deep understanding of the mass and fluid transfer phenomena among the body compartments of the patient when connected to the dialysis machine, namely to the dialyser.

Several mathematical models [2-4] have been developed so far to describe fluids and solutes kinetics during dialysis in terms of intra-corporeal mass and fluid transport. However, to get a proper calibration of these models, a detailed knowledge of the depurative characteristics of the dialysers would be necessary. In fact the assessment of the filtering performances of commercial dialysis membranes (i.e. Clearance, Dialysance, Ultrafiltration) is usually related to a limited number of catabolites disregarding any possible interaction between these catabolites and other solutes, which can affect the membrane permeability during the whole duration of the dialysis session.

To bridge this gap and acquire more information about the filtering characteristics of the dialysis membranes and about the patient-to-dialyser interaction, a dedicated test bench should be required.

Aim of this work is to develop a Two-pool Virtual Patient Simulator (TVPS) capable to replicate the intra-corporeal mass and fluid transfer during dialysis. The TVPS will allow the thorough investigation of the filtering performances of commercial or newly developed dialysers and of the patient-to-dialyser interaction.

MATERIALS AND METHODS

In the first phase of the project a total of 13 patients treated with 3 different dialysis techniques were monitored for two months at Servizio di Nefrologia e Dialisi, I.R.C.C.S San Donato to acquire a set of clinical data to be used as a reference point for the development of the TVPS.

Preliminary design of the TVPS

The preliminary project specifications of the TVPS were defined based on an earlier simplified physical simulator prototype developed by our group. [5]

The main function of the TVPS is to replicate intra- and extra-vascular compartments of the patient. The former compartment has been reproduced by means of a rigid reservoir and a set of semi-permeable hollow fibres, which represent the large arterial and venous vessels and the capillary system respectively; the latter has been instead simulated by means of rigid reservoirs connected to a suitable compliance, whose value is comparable to the physiological interstitial compliance.

The semi-permeable hollow fibres were arranged in modular filters, which were *ad hoc* designed and constructed (Fig. 1) to be placed inside the extra-vascular rigid reservoir (Fig. 2). The semi-permeable membrane therefore represents the interface between the intra and extra-vascular compartments.

The test fluids have been prepared so as to reproduce the rheological properties, osmotic pressure and the electrolytes and catabolites contents, which are characteristic of the blood and the interstitial fluid of a uremic patient. A peristaltic pump has been used to replicate the cardiac output of the patient.

Theoretical calculations and functional tests of the depurative and hydraulic properties of the membrane have been carried out to define the dimensions of each component of the TVPS and the most manageable and efficient configuration. A shunt, equipped with a variable resistance, was added to control pressure and mass transfer across the fibres, since the permeability of the artificial membrane is higher than the one of the capillary membrane [6-7].

The simulator design has been optimised according to an *ad-hoc* developed computational model, which allowed the quantification of fluid and mass transport in the TVPS and the determination of the number of filters to be used to replicate the capillary system.

Experimental tests

An average dialysis session of 3.5 hours has been simulated.

The initial conditions (volumes, electrolyte and catabolite concentrations, osmotic pressures) in the TVPS were set according to the average clinical quantities (Table 1).

PARAMETERS OF THE SIMULATED DIALYSIS SESSION

Technique	Standard Hemodialysis (Bicarbonate Dialysis)
Blood flow	300 ml/min
Dialysate flow	500 ml/min
Duration	210 mins
[Sodium] in the dialysate	140 mmol/l
[Bicarbonate] in the dialysate	34 mmol/l
Ultrafiltration rate	0,9 l/h
Initial extra-vascular volume	41 l
Initial intra-vascular volume	6 l
Weight loss	3 kg

Table 1. Settings of an average dialysis simulation test

The TVPS was connected to a dialysis machine Gambro AK200.
The scheme of the test circuit is shown in Figure 3.
The experimental tests (Fig. 4) were performed using two different types of molecules (Polygelin and Dextran) to replicate blood oncotic pressure.
Pressure, flow rates and volume variations of the two compartments were monitored in the TVPS.
Fluid samples were collected from the TVPS at scheduled intervals to evaluate the trend of solutes concentrations in the intra- and extra-vascular compartments.
To evaluate the accuracy of the project, the outcomes of the TVPS have been compared to the clinical average trends of solutes concentrations and volumes.

RESULTS AND DISCUSSION

The proper transfer efficiency of the TVPS capillary system, was obtained by using 10 filtering modules and by setting the shunt flow rate at 50% of the cardiac output of the Virtual Patient, as suggested by the computational model outcomes.
All the experimental results showed to nicely reproduce the clinical patterns of electrolytes and urea concentrations. The values of these concentrations differ less than 20% from the clinical data when Polygelin is used to prepare the simulation fluid, while differ less than 10% when Dextran is used.
The intra-vascular volume profile shows a good correlation with the clinical conditions, mostly when Dextran was used. Moreover, the use of Dextran in the intra-vascular working fluid, allows a closer replication of the plasma-refilling phenomenon. This is mainly due to the higher steric hindrance of the membrane to Dextran with respect to Polygelin.
Also the extra-vascular volume shows to well replicate the plasma refilling phenomenon by displaying a decreasing trend due to a net flow from the extra-vascular to the intra-vascular compartment.

CONCLUSION

The experimental results obtained by the TVPS prove the overall reliability of the TVPS in reproducing the clinical conditions of an average uremic patient undergoing HD therapy.
However the TVPS performances in the simulation of the solutes concentration need to be improved. Two main actions can be adopted to overcome this limit.
A first action can be the automation of the fluid preparation procedure and of the priming of the TVPS so as to carefully manage possible variations in mass and fluid balance during this phase of the test.
A second action can consist in a more distributed sampling along the virtual patient during the HD session so as to get accurate information about the hydraulic conditions (*e.g.* pressure, volumes and flow rates) into each district of the TVPS.
The optimisation of the TVPS based on the said actions can make it suitable for the characterisation of commercial or newly developed dialysers, based on a thorough investigation of the filtering performances. Moreover the optimised TVPS will also permit the evaluation of the patient-specific response to the treatment and to the use of different dialyser membranes.
It is also worth to be noticed that the evaluation of the patient-to-machine/dialyser membrane interaction might also be suggested as an additional requirement for the assessment of dialysers efficiency and reliability prescribed by the international standards.

ACKNOWLEDGEMENT

We want to sincerely thank “Servizio di Nefrologia e Dialisi, I.R.C.C.S San Donato” with Dott.ssa Maria Doria, all the clinical staff and all the patients for their precious contribution to the project.
The project was funded by the Italian Ministry of Education, University and Research (MIUR) through National Relevant Research Program grant (PRIN 2009) entitled “Theoretical and experimental simulation of fluid and mass transfer to optimise patient hydro-electrolytic equilibrium during dialysis” (prot. 20093EJLKR).

REFERENCES

[1] Report del Convegno Annuale della Società Italiana di Nefrologia, 2010.
[2] Ursino, M. and L. Colì, *Prediction of solutes kinetics, acid-base status and blood volume changes during profiled hemodialysis.* Annals of Biomedical Engineering, 1999. 28: p. 204-216.
[3] Ki Moo Lim et al. *Numerical simulation of the effect of sodium profile on cardiovascular response to hemodialysis.* Yonsei Med J 2008; 49(4), pp 581 – 591.
[4] Waniewski J. *Mathematical modeling of fluid and solute transport in hemodialysis and peritoneal dialysis.* Journal of Membrane Science 2006; vol 274, pp 24-37.
[5] Casagrande, G., et al., *Physical simulator of fluid and mass transfer during dialysis.* Publications acts of International Journal of Artificial Organs, 2013.
[6] Tabei, K., et al., *An index of plasma refilling in hemodialysis patients*. Nephron, 1996. 74(2): p. 266-274.
[7] Schneditz, D., et al., *Nature and rate of vascular refilling during hemodialysis and ultrafiltration*. Kidney International, 1992. 42: p. 1425-1433.

Fig. 1. Modular filter to replicate the capillary system, ad hoc constructed. It is possible to note the longitudinal openings realised on the case, which let the intra-vascular fluid interface with the extra-vascular fluid across the capillary membrane

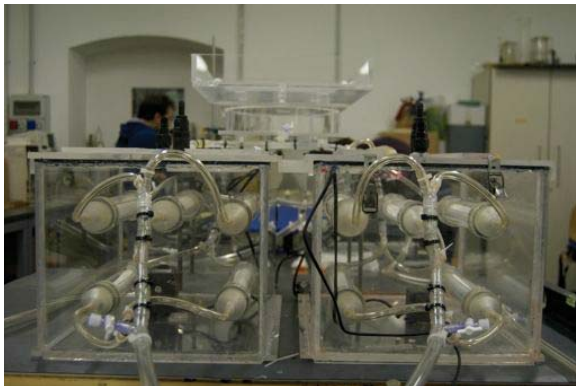

Fig. 2. Modular filters inserted in the extra-vascular reservoirs representing the Two-pool Virtual Patient Simulator. The upper tank represents the interstitial compliance.

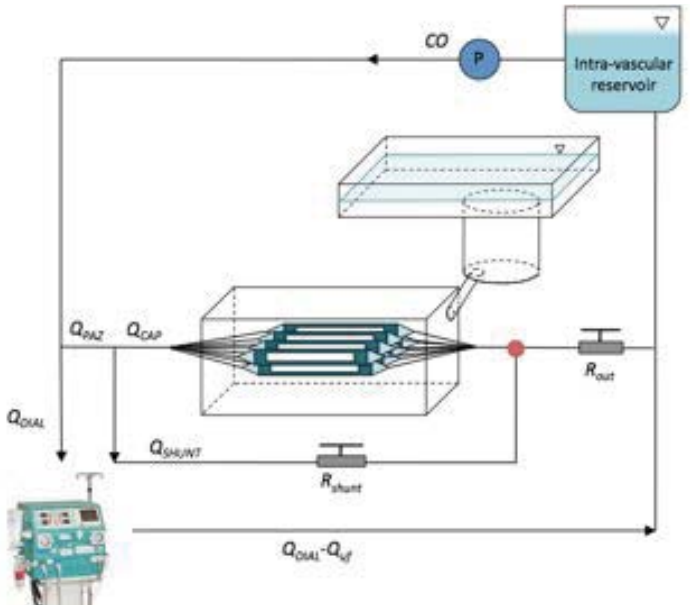

Fig. 3. Test circuit of the TVPS. CO = cardiac output; Q_{PAZ}=flow rate in the patient; Q_{CAP}=flow rate in the capillary system; Q_{SHUNT}=flow rate in the shunt; Q_{DIAL}=dialysis pump flow Q_{UF}=ultrafiltration rate; R_{SHUNT}=adjustable resistance of the shunt.

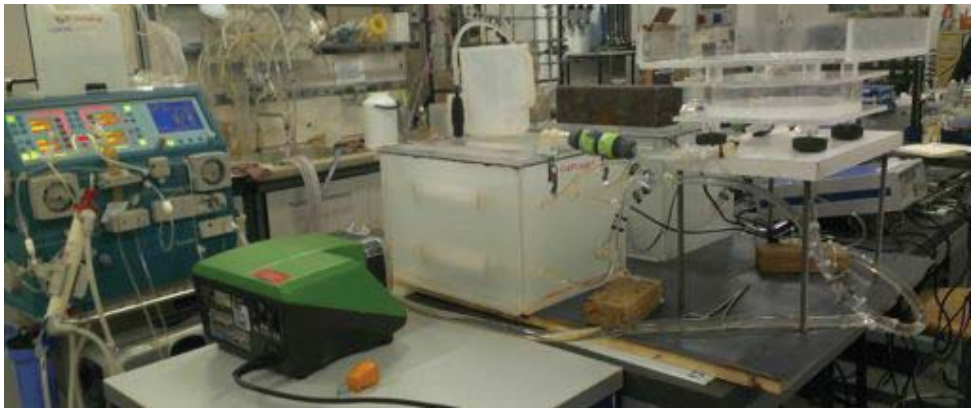

Fig. 4. The TVPS primed with the working fluids and connected to a commercial dialysis machine.

Mechanical behaviour of the heel pad in healthy and degenerative conditions

E.L. Carniel[1,2], C.G. Fontanella[2], and A.N. Natali[1,2]
[1] *Department of Industrial Engineering, University of Padova, Padova, Italy*
[2] *Centre for Mechanics of Biological Materials, University of Padova, Padova, Italy*

Abstract **- The aim of this work is to evaluate the mechanical response of the heel region in healthy and degenerative conditions by numerical methods. The heel pad acts as an interface between the calcaneum and the ground and its mechanical response is dependent on the properties of plantar and skin tissues. The plantar tissue has a specific honeycomb configuration, which is made up by adipose chambers enveloped by fibrous septa. Degenerative phenomena, as ageing, pathology or trauma, affect the histo-morphological configuration of this tissue and the mechanical properties. The biomechanical behaviour of the plantar fat pad is analyzed by a computational approach by means of the correlation between histo-morphological configuration and mechanical properties. Numerical meso-models composed by fibrous septa and adipose chambers are developed for both healthy and degenerative conditions. Moreover, a numerical macro-model of the heel region is developed and numerical analyses are performed to evaluate the influence of degenerative phenomena on the overall mechanical functionality of the heel structure.**

Keywords **- Soft tissue mechanics, plantar fat pad, degenerative phenomena, finite element analysis.**

I. Introduction

THE human heel pad, composed of plantar fat pad and skin, acts as an interface between the calcaneum and the ground, absorbing shock and distributing deformational effects in the surrounding foot tissues. Its ability to maintain body stability, to attenuate ground impact, to redistribute plantar pressures and to protect internal structures is due to its peculiar organization. The plantar fat pad is characterized by a honeycomb configuration in which fibrous septa envelope adipose compartments, which are further divided into fat globules by elastic transversal fibers. The fibrous septa originate from the calcaneus and extend toward the dermis, assuming specific shapes inside which the fibers are wound in spirals around the adipose chambers. The intact conformation of both fibrous and adipose tissues is a basic requirement for the proper functionality of the plantar fat pad. When degenerative phenomena, as aging, pathology or trauma, occur, adipose chambers get smaller, fibrous septa get thicker, fibrous components become disorganized because of breaking of collagen bundles and fragmentation of elastin strands. Such histo-morphological alterations induce significant modification of the tissue mechanical properties, as stiffening, lower strain threshold for injury, lower damping capabilities, and the plantar fat pad becomes unable to correctly perform its structural functionality [1],[2].

The relationship between histomorphological configuration and mechanical behaviour of the plantar fat pad tissue is investigated by a computational approach. Firstly, numerical meso-model of the plantar fat pad system are provided, accounting for different chamber dimensions and septa thickness, considering healthy and degenerative situations. These models are developed accounting for results from different experimental activities, with regard to both histological and mechanical investigations, and aiming at the identification of the tissue mechanics depending on histological configuration. Subsequently, a finite element model of the overall heel pad region is provided accounting for both healthy and degenerative conditions. The macro-model includes the plantar fat pad, the calcaneum, the skin and the other soft tissues. Parameters are identified accounting for the results from meso-models. For validation, indentation tests of the heel region are numerically analysed to investigate the influence of degenerative phenomena on the structural response of the system.

II. Materials and Methods

A. Numerical meso-model of plantar fat pad

Meso-models of the plantar fat pad in healthy and degenerative conditions are developed on the basis of previous models and specific histological measurements [1],[3]. In detail, adipose chambers are modeled as ellipsoids and hexagonal distribution is assumed. The model is composed by different layers, which are shifted each other according to the hexagonal scheme (Fig. 1a-b). Even if the actual distribution of tissue components is more spread, the assumed conformation well interpret the overall organization of the system. The numerical model is obtained by finite element discretization of the virtual solid model, using four-node tetrahedral elements (Fig. 1c-d). The mechanical behavior of the sub-components, as adipose chambers and fibrous septa, is described by specific constitutive formulations, as later reported. Numerical analyses are developed accounting for the boundary conditions of unconfined compression tests [2].

B. Plantar fat pad in healthy condition

The histological conformation of healthy adipose chambers suggests the isotropic and almost-incompressible behavior, while data from mechanical tests show the non-linear mechanical response. Accounting for such information, an hyperelastic isotropic constitutive formulation is assumed [3]. The septa are characterized by the anisotropic configuration of fibrous components and the non linear stress-strain behavior. A fiber-reinforced hyperelastic formulation is assumed with two collagen fibres families spirally wound around the adipose chambers, running in clockwise and

anticlockwise directions according to a 30 degrees angle [3].

C. Plantar fat pad in degenerative condition

In order to evaluate the effect of degenerative phenomena on the mechanical behaviour of adipose tissues and fibrous septa, further experimental investigations are analysed. Results from compression tests performed on degraded adipose tissue show the increase of tissue stiffness. An isotropic hyperelastic formulation is assumed. With regard to fibrous tissue, non enzymatic glycation processes of collagen structures usually develop because of degenerative phenomena, as aging or diabetes. Results from uniaxial tensile tests on collagen structures before and after non enzymatic glycation show a great increase of the tissue stiffness. Furthermore, glycation processes determine fragmentation and continuity loss of fibers and fibrils within the collagen structures. The consequent configuration of the collagen structures do not display distribution of the sub-components along any specific direction, and an isotropic model can be assumed.

D. Numerical macro-model of heel region

A numerical macro-model of the overall heel region is developed by finite element discretization of virtual models of plantar fat pad, skin, soft tissues (as muscles, plantar fascia and ligaments) and calcaneus (Fig. 2). Such models are obtained from MRI and CT images of cadaveric feet (Fig. 2a). The mechanical behavior of the calcaneus is defined by an orthotropic linear elastic formulation, while the soft tissues are described by an hyperelastic model. The anisotropic and nonlinear mechanical behavior of the skin is defined by a fiber-reinforced hyperelastic model [4]. A phenomenological visco-hyperelastic constitutive model is applied to interpret the mechanical response of the plantar fat pad [5]. Different sets of parameters are identified to specify the behavior of healthy and degenerative conditions, accounting for the stress-strain curves obtained by the meso-models. Specific numerical analyses are developed to evaluate the influence of degenerative phenomena on the overall mechanical behavior of the heel pad by indentation tests. The numerical model of the indenting platform is developed and boundary conditions are provided to fully fix the calcaneus and to move the platform towards the skin with a rate of 40 mm/s (Fig. 2c). The skin-indenter interface is modeled using a Columb contact strategy with a 0.42 friction coefficient.

III. Results

Numerical analyses are performed by the developed meso-models to evaluate the influence of degenerative phenomena on the compressive behaviour of plantar fat tissue. The comparison of results is reported in Fig. 3a and show the increase of tissue stiffness with degenerative phenomena, as reported by experimental activities. Furthermore, finite element analyses allow to investigate the stress distribution within the different sub-components and structures of plantar fat pad, as adipose chambers and fibrous septa (Fig. 3b-c).

Fig. 4 shows the results obtained by the numerical macro-model of the overall heel region. The contours of the displacement magnitude and minimum principal stresses fields are reported. The areas closer to the plantar region of contact between the indenter and the tissue are the mostly deformed. The analyses of the minimum principal stresses show that the stresses in the degradated heel pad are much larger compared to the healthy heel pad.

IV. Conclusion

Computational models are provided to investigate the influence of degenerative phenomena on the mechanical behavior of the heel pad. Numerical meso-models can be developed accounting for alterations of structural conformation and mechanical properties of plantar fat pad. The models well interpret the actual variations of stiffness due to degenerative phenomena. Numerical meso-models can be further applied to provide the stress-strain data that are required for the parameters identification of tissue constitutive formulations within numerical macro-models. Such models allow for the investigation of the overall functionality of the heel region. Results from numerical analyses show that the stress field in the degenerative configuration are larger in comparison with healthy heel pad, confirming the possibility of distortion of heel functionality.

With regard to the formulations proposed, as the meso- and the macro-models, both the approaches allow to deepen the knowledge of plantar tissues mechanics, finding application for the prevention of foot degradation. With regard to degenerative situations, critical mechanical conditions take place, particularly for subjects with low sensitivity to pressure and pain, as obese, elderly or neuropathic ones. Such conditions may induce micro-traumas of plantar tissues, which can degenerate to lacerations. Specific ortheses and footwear should be provided, accounting for damping materials. The proposed numerical models can be applied to investigate interaction phenomena between foot and ortheses [6], providing information for the footwear conformation design and materials properties identification.

References

[1] Y.N. Wang, K. Lee, W.R. Ledoux, “Histomorphological evaluation of diabetic and non-diabetic plantar soft tissue”, *Foot Ankle International*, vol. 32(8), pp. 802-810, 2011

[2] S. Pai, W.R. Ledoux, “The compressive mechanical properties of diabetic and non-diabetic plantar soft tissue”, *Journal of Biomechanics*, vol. 43, pp. 1754–1760, 2010.

[3] A.N. Natali, C.G. Fontanella, E.L. Carniel, “A numerical model for investigating the mechanics of calcaneal fat pad region”, *Journal of the Mechanical Behavior of Biomedical Materials* , vol. 5, pp. 216-223, 2012.

[4] A.N. Natali, C.G. Fontanella, E.L. Carniel, “Constitutive formulation and numerical analysis of the heel pad region", *Computer Methods in Biomechanics and Biomedical Engineering*, vol. 15(4), pp. 401-409, 2012.

[5] A.N. Natali, C.G. Fontanella, E.L. Carniel, and J. Miller-Young, “Biomechanical behavior of heel pad tissues: experimental testing, constitutive formulation and numerical modelling”, *Proceedings of the Institution of Mechanical Engineers, Part H: Journal of Engineering in Medicine*, vol. 225, pp. 449-459, 2011.

[6] C.G. Fontanella, A. Forestiero, E.L. Carniel, A.N. Natali, “ Analysis of heel pad tissues mechanics at the heel strike in bare and shod conditions”, *Medical Engineering and Physics*, vol. 35, pp. 441-447, 2013.

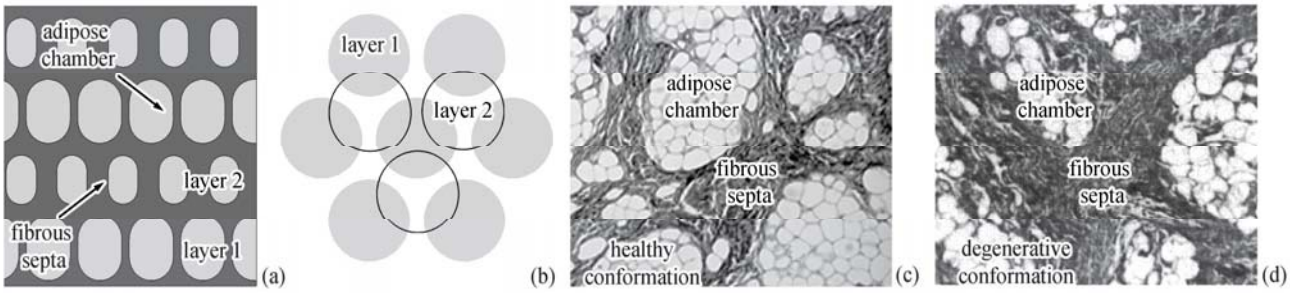

Fig. 1. Conformation of plantar fat pad tissue. Schematic representation of the distribution of adipose chambers and fibrous septa (a) according to an hexagonal scheme (b). Histology of plantar fat pad tissue with regard to healthy (c) and degenerative (d) conformations.

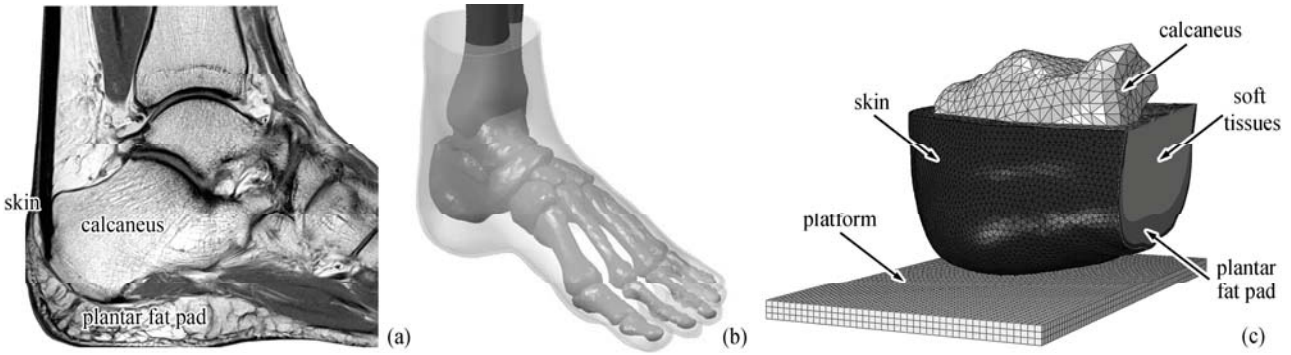

Fig. 2. Development of the numerical macro-model of the heel region. CT and MRI (a) images are processed to provide virtual solid models of the foot structure (b). Finite element discretization leads to the numerical model (c).

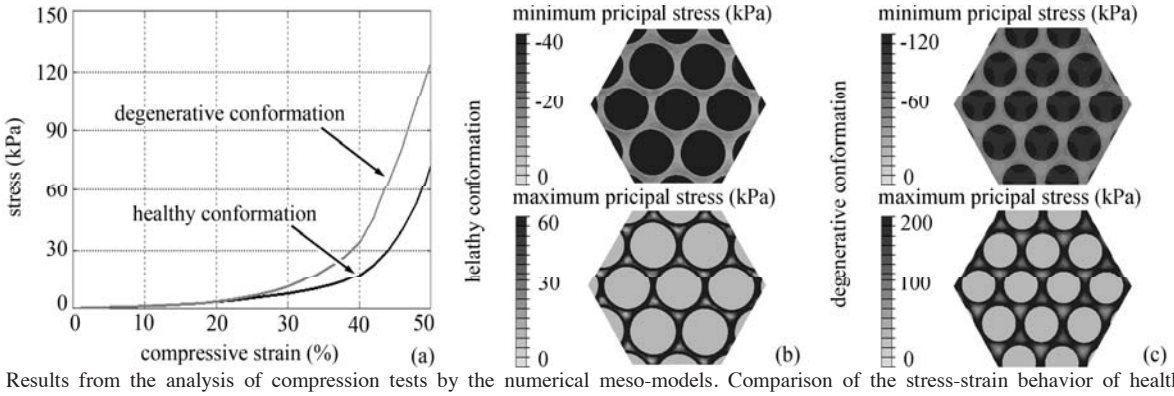

Fig. 3. Results from the analysis of compression tests by the numerical meso-models. Comparison of the stress-strain behavior of healthy and degenerative conformations (a). Contours of the minimum and maximum principals stress fields in plantar fat pad tissue in helathy (b) and degenerative (c) conditions.

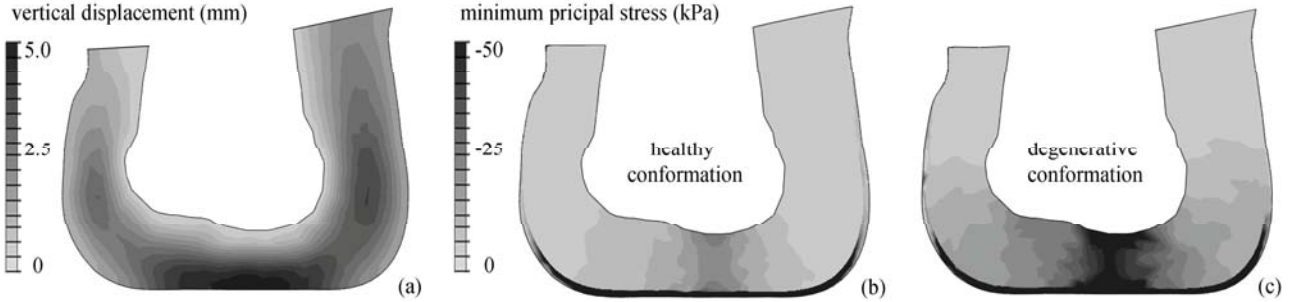

Fig. 4. Results from the analysis of indentations tests by the numerical macro-model. Contours of the vertical displacement filed (a) and the minimum principal stress field for healthy (b) and degenerative (c) conformations. Results are reported over a transversal section of the heel region.

Comparative evaluation of the effect of implant length and crown height in edentulous patients: a Finite Element study

G. Casaroli[1], N. Cavalli[2], L. Francetti[2], F. Galbusera[3] and T. Villa[1]
[1] *LaBS, Department of Chemistry, Materials and Chemical Engineering "G. Natta", Politecnico di Milano*
[2] *Department of Biomedical, Surgical and Dental Sciences, Università degli Studi di Milano*
[3]*IRCCS Istituto Ortopedico Galeazzi*

***Abstract*—Dental implants are widely used for rehabilitation of maxilla pathologies but in edentulous patients this treatment has some limits because of the excessive bone resorption. Short implants could be an alternative, but there is not a wide knowledge about their safety and strength of anchorage.**

In this study, a Finite Element Model was used to compare the bone stress state between single standard and short implants with crowns of different length used in clinical applications.

Results showed that under a sloping load the bone stress was higher in the cortical area than in the apical one, demonstrating that the cortical part is more involved in implant instability, and that it was higher with short implant and long crown than with the standard configuration. In spite of this, stress values were in a physiological range and can be considered biomechanically safe.

***Keywords*—Short dental implants, Finite Elements analysis, bone stress state.**

I. INTRODUCTION

OVER the years dental implants have been widely used for the rehabilitation of edentulous areas. Patient rehabilitated with implant-supported fixed partial dentures in the posterior region of the maxilla showed an improvement in the oral health quality of life if compared with those with removable partial dentures, particularly in the elderly ones.

Especially in the posterior region of jaws, reduced alveolar bone height represents a limitation in the use of dental implant and increases the probability of possible damages to some anatomical structures [1].

Short implants can be considered an alternative treatment option. Biomechanical studies demonstrate that the crestal portion of the implant body is the part that is most involved in load bearing, whereas very little stress is transferred to the apical portion [2]. The aim of this study is to demonstrate that the length of the implant has a low impact on its anchorage strength and that using an outsize crown due to the extensive resorption does not cause a dangerous state of stress in bone from a biomechanical point of view.

II. MATERIALS AND METHODS

A. Generation of the model

The 3D geometry of edentulous maxilla was reconstructed from computerized tomography (CT) of an edentulous patient. The structure symmetry permitted the reconstruction of a half maxilla. After generating a mesh using Avizo software, the mesh was transferred back to the segmentation software for material properties assignment. The Grey Value (GV) was used for Elastic Modulus calculation using the empirical formula

$$\rho = 1017 * GV - 13.4 \quad (1)$$

$$E = 5925 * \rho - 388.8 \quad (2)$$

where GV is Grey Value (ranging from 0 (black) to 255 (white)), ρ is density and E is Elastic Modulus [3]. The range of GVs was divided into 10 equal size intervals each representing a material. Then the mesh of the maxilla was imported in Abaqus 6.10 for the analysis. Implants of two different lengths were meshed and implanted in molar position. The implant dimensions were 4 mm diameter x 11 mm length (regular length implants) and 4 mm diameter x 6 mm length (short implants). A superstructure representing a porcelain crown was built using beam elements. Three configurations have been compared: regular implant with 8 mm crown (A) and short implant with 8 mm or 13 mm crown (B and C) (Fig. 1). The implant and the maxilla have been assembled locating the implant in molar position and the translational degrees of freedom of the implant's nodes were kinematical constrained to the corresponding degrees of freedom of the maxilla's elements where the implant's elements lied in. Two set of elements were created for the analysis: the first one considered the whole bone-implant interface and the second one only the coronal area. Both parts were 1.5 mm thick and the coronal one was 2.5 mm height.

B. Boundary conditions and loads

A symmetry boundary condition was applied to the nodes belonging to the plane of symmetry. The nodes belonging to sagittal plane, coronoid process and maxilla angle were kept fixed. A vertical and 45° sloping concentrated loads of 200 N representing the masticatory forces were applied to the crown.

III. RESULTS

Static analysis was performed and simulation results were evaluated in terms of Von Mises stresses, maximum and minimum principal stresses. Results have been analysed in terms of stress distribution using maximum and minimum values, first, second and third quartile; the value considered for the analysis was third quartile because it represents 75%

population. The finite elements analysis has been conducted for three different single implant configurations.

When a vertical load is applied, stress distribution is more homogeneous all around the implant than in the case of a sloping load; indeed in this case the stress is higher in coronal area with respect to the apical one (Fig. 2) . Von Mises stress distribution is 47, 57 and 27% higher in coronal area than in the interface for A, B and C configurations respectively when a sloping load is applied. On the contrary, when a vertical load is applied stress distribution is just the same for B and C while is 30% lower for A. Von Mises stress distribution, Maximum and minimum principal stress distribution are listed in table I.

TABLE I
STRESS VALUES IN STUDIED CONFIGURATIONS

	Von Mises		*Max Principal*		*Min Principal*	
Vertical load (MPa)						
A	2.07	1.46	0.46	0.24	-1.07	-0.49
B	3.02	3.25	0.46	0.38	-1.73	-1.86
C	3.02	2.95	0.46	0.45	-1.73	-1.66
Sloping load (MPa)						
A	7.16	10.55	3.27	6.92	-1.42	-1.93
B	10.48	16.49	4.37	9.49	-1.57	-2.44
C	15.16	19.32	6.74	11.02	-2.41	-2.13

IV. Conclusion

The higher stress in the coronal part of the bone generated by sloping load demonstrates that implant instability, if present, may be related to a local bone failure in this area. In contrast, vertical load generates higher stress state in the apical zone in all configurations for structural reasons. The effect of the length of the implant and the height of the crown both increase the stress state. In spite of this, the stress value is in a physiological range and it is not to be considered dangerous for clinical application. Therefore, short implants with higher crowns can be considered a safe alternative to standard implants from a biomechanical point of view.

References

[1] S. Annibali, M. P. Cristalli, D. Dell'Aquila, I. Bignozzi, G. La Monaca and A. Pilloni, "Short dental implant: a systematic review," in *J Dent Res*, 91 (1): 25-32, 2012.

[2] L.B. Lum, "A biomechanical rationale for the use of short implants," in *J Oral Implantol*, 17: 126-131, 1991.

[3] P. Xin, P. Nie, B. Jiang, S. Deng, G. Hu, S.G. Shen , "Material assignment in finite element modeling: heterogeneous properties of the mandibular bone," in *The Journal of cranial surgery*, 24(2): 405-410, 2013.

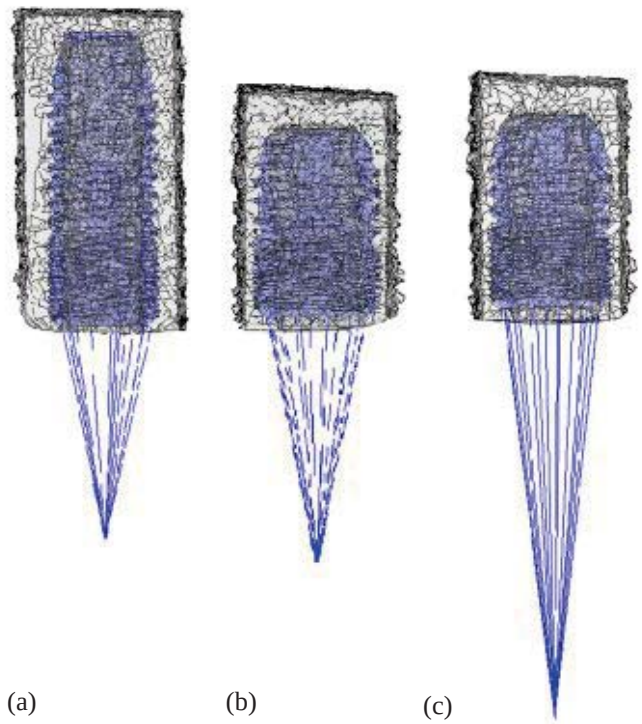

Fig. 1. Implant configurations: (a) Regular implant with regular crown, (b) short implant with regular crown and (c) short implant with long crown.

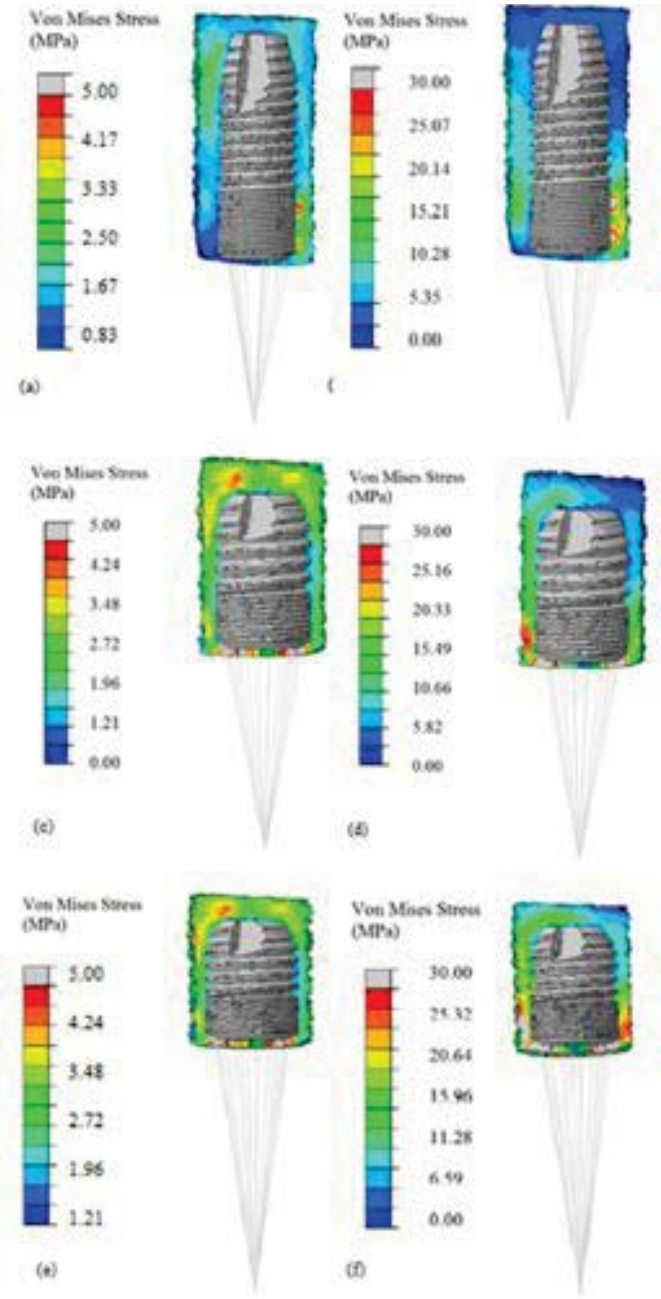

Fig.2 Von Mises state of stress generated by vertical (a, c and e) and sloping load (b, d and e) in studied configurations (standard implant with standard crown – a and b, short implant with standard crown – c and d, short implant with long crown – e and f).

Biomechanical characteristics of the swine knee meniscus

S. Cremonesi[1], L. Abbiati[1], G.M. Peretti[2,3], F. Boschetti[1,3]
[1]*LaBS, Dipartimento di Chimica, Materiali e Ingegneria Chimica, Politecnico di Milano, Milano, Italy*
[2]*IRCCS Istituto Ortopedico Galeazzi, Milano, Italy*
[3]*Dipartimento di Scienze Biomediche per la Salute, Università degli Studi di Milano, Milano, Italy*

***Abstract*— The purpose of this study was to examine the compressive and tensile properties of the swine meniscus as a function of anatomical origin (lateral vs. medial) and region (femoral, tibial, anterior, central and posterior). The extracted parameters are the tensile and compressive Young modulus, the aggregate modulus, the Poisson's ratio and viscoelastic properties.**

Results indicate significant differences in the extracted parameters depending on the anatomical location and on the position within the meniscus thickness. In particular, posterior regions resulted stiffer than anterior and central regions, and femoral layers resulted stiffer than the tibial ones.

***Keywords*— meniscus, compression, tension, modulus.**

I. Introduction

The menisci of the knee are complex fibrocartilaginous tissues that play important roles in load bearing, shock absorption, joint lubrication and stabilization [1].

Few studies in literature have been conducted on swine meniscus, most having characterized the human or bovine meniscus [2,3].

The objective of this study was to characterize the time-dependent behavior of the whole swine meniscus. The viscoelastic properties are observed by a mechanical response of the meniscus to confined and unconfined compression tests and to uniaxial tensile tests.

We measured the compressive Young modulus from unconfined compression tests, the aggregate modulus from confined compression tests and the tensile Young modulus and Poisson's ratio from tensile tests.

II. Materials and Methods

A. Specimen preparation

Ten menisci were analyzed (five medial and five lateral), each one was sectioned through the thickness in two parts obtaining the tibial (T) and the femoral (F) zones; within each zone three cylindrical plugs, perpendicular to the tibial and femoral surfaces, were obtained ($\Phi=7mm$) representing the anterior (A), central (C) and posterior (P) region; rectangular samples were also obtained from the femoral and tibial zones (Figure 1). Each specimen was rinsed in 0.9% saline solution and then frozen at -24°C until the time of testing. Before the test, each samples was thawed at room temperature for about 30 min. Cylindrical samples were tested in compression under confined configuration and, after re-equilibration in saline solution, under unconfined configuration. Rectangular samples were tested in tension.

All tests were performed at room temperature using an electromagnetic testing machine (Bose Elf3200, Bose, Eden Praire, MN, USA), equipped with a 220 N load cell.

B. Confined compression tests

A cylindrical disc of tissue was put on a rigid sintered stainless-steel filter, constrained laterally by a close-fitting impermeable stainless-steel confining chamber filled with saline, and then loaded by a stainless-steel piston ($\Phi=7mm$). After ensuring the contact between the specimen and the piston, the sample was subjected to a multi-ramp stress relaxation test, made of five increasing 4% strains at a velocity of 0.1%/s, followed by stress relaxation to equilibrium for 600 s. The aggregate modulus, H_A, was evaluated for each ramp from the equilibrium data as the ratio between the relaxation stress value and the fixed 4% strain.

C. Unconfined compression test

The cylindrical sample was placed in a Plexiglas chamber; after the contact between the sample and the piston ($\Phi=9mm$) was achieved, saline solution was added to the chamber to ensure sample hydration during the test. The test conditions were the same as the previous ones (confined compression test), i.e. multi-ramp stress relaxation test using the same strain, velocity and relaxation time values. The compressive Young modulus, E, was obtained for each ramp from the equilibrium data as the ratio between values of relaxation stress and the corresponding values of strain.

D. Uniaxial Tension Test

After thawing the sample to be tested at room temperature, one side of the sample surface was marked by waterproof India ink to obtain a grid for optical strain measurements. The specimen was then mounted between the two machine jaws. A custom made chamber filled with saline was used to keep the sample hydrated during the test. The specimen was submitted to a multi-ramp stress-relaxation test, made of ten increasing 4% strains at a velocity of 0.1%/s, followed by stress relaxation to equilibrium for 1200 s. The tensile Young modulus was determined for each ramp from the equilibrium data as the ratio between the relaxation stress value and the fixed 4% strain.

III. Results

Typical stress-relaxation plots of our tests are shown in Figure 2.

The compressive Young modulus, E, of the medial and lateral meniscus increases with strain for every zone (A, C, P) and for each layer (T and F). Due to high variability of results, it is not possible to observe any difference of E among the A, C, and P zones (Fig. 3). Femoral layers show higher E values than T layers (Fig. 4), although differences are not statistically significant (t-test, $p>0.05$). Similar results are obtained for the aggregate moduli.

Stress-strain plots obtained from the equilibrium stresses of the tension tests for a few samples are shown in Fig. 5. The plots show a great variability among different samples, the value of strain relative to the peak stress also varying among samples. The tension Young modulus, E_{tr}, for strains up to 16% is averaged among samples and shown in Fig. 6. Values of E_{tr} increase with strain, with generally higher values for the T layers compared to the F layers, although differences are not statistically significant. Fig. 6 also shows a typical image of a sample under tension with the grid for evaluation of axial and lateral strains to be used for the optical evaluation of the Poisson's coefficient (preliminary results indicate values higher than 1, a sign of anisotropy).

IV. Conclusion

We have performed a mechanical characterization of ten swine menisci by means of compression and tension tests. The results of our investigation show that the meniscus is a non linear, anisotropic, non-homogeneous material: mechanical parameters increase with strain, depend on the direction of load, vary among zones (anterior, central, posterior), and layers (femoral or tibial).

References

[1] P. Bursac,"Dynamic compressive behaviour of human meniscus correlates with its extra-cellular matrix composition", Biorheology 46, pp. 227–237 , 2009.

[2] H. N. Chia, "Compressive Moduli of the Human Medial Meniscus in the Axial and Radial Directions at Equilibrium and at a Physiological Strain Rate", *Journal of orthopaedic research July 2008*

[3] C. S. Proctor, "Material Properties of the Normal Medial Bovine Meniscus", *Journal of Orthopaedic Research* 7, pp. 771-782, New York, 1989.

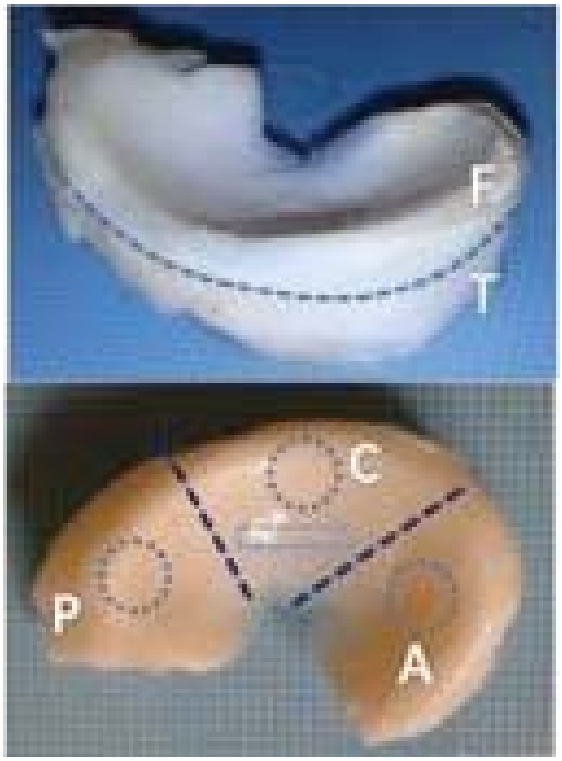

Fig 1. Sample preparation. Cylindrical plugs and rectangular samples (bottom image) were obtained for compression and tension tests respectively, after sectioning the meniscus through the thickness, in two layers, namely the femoral layer, F and the tibial one, T (top image).

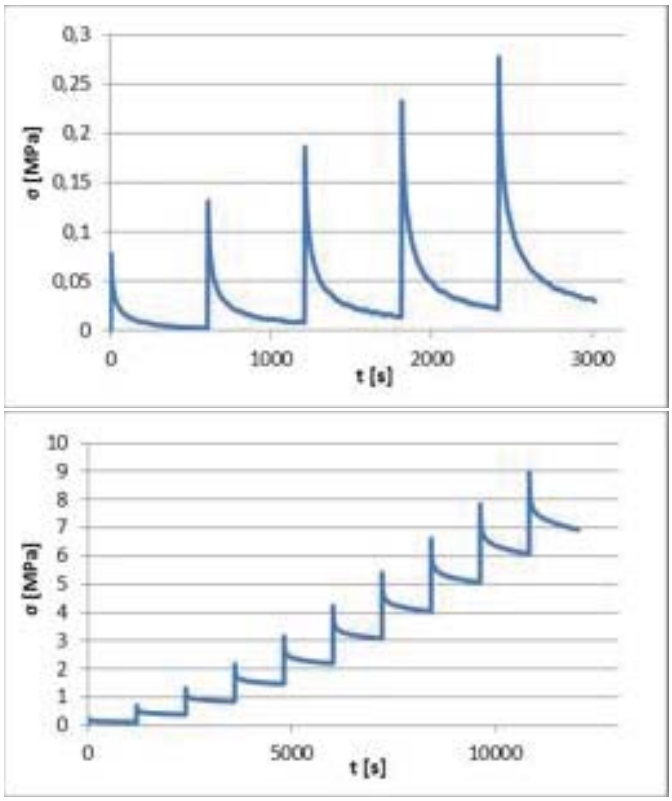

Fig. 2. Typical stress-relaxation plots for compression (top) and tension (bottom) tests.

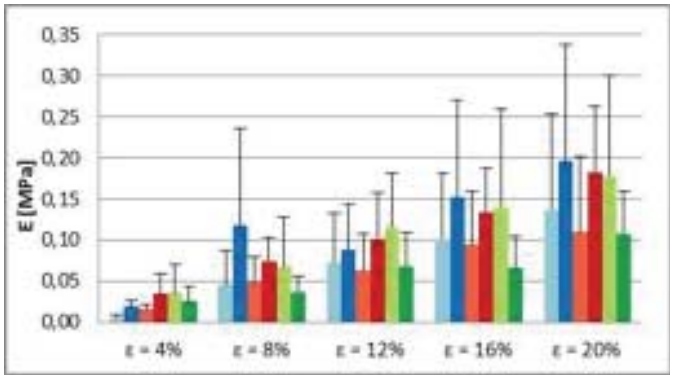

Fig.3: Average of compressive Young moduli, E, of medial (light colours) and lateral (dark colours) menisci for the anterior (blue), central (red) and posterior (green) regions.

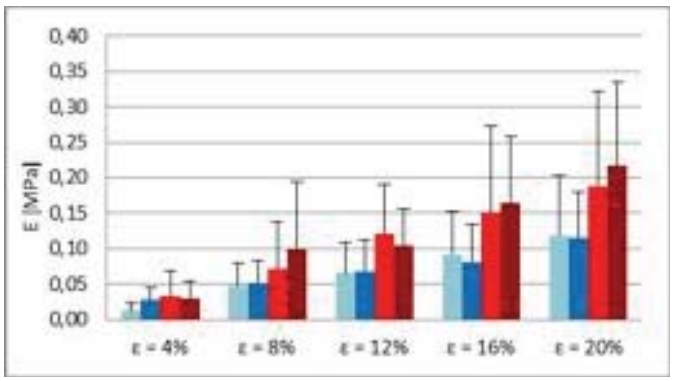

Fig.4: Average of the compressive Young moduli, E, of medial (light colours) and lateral (dark colours) meniscus; blue: samples from the tibial section, and red: samples from the femoral sections.

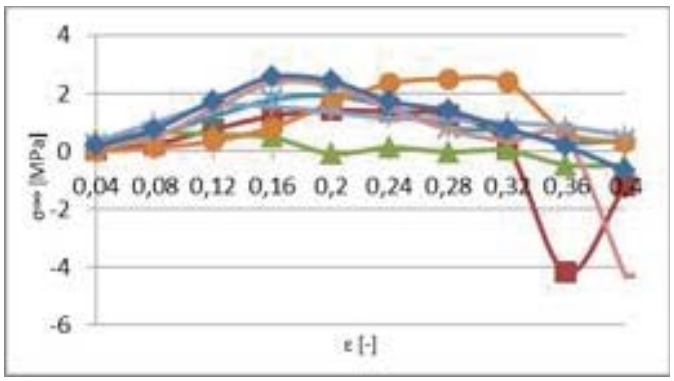

Fig.5: Examples of stress-strain plots from the equilibrium data of tensile stress-relaxation tests.

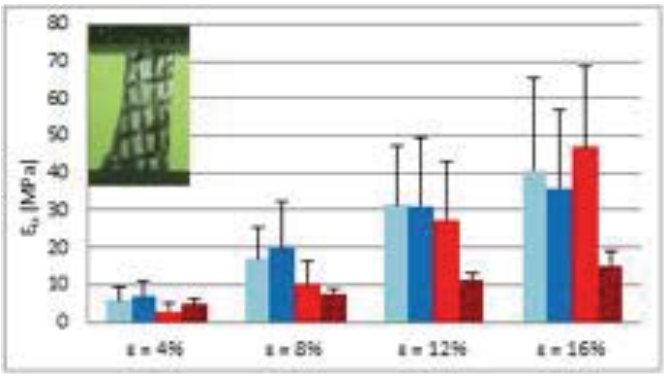

Fig. 6. Average of the tensile Young moduli, E_{tr}, of medial (light colours) and lateral (dark colours) menisci; blue: samples from the tibial section, and red: samples from the femoral sections. A typical image for optical evaluation of the Poisson coefficient from tension tests is also shown.

Biomechanics of Medial patello-femoral ligament: Quasi-linear viscoelastic properties

G. Criscenti[1,2], C. De Maria[2], M.Tei[1,3], E. Sebastiani[1,3],G. Placella[1,3],A. Speziali[1,3] and G. Cerulli[1,3]
[1] *Istituto di Ricerca Traslazionale per l'Apparato Locomotore -Nicola Cerulli- LPMRI, Via Einstein 12, 52100 Arezzo, Italy*
[2] *Research Center "E. Piaggio", University of Pisa, Largo Lucio Lazzarino 1, 56126 Pisa, Italy*
[3] *Department of Orthopedic surgery, University of Perugia, via S.Andrea delle Fratte 1, 06134 Perugia, Italy*

***Abstract*— The Medial Patello-femoral Ligament (MPFL) is considered the most important passive patellar stabilizer and it displays time- and history-dependent viscoelastic behavior. In this work, 15 human knees have been tested to evaluate the quasi-linear viscoelastic properties of this ligament.**

***Keywords*—Medial patello-femoral ligament, quasi-linear viscoelasticity, ligament biomechanics.**

I. Introduction

THE Medial Patellofemoral Ligament (MPFL) displays time- and history-dependent viscoelastic behavior, and is nonlinear in its stress-strain response. This behavior results from the complex interaction among collagen, elastin, proteoglycans and water and it is usually described by the quasi-linear viscoelastic theory (QLV) proposed by Fung [1]. In order to describe the viscoelastic behavior of the MPFL, the objective of this study was to determine and validate the five constants used by the QLV theory to describe the instantaneous elastic response and reduced relaxation function on experiments with finite ramp times followed by stress relaxation to equilibrium [2].

II. Materials and Methods

A. Preparation of the specimens

A total of 15 human cadaveric knees from 6 women and 8 men with a mean age of 75 ± 9 years were used. None of these showed patellar instability, knee injuries, surgical procedures or arthritic deformations. The cadavers were dissected after they have been stored for 24 hours at 4°C and then were preserved in a sterile gauze, sealed in a polyethylene bag, labelled and stored at -18°C. They were thawed at a temperature of 4°C when required. Finally, the result of dissection was the femur-MPFL-patella complex where the MPFL was the only link between the femur and patella (Fig. 1). The MPFL was found in all the examined knees. After dissection, the length, the thickness, the width and the cross-sectional areas of the MPFL at patellar insertion, mid-substance, and femoral insertion were measured using a caliber and a micrometer.

B. Stress relaxation tests

Fifteen human fresh frozen MPFL were dissected to obtain the correct length-to-width aspect ratio (4:1) and a constant cross-sectional area. The specimens were left in a saline bath at 37°C for 30 minutes, then were fixed with cyanoacrilate and sandpaper in standard clamps and aligned to the 5kN load cell of an Instron 5965 material-testing machine. Strain at the midsubstance was measured using a custom-made optical system composed of a camera and 4 markers (3 mm diameter) positioned on four different areas to evaluate the ligament elongation and eventual slippage (Fig. 2). In order to reduce tissue hysteresis, the specimens were preloaded with a force of 1N and preconditioned by a series of ten cycles until reaching the strain of 3% with a strain rate of 0.1%/s. Subsequently, a stress relaxation test was performed by elongating the MPFL to 6% strain and held for 60 minutes. The time until the peak load was 19,9 s (t_0). The slow loading rate was selected to prevent the possible errors as inaccurate strain measurements and overshoot related to fast strain rate [3]. It implies a linear behaviour of strain-time curve before t_0 and a constant one for $t > t_0$. The total percentage of stress relaxation was defined in Eq. (1):

$$\%SR = \frac{\sigma(t_0) - \sigma(t_\infty)}{\sigma(t_0)} \cdot 100 \quad (1)$$

where $\sigma(t_0)$ was the peak stress at t_0 and $\sigma(t_\infty)$ was the the stress measured at the end of the test. The nonlinear stress-strain and stress-time curves were obtained from the loading and relaxation phases of this test. These experimental data were used in combination with the quasi-linear viscoelastic theory (QLV) to characterize the tissue's reduced relaxation function, G(t), (described by constants C, τ_1 and τ_2) and its elastic response, $\sigma^e(\varepsilon)$ (described by constants A and B). For validation, the obtained constants were used to predict the results of a separate cyclic stress relaxation experiment [4]. In particular, 10 cycles of deformation between 4% and 6% at 0.3%/s and the corresponding peak stresses were recorded.

C. Quasi-linear viscoelastic theory (QLV)

The QLV theory was utilized to describe the time- and history-dependent viscoelastic and nonlinear mechanical properties of the MPFL. The Fung's theory assumes that the stress relaxation behavior of soft-tissue is expressed by the Eq. (2).

$$\sigma(t) = G(t) * \sigma^e(\varepsilon) \quad (2)$$

where $\sigma^e(\varepsilon)$ is the instantaneous elastic response and represents the maximum stress in response to an instantaneous step input of strain, ε. G(t) is the reduced relaxation function, which represents the time dependent stress response of the tissue normalized by the stress at the time of the strain step input. This function was proposed by Fung to describe the sensitivity of soft tissues to strain rate.
Using the Boltzmann superposition principle, the stress at time *t*, σ(t) is given by the convolution integral of the strain history and $G(t)$ (Eq. (3)):

$$\sigma(t) = \int_{-\infty}^{t} G(t-\tau)\frac{\partial \sigma^e(\varepsilon)}{\partial \varepsilon}\frac{\partial \varepsilon}{\partial \tau}\partial\tau \quad (3)$$

Fung chose the concept of a continuous relaxation spectrum and described the reduced relaxation function as in Eq. (4):

$$G(t) = \frac{1 + C[E_1(t/\tau_2) - E_2(t/\tau_1)]}{1 + C\ln(\tau_2/\tau_1)} \quad (4)$$

and

$$E_1(y) = \int_y^{\infty} \frac{e^{-z}}{z} dz \quad (5)$$

where Eq. (5) is the exponential integral, and C, τ_1 and τ_2 are material constants. The dimensionless constant C represents the magnitude of viscous effects and is related to the percentage of relaxation. The time constants τ_1 and τ_2 describe initial and late relaxation, respectively, relating to the slope of the stress-relaxation curve at early and late time periods. The instantaneous elastic response was described by the exponential approximation in Eq. (6):

$$\sigma^e(\varepsilon) = A(e^{B\varepsilon} - 1) \quad (6)$$

where A and B are material constants [4]. The constant B represents the rate of change of the slope of the stress-strain curve and the product AB is the initial slope of the curve. Utilizing the methodology proposed by Abramowitch et al [2], we considered the use of slow strain rates during the loading phase of a stress relaxation test. This method showed a unique solution that was minimally sensitive to systematic and random experimental noise. Substituting Eqs. (4) and (6) into Eq. (3), the stress resulting from elongating the sample with a constant strain rate γ over the time $0 < t < t_0$ was:

$$\sigma(t) = \frac{AB\gamma}{1 + C\ln(\tau_2/\tau_1)} \int_0^t \left\{1 + C\left(E_1\left[\frac{t-\tau}{\tau_2}\right] - E_1\left[\frac{t-\tau}{\tau_1}\right]\right)\right\} e^{B\gamma\tau}\partial\tau \quad (7)$$

Similarly, the stress relaxation from t_0 to $t = \infty$ was:

$$\sigma(t) = \frac{AB\gamma}{1 + C\ln(\tau_2/\tau_1)} \int_0^{t_0} \left\{1 + C\left(E_1\left[\frac{t-\tau}{\tau_2}\right] - E_1\left[\frac{t-\tau}{\tau_1}\right]\right)\right\} e^{B\gamma\tau}\partial\tau \quad (8)$$

D. Parameters estimation and validation

On the basis of the minimal strain rate sensitivity of stress-strain curve for ligaments, constant A was determined by curve-fitting Eq. (6) to the experimental stress–strain data obtained from the loading portion of the stress relaxation experiment. Constants B, C, τ_1 and τ_2 were obtained substituting constant A in Eq. (7) and Eq. (8) using simultaneously curve fitting of the experimental stress-time data of the loading and relaxation portions of the stress relaxation test. For nonlinear optimization, this study utilized a modified Levenberg–Marquardt algorithm [2].

To validate our results, the constants obtained with the stress-relaxation experiment were used in Eq. (3) to predict the theoretical peak stresses at every cycle (determined on the basis of an approximated cyclic strain–time history) from a separate cyclic stress relaxation test [4]. These peak stresses were then compared to those obtained experimentally during the cyclic stress-relaxation test.

III. Results

The obtained constants are summarized in Table I.

TABLE I
CONSTANT ESTIMATION

	A *(MPa)*	*B*	*C*	τ_1 *(s)*	τ_2 *(s)*
Mean	1.21	26.03	0.11	6.32	903.5
SD	0.96	4.16	0.02	0.02	504.7

At the end of the loading phase, the corresponding stress was 4.1 ± 3.2 MPa and presented a non-linear trend. Most of the relaxation occurs within the first 20 minutes. After 60 minutes, the total stress relaxation was 32,7 ± 4,7%. The QLV theory allows a proper fit of the experimental data for each sample evaluated with a $R^2 = 0{,}993$ (Fig. 3). τ_2 measured more than three order of magnitude larger than τ_1, suggesting that the assumption of a continuous relaxation spectrum is valid. For validation, the constants A, B, C, τ_1 and τ_2 obtained from the strain history approach could accurately describe the experimental data of the cyclic stress relaxation test for each specimen. Fig. 2 shows that the average peak stresses of theoretically predicted values closely match the average experimentally measured values. Error between the prediction and experimental data ranged from 0.5% to 3.1% for the best prediction and 9.7% to 17.4% for the worst one. In general, the prediction of the initial peak stress was the most erred for all specimens and the average error for this peak measured 6.5 ± 6.1% across all specimens.

IV. Conclusions

The obtained results demonstrate that the QLV theory could be successfully used to describe the viscoelastic behavior of the human medial patello-femoral ligament. Utilizing the methodology proposed by Abramowitch et al that involves the use of slow strain rate during the loading phase of a stress relaxation test, the five constant of QLV theory were determined. The study of the viscoelastic properties is fundamental to understand the contribution of the medial patello-femoral ligament as patellar stabilizer and for the selection of methods of repair and reconstruction.

References

[1] Y. C. Fung, “Stress Strain History Relations of Soft Tissues in Simple Elongation”, in *Biomechanics: Its Foundations and Objectives*, eds. Y. C. Fung, N. Perrone, and M. Anliker, PrenticeHall, Englewood Cliffs, NJ, 1972, pp. 181–207.

[2] S. D. Abramowitch and S. L.-Y. Woo, “An Improved Method to Analyze the Stress Relaxation of Ligaments Following a Finite Ramp Time Based on the Quasi-Linear Viscoelastic Theory”, *J. Biomech. Eng.*, vol. 126, no. 1, p. 92, Mar. 2004.

[3] J. R. Funk, G. W. Hall, J. R. Crandall, and W. D. Pilkey, “Linear and Quasi-Linear Viscoelastic Characterization of Ankle Ligaments”, *J. Biomech. Eng.*, vol. 122, no. 1, p. 15, Feb. 2000.

[4] S. L.-Y. Woo, M. A. Gomez and W. H. Akeson, “The Time and History-Dependent Viscoelastic Properties of the Canine Medial Collateral Ligament”, *J. Biomech. Eng.*, vol. 103, no. 4, p. 293, Jun. 2009.

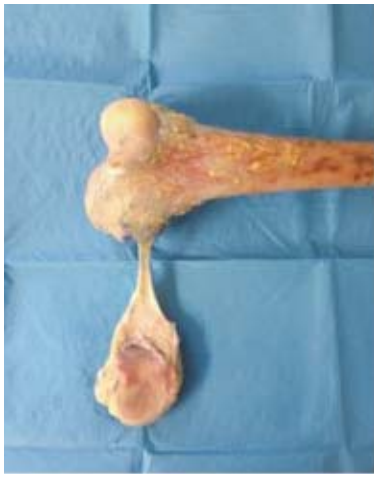

Fig. 1. MPFL dissected specimen

Fig. 2. Isolated ligament Stress relaxation test setup

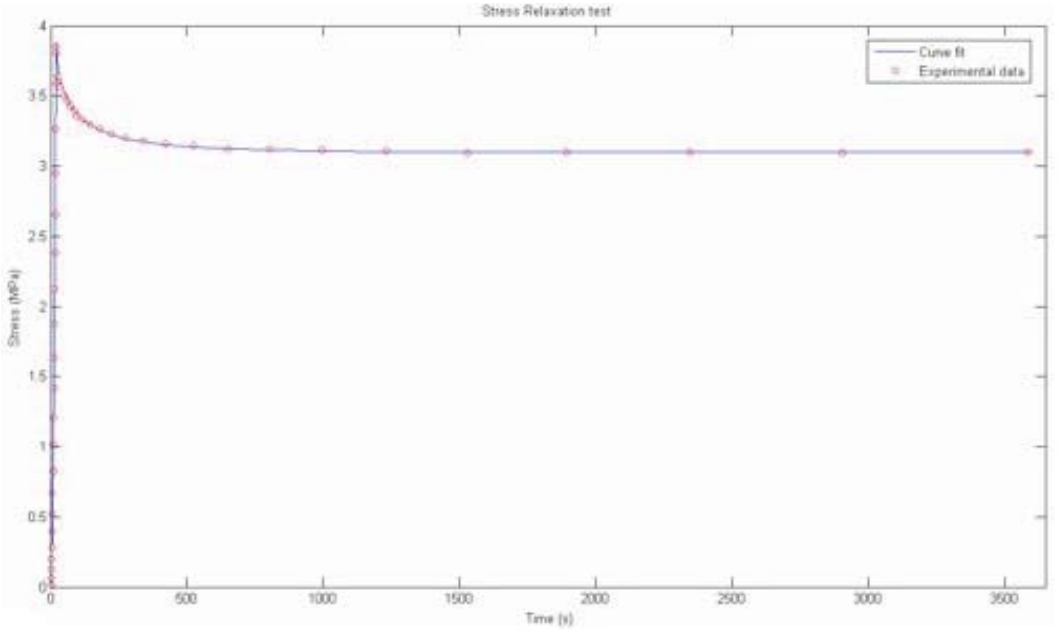

Fig. 3. Typical curve fitting of the experimental data with the QLV theory

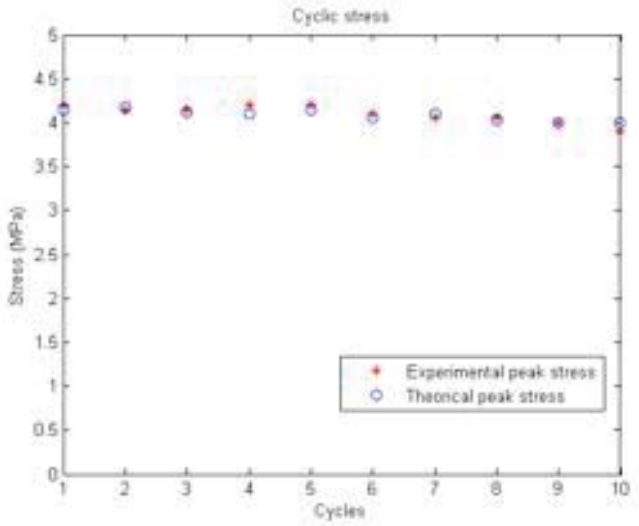

Fig. 4. Best prediction of peak stresses of a cyclic loading history based on the constant obtained from the stress relaxation experiment using the strain history approach for individual specimens

Influence of boundary conditions in an image-based model of left coronary tree

S. Cristofanelli[1], D. Gallo[1], J.C. Kim[2], D. Massai[1] and U.Morbiducci[1]
[1] Department of Mechanical and Aerospace Engineering, Politecnico di Torino, Turin, Italy
[2] Department of Nephrology, Ospedale San Bortolo, Vicenza, Italy

***Abstract*—The onset and development of vascular pathologies have been linked to disturbances of blood flow and altered wall shear stress (WSS). The aim of this work is to go into detail of the relationship between local hemodynamics and disorder using computational fluid dynamics (CFD), in particular evaluating the impact that the different strategies applied at boundaries have on local flow. Hemodynamic simulations data of left coronary artery (LCA) tree model were obtained varying imposed boundary conditions (BCs). WSS-based descriptors and helicity-based indicators of intraluminal flow structures were obtained from the simulations. Assumptions at boundaries influence the magnitude of WSS-based descriptors, rather than their distribution. Atherosusceptible areas are located close to bifurcations and in tortuous segments. Furthermore, in proximity of bifurcations the bulk flow arranges in complex helical flow patterns, which could be related to perfusion. This topology is modestly influenced by BCs but principally by geometry.**

***Keywords*—CFD, WSS, helical flow, arterial disease.**

I. INTRODUCTION

Coronary artery disease (CAD) is the most common type of cardiovascular disorder. There is evidence that initiation and progression of CAD can be linked to disturbances of blood flow, in particular to altered wall shear stress (WSS). Moreover, intraluminal flow patterns play a key role in determining WSS luminal distribution [1-2] and markedly contributes to regulate the transport of atherogenic particles at the luminal surface [3].In recent years, computational fluid dynamics (CFD) studies have been coupled with imaging techniques to provide detailed hemodynamic information, which cannot be obtained from cardiac imaging alone. In order to elucidate the role of blood flow in atherosclerosis, numerous CFD studies have been conducted to link hemodynamic parameters and the disease, in order to diagnose and predict the development and progression of CAD. However, computational modelling requires assumptions that might influence the predicted hemodynamic scenario. In the present work, we aim at evaluating the effect of different inlet and outflow boundary conditions (BCs) on WSS related vessel wall descriptors and on helical bulk flow topology inside a realistic left coronary artery (LCA) tree model. To do it, six different sets of BCs were analysed, varying both inflow and outflow BCs.

II. METHODS

An image-based model of LCA tree (Fig. 1A) was reconstructed from CTA images using the open-source software Vascular Modelling Toolkit (VMTK, www.vmtk.org). The finite volume method was applied to perform numerical simulations under unsteady flow conditions. The general purpose CFD code Fluent (ANSYS Inc., USA) was used. After a sensitivity analysis to determine the proper grid refinement, a $8 \cdot 10^5$ tetrahedral cells discretization was used. Blood was modelled as a homogeneous, incompressible fluid. The non-Newtonian nature of blood flow was taken into account using the Carreau model [4].The inlet flow rate waveform was derived from Doppler measurements (Fig. 1B) and prescribed as inflow BC in terms of velocity profile. For the inflow velocity profile, two different assumptions (i.e., parabolic or flat) were considered. As for the BCs at outlet sections of the model, three different outflow BCs strategies were examined: (1) reference pressure, (2) constant outflow ratio based on Murray's law [5], and (3) constant outflow ratio based on Doriot's fit [6]. In detail, given the flow rates in the daughter branches Q_{d1} and Q_{d2} (where for d1 is intended the daughter branch with larger diameter D_{d1}), Murray's law asserts that their ratio is proportional to the third power of ratio of diameters as in Eq. (1):

As for Doriot's fit, it is a specialization of the generalized Murray's law to coronary hemodynamics [6]. More in detail, based on in vivo measurements, the relationship in Eq. (1) has been modified as follows:

Combining the described inflow and outflow BCs, six different case studies were obtained, summarized in Table I.

TABLE I
BCS TREATMENT SCHEMES IMPLEMENTED ON THE LCA MODEL

BCs treatment scheme	*Inlet condition*	*Outlet condition*
S1	PP	RF
S2	PP	MCOR
S3	PP	DCOR
S4	FP	RF
S5	FP	MCOR
S6	FP	DCOR

PP parabolic velocity profile, FP flat velocity profile, RF reference pressure, MCOR Murray's constant outflow ratio, DCOR Doriot's constant outflow ratio

The no-slip condition was imposed at the walls, which were

assumed to be rigid. The luminal distributions of three WSS-based descriptors, i.e., the Time Averaged WSS (*TAWSS*), the Oscillating Shear Index (*OSI*), and the Relative Residence Time (*RRT*) were computed:

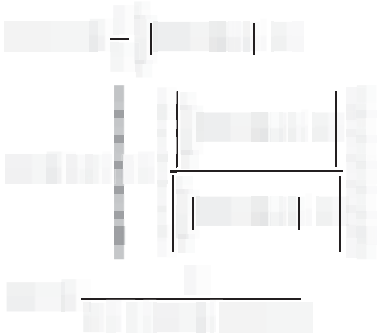

where T is the overall interval of the cardiac cycle and $\mathbf{s}$ is the position on the vessel wall. Regions with low *TAWSS* values (i.e. *TAWSS*<0.4 Pa) are associated with high atherogenic potency, while regions with high *OSI* and *RRT* values correspond to potential sites of intimal thickening. For a given scheme, disturbed shear was quantified as the fraction of the surface area (SA_{rel}) exposed to *OSI* and *RRT* above (or *TAWSS* below) a threshold value representing the 80th (20th for *TAWSS*) percentile of the descriptor distribution over the combined surface of all six schemes. Intraluminal flow structures were quantitatively characterized in terms of helical flow. Recently, a Lagrangian-based 4D descriptor has been introduced (based on theoretical remarks on helicity) and applied in order to obtain a "measure" of the helical structure of the blood flow. Technically, we emitted idealized elements of blood at two different phases of the cardiac cycle (i.e. systolic peak, T1, and diastolic peak, T2, Fig. 1B), and we tracked their motion into the coronary tree along three simulated cardiac cycles. Considering the generic element of blood k moving into the LCA tree, its motion can be characterized by the mean quantity hfi_k (computed along the trajectory described by the element of blood):

where $\mathbf{V}$ and $\boldsymbol{\omega}$ are the velocity and vorticity vectors, N_k is the number of points j along the k-th trace for which the Local Normalized Helicity (LNH) was calculated.

III. RESULTS

Our findings show that low *TAWSS* regions are mainly located in the left anterior descending (LAD) branch, while high *OSI* regions are located in the left circumflex (LCx) branch and in the first segment of LAD (data not shown). High *RRT* values are observed in both branches, with a predominance in LAD (Fig. 2A). Overall, the spatial distribution of the three WSS-based descriptors is similar, independently of the applied outflow BC strategy, even though differences in magnitude are noticeable (data not shown). To better understand how each outflow BC scheme influences the flow rate distribution at the outlets, the mean outflow ratios (computed as the ratio between the mean flow rate at one single outlet and the mean inlet flow rate) are shown in Fig. 2A. Results from the quantification of SA_{rel} are shown in Fig. 2E. It can be noticed that the application of schemes S1 and S4 leads to lower SA_{rel} values for *TAWSS* than the other BCs schemes, potentially reducing areas of flow stagnation. When applied, the imposition of a constant outflow ratio at outlet sections (S2, S3, S5 and S6) generate larger SA_{rel} values both for *OSI* and *RRT*: this may indicate that wider regions of oscillating WSS are generated when these schemes are applied. Differences in SA_{rel} when different BC idealized velocity profile are prescribed (i.e. schemes S1*vs*S4, S2*vs*S5 and S3*vs*S6) are negligible (around 4%). Marked differences are found when considering the effect of different outflow BCs, in particular when reference pressure schemes (S1, S4) are compared with the other schemes. Among the descriptors, *OSI* seems to be the most sensitive to the BCs scheme. The visualization of pathlines highlights the presence of 3D flow patterns, thus confirming that complex fluid structures develop within the branching regions, where high values of LNH are found (Fig. 3A and 3B). The probability density functions (PDFs) of hfi_k values of blood elements emitted at time T2 (Fig. 3C) show that all the investigated BC schemes are characterized by very similar PDF distributions, with peaks (corresponding to the mode of the distribution) located between 0.1 and 0.2.

IV. DISCUSSION AND CONCLUSION

The results obtained suggest that the WSS-based descriptors are sensitive to the variation of the flow division ratio consequent to imposed outlet BCs. On the other hand, assumptions done on the velocity profile at the inflow do not markedly influence WSS-based descriptors distribution.

The bulk flow arranges in complex helical structures in proximity of bifurcation regions. The BCs scheme modestly influence the bulk flow topology as measured by helicity-based descriptors, hinting at a major role of geometry in determining bulk flow features. Moreover, the quantitative characterization of the blood flow in the bulk might become a powerful instrument to relate bulk flow topology and organization with the onset and development of pathological event at the vascular wall.

REFERENCES

[1] U. Morbiducci, R. Ponzini, M. Grigioni, and A. Redaelli, "Helical flow as fluid dynamic signature for atherogenesis in aortocoronary bypass. A numeric study", *J Biomech.*, vol. 40, pp. 519-534, 2007.

[2] U. Morbiducci, R. Ponzini, G. Rizzo, M. Cadioli, A. Esposito, F. De Cobelli, A. Del Maschio, F.M. Montevecchi, and A. Redaelli, "In vivo quantification of helical blood flow in human aorta by time-resolved three-dimensional cine phase-contrast MRI", *Ann. Biomed. Eng.*, vol. 37, pp. 516-531, 2009.

[3] X. Liu, F. Pu, Y. Fan, X. Deng, D. Li, and S. Li, "A numerical study on the flow of blood and the transport of LDL in the human aorta: the physiological significance of the helical flow in the aortic arch", *Am. J. Physiol. Heart Circ. Physiol.*, vol. 297, pp. H163-H170, 2009.

[4] P.J. Carreau, "Rheological equations from molecular network theories", *J Rheol.*, vol. 16(1), pp. 99-127, 1972.

[5] C.D. Murray, "The physiological principle of minimum work: I. The vascular system and the cost of blood volume", *Proc. Natl. Acad. Sci. USA*, vol. 12(3), pp. 207-214, 1926.

[6] P.A. Doriot, P.A. Dorsaz, L. Dorsaz, E. De Benedetti, P. Chatelain, P. Delafontaine, "In-vivo measurements of wall shear stress in the pathogenesis of atherosclerosis", *Lab. Invest.*, vol. 85(1), pp. 9-23, 2000.

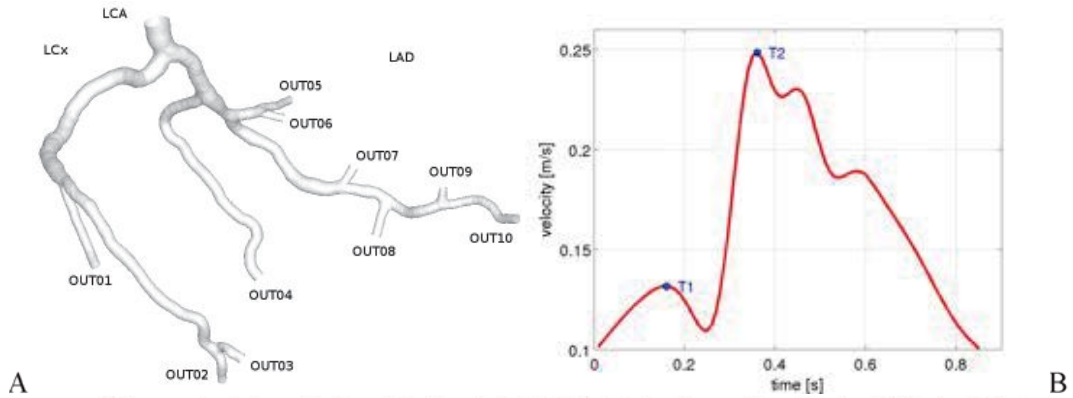

Fig. 1. A) LCA reconstructed model, the subdivision in LAD (Left Anterior Descending artery) and LCx (Left Circumflex artery) branches is underlined and the nomenclature of outlets is highlighted. B) Imposed flow rate waveform, injection time instants are shown (T1: systolic peak, T2: diastolic peak called).

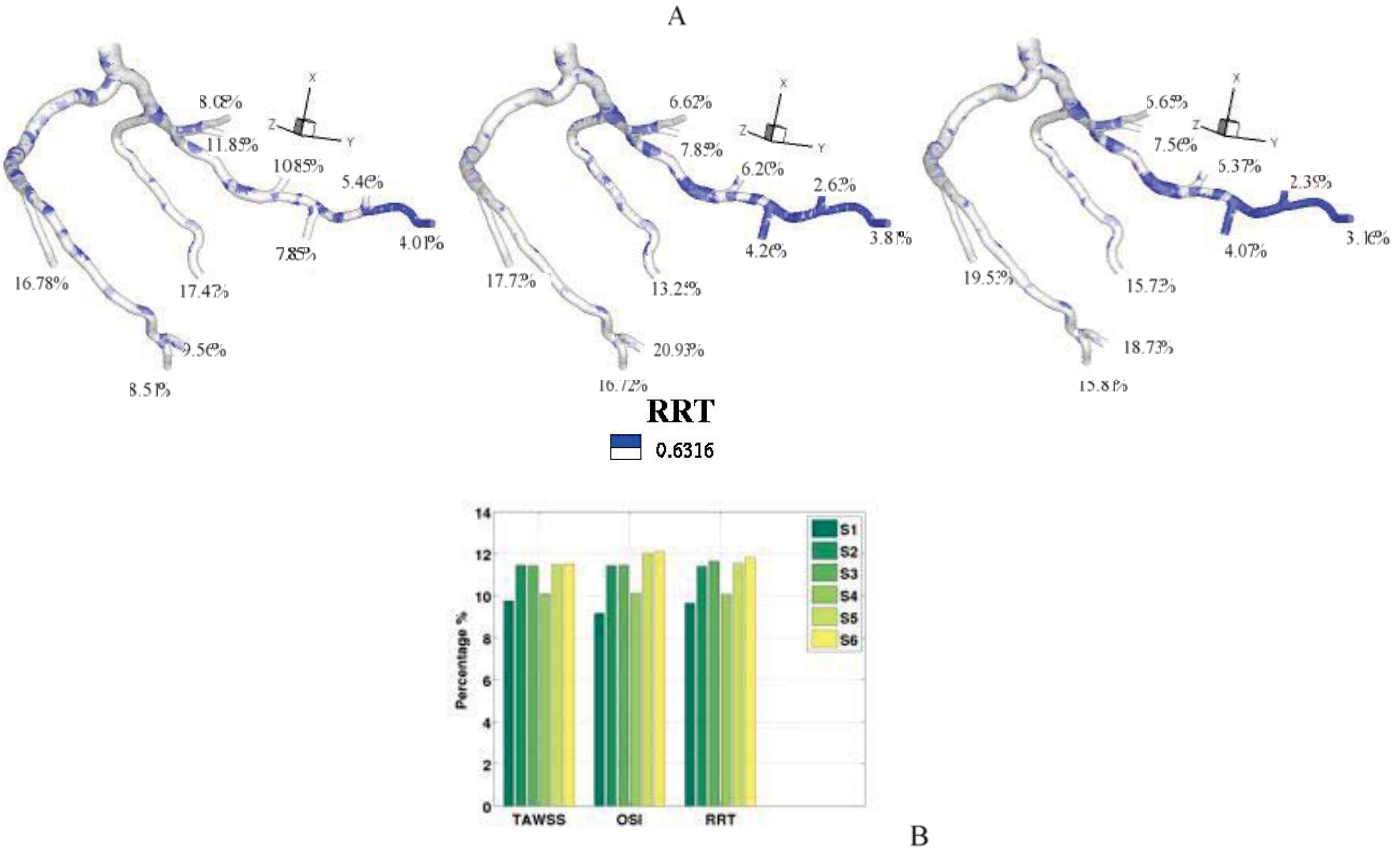

Fig. 2. A) Atheroprone regions for RRT index in S1, S2 and S3 cases (from left to right), percentage subdivision of flow rate is shown for every outlet. B) Calculated percentage of atheroprone surface area over the six analyzed models and throughout the three wall indexes.

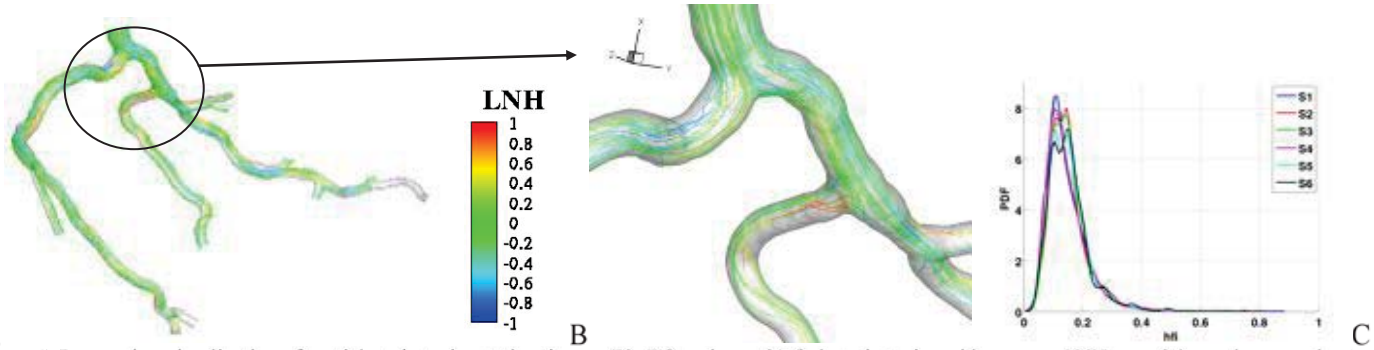

Fig. 3. A) Lagrangian visualization of particle trajectories at time instant T2, BCs scheme S1. Only trajectories with average LNH over 0.3 are shown, colored by LNH values. B) Zoom of the first segment of domain. C) The probability density functions of hfi_k at time instant T2 for six schemes.

Stiffness, strength and strain distribution in the augmented vertebrae

V. Danesi[1], S.J. Ferguson[2], N. Brandolini[3], P. Erani[3], M. Viceconti[4] and L. Cristofolini[1]
[1]*Department of industrial engineering, University of Bologna, Italy*
[2]*Institute for Biomechanics, ETH Zurich, Zurich, Switzerland*
[3]*Laboratorio di Tecnologia Medica, Istituto Ortopedico Rizzoli, Bologna, Italy*
[4]*Department of Mechanical Engineering, University of Sheffield, United Kingdom*

***Abstract*— The aim of the present study was to investigate the biomechanical efficacy of prophylactic augmentation in preventing fracture of non-fractured vertebral bodies. More specifically, as there are hints that the effect of augmentation depends on the quality of augmentation itself, we aimed at identifying which operator-dependent factors make prophylactic augmentation effective/ineffective in reducing the risk of fracture. Non-destructive and destructive tests were carried out on single vertebrae of 5 sets of three adjacent vertebrae. The central vertebra was tested in the natural condition as a control, while the two adjacent vertebrae were tested pre- and post- prophylactic augmentation. A subset of specimen was instrumented with strain gauges. CT imaging again augmentation was performed to assess the quality of augmentation. Prophylactic augmentation increased the force and work required to completely destroy the vertebrae in all specimens. However, the first-failure event in 5 augmented specimens occurred with a force and work lower than the control specimens. Vertebral strength augmentation was influenced strongly by the kind of surgical access, the cement distribution inside the vertebral body, and the volume fraction of cement injected. In summary, this study shows that prophylactic augmentation avoids complete collapse of the vertebra in all cases. However, inadequate augmentation increases the risk of partial fractures. The positive/detrimental effect depends on a combination of factors describing the quality of augmentation.**

***Keywords*—Prophylactic augmentation, vertebral body, *in vitro* mechanical testing, strength.**

I. Introduction

There are cases in which vertebrae are at high risk of fracture, such as in with low bone mineral density or metastatic lesion. One prophylactic strategy that has recently been proposed as a mechanism for reducing fracture risk is the mechanical reinforcement of the vertebral body by injection of a foreign augmentation material. This treatment is meant to increase vertebral failure strength in selected weaker vertebrae [1]. While many studies have been undertaken to investigate the biomechanical effects of vertebroplasty on fractured single vertebral bodies [2-4] or spine segment [1], [5]-[6], very little data exist regarding the effect of prophylactic augmentation on non-fractured vertebrae. The aim of the present study was to investigate the biomechanical efficacy of prophylactic augmentation on non-fractured vertebral bodies to prevent vertebral fractures. More specifically, we wanted to identify those operator-dependent factors that make prophylactic augmentation effective/ineffective in reducing the risk of fracture. For this reason, the stiffness, strain distribution and strength of the natural and augmented vertebrae were measured *in vitro*.

II. Materials and Methods

Non-destructive and destructive tests were carried out on non-treated and augmented vertebrae under axial and torsional loading (Fig.1). Tests were performed on 5 sets of three adjacent vertebrae, to enable comparison between matching vertebrae (augmented vs non-treated control):

- The central vertebra of each set served as a control and was tested non-destructively and destructively only in the non-augmented condition.
- The two adjacent vertebrae were subjected to prophylactic augmentation: they were tested non-destructively both before and after augmentation, while destructive test was carried out in the augmented state.

All the surrounding soft tissues were removed, including the ligaments. Three specimens were instrumented with 8 strain gauges each, equally spaced around the vertebral body, at mid-height. Augmentation was performed on nine vertebrae after non-destructive pre-augmentation mechanical testing. Specimens were CT-scanned again post-augmentation to assess the amount and distribution of cement inside the vertebral body. The following indicators were obtained from the augmentation files and the CT-scans:

- Access (uni-pedicular, bi-pedicular);
- Volume of cement injected;
- Degree of filling of the vertebral body (injected volume / volume of the vertebral body);
- Para-vertebral leakage (yes, no);
- Placement in the sagittal plane (centered, in contact with the anterior cortical shell);
- Distribution in a transverse plane (One-mass or Two-masses);
- Sphericity of fill (Sphere, ellipse or diffuse);
- Achievement of endplate contact (none, one, both).

The following data were extracted from the load-displacement curves of the destructive tests, which differed between specimens, according to the augmentation quality:

- The first-failure event was defined as the 0.2% offset of the load-displacement curve;
- Ultimate load was defined as the point after which load fell to less than 50%;
- The work required to reach the first-failure event and the ultimate load was computed for each specimen;

III. Results

In axial-compression, the augmented vertebrae were on average only 3% stiffer (range -45% to +32%: only 5 vertebrae out of 9 were stiffer) than in the pre-augmented condition ($p=0.86$). In torsion, the augmented vertebrae were

on average only 9% stiffer (range -19% to +39%) than in the pre-augmented condition (p=0.17). Differences between strain measurement locations were not significant for the magnitude and direction of principal strains (p>0.3).

The magnitude of the principal strains measured during the non-destructive testing in the same vertebra after augmentation was on average lower than before augmentation. For axial-compression, the principal compressive strain decreased on average by 18% due to augmentation (p=0.0002). The principal tensile strain decreased on average by 59% (p=0.75). In torsion, both principal strain components decreased on average by 12% (p<0.01). For axial-compression, the direction of principal strains (nearly aligned with the vertebral body) varied on average by 6° (p=0.73). In torsion, the direction of principal strains (close to +/-45° from the anatomical axis) varied on average by 6° (p=0.0007).

During the destructive tests the augmented vertebrae showed the first-failure event at a force that was on average 121% of the controls (p=0.37) (Fig.2). Four specimens out of nine started failing with a force that was larger (119% up to 237% of the controls) (Fig.2). However, five specimens started failing with a force that was slightly lower (77% to 94% of the controls) (Fig.2). The work required by the augmented vertebrae to reach the first-failure event was on average 155% of the controls (p=0.26) (Fig.2). Seven specimens out of nine started failing with a work that was larger (104% to 399% of the controls) (Fig.2). However, two specimens required less work to start failing (75% to 98% of the controls) (Fig.2). The ultimate force of the augmented vertebrae was on average 295% of the controls (consistently higher for all specimens, range: 169% to 541%, p=0.008) (Fig.2). The work up taken by the augmented vertebrae to reach the ultimate failure was on average 280% of the controls (consistently higher for all specimens, range: 156% to 598%, p=0.008) (Fig.2).

In an attempt to understand the reason(s) for the large variability of the mechanical outcome of augmentation, correlation between the augmentation parameters and the mechanical outcome was assessed:

- Access: the specimens prepared with a uni-pedicular access had higher first-failure force and work, as well as higher ultimate force and work than the bi-pedicular ones;
- Degree of filling: the specimens whose vertebral body was filled by more than 25% had higher first-failure and ultimate force and work than those filled less than 25%;
- Para-vertebral leakage: the specimens with leakage had lower first-failure and ultimate force and work, as well as higher ultimate force and work;
- Placement in the sagittal plane: the specimens in which the cement mass was in contact with the anterior cortical shell had higher first-failure and ultimate force and work;
- Distribution in a transverse plane: the cases where the cement formed a unique mass had higher first-failure and ultimate force and work than when the cement formed two separate masses;
- Sphericity of fill: the ellipsoid was associated with higher first-failure force, and ultimate force and work; a spherical cement mass was associated with the highest first-failure work.
- Endplate contact: achievement of contact with both endplate was associated with an increase of all magnitudes, except the first-failure force.

IV. DISCUSSION

While the biomechanical effects of vertebroplasty on fractured vertebrae has been thoroughly investigated, very little data exist regarding the effects of prophylactic augmentation on non-fractured vertebrae. The aim of the present study was to investigate the biomechanical efficacy of prophylactic augmentation in preventing fractures of a non-fractured vertebral body. In particular, this study identified which operator-dependent factors make prophylactic augmentation effective/ineffective. Our findings show that, prophylactic augmentation increased in all specimens the force and work required to completely destroy the vertebrae. However, the first-failure event (which is in all cases associated with some undesirable stage of damage) in five specimens occurred with a force and work lower than the control specimens. This indicates, while in all cases prophylactic augmentation reduced the risk of complete failure, in some cases prophylactic augmentation increases the risk of partial failure. A correlation between some indicators of the quality of augmentation, and the strengthening/weakening effect with respect to the first-failure event showed that the strength of augmented vertebrae increased for uni-pedicular approach, when the cement distribution formed a single ellipse-shaped mass in the transverse plane versus an anterior position in the sagittal plane and was in contact with at least one endplate.

V. CONCLUSION

In summary, this study shows that prophylactic augmentation avoids complete collapse of the vertebra in all cases. However, inadequate augmentation increases the risk of partial fractures. The positive/detrimental effect depends on a combination of factors describing the quality of augmentation.

ACKNOWLEDGEMENTS

Partially funded by EC: “Osteoporotic Virtual Physiological Human Project VPHOP” (FP7-ICT2008-223865).

REFERENCES

[1] Kayanja, M.M., D. Togawa, and I.H. Lieberman, Biomechanical changes after the augmentation of experimental osteoporotic vertebral compression fractures in the cadaveric thoracic spine. The Spine Journal, 2005. 5(1): p. 55-63.

[2] Ikeuchi, M., et al., Mechanical augmentation of the vertebral body by calcium phosphate cement injection. J Orthop Sci, 2001. 6(1): p. 39-45.

[3] Higgins, K.B., et al., Biomechanical effects of unipedicular vertebroplasty on intact vertebrae. Spine (Phila Pa 1976), 2003. 28(14): p. 1540-7; discussion 1548.

[4] Belkoff, S.M., et al., An ex vivo biomechanical evaluation of an inflatable bone tamp used in the treatment of compression fracture. Spine (Phila Pa 1976), 2001. 26(2): p. 151-6.

[5] Berlemann, U., et al., Adjacent vertebral failure after vertebroplasty. A biomechanical investigation. J Bone Joint Surg Br, 2002. 84(5): p. 748-52.

[6] Oakland, R.J., et al., The biomechanical effectiveness of prophylactic vertebroplasty: a dynamic cadaveric study. J Neurosurg Spine, 2008. 8(5): p. 442-9.

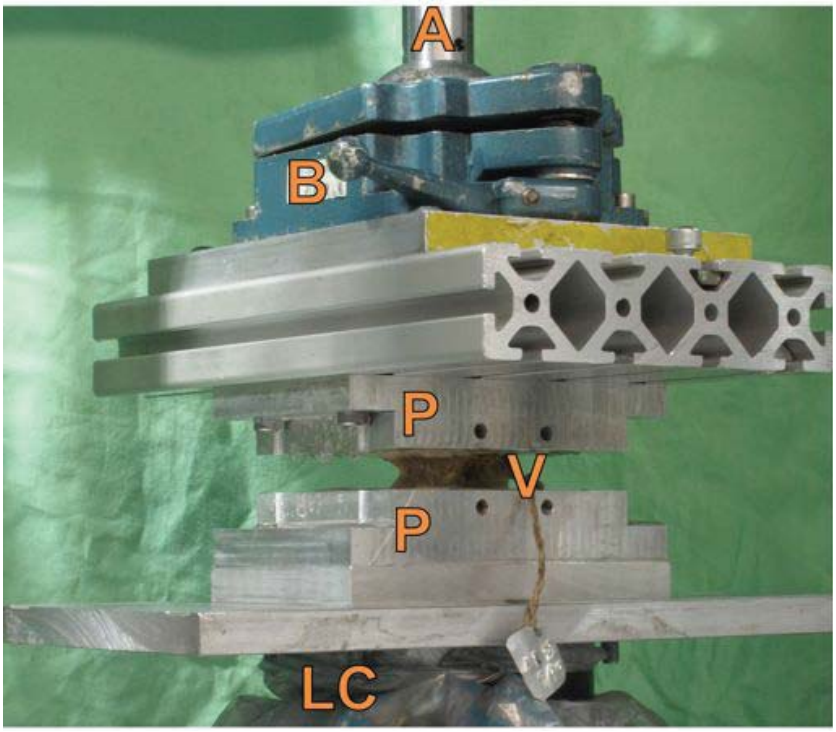

Fig. 1: – *In vitro* loading setup: the superior and inferior endplates of the vertebra (V) were potted with acrylic cement in two aluminum pots (P). Load (axial force or torsion) was delivered to the specimen by the actuator of the testing machine (A), through a lockable ball-joint (B). The specimen was mounted on top of the six-component load cell (LC, partially hidden by a polyethylene protection).

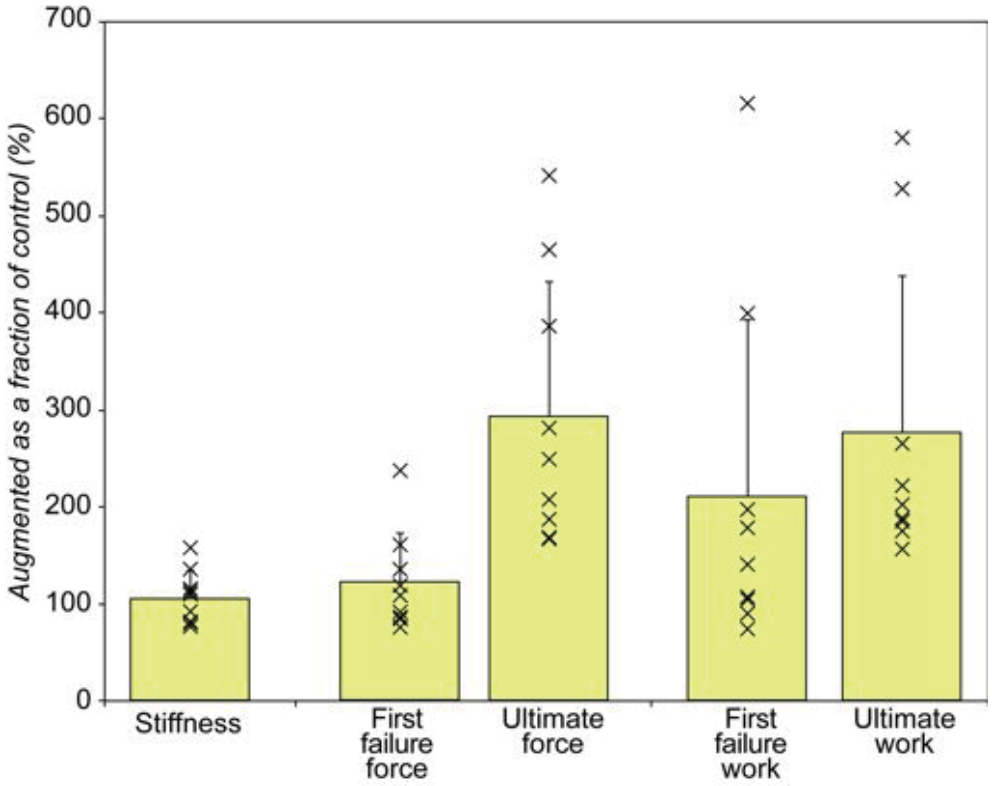

Fig. 2: – Mechanical outcome of augmentation: the values of stiffness, force and work to the first-failure event and to ultimate failure are plotted for the augmented vertebrae as a fraction of the adjacent control. The average and standard deviation (all specimens pooled together) are represented in bar chart form, together with the individual data points. A value of 100% indicates no variation with respect to the control; a value larger than 100% indicates that augmentation increased the strength/toughness of the vertebral body.

Fluid Dynamic Performance of New Polymeric Heart Valves Prototypes tested under Continuous and Pulsatile Flow Condition

F. De Gaetano[1], M. Serrani[1], P. Bagnoli[1], J. Brubert[2], J. Stasiak[2], G. Moggridge[2], and M. L. Costantino[1],
[1] *LaBS, Department of Chemical, Material and Chemical Engineering "Giulio Natta", Politecnico di Milano, Milan, ITALY*
[2] *Department of Chemical Engineering & Biotechnology, University of Cambridge, Cambridge, UK*

***Abstract* — Two categories of valve prostheses are currently available: mechanical and biological valves. The former show longer duration performances, on the other hand they induce high pressure drops during operation. The latter have preferable fluid dynamic performances but do not display high durability. The potential of Polymeric Heart Valves (PHV) is to combine the haemodynamic properties of biological valves with the durability of mechanical valves. This work present a hydrodynamic evaluation of two groups of newly developed supra-annular tri-leaflet prosthetic heart valves made from styrenic block co-polymers. The two types of PHVs were tested under continuous and pulsatile flow conditions as prescribed by ISO 5840 Standard. A specially designed pulse duplicator allowed testing of the valve prototypes at different flow rate and frequency conditions.**

***Keywords*—Heart Valve, pulse duplicator, pulsatile flow, styrenic block co-polymer.**

I. INTRODUCTION

The aim of PHV prototypes is to replicate the function of native heart valves, bio-inspired PHVs may mimic not only shape, but also structural properties. Styrenic block co-polymer elastomers may have a suitable micro-morphology which may mimic the structure function of anisotropic collagen in the native valve. The arrangement of these micro domains can be optimized to enhance valve durability under physiological stress during the cardiac cycle.
A computational model based on the experimentally determined mechanical properties of the polymer [1], was developed using finite element analysis of a single leaflet. This FEM provided boundary and stress conditions that minimise the state of stress and therefore optimises the orientation of the micro-morphology. PHVs prototypes were produced by compression moulding technique. The aim of this work is to characterise the performance of styrenic block-copolymer PHVs under continuous and pulsatile conditions.

II. MATERIAL AND METHODS

PHVs prototypes were manufactured by compression moulding technique from two different material:

- Group A: poly(styrene-isoprene/butadiene-styrene) block copolymers with 19% wt polystyrene fraction
- Group B: poly(styrene-isoprene-styrene) block copolymers with 30% wt polystyrene fraction

16 PHVs, were tested in total, 8 PHVs from Group A and from Group B. The tests were performed under continuous and pulsatile flow as recommended by ISO5840 Standard.
The experimental test bench used to evaluate PHVs' performance in continuous flow conditions (Fig. 1) comprised: a reservoir, a conventional centrifugal pump and a PHVs housing unit designed according to the guidelines of the ISO5840 Standard.
The valves were tested at flow rates ranging from 0 to 10 l/min in increments of 0.5 l/min. Transvalvular pressure drop was measured at different times in order to verify the repeatability of the tests. Three measurements were acquired for each valve.
The experimental setup for the regurgitation test comprised of a housing for the valve (the same as in the continuous flow tests); a reservoir positioned at the valve level to provide a constant pressure upstream the valve, and a reservoir placed at different heights to vary the backpressure on the valve.
During testing the height of the reservoir was changed to provide a backpressure in the range of 28 mmHg to 128 mmHg (5 mmHg steps). Regurgitation rate at each backpressure was determined and used to calculate the mean regurgitation rate for each valve.
The circuit specifically designed and built up to perform tests under pulsatile flow is shown in Fig. 2.
The pulse duplicator consists of the following elements: the driving system made of a piston pump; the ventricular element, simulating the left ventricle; the aortic valve housing; the Resistance-Compliance-Resistance (RCR) analogue to replicate the peripheral compliance and the resistance (aortic and peripheral) of the cardiovascular system; the reservoir simulating the left atrium and the mitral valve housing (the same used for the continuous flow tests).
The pumping system was controlled by a software that allows the user to set different flow rate waveforms or different frequencies. The systolic flow rate was replicated by the Swanson and Clark waveform [2] while a modified Talukder and Reul waveform [3] was used to produce the diastolic waveform. The pumping system was filled up with distilled water according to ISO5840 Standard.
The PHVs were tested under different flow rates and backpressures, as required by the ISO5840 Standard. Transvalvular pressure drop was measured at a constant frequency (70 bpm) and variable flow rate (2 l/min, 3.5 l/min, 5 l/min and 7 l/min). Regurgitation volume was determined by testing each valve at a mean flow rate of 5 l/min at three different frequencies (45 bpm, 70 bpm, 120 bpm). At each frequency three backpressures were tested (80 mmHg, 120 mmHg, 160 mmHg). Each valve has been tested for at least 15 consecutive cycles at each test condition.
Continuous and pulsatile flow tests were performed using distilled water at 25°C.

III. RESULTS AND DISCUSSION

The dimensions of the tested PHVs are shown in Fig. 3. The significance of the statistical difference between the two

groups ($p<0.01$) was evaluated using a two sample location Student's *t*-test.

A. Continuous Flow test

Group A showed a lower mean transvalvular pressure drop (8.36 ± 1.33 mmHg) than group B (15.26 ±1.87 mmHg). A statistically significant difference between the two groups was found ($p = 3.2e^{-4}$) (Fig. 4). According to these data, Group B valves showed to be stiffer than Group A valves, as expected, due to higher polystyrene fraction within the material.

Also the mean regurgitation displayed by Group A valves is lower (175.3 ± 19 ml/min) than Group B valves (264 ± 26 ml/min), but in this case no statistically significance is given by the *p* value ($p = 0.077$) (Fig. 5).

Thus, the polystyrene content of the material does not seem to affect regurgitation. The slight different regurgitation (Fig. 6) between the two groups may be ascribed to the different leakage area formed during the closing phase of the leaflets.

B. Pulsatile Flow Test

All the PHVs exceed the minimum performance requirements provided in ISO5840 Standard (Table I).

TABLE I
PERFORMANCES OF PHVS

	Regurgitation [% stroke volume]	*EOA [cm^2]*
ISO 5840	<10%	>1
Valve 1 19% styrene	6.08 ± 0.10	1.52 ± 0.16
Valve 2 19% styrene	7.44 ± 0.10	1.50 ± 0.17
Valve 3 19% styrene	7.93 ± 0.9	1.37 ± 0.25
Valve 4 19% styrene	5.93 ± 0.10	1.36 ± 0.10
Valve 5 19% styrene	9.84 ± 1.47	1.41 ± 0.11
Valve 6 19% styrene	5.97 ± 0.15	1.39 ± 0.36
Valve 7 19% styrene	7.26 ± 0.13	1.43 ± 0.28
Valve 8 19% styrene	6.53 ± 0.07	1.58 ± 0.14
Valve 1 30% styrene	6.84 ± 0.13	1.23 ± 0.10
Valve 2 30% styrene	6.15 ± 0.18	1.04 ± 0.04
Valve 3 30% styrene	7.16 ± 0.20	1.13 ± 0.06
Valve 4 30% styrene	8.10 ± 0.12	1.16 ± 0.08
Valve 5 30% styrene	7.45 ± 0.18	1.16 ± 0.12
Valve 6 30% styrene	5.47 ± 0.09	1.39 ± 0.08
Valve 7 30% styrene	6.04 ± 0.10	1.25 ± 0.11
Valve 8 30% styrene	5.57 ± 0.13	1.29 ± 0.09

The table shows the ISO5840 specifications vs PHVs performances. The ISO5840 specifications correspond to the following pulsatile flow condition: beat rate = 70 cycle/min, simulated cardiac output = 5.0 l/min, mean aortic pressure 100 mmHg and systolic duration = 35%.

Tests showed that the mean transvalvular pressure drops recorded in Group A were statistically lower (12.20 ± 1.41 mmHg) than the one recorded in Group B (17.09 ± 3.39 mmHg) ($p = 0.0019$).

Also the maximum transvalvular pressure drops were statistically different ($p = 3.3e\text{-}05$) in Group A and Group B. Group A: 30.09 ± 4.7 mmHg; Group B: 43.98 ± 4.52 mmHg.

Mean regurgitation volume was comparable within the two groups (7.13% ±1.33% group A versus 6.60% ± 0.94% group B), but with no statistical significance ($p > 0.05$).

The results of this work showed that the performances of PHVs under pulsatile tests (Fig. 7) are comparable with those of some bi-leaflet mechanical prostheses currently on the market [4], having a comparable tissue annulus diameter (TAD) (Table II).

TABLE II
COMPARISON OF PERFORMANCES BETWEEN PHVS AND 5 COMMERCIALLY AVAILABLE BI-LEAFLET MECHANICAL VALVES

	Regurgitation [% stroke volume]	*MSPD [mmHg]*
GROUP A	7.13 ± 1.33	12.20 ± 1.41
GROUP B	6.60 ± 0.94	17.09 ± 3.39
ATS	11.00 ± 1.51	15.28 ± 2.96
Carbomedics Top Hat	10.76 ± 0.76	15.05 ± 2.05
On-X	9.23 ± 1.89	14.47 ± 4.33
SJM Regent	12.34 ± 2.30	8.69 ± 0.82
Sorin Bicarbon Slimline	6.20 ± 1.26	10.42 ± 2.21

Table showing the hydrodynamic performances of the two groups of valves and commercially available bi-leaflet mechanical valves in the following pulsatile flow condition: beat rate = 70 cycle/min, simulated cardiac output = 5.0 l/min, mean aortic pressure 100 mmHg and systolic duration = 35%.
MSPD: mean systolic pressure difference.

IV. CONCLUSION

An experimental hydrodynamic evaluation of PHVs manufactured from block copolymers with different polystyrene fractions has been performed (under steady state and pulsatile flow conditions). The result demonstrate that the transvalvular pressure drop is directly related to the rigidity of the heart valve leaflets, indicated by the percentage of polystyrene (19% or 30%) in the material, and is statistically lower for PHVs with 19% of polystyrene.

No statistical differences were found between the two Groups in static and dynamic regurgitation tests.

However, all the 16 PHVs met the minimum requirements specified in ISO5840 Standard, in terms of both regurgitation and EOA (Table I), demonstrating their effectiveness. Further design improvements are ongoing to minimise regurgitation and maximise EOA.

REFERENCES

[1] Stasiak J, Moggridge G D, Zaffora A, Pandolfi A and Costantino M L. Engineering orientation in block copolymers for application to prosthetic heart valves. *Functional Material Letters* Vol.3, No. 4(2010) 249-252.

[2] Swanson W.M., Clark R.E., "A simple cardiovascular system simulator: design and performance" Journal of Bioengeneering, 1976; 1: 135-45;

[3] Talukder N., Reul H., "Fluid mechanics of natural cardiac valves", The Arterial System Dynamics, 1978; 269:274.

[4] Bottio T., Caprili L., Casarotto D., Gerosa G., "Small aortic anulus: the hydrodynamic performance of 5 commercially avaible bileaflet mechanical valves", *The Journal of Thoracic and Cardiovascular Surgery*, 2011; 128(3): 457-462.

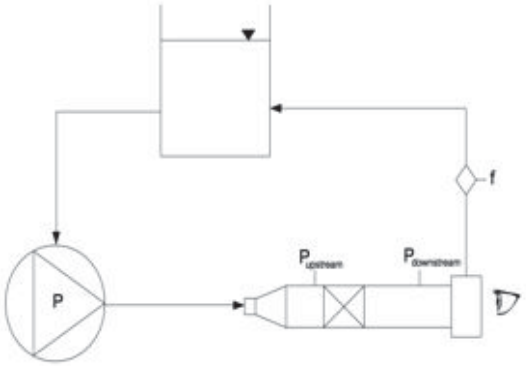

Fig. 1. Outline of the experimental set up for continuous flow tests. Shown on the diagram are the locations of upstream and downstream pressure measurements, the flow rate measurement location and the observation point from which pictures of the valve opening at each flow rate were taken.

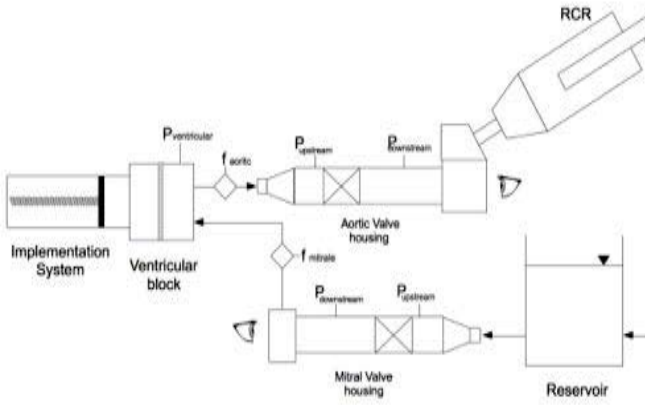

Fig. 2. Schematic of the experimental set-up used for the pulsatile flow tests. Shown on the diagram are the locations of upstream and downstream pressure measurements, the flow rate measurement location and the observation point from which pictures of the valve opening were taken.

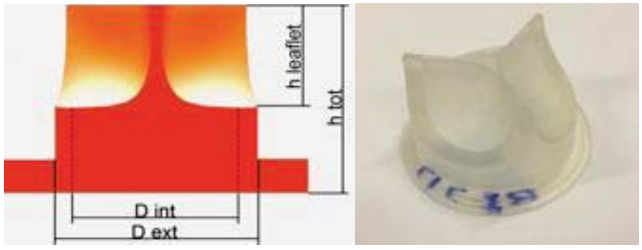

Fig. 3. Sketch (left) and picture (right) of a PHV. The dimensions are: h leaflet = 10.7 ÷ 10.9 mm; h tot = 21 mm; D int = 22 mm; D ext = 28 mm; Tissue Annulus Diameter (TAD) = 22 mm; thickness leaflet = 0.36 ÷ 0.42 mm.

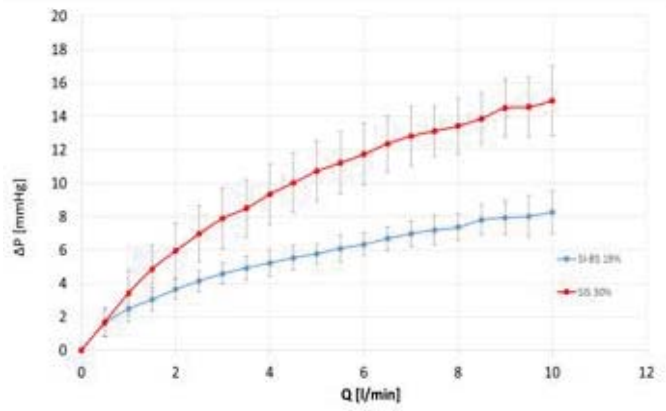

Fig. 4. Comparison of transvalvular pressure drops in continuous flow tests between the two Groups of valves (mean among 8 valves).

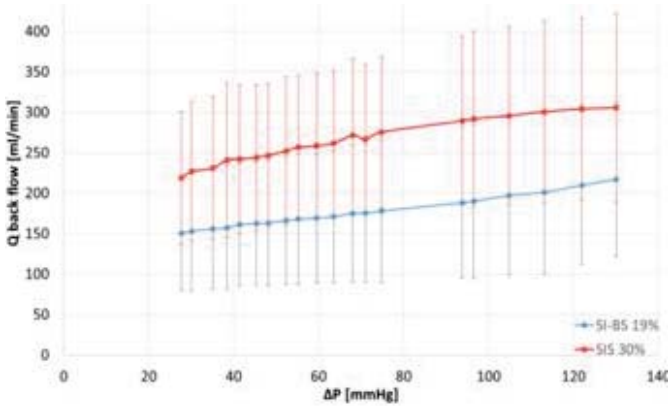

Fig. 5. Comparison regurgitation in continuous flow tests between the two Groups of valves (mean among 8 valves).

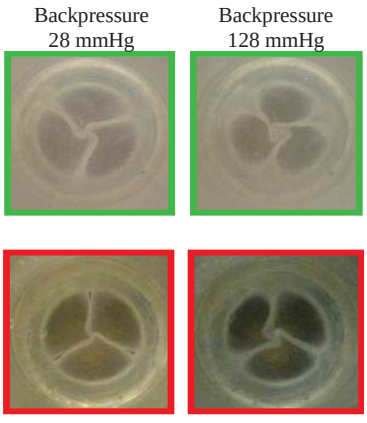

Fig. 6. Pictures of two PHVs (top valve #5 of group A; bottom valve #4 of group B) during static regurgitation tests, at two different backpressure (28 mmHg on the left and 128 mmHg on the right).

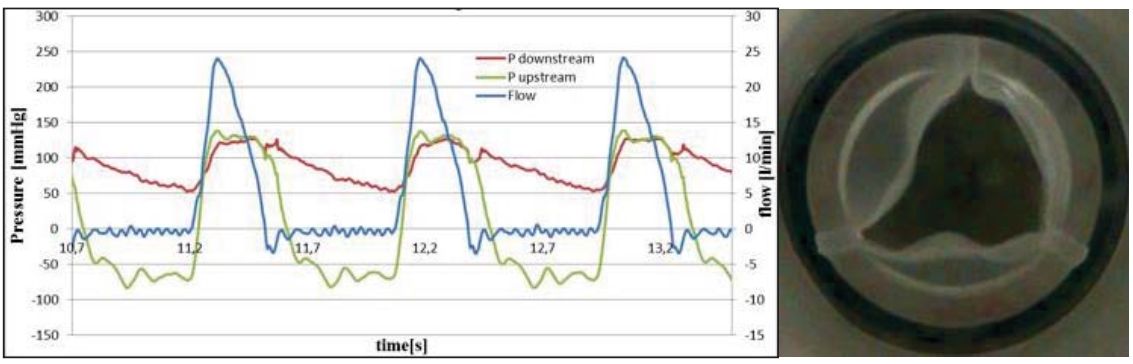

Fig. 7. Pressure and flow courses of the PHV. The picture on the right shows the maximum opening of the leaflet at the peak flow.

Multiscale CFD and hemodynamic shearing device to support design of blood contact devices

A. Dimasi[1], A. Pelosi[1], F. Consolo[1], G. B. Fiore[1], S. Reggiani[2], and A. Redaelli[1]
[1] *Department of Electronics, Information and Bioengineering, Politecnico di Milano, Milan, Italy*
[2] *Sorin Group Italia, S.r.l., Mirandola (MO), Italy*

***Abstract*—The onset of thromboembolic phenomena in blood contact devices (BCDs) is still a relevant concern in the cardiovascular field. In this work, we present a methodology that combines multiscale computational analyses with experimental techniques, that enables the evaluation of flow-induced thrombogenic potential of BCDs. This methodology was applied to a sample case study, featuring a hollow-fiber membrane blood oxygenator with integrated heat exchanger. The suitability of this approach as an effective tool for BCDs design has been successfully demonstrated: specifically, results provided a-priori indications for design optimization, allowing to reduce time and costs associated to physical prototyping and testing.**

***Keywords*—computational fluid dynamics, multiscale analysis, device thrombogenicity, device thrombogenicity emulator.**

I. Introduction

In industry, current criteria for the design of blood recirculating devices (BRDs) used in extracorporeal circulation (ECC) are mainly focused on macroscale parameters, such as the minimization of pressure losses and priming volumes, and on the optimization of gas and heat transfer efficiency. The typical industrial design approach is still largely based on time-consuming empirical tests, and the device fluid dynamics is mainly investigated using experimental techniques.

Currently, one of the major challenges in ECC device design is the minimization of flow-induced platelet activation, which is a major precursor of thromboembolic complications [1]. Flow-induced platelet activation is a complex phenomenon that takes place at different length and time scales that are challenging to couple. In the last decade, computational fluid dynamics (CFD) methods have proven their effectiveness in the design process of a wide range of BRDs for ECC [2]; the advantages of CFD reside in its capability to evaluate the performance of a device at an early stage of the design process, thus reducing the costs and time needed to manufacture and test physical prototypes. The design process of BRDs should be oriented to minimize platelet activation phenomena; in particular, the optimization of the blood flow path geometries, aimed at the reduction of dangerous flow patterns, would help reducing the onset of flow-induced platelet activation. Although this concept is well consolidated in the scientific literature [3], utilization of thrombogenicity-oriented design criteria is still not common practice in industry.

The present work aims at introducing a complete modeling strategy, that couples macroscale and microscale flow effects on platelets, for the design optimization of BRDs for ECC, focusing on hollow-fiber membrane oxygenators and blood heat exchangers.

II. Materials and Methods

Hollow-fiber membrane oxygenators (OXY) and polymeric heat exchangers (HE) for blood are characterized by the presence of an inner core composed of micrometric polymeric fibers, in which gas and heat exchange occur. The sole macroscopic approach is unsuitable to capture the actual microscopic flow phenomena that occur at the fibers level, and thus to assess the extent of the viscous stresses associated with these phenomena. The modeling strategy here presented combines a macroscale quantification of the velocity and pressure fields with a microscale analysis at the fiber level, in order to achieve a complete description of the fluid-dynamic behavior of ECC devices [4].

Moreover, CFD simulations were integrated with a transient analysis based on a Lagrangian approach of the mechanical load experienced by platelet-like particles, in order to gather data concerning the stress history experienced by blood after repeated recirculation within the device. From these data, representative shear stress loading waveforms were selected to be reproduced *in vitro*. Selected shear stress loading curves waveforms were then programmed into a Hemodynamic Shearing Device (HSD) that replicated the stress histories on human platelet samples, in order to quantify the amount of shear-induced platelet activation [5].

A. Macroscale analysis

CFD simulation was performed to assess the pressure and velocity fields within the OXY and HE and to determine their macroscopic shear stress distribution. The rheological properties of the working fluid approximated the behavior of blood at 34% hct, a representative condition during ECC, with density ρ equal to 1,052 kg/m^3 and shear-rate dependent viscosity, through the power-law model proposed by Ballyk [6]. The viscous k-ω turbulence model with low Re corrections was adopted, while laminar flow conditions were assumed in the fiber bundles. Steady-state analyses were performed using the SIMPLE method for pressure-velocity coupling with a second order upwinding scheme.

B. Microscale analysis

A geometrical replication of a fiber bundle subunit, characterized by periodical arrays of two-layered microfibers, was used to accurately compute the shear stress that acts on the blood flowing within the fiber bundles. Fully developed laminar flow around the fibers was modeled using periodic boundary conditions that were assigned to all the external walls of the repetitive subunit.

C. Lagrangian particle tracking

Once convergence was reached for the steady-state solution, neutrally buoyant spherical particles (D = 3μm) representing the platelets were injected into the fluid domain at the inlet section. A transient two-phase simulation was performed to evaluate the time-dependent shear stress acting on the platelets through a discrete phase modeling (DPM) approach, allowing identification of the trajectory and loading history of each particle flowing through the device in a Lagrangian reference frame. A fully coupled approach was adopted to account for the mutual influence between the fluid and the platelets. This approach solves the discrete and continuous phase equations alternately until the solutions in both phases converge.

The shear stress along each particle trajectory was exported and its related linear stress accumulation (SA) [7] has been calculated, as in Eq. (1)

$$SA = \int_{t_0}^{t} \tau(s) ds \quad (1)$$

where τ is the shear stress along a single trajectory, obtained by summing the macroscale and the microscale contributions. In order to identify a limited number of device-specific trajectories, the probability distribution function of SA has been considered: indeed, SA distribution can be seen as a synthetic description of the overall flow-related thrombogenic potential of the device.

D. Experimental setup

Three device-specific trajectories were selected from the numerical simulations and replicated in vitro through a hemodynamic shearing device (HSD), i.e. a device combining the cone-and-plate and Couette viscometer features, designed to emulate dynamic shear stress conditions on platelet samples. Following previously-published protocols [8], gel-filtered platelets were extracted from whole human blood and exposed to device-specific loading waveforms. Activated platelet samples were assayed using the modified prothrombinase-based assay and thrombin generation, expressed as change in absorbance per unit time, and quantified using a spectrophotometer.

III. RESULTS

In fig. 1 (left panel) the fluid domain of the OXY and HE macroscale model is shown and the three selected device-specific trajectories are depicted: they correspond to the 10^{th}, 50^{th} and 90^{th} percentile of SA probability distribution function; in the right panel a magnification of the microscale model of HE fiber bundle is represented, where platelet trajectories within the fibers are shown.

The contour maps of velocity and shear stress distribution within the HE fibers obtained from the microscale analysis are displayed in fig. 2 and 3, respectively. The CFD analyses revealed the presence of a non-uniform distribution of shear stress and velocity within the fiber bundles, with a shear stress ranging from 0.093 Pa and 0.18 Pa at the maximum distance from the fiber walls, to a maximum value of 13 and 23 Pa at the fiber walls in the HE and OXY, respectively.

From the HSD tests, the platelet activation state (PAS) and rate was obtained for the three selected loading waveforms. For each time point, PAS was normalized with respect to the maximum level of PAS, obtained by sonication (fig. 4), thus, all PAS values are expressed as a fraction of the thrombin generation of fully activated platelets.

IV. CONCLUSION

This work presented a composite methodology which combines multiscale numerical models with experimental techniques to measure flow-related device thrombogenicity. The method was applied to the fluid-dynamic characterization of hollow-fiber membrane oxygenators and polymeric heat exchangers for blood, and allowed the prediction of thrombogenicity effects of a given device due to design modifications, thus limiting the need for expensive and time-consuming experiments on physical prototypes, and costly preclinical and clinical trials.

ACKNOWLEDGEMENT

The authors would like to acknowledge Sorin Group Italia, Mirandola (MO) for providing the experimental facilities required for this study and Prof. Michalis Xenos for his valuable support in the setup of the computational simulations.

REFERENCES

[1] J. Schaadt, "Oxygenator thrombosis: an international phenomenon," *Perfusion*, vol. 14, issue 6, pp. 425-435

[2] G.B. Fiore, U. Morbiducci, R. Ponzini, and A. Redaelli, "Bubble trucking through computational fluid dynamics in arterial line filters for cardiopulmonary bypass," *ASAIO Journal*, vol. 55, issue 5, pp. 438-444

[3] D. Bluestein, S. Einav , and M.J. Slepian , "Device thrombogenicity emulation: A novel methodology for optimizing the thromboresistance of cardiovascular devices," *Journal of Biomechanics*, vol. 6, pp. 338–344, 2013.

[4] A. Pelosi, J. Sheriff, M. Stevanella, G.B. Fiore, D. Bluestein and A. Redaelli, "Computational evaluation of the thrombogenic potential of a hollow-fiber oxygenator with integrated heat exchanger during extracorporeal circulation," *Biomechanics and Modeling in Mechanobiology*, 10.1007/s10237-012-0445-0, 2013.

[5] G. Girdhar, M. Xenos, Y. Alemu, W.C. Chiu et al, "Device thrombogenicity emulation: a novel method for optimizing mechanical circulatory support device thromboresistance," *PLoS One*, vol. 7, issue 3, e32463, 2012.

[6] P. D. Ballyk, D. A. Steinman, and C. R. Ethier, "Simulation of non-Newtonian blood flow in an end-to-side anastomosis," *Biorheology*, vol. 31, pp. 565–586, 1994

[7] M. Xenos, G. Girdhar, Y. Alemu, J. Jesty, M. Slepian et al., "Device thrombogenicity emulator (DTE)-design optimization methodology for cardiovascular devices: a study in two bi-leaflet MHV designs," *Journal of Biomechanics*, vol. 43, pp. 2400–2409, 2010

[8] J. Sheriff, J.S. Soares, M. Xenos, J. Jesty, M. Slepian, and D. Bluestein, "Evaluation of Shear-Induced Platelet Activation Models Under Constant and Dynamic Shear Stress Loading Conditions Relevant to Devices," *Annals of Biomedical Engineering*, vol. 41, pp. 1279-1296, 2013.

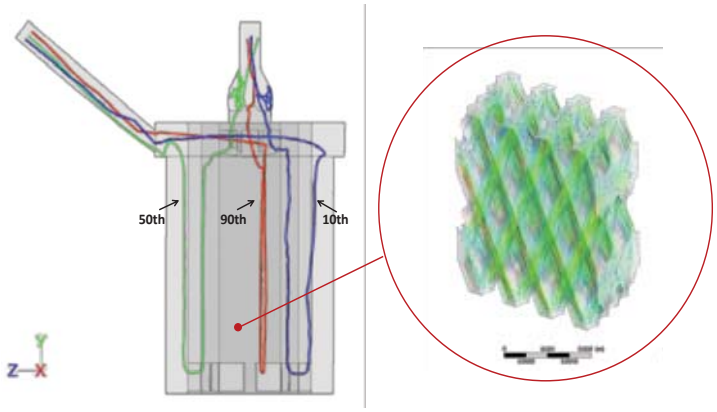

Fig. 1. 3D CAD geometry of the multiscale model with a magnification of the microscale model of a fiber bundle subunit.

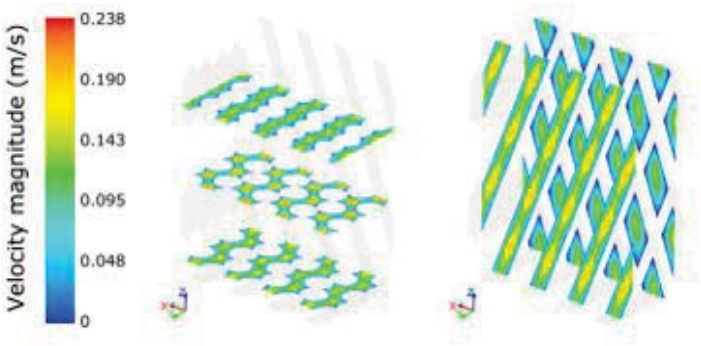

Fig. 2. Contour maps of velocity magnitude in three transversal and two longitudinal sections of the microscale HE model.

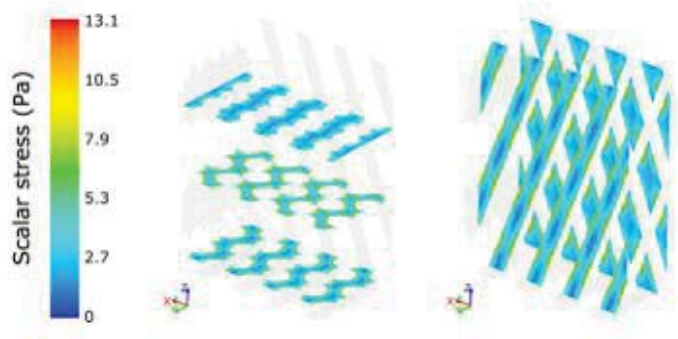

Fig. 3. Contour maps of scalar stress in three transversal and two longitudinal sections of the microscale HE model.

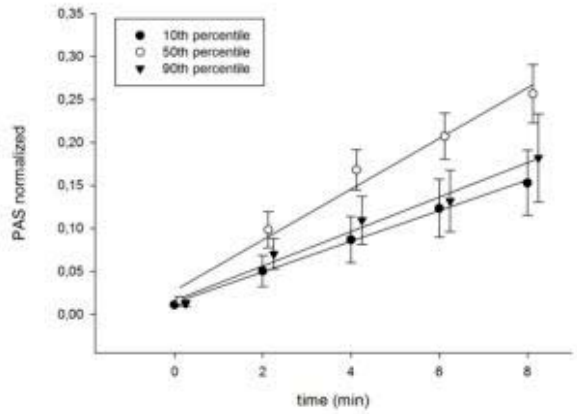

Fig. 4. PAS normalized, measured at different time points after the application of three representative loading waveforms derived from multiscale CFD simulations.

Nitinol peripheral stents: experimental validation of fatigue computational analyses.

E. Dordoni[1], D. Allegretti[1], L. Petrini[2], C. Silvestro[3], C. Guala[3],
G. Dubini[1], F. Migliavacca[1] and G. Pennati[1]
[1] *Laboratory of Biological Structure Mechanics, "Giulio Natta" Department, Politecnico di Milano, Italy*
[2] *Civil and Environmental Engineering Department, Politecnico di Milano, Italy*
[3] *Medtronic Peripheral Therapies, Roncadelle (BS), Italy*

***Abstract*—Treatment of stenotic lower limbs is commonly performed using Nitinol peripheral stents. However, the large and cyclic deformations of the femoral arteries might cause long-term failure of the implanted device. Finite element analysis (FEA) may be a useful tool to study the in vivo stent fatigue behavior. A preliminary investigation to verify the predictive capability of fatigue computational analyses should be performed using simple and well-controlled experimental tests. This study consists of a combined numerical-experimental activity, aimed at the validation of the fatigue FEA. In particular we experimentally investigated the fatigue behavior of a commercial stent when subjected to cyclic axial compression, in the expanded configuration and after the implantation in a silicon tube, resembling the arterial vessel. An experimental set-up to impose the tube pre-stretch (10% of the tube length) in a controlled way was developed. The experimental tests were reproduced by means of FEA. The numerical results were compared with experimental evidences and revealed good agreement.**

***Keywords*—Nitinol, stent fatigue, peripheral arteries, FEA validation**

I. Introduction

THE femoro-popliteal (FP) artery disease is often characterized by diffuse lesions, with frequent long occlusions [1], and it is one of the major manifestations of systemic atherosclerosis. It is evaluated to be present in 3% of people in the age range 40–59 years increasing to 15% to 20% in persons over 70 years and in a fifth of them symptoms can become severe and progressive, causing major lifestyle limitations [2].

FP arteries are subjected to unique biomechanical forces: in addition to blood pulsatility in the vessels, these segments are also subjected to dynamic loadings related to lower limbs daily movements [3]. In particular, the superficial femoral artery undergoes dramatic cyclic deformations, including axial compression and extension, radial compression, bending, and torsion [4]. Accordingly, peripheral arteries are exposed to about 1 million cycles per year of large deformations, which are superimposed to the cyclic loading due to the arterial blood pressure (40 millions cycles per year).

Nitinol stents are nowadays widely used for the treatment of occlusions in peripheral arteries. Their pseudo-elastic behavior assures the recovery of the expanded configuration at the end of each loading cycle and hence the preservation of the normal blood stream [5]. However, the risk of stent fatigue rupture due to cyclic loads related with the patient daily activities is source of concerns for Nitinol devices: in some recent clinical studies the rupture is related with the re-occlusion of the artery [6]. Accordingly, the assessment of the risk of stent fatigue rupture is of primary importance to assure the effectiveness of stenting procedure. The complexity of material behavior, stent geometry and loading conditions suggests the finite element analysis (FEA) as a useful tool to study the *in vivo* stent fatigue behavior. A preliminary investigation to verify the predictive capability of complex fatigue computational analyses should be performed using simple and well-controlled experimental tests.

.

II. Experimental tests

In this study we investigated the fatigue behavior of a commercial stent from Invatec (now Medtronic Endovascular Therapies, Roncadelle, BS, Italy). In particular, the stent was subjected to cyclic axial compression in two different conditions: i) after free expansion and ii) after the implantation in a silicon tube. The former case allows to investigate the influence of the stent geometry and material properties on the fatigue behaviour. Since the interaction between stent and vessel wall plays a crucial role on the device stent fatigue resistance [7], the latter case allows to take into account, in a simplified way, this interaction using a tube, resembling the arterial vessel.

An ad hoc experimental set-up was developed to expand the stent into a pre-streched tube, according with the *in-vivo* conditions. The set-up is depicted in Figure 1.One stent type (8 mm outer diameter; 45 mm length dimensions) was tested. Three different silicon tubes were chosen, having the same inner diameter of 4 mm (and therefore the same stent oversizing ratio) but different external diameter and Young's modulus, and consequently different axial stiffness. These values are reported in Table I. Using the experimental set-up, the tubes were pre-stretch of 10% of their length. Afterwards, the Maris Plus stents were deployed into the stretched tubes in a temperature controlled environment (37°C).

TABLE I
SILICON TUBE CHARACTERISTICS

Tube	*External Diameter*	*Young modulus*	*Stiffness*
1	7	3,7	0,96
2	6	3,51	0,55
3	6	1,94	0,30

.

For both the conditions, cyclic axial tests up to 10^5 cycles in displacement control were performed on the MTS 858 MiniBionix servo-hydraulic testing machine (MTS Corp., Minneapolis, MN, USA) at a temperature of 37°.

For the free expanded configuration, the tests were performed at a frequency of 20 Hz, with a visual inspection of rupture every 10 thousand cycles (Figure 2 left). 5 testing conditions were considered: 4 cyclic tensile tests with a high (11mm and 2.5mm) and a low value (8mm and 2.2mm) for mean and alternate axial displacement, respectively, and 1 cyclic compression test (2.4 mm for mean and 2.2 for alternate displacement) were chosen.

For the confined configuration, the tests were performed at a frequency of 10 Hz, with a visual inspection of rupture every 10 thousand cycles, imposing to the tube a displacement of ± 10% its length.

III. FINITE ELEMENT MODEL VALIDATION

To validate the capability of the numerical approach of predicting Nitinol stent fatigue failure, the experimental tests were reproduced by means of FEA (Figure 2 right and Figure 3) and the numerical and experimental results were compared.

Numerical results were analyzed plotting the amplitudes (ε_1^a) and mean values (ε_1^m) of the first principal strain in all the stent elements on a constant-life diagram: these values were compared with the limit curve of the stent material previously experimentally obtained [8]. It allowed to identify the conditions leading to fatigue fracture of the stents, as well as the specific locations of failure. These numerical results were compared with experimental evidences obtained from the performed tests (Figure 4).

IV. CONCLUSION

The good agreement between numerical prediction and experimental evidence allows to conclude that FEA is able to catch the most important aspects of the Nitinol stent fatigue behaviour during *in-vitro* tests. It also suggests that this methodology may be successfully used to study the more complex *in vivo* load conditions.

These results are particularly interesting for biomedical companies that aim to improve their devices.

ACKNOWLEDGEMENT

This work is within the project ‘‘RT3S - Real Time Simulation for Safer vascular Stenting’’ funded by the European Commission under the 7th Framework Programme, GA FP7-2009-ICT-4-248801

.

REFERENCES

[1] T. Zeller, “Current state of endovascular treatment of femoro-popliteal artery disease”, *Vascul. Med*. vol. 12, pp. 223-234, 2007.

[2] Vascular Society of Great Britain and Ireland Document, “The Provision of Services for Patients with Vascular Disease”, 2009.

[3] A.J. Klein, S.J. Chen, J.C. Messenger, A.R. Hansgen, M.E. Plomondon, J.D. Carroll, and I.P. Casserly,“ Quantitative assessment of the conformational change in the femoro-popliteal artery with leg movement”, *Cath. Cardiovasc. Interv.*, vol. 7, pp 787-798, 2007.

[4] C.P. Cheng, N.M. Wilson, R.L. Hallett, R.J. Herfkens and C.A. Taylor. “In Vivo MR Angiographic Quantification of Axial and Twisting Deformations of the Superficial Femoral Artery Resulting from Maximum Hip and Knee Flexion”, *J. Vasc. Interv. Radiol.,* vol. 17, pp. 979–987, 2006.

[5] Y. Nakagawa, J. Yajima, Y. Oikawa, K. Ogasawara, H. Kirigaya, K. Nagashima, R. Funada, S. Matsuno, T. Inaba, M. Nakamura, H. Sawada, and T. Aizawa, “Clinical outcomes after percutaneous peripheral intervention for chronic total occlusion of superficial femoral arteries: comparison between self-expandable nitinol stent and stainless steel stent.”, *J. Cardiol.,* Vol. 53, pp. 417-421, 2009.

[6] J.M. Gibbs, C.S. Peña, and J.F. Benenati, “Treating the diseased superficial femoral artery”, *Techniques in vascular and interventional radiology*, vol. 13, pp. 37-42, 2010.

[7] A. Meoli, E. Dordoni, L. Petrini, F. Migliavacca, G. Dubini, and G. Pennati, “Computational modelling of in vitro set-ups for peripheral self-expanding Nitinol stents: the importance of stent–wall interaction in the assessment of the fatigue resistance”, *Cardiovasc Eng Technol.,* vol. 4, pp. 474-484, 2013.

[8] L. Petrini, W. Wu, E. Dordoni, A. Meoli, F. Migliavacca, andG. Pennati, “Fatigue behaviour characterization of nitinol for peripheral stents”, *Functional Materials Letters*, vol. 5, 1250012-1:4, 2012.

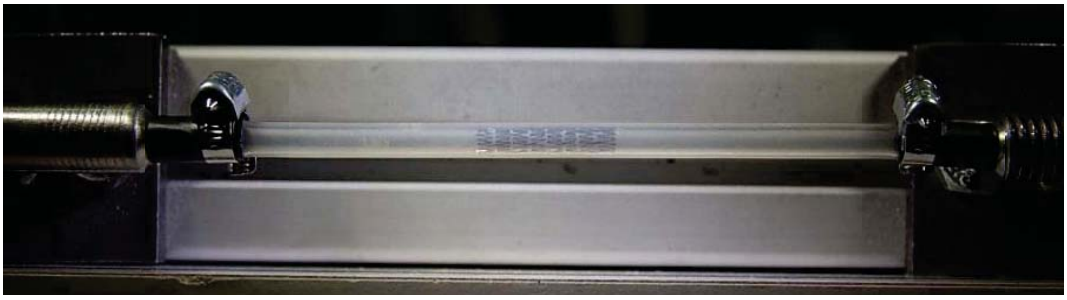

Fig. 1. Experimental configuration of a stent deployed in a pre-stretched silicon tube.

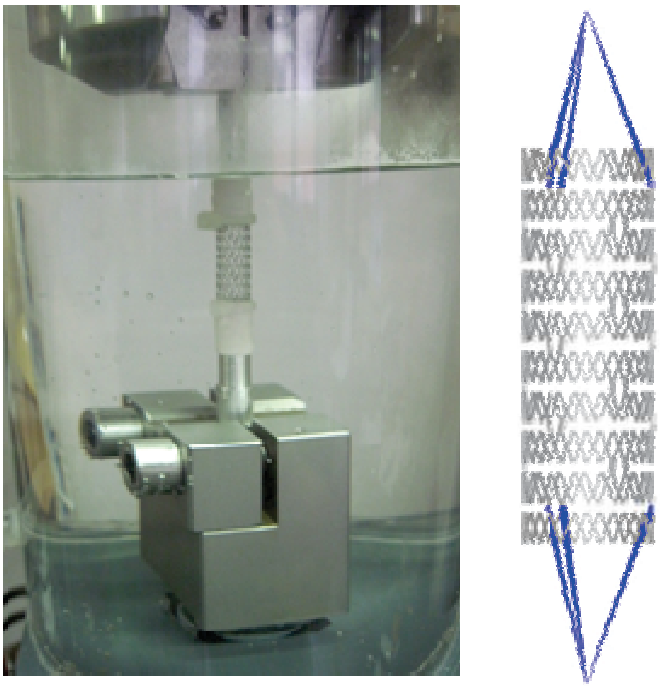

Fig. 2. Experimental set-up for fatigue testing of stents in the free expanded condition (left) and the corresponding numerical model (right).

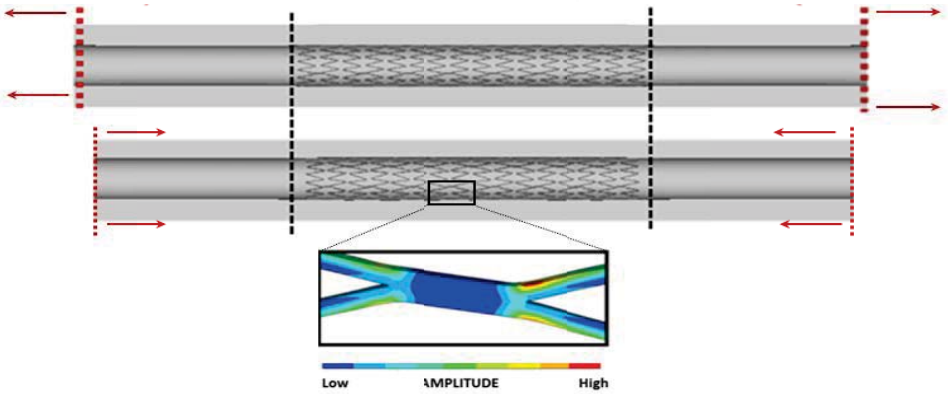

Fig. 3. Numerical results of the simulation of a cyclic test on the stent deployed in a pre-stretched silicon tube.

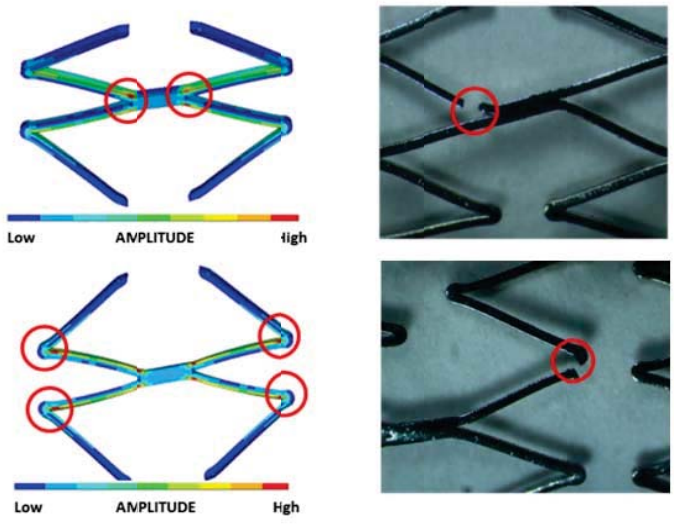

Fig. 4. Comparison between numerical (left) and experimental (right) results for the free expanded condition. The most stressed points in the numerical models and break points in the experimental tests coincide.

Model of a stable passive bipedal walker provided with spring-damping legs

E. Etenzi[1], V. Monaco[1], and S. Micera[1,2]
[1] *The BioRobotics Institute, Scuola Superiore S.Anna, Pisa, Italy*
[2] *Translational Neural Engineering Laboratory, School of Engineering, Ecole Polytechnique Federale de Lausanne, Lausanne, Switzerland*

***Abstract*— In the literature it has long been demonstrated that a simple model of passive walker with stiff limbs is able to accurately describe pendulum-like mechanism underlying the human locomotion [1]. Moreover the model with flexible limbs correctly represent also the phase of double support, and to reproduce the ground reaction force [2].**

However, among the models proposed so far, no one takes into account the dissipative effects that necessarily occur during the human gait. The main objective of this work is to investigate the asymptotic stability of a mathematical model of a passive walker provided with elastic and damping elements, using a Poincarè Map. The second objective is instead to validate the model using data available from literature [4]. In particular we looked at a group of people with average mass of 61.7 kg, average legs' length of 0.86 m and that was walking at 0.87 m/s . When the input parameters of the model are l_0 = 0.86 m, m = 61.7 kg we obtained asymptotically stable solutions of walking at an average speed of v = 0.88 m/s .

***Keywords*—passive walker, damping, model.**

I. Introduction

Human locomotion is a very efficient motor task and allows the forward progression of the center of mass by taking advantage of the inverted pendulum mechanism [1]. As matter of fact, an inverted pendulum model with rigid legs is able to walk along an inclined plane with a stable dynamics and reproduces the trajectory of the center of mass like for the human gait [3]. However, this "simple" model does not correctly describe the interaction between foot and floor (i.e., ground reaction force; GRF), and the resulting gait does not show a double support phase. Geyer and colleagues introduced a compliant spring-based walking model in order to overcome previous limitations [2]. They observed that this paradigm can correctly reproduce both the GRF patterns and the timing of the gait cycle. Despite of this, their model is fully conservative, that is, it cannot emulate any eccentric work achieved during the gait cycle. The present work aims at investigating the behaviour of a passive walker provided with compliant legs constituted by the parallel of spring and damping elements (Figure 1). The main goal consists in verifying whether this approach is able to reproduce both kinematics and kinetics features of the gait cycle of young subjects while walking at three different speeds: 0.63 ± 0.08, 0.87 ± 0.06 and 1:14 ± 0.09 m/s. Anthropometric features of the model (i.e., mass m = 61.7 kg, resting leg length l_0 = 0.86 m, and angle between legs at the heel strike β = 31; 39; 47 deg respectively) are extrapolated from previous literature [4].

II. Materials and Methods

The proposed model consists of a passive walker with telescopic compliant legs provided with a couple of spring and damping elements in parallel (k and b are respectively the elastic and the damping constant). The whole mass, m = 61.7 kg, is concentrated in the center of gravity and the system is designed to walk along an inclined plane (slope γ) in order to balance the energy lost due to damping element with that gained due to the lowering the center of mass. The dynamics of the single support (Figure 1, left), with respect to the $(x; y)_R$ reference frame, is described by the following equation:

$$m\ddot{x} = A\cos(\theta) + mg\sin(\gamma) \quad (1)$$

$$m\ddot{y} = A\sin(\theta) - mg\cos(\gamma) \quad (2)$$

where $A = \left[k(l_0 - l_1) - b\frac{dl_1}{dt} \right]$, $l_1 = \sqrt{x^2 + y^2}$ and x; y are the coordinates of the center of mass. The single support ends when the swinging limb touches the ground with an angle of attack α_0. This is calculated after setting the angle between the two legs, β , in accordance with experimental data (i.e., $\alpha_0 = \pi - \beta - \theta$). During the double support, b varies according to the dynamic of the system. The dynamics of the double support (Figure 1, right), with respect to the $(x; y)_R$ reference frame, is described by the following equation: :

$$m\ddot{x} = A\cos(\theta) - B\cos(\alpha_0) + mg\sin(\gamma) \quad (3)$$

$$m\ddot{y} = A\sin(\theta) + B\sin(\alpha_0) - mg\cos(\gamma) \quad (4)$$

where:

$$B = \left[k(l_0 - l_2) + b\frac{x\dot{x} - y\dot{y}}{\sqrt{x^2 + y^2}} \right], l_2 = \sqrt{(d - x)^2 + y^2}$$

and d is the abscissa of the foot when it strikes the ground. The double support ends when the GRF related to the trailing leg becomes zero. The stability of the model was studied by using the Poincarè Map. Specifically, the return map was generated with state variables at the heel strike. Stable solutions have been looked for in a limited domain of k, β, and γ (i.e., k range: 18-23 kN/m; β range: 50-1000 N/(m/s); γ range: 0.5-13 deg).

III. Results

The Poincarè Map allowed to identify three stable fixed points which related speeds, respectively 0.54 m/s, 0.88 m/s and 1.27 m/s, likely resembled experimental ones. These

solutions were obtained by setting model parameters as follows:

- k = 23 kN/m, β = 450 N/(m/s), γ = 1:5 deg, for the slowest speed.
- k = 20 kN/m, β = 600 N/(m/s), γ = 3:5 deg, for the medium speed.
- k = 21 kN/m, β = 950 N/(m/s), γ = 7 deg, for the fastest speed.

Figure 2 shows both the trajectory of the center of mass (upper subplot) and the GRF (lower subplots) for the model walking at medium speed. The main discrepancy between experimental and estimated spatio-temporal parameters concerned the cadence and the duration of the stance phase (Table I). Specifically, the estimated stance phase was always smaller than the experimental one. Conversely, the cadence of the model: at slowest speed, was higher than the measured one; at fastest speed, was lower than the measured one.

TABLE I
EXPECTED VALUES FROM LITERATURE VERSUS CALCULATED VALUES FROM LITERATURE

Low speed		
	Expected values	Calculated values
Mean speed [m/s]	0.63 ± 0.08	0.54
Cadence [steps/min]	87 ± 5	102
Stance phase	67 ± 2	57
Medium speed		
	Expected values	Calculated values
Mean speed [m/s]	0.87 ± 0.06	0.88
Cadence [steps/min]	101 ± 6	106
Stance phase	66 ± 1	55
High speed		
	Expected values	Calculated values
Mean speed [m/s]	1.14 ± 0.09	1.27
Cadence [steps/min]	113 ± 5	107
Stance phase	65 ± 2	52

IV. CONCLUSION

Our results showed that the proposed model is able to walk in stable dynamical conditions for arbitrarily long distances without falling or changing direction of motion (Figure 2).
It is important to remark that, although the spring-damper paradigm has been already introduced by previous authors [5], from the best of our knowledge, this is the first case where its dynamical stability has been systematically investigated. Results also showed that the best agreement between estimated and measured gait parameters were obtained at medium speed (Table 1). At faster and lower speeds, the model was not able to correctly predict experimental data. This discrepancy may be ascribed to the limited domain of variables k, b, and g and suggests that further investigations are required to look for solutions closer to experimental data. Noticeably, at medium speed, results have been obtained with an elastic constant, k, very close to that measured in healthy people while walking at most comfortable speed (i.e., K=21850 kN/m; see [5]). Moreover, the oscillation of the center of mass is about 4 cm, as is the case of humans locomotion, and GRF are characterized by a patterns similar to real ones (Figure 2), even though they were affected by a pronounced asymmetry. On the whole, the proposed model is able to reproduce some of the main physical features of the human locomotion above all at medium walking speeds. Further investigations are required to extend these results in a wider domain.

REFERENCES

[1] M. Garcia, A. Chatterjee, A. Ruina, M. Coleman, *The simplest walking model: Stability, complexity, and scaling*. , J. Biomech. Eng. Trans. Asme, 1998.
[2] H. Geyer, A. Seyfarth, R. Blickhan, *Compliant leg behaviour explains basic dynamics of walking and running*. , Proc. R. Soc. B doi:10.1098/rspb.2006.3637.
[3] M. J. Coleman, A. Ruina, *Motions of a rimless spoked wheel: a simple 2d systems with impacts*. , Cornell University 2002.
[4] V. Monaco, L. A. Rinaldi, G. Macri,S. Micera, *During walking elders increase eorts at proximal joints and keep low kinetics at the ankle*., J. Clinical Biomechanics, 2009.
[5] S. Siegler, R. Seliktar, W. Hyman, *Simulation of human gait with the aid of a simple mechanical model*., Biomech. 1982;15(6):415-25.

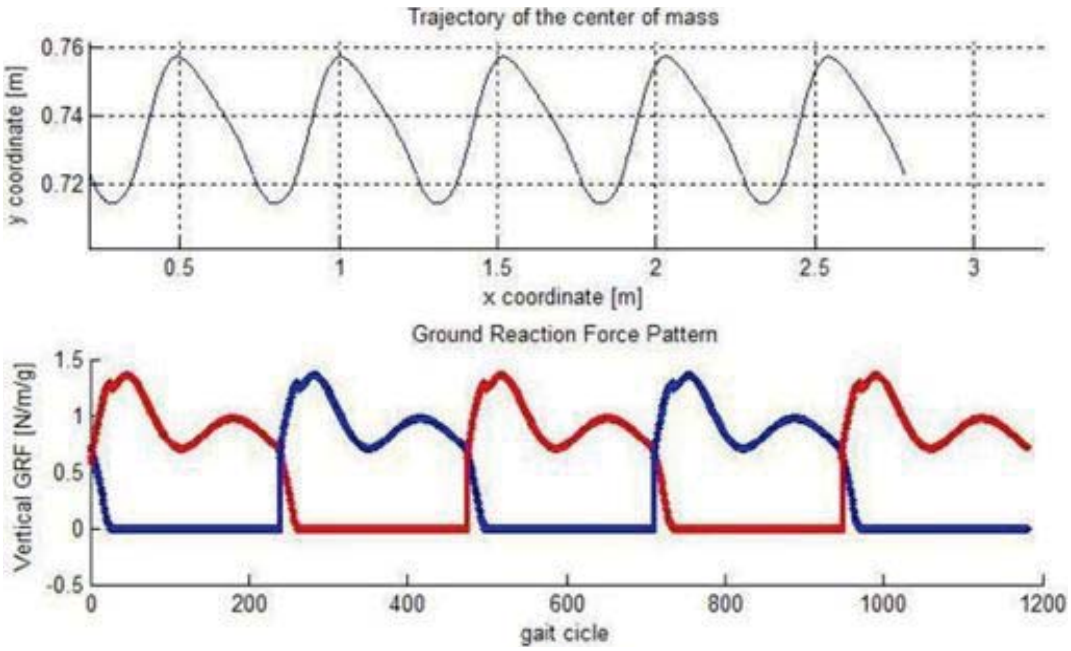

Figure 1: On the top: The trajectory of the center of mass in the reference system integral with it. On the bottom: The ground reaction force pattern along the y axis.

Isogeometric Analysis: a novel computational approach to evaluate the performance of endovascular stents

M. Ferraro[1], F. Auricchio[1,2], M. Conti[2], S. Morganti[3], and A. Reali[2]

[1] *CESNA Centro di Simulazione Numerica Avanzata , IUSS Pavia, Piazza della Vittoria 15, 27100 Pavia, Italia*
[2] *DICAR Dipartimento di Ingegneria Civile e Architettura, Università di Pavia, Via Ferrata 3, 27100 Pavia, Italia.*
[3] *DIII Dipartimento di Ingegneria Industriale e Informazione, Università di Pavia, Via Ferrata 3, 27100 Pavia, Italia.*

***Abstract*—Isogeometric Analysis (IGA) has recently emerged as a cost-effective alternative to classical isoparametric FEM [1]. The main feature of the method consists of using typical CAD basis functions for both geometric description and variable approximation. This implies the ability to describe exactly the computational domain geometry throughout the analysis process, and to include, at the same time, the capability to control the basis function regularity. The aim of this work is to develop a novel computational framework based on IGA to evaluate the performance of commercially available carotid artery stents. Analyses involving large deformations and different material models (hyper elastic, shape memory alloys) are performed within the numerical solver FEAP and its additional package for IGA. The results obtained with IGA and standard FEM for a typical stent bending test are compared and discussed.**

***Keywords*—IGA, Carotid Artery Stenting, FEAP**

I. Introduction

Cardiovascular diseases are the main cause of death in western countries and they are responsible for hundreds of thousands of early deaths world-wide. The current trend in clinical procedures requires high-tech and minimally invasive devices, in particular for cardiovascular applications (e.g., stents, valves, endoprosthesis, etc). Design, development, and performance assessment of these devices are a natural field of application for computational biomechanics, typically based on numerical tools such as the Finite Element Method (FEM). Isogeometric Analysis (IGA) has recently emerged as a cost-effective alternative to classical isoparametric FEM [1]. The main feature of the method consists of using typical CAD basis functions (e.g., *Non-Uniform Rational B-Splines*, the so called NURBS) for both geometric description and variable approximation in an isoparametric fashion. This approach implies the ability to describe exactly the computational domain geometry throughout the analysis process, thus simplifying the mesh refinement process, and to include, at the same time, the capability to control the basis function regularity. The aim of this work is to develop a novel computational framework based on IGA to evaluate the performance of commercially available carotid artery stents. Analyses involving large deformations and different material models (elastic, shape memory alloys) are performed within the numerical solver FEAP and its additional package for IGA. A typical experimental benchmark for carotid artery stents, i.e., bending test, have been reproduced numerically both using IGA and classical isoparametric FEM, and the results have been compared and discussed.

II. NURBS-based IGA

This section aims at describing the trivariate NURBS structure used for the discretization (for details please refer to [1]–[3]. NURBS are obtained from B-splines, which form a piecewise polynomial basis constructed from a non-decreasing, real-valued vector, the so called knot vector $\boldsymbol{\Xi} = [\xi_1^j, \xi_2^j, \xi_3^j, ..., \xi_{n_j+p_j+1}^j]$, where j represents the $j-th$ parametric dimension ($j = \{1, 2, 3\}$ for solid models). The knots partition the parameter space into elements and identify the basis features among them. Given a set of knot vectors it is possible to recursively define the B-spline basis functions as

$$N_{i,0}(\xi) = \begin{cases} 1 & if\ \xi_i \leq \xi < \xi i + 1 \\ 0 & otherwise \end{cases} \tag{1}$$

$$N_{i,p}(\xi) = \frac{\xi - \xi_i}{\xi_{i+p} - \xi_i} N_{i,p-1}(\xi) + \frac{\xi_{i+p+1} - \xi}{\xi_{i+p+1} - \xi_{i+1}} N_{i+1,p-1}(\xi) \tag{2}$$

A B-Spline curve can be obtained as linear combination between the basis functions $N_{i,p}$ and the control point coordinates B_i defined in $\mathcal{R}^d$. The main feature of B-Splines is the chance to have different level of continuity along the elements. In general, basis functions of order p present $p-m$ continuous derivatives across the the knot ξ_i, i.e., the basis is C^{p-m}, where m is the knot multiplicity in the knot vector. This structure allows to increase the inter element regularity with respect to traditional C^0 FEM basis. NURBS were introduced in order to overcome the limit of B-Splines to exactly represent a wide range of geometric objects. A $p-th$ order NURBS curve is represented as

$$\mathbf{C}(\xi) = \sum_{i=0}^{n} R_{i,p}(\xi) w_i \mathbf{B_i}; \quad R_{i,p}(\xi) = \frac{N_{i,p}(\xi) w_i}{\sum_{i=0}^{n} N_{i,p}(\xi) w_i}. \tag{3}$$

where B_i are the control points coordinates defined in $\mathcal{R}^d$, w_i are the *weights*, ξ is the knot representing the parametric coordinates and $N_{i,p}(\xi)$ are the p-th order B-spline basis functions. Taking advantage of the tensor product nature of NURBS it is possible to extend eq. 3 to trivariate solid structures as follows

$$\mathbf{V}(\xi_1, \xi_2, \xi_3)_d = \sum_{i=0}^{n_1} \sum_{j=0}^{n_2} \sum_{k=0}^{n_3} R_{i,p}(\xi_1) S_{j,q}(\xi_2) T_{k,r}(\xi_3) (\mathbf{B_{i,j,k}})_d. \tag{4}$$

where $\mathbf{B_{i,j,k}}$ are the control point coordinates, p, q, r are the polynomial degrees for each parametric direction and $R_{i,p}$,

$S_{j,q}$, $T_{k,r}$, are the NURBS basis functions defined as in eq. 4 and $d = \{1, 2, 3\}$.

III. Material and Methods

A. Stent Model

In this study we exploited a novel computational framework that combines the CAD software Rhinoceros v. 4.0 SR8 (McNeel and Associated, Seattle, WA, USA) with the general purpose solver FEAP. Since no data are available from the manufacturer, the main geometrical features of such devices are derived from high-resolution micro-CT scans of the stent in the delivery system (see figure 1-a). Subsequently, the stent model to be embedded in bending analysis is generated through the following steps:

- A planar CAD geometry (see figure 1-b), corresponding to the unfolded stent, is generated. Subsequently a 2D CAD surface is generated for each NURBS patch.
- The NURBS data (control points, knots and weights) are exported as text files by mean of an in-house code developed in VBScript;
- The final stent configuration (fig. 1-c) is obtained by mean of an in-house code in Matlab (The Mathworks Inc., Natick, MA, USA) and subsequently exported in a format suitable for the solver FEAP.

The stent model (Bard ViVEXX Carotid Stent - C. R. Bard Angiomed GmbH Co., Germany) is composed by 87 NURBS patches for a total number of 29950 control points. Since the aim of this work is to perform a comparison between IGA and FEM, we extended the framework capability in order to get in addition an equivalent FEM mesh.

B. Constitutive models

Given the comparative nature of this work, the following constitutive models have been considered: (i) neo-Hookean hyperelastic material; (ii) the SMA model presented by Auricchio et al. [4] has been implemented in a large displacement - small strain regime.

C. Analysis setup

Following the approach proposed by Auricchio et al. [5], the stent bending is simulated through a displacement-based analysis under large deformation regime. A displacement of 11 mm along the Y direction was imposed for all the control points referring to the distal extremity of the stent while the proximal one was blocked. The deformed configuration is depicted in fig. 2. Different refinements, both for IGA and FEM, were considered and briefly resumed in tables I, II and III. In particular for IGA we considered both h (knot insertion) and k (degree elevation and knot insertion) refinement techniques (for details, please refer to [1]).

IV. Results

Reaction force at the distal extremity is the main quantity evaluated in bending tests [6], so we used it as reference to evaluate the convergence of the two methods. Moreover the elastic energy value has been considered with the Neohookean material (fig3-c). The results show that IGA has a better behavior respect to classic FEM, both considering the number of degrees of freedom (fig3-a) and CPU time (fig3-b). Moreover the IGA benefits result more evident when degree elevation is applied.

Mesh	DOF	p	q	r
IGA 1	29950	3	1	1
IGA 2	68175	3	1	1
IGA 3	193125	3	1	1

TABLE I
Isogeometric Analysis of stent bending: h refined IGA model

Mesh	DOF	p	q	r
$IGAP2$ 1	68175	3	2	2
$IGAP2$ 2	122700	3	2	2
$IGAP2$ 3	347625	3	2	2

TABLE II
Isogeometric Analysis of stent bending: k refined IGA model

Mesh	DOF	p	q	r
FEM 1	16050	1	1	1
FEM 2	73575	1	1	1
FEM 3	202092	1	1	1

TABLE III
Isogeometric Analysis of stent bending: FEM model

V. Conclusion

In the present study we present a novel computational framework able to integrate CAD models and computational tools in order to perform IGA for the evaluation of carotid artery stents performance. The results suggest that IGA is able not only to represent exactly the computational domain, but also to get better approximation of the solution with a reduced number of degrees if freedom with respect to traditional FEM. We think that IGA for vascular biomechanics can give, in the next future, a crucial contribution to the integration of medicine and numerical analysis.

VI. Acknowledgment

This work is supported by the European Research Council through the FP7 Ideas Starting Grant project no. 259229. The authors would also like to acknowledge Prof. R.L. Taylor and Eng. E. Boatti.

References

[1] Hughes, T.J.R., Cottrell, J.A, Bazilevs, Y. Isogeometric analysis: CAD, finite elements, NURBS, exact geometry, and mesh refinement. *Computer Methods in Applied Mechanics and Engineering* , Vol. **194**, 4135-4195, 2005.

[2] Cottrell, J.A, Hughes, T.J.R., Bazilevs, Y. *Isogeometric Analysis. Towards integration of CAD and FEA*. Wiley, 2009.

[3] Piegl, L.A., Tiller W. The NURBS book. *Springer*, 1997.

[4] Auricchio, F.,Petrini L., A three-dimensional model describing stress-temperature induced solid phase transformations. Part I: solution algorithm and boundary value problems, *International Journal for Numerical Methods in Engineering*, vol. 61, pp. 807–836, 2004.

[5] Auricchio, F., Arghavani, J., Conti, M., Morganti, S., Reali, A., Stefanelli, U. Shape-memory alloys: effective 3D modeling, computational aspects and analysis of actuator and biomedical devices. *Proceedings of ACTUATOR10 - International Conference and Exhibition on New Actuators and Drive Systems* ,2010.

[6] S. Müller-Hülsbeck, P. Sch´afer, N. Charalambous, S. Schaffner,M. Heller, T. Jahnke, *Comparison of carotid stents: an in-vitro experiment focusing on stent design.*, Journal of Endovascular Therapy, 2009, vol.16, pp.168 - 177.

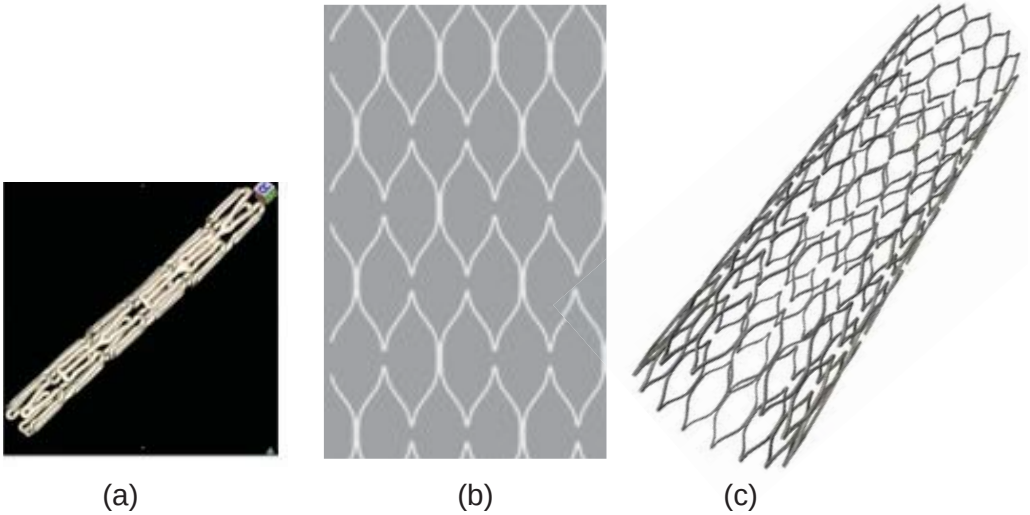

Fig. 1. IGA stent generation: (a) detail of a high resolution micro-CT performed on a real stent within the delivery system ; (b) planar CAD geometry resembling the stent design pattern; (c) IGA suitable stent model.

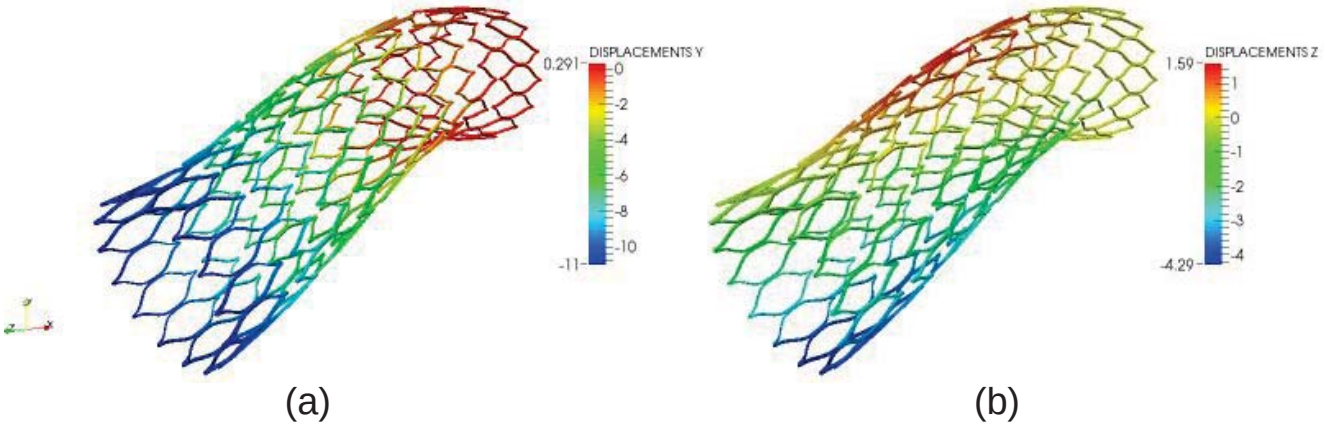

Fig. 2. Stent bending analysis: (a) Displacement on Y direction contour plot; (b) Displacement on Z direction contour plot.

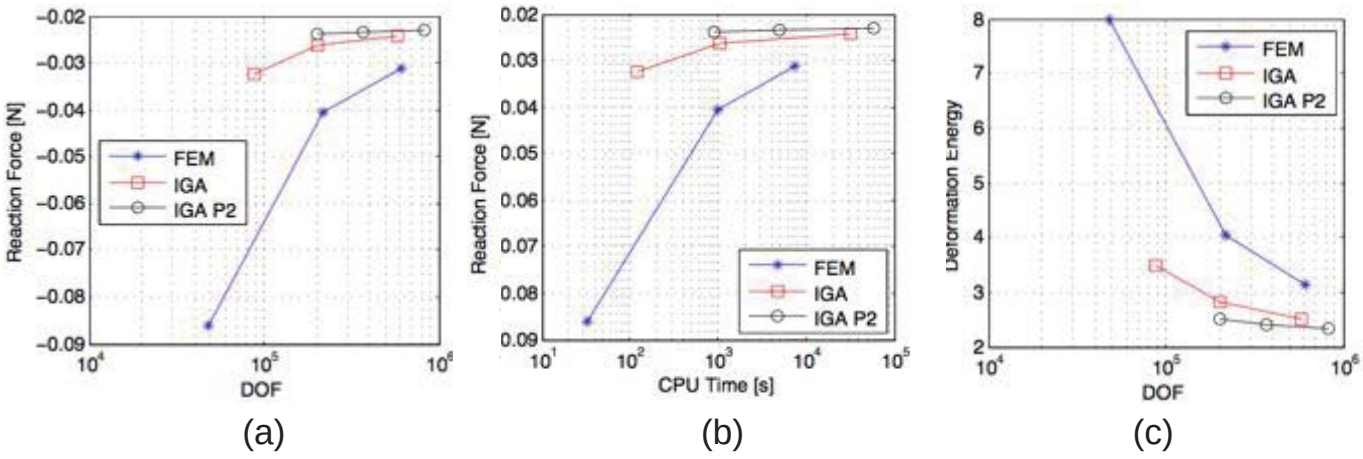

Fig. 3. Convergence of stent bending analysis: (a) SMA constitutive model reaction force versus DOF number; (b) reaction force versus CPU time; (c) Neohookean constitutive model deformation energy versus DOF number.

Fluid dynamics in porous scaffolds stimulated with cyclic squeeze pressure in the S^{2}PR bioreactor

M. Ferroni[1], S. Giusti[2], G. Spatafora[1], F. Boschetti[1], and A. Ahluwalia[2]

[1] *Laboratory of Biological Structure Mechanics, Chemistry Materials and Chemical Engineering Department "Giulio Natta", Politecnico di Milano, Milano, Italy*

[2] *Research Center E. Piaggio, University of Pisa, Via Diotisalvi 2, 56126 Pisa, Italy*

***Abstract*—In cardiac tissue engineering, the use of bioreactors is fundamental for applying controlled mechanical stimuli on the cells and recreate a physiological environment for cardiomyocytes cultures. This work is focused on an innovative Sensorized Squeeze PRessure (S^{2}PR) bioreactor, able to apply a periodic contactless hydrodynamic pressures on 3D porous constructs. The fluid-dynamic environment inside the bioreactor was fully characterized using computational models, focusing on the pressures and fluid velocity profiles generated in the porous scaffold during the cyclic stimulation.**

***Keywords*—CFD models, bioreactor, 3D porous cryogel, cardiac tissue engineering.**

I. Introduction

CULTURE conditions are an important aspect of engineering myocardial tissue. In fact, the heart is a dynamic organ subjected to several physiological stimuli (e.g. mechanical stretch, electrical stimulation, pressure, perfusion) that impact on the tissues growth and function [1]. In cardiac tissue engineering, several studies demonstrated the role of mechanical forces and fluid movement on the organization and function of cardiomyocytes. In particular, fluid movement can increase the oxygen and nutrient transport [2], whereas mechanical forces can activate mechanotrasduction pathways and induce cell alignment and cytoskeleton re-organization [3], [4].

In this work, we present Computational Fluid-Dynamical (CFD) models of the Sensorized Squeeze PRessure bioreactor (S^{2}PR), used for studying the effect of hydrodynamic stimuli on neonatal cardiomyocytes seeded in porous 3D constructs. This bioreactor has already been tested on different cell cultures (i.e. chondrocytes, cardiomyocytes), demostrating the ability of the squeeze stimulus to induce changes in the ECM synthesis and cytoscheletal organization of cells [5], [6]. The fluid dynamic environment created around and inside the porous scaffold was fully characterized using 2D axial symmetric macro-scaled models of S^{2}PR bioreactor. Then, the fluid dynamics predicted by the 2D models was applied to 3D micro-scaled sub-models of gelatin porous cryogels, in order to evaluate the fluid-induced forces in the porous construct during stimulation in the S^{2}PR bioreactor.

II. Material and Methods

A. S^{2}PR Bioreactor

The design of the S^{2}PR bioreactor is inspired by the SQPR 2.0, an innovative stimulation chamber which imposes a cyclic, hydrodynamic and contactless overpressure on cell cultures, using a simple vertical piston movement [5]. The entity of the stimulus mainly depends on the piston velocity and the distance between the two approaching surfaces, called meatus. In addition, during the cyclic piston movement, culture media flows through the cell-seeded construct enhancing the diffusion of oxygen and nutrients. In order to precisely apply and measure the desired stimulus on a cell culture, the S^{2}PR is provided with a force and a position sensor, assuring high precision and control of the piston movement (Fig. 1). In particular, the force sensor (Flexiforce A201, Tekscan, Inc. MA, USA), placed under the sample brace, is able to detect any contact between the piston and the scaffold (Fig. 2), whereas the position sensor embedded in the motor shaft (Fig. 1) continuously matches all the data from the force sensor, to assure an accuracy in the piston motion of 5 μm. Furthermore, the presence of the force sensor allows compressive tests on the stimulated construct for real-time evaluation of the matrix production, which is linked to the stiffness of the scaffold.

The S^{2}PR is a highly automated system with a dedicated GUI from which the user can set all the stimulation parameters such as the maximum value of the hydrodynamic pressure applied, the frequency of the stimulus and the duration of the experiment.

B. Gelatin Cryogel

Porous gelatin cryogels were fabricated using the freeze-dry method from gelatin 5% w/v (Type A gelatin from pig skin) in deionized water, chemically crosslinked with glutaradheyde (GTA) 100 mM, as previously reported [7], [8]. Gelatin cryogels have been fully characterized in an aqueous environment, pointing out a porosity of 90 %, a permeability of $13 \cdot 10^{-12} m^2$ and an elastic modulus of around 12 kPa [8].

C. Computational Model

Computational models were implemented using the commercial software Comsol Multiphysics in order to characterize the local fluid dynamics applied on the scaffold with the S^{2}PR bioreactor. In particular, these models were used to evaluate pressure and velocity profiles around the 3D construct. The time-dependent 2D models assume an axial symmetric geometry, considering a transverse section of the bioreactor chamber. Here, the piston moves the culture media, considered as incompressible, homogeneous and Newtonian fluid, with

a density $\rho = 1029\frac{kg}{m^3}$ and a constant dynamic viscosity $\mu = 4.77 \cdot 10^{-3} Pa \cdot s$. Navier-Stokes equations for incompressible fluid were used for the fluid flow in the bioreactor chamber, whereas Brinkman equations are applied for the flow in the porous scaffold. In order to simulate the correct stimulation on the scaffold, the velocity profile, evaluated by the laminar flow mode, is considered as a boundary condition of the Brinkman module. Moreover, the arbitrary Lagrangian-Eulerian (ALE) method is used to model the piston movement to apply the moving mesh mode to specify stationary or transient deformation of the simulation domain. As previously described, the piston moves vertically in the fluid, approaching and receding from the base, without touching the scaffold. The approaching velocity is $11.6mm/s$ while the receding one is $2mm/s$, both with an excursion of $1mm$, at a frequency of $1Hz$.

From these models, pressure and velocity profiles of the fluid around the porous scaffold are exported and processed, in order to be further used as inputs for the 3D sub-models of the gelatin cryogel.

III. RESULTS

2D sub-models were used to analyse the flow condition around the scaffold, evaluating the pressure, shear stress and flow velocity at specific time-points.

Figure 4 shows the changes in direction and intensity of the fluid velocity in the bioreactor chamber according to the piston movement. In fact, the fluid goes out from the meatus when the piston moves down, reaching the highest velocity when it is at the lowest position (time 1, Fig. 4 on the left), whereas the culture medium flows slowly into the meatus from the lateral sides of the chamber when the piston recedes from the scaffold (time 2, Fig. 4 on the right). Figure 3 shows the distribution of the pressure on the upper face of the scaffold at time 1, pointing out a parabolic profile from the center to the edge of the scaffold. Results showed that the pressure values and distribution also change as a function of the time. In figure 5 we can see the entire geometry of the scaffold inside the chamber and a zoom of an ideally reconstructed scaffold [9], [10], according to the real value of porosity (90%), pore diameter ($150 \cdot 10^{-3} mm$) and permeability ($13 \cdot 10^{-12} m^2$).

IV. CONCLUSION

The results of the three 2D axial symmetric models highlighed the importance of charactering time-dependent movement of the piston in the presence of porous cryogels, even considering just the macro-properties of the scaffold (permeability and porosity). Moreover, pressure and velocity profiles around to the scaffold are in accordance with our stationary models and pressure measurements reported in [5].

As previously outlined, these results will be used as boundary conditions for 3D scaffold micro-scale sub-models, in order to evaluate the shear stress and pressure values inside the scaffold, which directly affect cells seeded and grown in the construct. The micro-scaled model (Fig. 5) is developed as a simplified geometry of the actual scaffold, from 3D reconstructions of the sample, and shear stresses will be used to estimate the shear stresses acting on the cardiomyocytes. Moreover, the oxygen consumption of the cardiomyocytes at the fluid-solid interface of the micro-model will be added in the CFD models, to verify that the fluid-dynamic environment created in the 3D scaffolds by the S^2PR bioreactor improves oxygen transport without damaging the cells.

ACKNOWLEDGMENT

The study was co-funded by the Italian Ministry of Education, University & Research (MIUR) (Project PRIN 2010, MIND).

REFERENCES

[1] K. Y. Ye and L. D. Black, "Strategies for tissue engineering cardiac constructs to affect functional repair following myocardial infarction." *Journal of cardiovascular translational research*, vol. 4, no. 5, pp. 575–91, Oct. 2011. [Online]. Available: http://www.pubmedcentral.nih.gov/articlerender.fcgi?artid=3182851\&tool=pmcentrez\&rendertype=abstract

[2] G. Vunjak-Novakovic, M. Radisic, and B. Obradovic, "Cardiac tissue engineering: effects of bioreactor flow environment on tissue constructs," *Journal of Chemical Technology & Biotechnology*, vol. 81, no. 4, pp. 485–490, Apr. 2006. [Online]. Available: http://doi.wiley.com/10.1002/jctb.1467

[3] V. F. Shimko and W. C. Claycomb, "Effect of mechanical loading on three-dimensional cultures of embryonic stem cell-derived cardiomyocytes." *Tissue engineering. Part A*, vol. 14, no. 1, pp. 49–58, Jan. 2008. [Online]. Available: http://www.liebertonline.com/doi/abs/10.1089/ten.2007.0092http://www.pubmedcentral.nih.gov/articlerender.fcgi?artid=2562769\&tool=pmcentrez\&rendertype=abstract

[4] M. Shachar, N. Benishti, and S. Cohen, "Effects of mechanical stimulation induced by compression and medium perfusion on cardiac tissue engineering." *Biotechnology progress*, vol. 28, no. 6, pp. 1551–9, 2012. [Online]. Available: http://www.ncbi.nlm.nih.gov/pubmed/22961835

[5] C. De Maria, S. Giusti, D. Mazzei, A. Crawford, and A. Ahluwalia, "Squeeze pressure bioreactor: a hydrodynamic bioreactor for noncontact stimulation of cartilage constructs." *Tissue engineering. Part C, Methods*, vol. 17, no. 7, pp. 757–64, Jul. 2011. [Online]. Available: http://online.liebertpub.com/doi/abs/10.1089/ten.tec.2011.0002http://www.ncbi.nlm.nih.gov/pubmed/21410315

[6] S. Giusti, F. Pagliari, F. Vozzi, A. Tirella, D. Mazzei, M. Cabiati, S. Del Ry, and A. Ahluwalia, "SQPR 3.0: A Sensorized Bioreactor for Modulating Cardiac Phenotype," *Procedia Engineering*, vol. 59, pp. 219–225, Jan. 2013. [Online]. Available: http://linkinghub.elsevier.com/retrieve/pii/S187770581301028X

[7] A. Bigi, G. Cojazzi, S. Panzavolta, K. Rubini, and N. Roveri, "Mechanical and thermal properties of gelatin films at different degrees of glutaraldehyde crosslinking." *Biomaterials*, vol. 22, no. 8, pp. 763–8, Apr. 2001. [Online]. Available: http://www.ncbi.nlm.nih.gov/pubmed/11246944

[8] A. Spinelli, B. Vinci, A. Tirella, M. Matteucci, L. Gargani, A. Ahluwalia, C. Domenici, E. Picano, and P. Chiarelli, "Realization of a poro-elastic ultrasound replica of pulmonary tissue." *Biomatter*, vol. 2, no. 1, pp. 37–42, 2012. [Online]. Available: http://www.pubmedcentral.nih.gov/articlerender.fcgi?artid=3849056\&tool=pmcentrez\&rendertype=abstract

[9] F. Boschetti, M. Raimondi, F. Migliavacca, and G. Dubini, "Prediction of the micro-fluid dynamic environment imposed to three-dimensional engineered cell systems in bioreactors," *Journal of Biomechanics*, vol. 39, pp. 418–425, Dec. 2004. [Online]. Available: http://linkinghub.elsevier.com/retrieve/pii/S187770581301028X

[10] M. Cioffi, F. Boschetti, M. Raimondi, and G. Dubini, "Modeling Evaluation of the Fluid-Dynamic Microenvironment in Tissue-Engineered Constructs: A Micro-CT Based Model," *Wiley InterScience*, vol. 93, pp. 418–425, Sep. 2005.

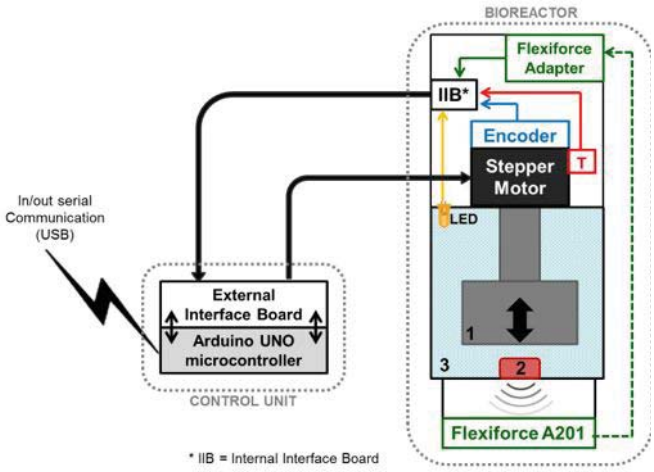

Fig. 1. Functional block diagram showing the architecture of the S^2PR bioreactor

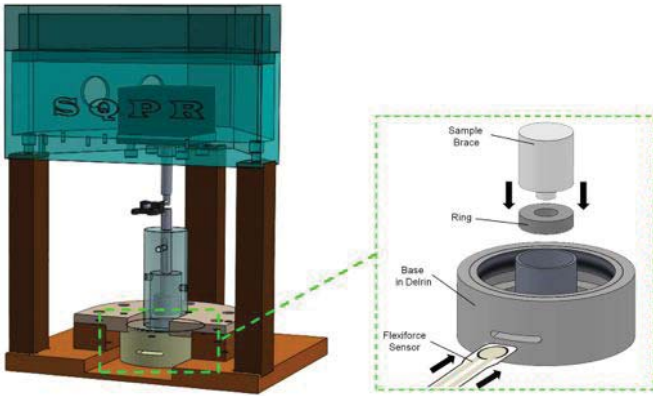

Fig. 2. CAD drawing of the S2PR bioreactor, including the exploded view of the base, with the force sensor

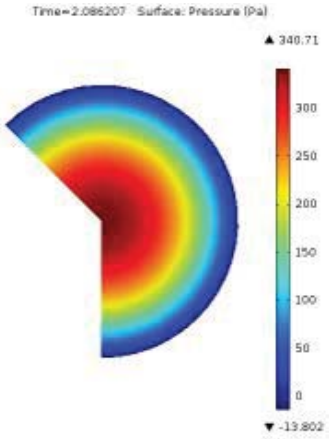

Fig. 3. Pressure distribution on the upper face of the scaffold when the piston is at its lowest position.

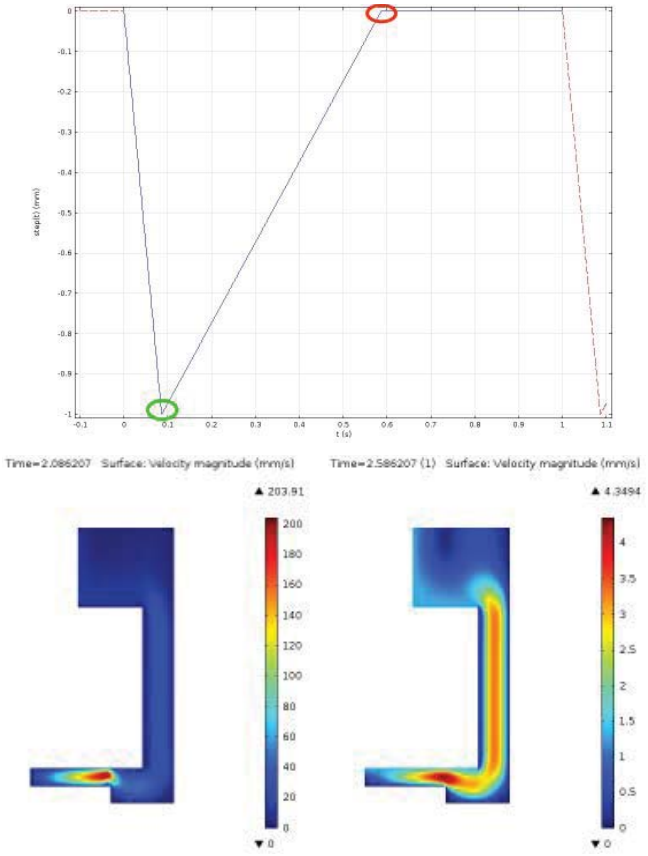

Fig. 4. Two velocity profiles at different time-points of the cyclic piston movement: when the piston is in the lowest (green circle and profile on the left) and in the highest (red circle and profile on the right) position with respect to the base of the bioreactor.

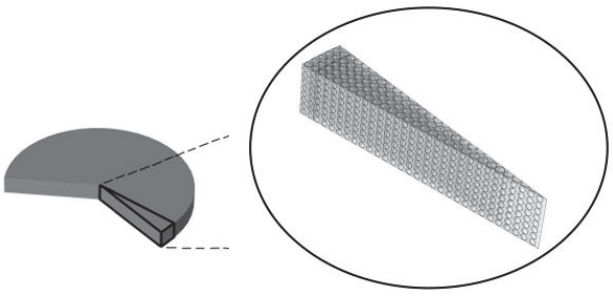

Fig. 5. Detail of the ideally reconstructed scaffold used in the micro-scaled 3D models, obtained from 3D reconstructions of the sample.

Numerical analysis of the biomechanical behaviour of the forefoot

C.G. Fontanella[2], E.L. Carniel[1,2], and A.N. Natali[1,2]
[1] *Department of Industrial Engineering, University of Padova, Padova, Italy*
[2] *Centre for Mechanics of Biological Materials, University of Padova, Padova, Italy*

Abstract **- The investigation of foot biomechanical response is addressed to specific tissues and structures within the forefoot region. The analysis is performed by a computational approach, which allows the investigations of tissues response accounting also for interaction phenomena with ortheses and footwear. In the present work, particular attention is paid to forefoot plantar tissues which play a prominent role in foot biomechanics, because of their contribution to attenuate ground impacts, to redistribute plantar pressures and to protect internal foot structures. The development of reliable computational models requires the definition of constitutive formulations that interpret the mechanical response of the biological tissues. Constitutive parameters are evaluated by the analysis of experimental data from "in vitro" tests on tissue samples. A 3D finite element model of the forefoot region is developed starting from the analysis of biomedical images. The reliability of model and parameters is assessed by the comparison of experimental and numerical results pertaining to "in vivo" indentation tests. The numerical model developed allows to evaluate the mechanical response of forefoot plantar tissues in terms of stress and strain distribution during the gait cycle.**

Keywords **- Soft tissue mechanics, forefoot plantar soft tissue, constitutive model, computational analysis.**

I. Introduction

DURING walking process, the forefoot plays a relevant mechanical role in the last phases of the step, when propulsion is given to leave the ground. The plantar soft tissues of the metatarsal region have to absorb the action induced, providing a valid transfer and distribution of forces to the structures of the foot, and play an essential role in weight bearing [1]-[2]. In order to better investigate the biomechanical behaviour of the forefoot region, numerical methods represent a valid approach, capable to evaluate stress and strain fields within the tissues.

This work aims to develop a numerical model of the forefoot, giving particular attention to the constitutive investigation of plantar soft tissues. A solid model of the forefoot is developed by the processing of biomedical images. Finite element discretization procedures are applied, leading to the numerical model. The mechanical behaviour of the different biological tissues is described by specific constitutive formulations. The constitutive analysis accounts for histological and morphometric data and results from mechanical tests. The plantar soft tissue is composed of adipose chambers circumferentially bounded by connective septa. Such honeycomb configuration deeply affect the compressive strength and the damping capabilities of the tissue. In literature, "in vitro" compression and stress relaxation tests were performed on plantar soft tissue specimens from the forefoot region [1]. The "in vivo" behaviour of tissues was investigated by indentation tests [2]. In agreement with the tissue structural configuration, the experimental activities show the typical features of the plantar soft tissue mechanical behaviour, as large displacement and strain, non-linear stress-strain behaviour and time-dependent response. Accounting for such mechanical features, a visco-hyperelastic model is developed. The identification of constitutive parameters is performed by the minimization of the discrepancy between model results and experimental data from the "in vitro" tests. In order to account for the actual behaviour of the tissues within the foot structures, the reliability of the parameters is improved by the computational analysis of "in vivo" indentation tests considering complex numerical models that mimic the experimental testing on foot structures.

Numerical analyses are finally performed to investigate the plantar soft tissue response during walking, with particular regard to push off phenomena. The activities allow to identify the tissues mechanical functionality by the evaluation of the stress and strain fields.

II. Materials and Methods

A. Numerical model

The numerical model of the forefoot has to account for an averaged configuration of the human foot. A virtual solid model is preliminarily obtained from the analysis of CT and MRI images to pick out the bones and the soft tissues, respectively (Fig. 1a). In detail, the model accounts for metatarsal and phalangeal bones, cartilages, soft tissues (which include muscles and connective tissues), plantar soft tissue and skin (Fig. 1b). Subsequently, the solid model is scaled and morphed according to anthropometric data reported in literature to address an averaged configuration [2]. After discretization, the finite element model is composed of about four hundred thousands four-node tetrahedral elements (Fig. 1c).

B. Constitutive formulation

Specific attention is paid to the plantar soft tissue, because of its relevant mechanical role during the daily gait activities. A visco-hyperelastic model is developed to interpret the typical properties of the tissue, with particular regard to non linear elasticity and viscous phenomena. Constitutive parameters are evaluated by the inverse analysis of "in vitro" experimental tests [3]. In detail, tests have been performed by Ledoux and Blevins (2007) [1] on specimen from submetatarsal plantar soft tissue, accounting for compression, hysteresis and stress relaxation conditions.

Hyperelastic formulations are adopted to define the mechanical behaviour of the cartilages and soft tissues, according to models and parameters from literature [3],[4],[5], while skin is described by a specific fibre-reinforced hyperelastic model [3]. Each bony element is defined assuming an orthotropic, linear elastic constitutive model [3].

C. Computational analyses

Preliminary, numerical analyses are developed to validate the numerical model and the constitutive formulations. Accounting for the "in vivo" indentation experimental setup described by Klaesner et al. (2002) [2], a numerical model of the indenter is provided and positioned perpendicular to the skin of the foot under the metatarsal heads. The superior surface of the metatarsal bones are fully fixed and the indenter is moved upward to the plantar skin. The interaction phenomena between indenter and skin are specified by a Coulomb contact strategy, according to a 0.42 friction coefficient [4],[5].

Finally, the developed numerical model is applied to investigate the plantar soft tissue mechanical functionality during walking activity. The forefoot region is particularly stressed during the push off step of the gait cycle. Specific rotational boundary conditions are applied to the bony segments of the model to analyse the phenomenon, while the interaction between skin and ground is defined by a Coloumb contact strategy, according to a 0.67 friction coefficient [4],[5].

III. Results

The identification of constitutive parameters is performed by the analysis of data from "in vitro" tests. In Figure 2, the comparison of experimental and models results from typical test conditions is reported.

Numerical analyses of indentation tests under the first, third and fifth metatarsal heads are performed to evaluate the reliability of the constitutive model and parameters, as the capability of the formulation to interpret tissues mechanics within the overall biological structure. The comparison of experimental and numerical results is reported for indentation tests performed under the third metatarsal head (Fig. 3a), in terms of force-displacement data. In detail, results from numerical investigation are reported within the domain of experimental data. The contours of numerical results are proposed, with regard to vertical displacement (Fig. 3b) and minimum principal stress (Fig. 3c) fields.

The Fig. 4 shows the minimum principal stretch fields during the push off. Results are reported on a longitudinal section at the level of the third metatarsal head at subsequent phases of the push off.

IV. Conclusion

The good agreement between experimental and numerical results suggests the ability of constitutive formulation and parameters to interpret the actual mechanical behaviour of the biological tissues and structures. With particular regard to plantar soft tissue, the mechanical response is identified accounting for experimental data from investigations performed according to different loading situations and developed on different foot conformations by different authors. The action makes it possible to avoid a subject specific formulation. In this context, model results do not interpret the mechanical behaviour of the tissue from a specific foot but the average mechanical response.

In this work, the main topic pertains to the constitutive analysis of plantar soft tissue. Such activity is defined within the framework of numerical modelling of foot tissues and structures. Numerical models can be adopted to integrate experimental results in the investigation of specific conditions, such as the mechanical response of plantar tissues during the gait cycle [5]. The results of the numerical analyses, in terms of stress and strain, make it possible to evaluate the mechanical role of the plantar soft tissue in load distribution. The effort can lead to the possibility to have a proper evaluation of the biomechanical behaviour of the foot during the different phases of the gait cycle. Moreover, numerical analyses allow for the evaluation of interaction phenomena between foot and ortheses or footwear products [5], to estimate reliability and comfort as relevant tasks for medical and industrial applications.

The analysis of the biomechanical behaviour of the foot, with particular regard to plantar soft tissue, has a relevant socio-economical impact, because of the increasing evidence of foot problems related to pathology, as diabetes, obesity and aging [6]. In this way, a mention must be given to the possibility to account for degenerative phenomena of hard and mostly soft tissues within the constitutive formulations. In this sense, complex constitutive formulations, as visco-hyperelasto-damage models, have been already provided with regard to soft biological tissues. More extended experimental investigations are required for a reliable investigation of this aspect of foot biomechanics.

References

[1] W.R Ledoux, J.J. Blevins, “The compressive material properties of the plantar soft tissue”, *Journal of Biomechanics*, vol.40, pp. 2975-2981, 2007.

[2] J.W. Klaesner, M.K. Hastings, D. Zou, C. Lewis, and M.J. Muller, “ Plantar tissue stiffness in patients with diabetes mellitus and peripheral neuropathy”, *Archives of Physical Medicine and Rehabilitation,*vol. 83, pp.1796-1801, 2002.

[3] A.N. Natali, C.G. Fontanella, E.L. Carniel, and J. Miller-Young, “Biomechanical behavior of heel pad tissues: experimental testing, constitutive formulation and numerical modelling”, *Proceedings of the Institution of Mechanical Engineers, Part H: Journal of Engineering in Medicine,* vol. 225, pp. 449-459, 2011.

[4] A.N. Natali, C.G. Fontanella, E.L. Carniel, “Constitutive formulation and numerical analysis of the heel pad region", *Computer Methods in Biomechanics and Biomedical Engineering*, vol. 15(4), pp. 401-409, 2012.

[5] C.G. Fontanella, A. Forestiero, E.L. Carniel, A.N. Natali, “ Analysis of heel pad tissues mechanics at the heel strike in bare and shod conditions”, *Medical Engineering and Physics*, vol. 35, pp. 441-447, 2013.

[6] A.N. Natali, C.G. Fontanella, E.L. Carniel, “A numerical model for investigating the mechanics of calcaneal fat pad region”, *Journal of the Mechanical Behavior of Biomedical Materials* , vol. 5, pp. 216-223, 2012.

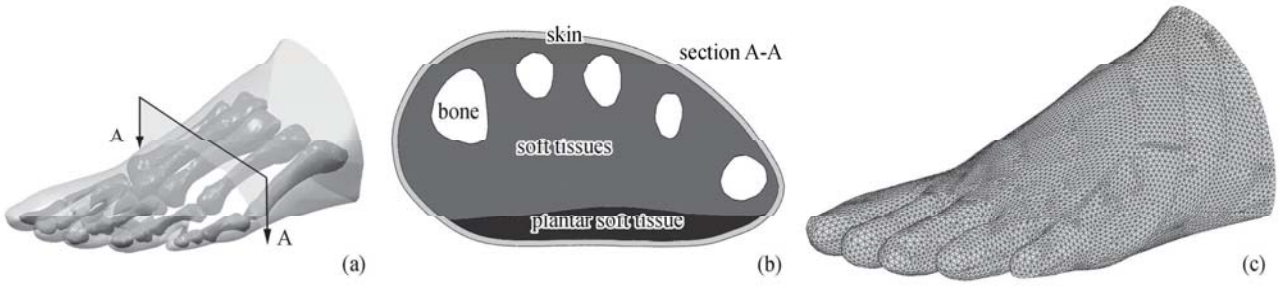

Fig. 1. Virtual solid model of the forefoot region (a) with indication of the transversal section A-A to show bones, soft tissues, skin and plantar soft tissue (b). External view of the finite element model of the overall region (c).

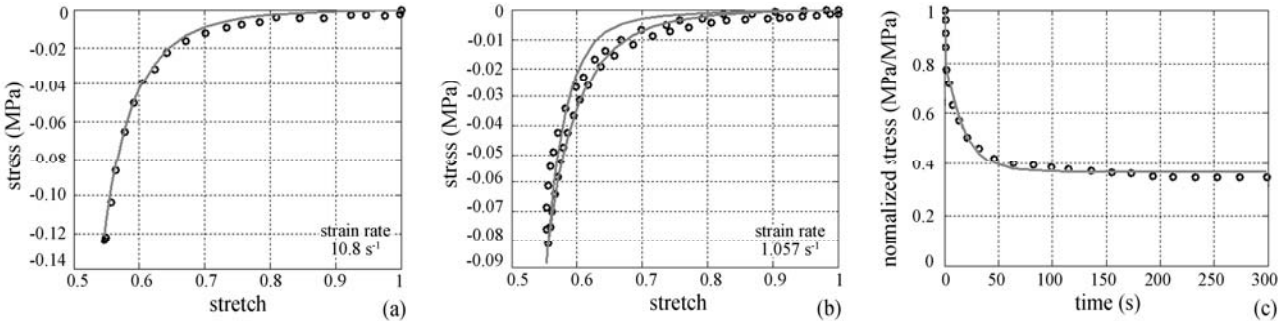

Fig. 2. Example of results from "in vitro" compression (a), hysteresis (b) and stress relaxation (c) tests on plantar soft tissue specimens. Experimental data (empty circles) are compared with model results (continuous lines).

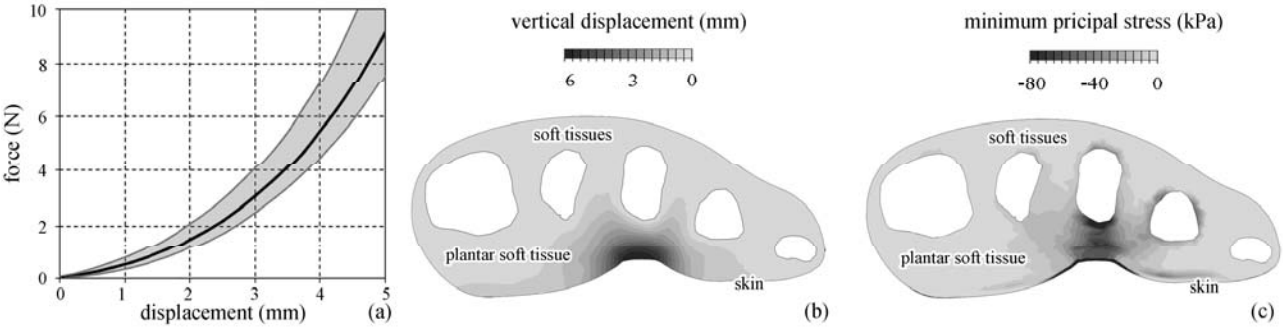

Fig. 3. Example of results from "in vivo" indentation tests (a). Numerical results (black continuous line) are reported within the domain of experimental data (gray region). Contours of the vertical displacement (b) and the minimum principal stress (c) fields are reported on a transversal section when a 5 mm indentation depth is applied.

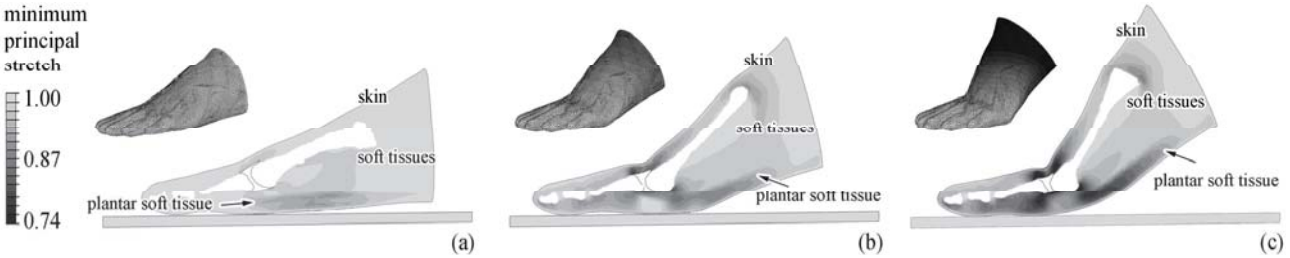

Fig. 4. Results from the numerical analysis of the push off. The minimum principal stretch field is reported over a longitudinal section at the level of the third metatarsal accounting for subsequent steps of the push off.

Biomechanical behaviour of the foot ankle ligaments

A. Forestiero[1,2], E. L. Carniel[1,2] and A. N. Natali[1,2]
[1]*Department of Industrial Engineering, University of Padova, Padova, Italy*
[2]*Centre for Mechanics of Biological Materials, University of Padova, Padova, Italy*

***Abstract* - In order to investigate the influence of ankle ligaments on the biomechanics of the foot a refined finite element model is developed. The three dimensional solid and numerical models of the foot are obtained starting from CT and MRI images. The biological tissues are defined by means of specific constitutive formulations. Numerical analyses that interpret particular experimental tests are performed. The reliability of the computational model is verified by means of the comparison between numerical results and experimental data. As preliminary approach to the investigation of damage phenomena, also numerical analyses that interpret the tears of some ankle ligaments are reported.**

***Keywords* - Foot, ankle ligaments, constitutive model, numerical analysis.**

I. Introduction

THE human foot is a complex biomechanical structure that provides support and balance during standing and stabilizing the body during gait. The ankle and subtalar joint are the most frequently injured region of the lower limb [1] in particular because of ligaments tears. In order to investigate the effects of ligament injuries, different authors performed mechanical experimental tests on the foot with intact ligaments and after the serial sectioning [2]-[4]. In this work the experimental data obtained with the Hollis Ankle Arthrometer are used [5].

The aim of this research activity is to integrate experimental and numerical data in order to provide a general reliable procedure for the investigation of foot and ankle mechanics under several loading conditions, accounting also for ankle ligaments tears.

The complex mechanical behaviour of the foot and the necessity of obtaining reliable results require an accurate modelling of the foot structure in terms of 3D anthropometrical characteristics and constitutive formulation of materials. At this purpose, a finite element model of the foot is developed accounting for the morphometric characteristics of a normotype subject and specific constitutive formulations are developed. Numerical analyses that interpret the biomechanical behaviour of the foot with all ligaments and considering the effects of local rupture are performed in consideration of experimental data [2]-[4].

II. Materials and methods

A. Experimental test

The experimental data considered are mainly referred to the tests performed by Kovaleski et al. [5]. The ankle arthrometer device consists of an adjustable plate fixed to the foot, a tibial pad attached to the tibia and a load-measuring handle attached to the footplate through which the load is applied. The experimental data describe the relative motion of the ankle-subtalar joint during the application of external loads to human cadaveric foot specimens. During the experimental test the specimen is placed on the footplate and is secured using a heel and a dorsal clamp to prevent the rotation of the hindfoot. The goal of the experimental activities is the simulation of standard clinical tests exploited in the evaluation of ligaments conditions. In detail the load to perform the anterior-posterior and the inversion-eversion movements are applied in line with the footplate through the load handle. For the anterior and posterior trial the ankle is loaded with a force from 0 to 125 N and from 0 to -125 N, respectively. With regard to the inversion-eversion rotation the ankle is loaded with a torque from 0 to 4 Nm and from 0 to -4 Nm, respectively. The displacement and the angular rotation of the foot obtained in 1.5 s are measured and data are evaluated by direct contacts with the authors [5].

B. Constitutive formulations

In order to properly characterise the biological tissues of the foot, constitutive formulations that describe the different mechanical behaviour of tissues are adopted. More in detail, the bone mechanical behaviour is defined by an orthotropic linear elastic constitutive model [6], the skin and the cartilaginous elements are described by specific hyperelastic constitutive models [6],[7] while the adipose tissue assuming a visco-hyperelastic model [7]. Soft tissues around the bony segments are considered to be homogeneous and are defined by an almost-incompressible hyperelastic model. Particular attention is paid on the characterization of the ankle ligaments tissues. At this purpose, a specific fibre-reinforced visco-hyperelastic constitutive model is adopted [7]. In agreement with experimental evidence, the constitutive formulation is capable of accounting for the typical features of ankle ligaments mechanical behaviour, as anisotropic configuration, geometrical and material non-linearity and time-dependent phenomena.

All the constitutive models previously cited are implemented in the general purpose finite element software ABAQUS 6.8 (Dassault Sistèmes Simulia Corp., Providence, RI) by specific routines.

C. Numerical analysis

A refined numerical model of the foot is developed accounting for the morphometric properties of a male subject. In detail, the virtual solid models of the bone segments are

defined starting from CT images, while models of soft tissues are mostly performed by the analysis of MRI data.

The overall model consists of 30 bony segments, including the distal segments of the tibia and fibula and the 28 foot bones. The solid model is developed with particular attention for the morphometric aspects of the ankle and subtalar joints. As reported in detail in [6], an accurate definition of the configuration of hindfoot ligaments and cartilages is performed. The numerical model of the foot is obtained through the finite element discretization of the solid model by means of specific software, adopting tetrahedral elements.

The solid and numerical models of the foot are reported in Fig. 1.

In order to evaluate the reliability and accuracy of the results, numerical analyses that interpret the previously described experimental tests are performed. At this purpose the specific load and boundary conditions of the experimental set-up are assumed. In detail, to interpret the anterior-posterior test, the tibia and the fibula are fixed and the displacement is applied to the calcaneus along the longitudinal axis of the foot. The anterior motion is defined as the displacement obtained by a load that ranges between 0 and 125 N, while the posterior motion is defined as the displacement obtained by a load that ranges between 0 and -125 N. With regard to the inversion-eversion test, the movements are defined fixing the calcaneus and the talus and imposing a rotation of the tibia and fibula around the longitudinal axis of the foot. Inversion rotation is defined as the angular displacement produced in response to a torque from 0 to 4 Nm, while the eversion rotation is defined as the angular displacement produced in response to a torque from 0 to -4 Nm.

Furthermore, in order to evaluate the influence of ankle ligaments in foot biomechanics, numerical analyses that interpret the anterior and the inversion test after the rupture of some ankle ligaments are performed. In detail, the investigation entails the removal of ligaments that reached the highest values of maximum principal strain, identified in the condition of intact foot, also accounting for results from experimental activities [2]-[4].

III. Results

With regard to the anterior-posterior test the numerical results are reported in Fig. 2. In detail, the comparison between the mean values of the experimental and numerical displacements of the foot when it is loaded in anterior and posterior direction is shown in Fig. 2a. Contours of the maximum principal strain for an anterior displacement of 8 mm are reported in Fig. 2b. It is possible to notice that the most loaded ligaments are the anterior talo-fibular ligament (ATFL) and the anterior tibio-talar ligament (ATTL).

Concerning the inversion-eversion test, the results are illustrated in Fig. 3. The comparison between the mean values of the experimental and numerical angular displacement of the foot when it is loaded with inversion and eversion torques is reported in Fig. 3a. Numerical results for a 17° of inversion rotation are reported. In detail, contours of the maximum principal strain are illustrated in Fig. 3b, showing that the most involved ligaments are the ATFL and the calcaneo-fibular ligament (CFL).

With the aim to evaluate the foot biomechanical response after potential ligaments rupture and to identify the contribution of specific ligaments to the ankle overall structural behaviour, further numerical analyses are performed. Keeping the previously described loading conditions, with a force of 125 N, the removal of ATFL determines an increase of anterior displacement of 13%. Under a torque of 4 Nm to represent inversion condition and removing ATFL and CFL, the angular rotation increases of 18%.

IV. Conclusion

The numerical method proposed in this work reports a computational approach for the investigation of the biomechanics of the foot with particular regard to the influence of ankle ligaments.

The suitability and the accuracy of the developed procedure in the evaluation of the biomechanical behaviour are confirmed by the comparison between experimental and numerical results. This investigation proposed the basis for the interpretation of the foot response in case of ankle joint trauma such as severe sprains up to the failure of the ankle ligaments, aiming at the interpretation of a relevant clinical problem. The study of the hindfoot behaviour with intact or removed ligaments represent limit conditions useful also for the preliminary investigation of degenerative phenomena. The general analysis of evolutionary degenerative conditions of hindfoot ligaments, caused by the integrated effect of aging, pathologies and traumas, up to the over mentioned failure, requires more extended experimental data for the definition of the evolutionary constitutive response mostly with regard to deformation strain rate to interpret viscous phenomena, as already in progress.

References

[1] J. Shin, N. Yue, C.D. Untaroiu, "A finite element model of the foot and ankle for automotive impact applications", *Ann Biomed Eng*, vol. 40(12), pp. 2519-2531, 2012.

[2] J.E. Kovaleski, M.J. Hollis, P.M. Norrell, J.R. Vicory, R.J. Heitman, "Sex and competitive status in ankle inversion-eversion range of motion of college students", *Percept Motor Skill*, vol. 99, pp. 1257-1262, 2004.

[3] S.J. Lapointe, S. Siegler, H. Hillstrom, R.R. Nobilini, A. Mlodzienski, L. Techner, "Changes in the flexibility characteristics of the ankle complex due to damage to the lateral collateral ligaments: an in vitro and in vivo study", *J Orthopaed Res,* vol. 15, pp. 331-341, 1997.

[4] S.I. Ringleb, A. Dhakal, C.D. Anderson, S. Bawab, R. Paranjape, "Effects of lateral ligament sectioning on the stability of the ankle and subtalar joint", *J Orthopaed Res,* vol. 29, pp. 1459-1464, 2011.

[5] J.E. Kovaleski, J.M. Hollis, R.J. Heitman, L.R. Gurchiek, A.W. Pearsall, "Assessment of ankle-subtalar joint complex laxity using an instrumented ankle arthrometer: an experimental cadaveric investigation", *J Athl Training*, vol. 37(4), pp. 467-474, 2002.

[6] A.Forestiero, E.L. Carniel, C. Venturato, A.N. Natali, "Investigation of the biomechanical behaviour of hindfoot ligaments", *Proc Inst Mech Eng Part H: J Eng In Med,* vol. 227(6), pp. 683-692, 2013.

[7] A.N. Natali, C.G. Fontanella, E.L. Carniel, "Constitutive formulation and numerical analysis of the heel pad region", *Comput Methods Biomech Biomed Engin,* vol. 15(4), pp. 401-409, 2012.

[8] A. Forestiero, E.L. Carniel, A.N. Natali, "Biomechanical behaviour of ankle ligaments: constitutive formulation and numerical modelling", *Comput Methods Biomech Biomed Engin,* vol. 17(4), pp. 395-404, 2014.

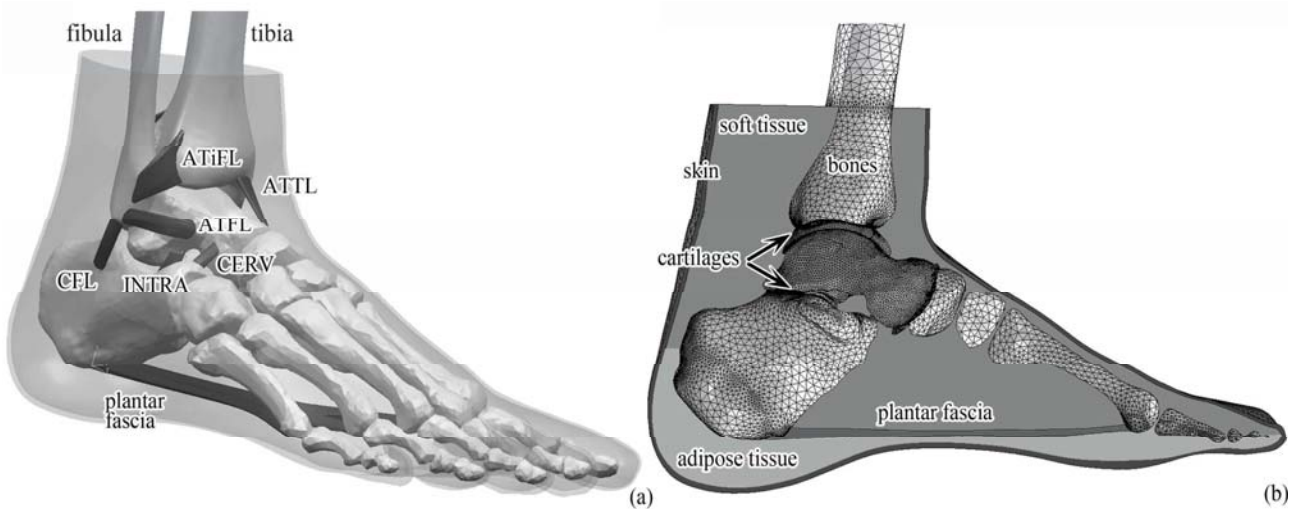

Fig.1. Representation of the foot by solid model (a) and longitudinal section of the numerical model (b).

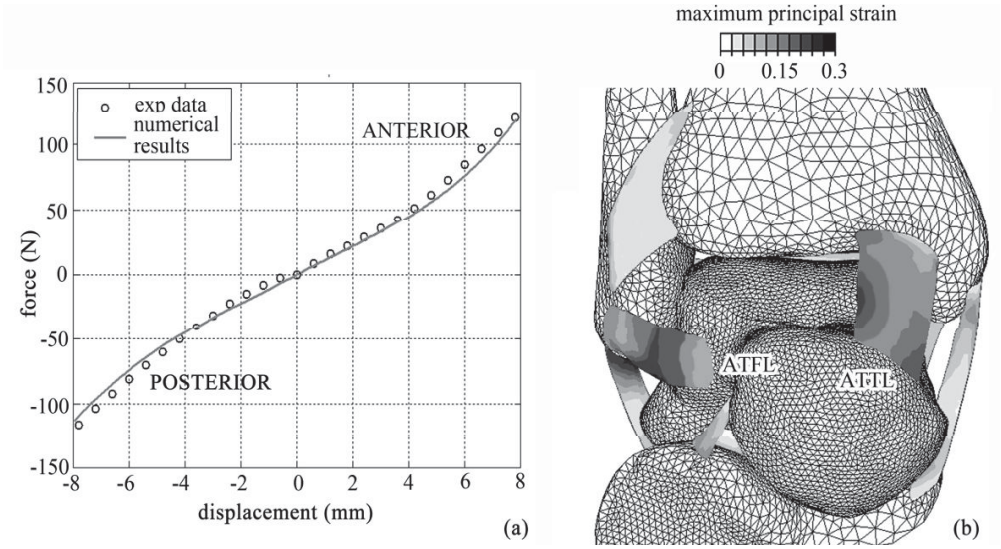

Fig.2. Numerical results for the anterior-posterior test: comparison between experimental and numerical results (a) and contours of the maximum principal strain for an anterior displacement of 8 mm reported on the frontal view of the ankle (b).

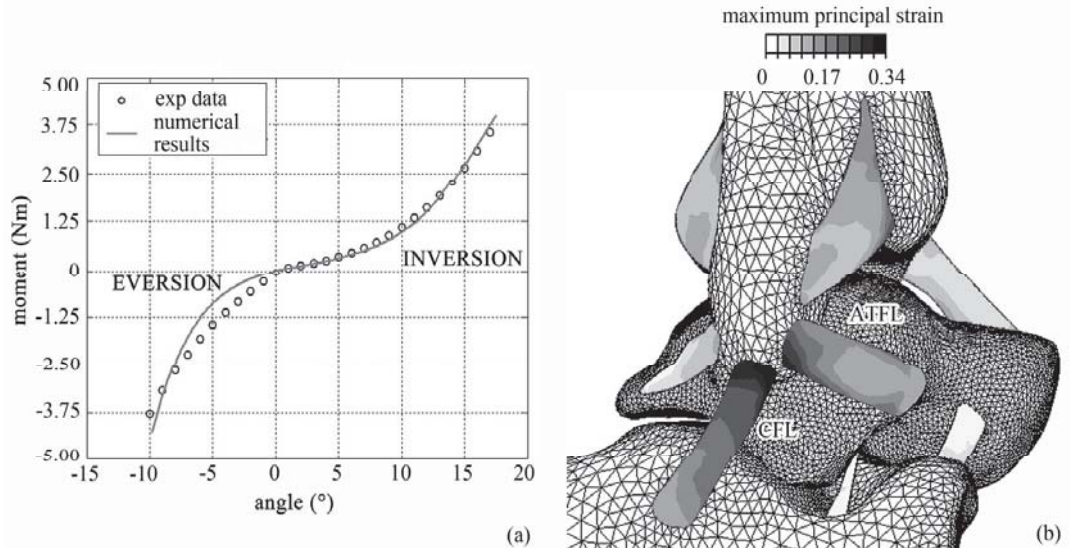

Fig.3. Numerical results for the inversion-eversion test: comparison between experimental and numerical results (a) and contours of the maximum principal strain for an inversion of 17° reported on the lateral view of the ankle (b).

Investigation of gastrointestinal tissues and structures biomechanical response

A. Frigo[1,2], E.L. Carniel[1,2], V. Gramigna[3], M. Mencatelli[3], G. Bonsignori[3], G. Favaro[2], C. Stefanini[3], and A.N. Natali[1,2]

[1] *Department of Industrial Engineering, University of Padova, Padova, Italy*
[2] *Centre for Mechanics of Biological Materials, University of Padova, Padova, Italy*
[3] *The BioRobotics Institute, Scuola Superiore Sant'Anna, Pisa, Italy*

***Abstract* - The gastrointestinal tract is a primary district of the living organism that shows a complex configuration in terms of biological tissues and structural conformation. The investigation of the mechanical behaviour in healthy and degenerative conditions is mandatory to define innovative diagnostic and surgical procedures. Computational methods allow the evaluation of tissues mechanical behaviour and interaction phenomena with biomedical devices, surgical instrumentations and prosthetic elements. The development of computational models of gastrointestinal structures requires data from histological analysis and mechanical testing, together with engineering and mathematical skills for the definition of constitutive formulations and numerical procedures. An outline of the computational mechanics approach to the investigation of the gastrointestinal tissues and structures is reported with regard to the colon region.**

***Keywords* - Constitutive analysis, gastrointestinal tissues, computational biomechanics, experimental biomechanics.**

I. Introduction

The gastrointestinal tract consists of different regions, as oral cavity, oesophagus, stomach, small and large bowels, rectum and anus, where nutrients transformation and adsorption take place. Functional processes are mediated by the mechanics of the different regions. Pathologies and degenerative phenomena may affect the proper behaviour of gastrointestinal district and represent a relevant social-health problem. Different techniques have been provided for gastrointestinal tissues screening and surgery, aiming at the less invasive action. The design of procedures and devices is correlated with the analysis of the tissues and organs from a biomechanical point of view. Such analyses can be performed by means of a computational mechanics approach, which requires the development of numerical models that interpret the actual configuration and mechanical behaviour of gastrointestinal organs, structures and tissues [1]. The investigation of colon tissues and structures is here proposed to address the general framework for the development of computational models. The first step of the procedure pertains to the morphometrical and histological analysis, in order to identify the structural configuration and preliminarily evaluate the mechanical response. These data influence the proper planning and design of mechanical tests to be developed. The integration of data from mechanical tests and histological investigations allows to define the constitutive framework [2],[3]. Constitutive parameters are preliminarily identified by the inverse analysis of mechanical tests developed on tissue samples, accounting for analytical models [4],[5]. The reliability of the achieved parameters must be updated and assessed by further experimental investigations. In fact, the preparation of tissue specimens may entail potential damages because of the operational procedure. Further tests should be developed at the structure level, as mechanical tests that are performed on tubular segments (i.e.: inflation tests) [6]. At the purpose, numerical models must be developed because of the complex conformation of the tubular samples morphometry and the experimental boundary conditions. The comparison of experimental data and numerical results allows to define the parameters and represents also the basis for assessing the reliability of the overall procedure.

II. Materials and Methods

A. Morphometrical and histological configuration

Colon wall consists of the four main layers of the gastrointestinal organs, as mucosa, submucosa, muscularis externa and serosa (Fig. 1a-b). The mucosal layer is mainly composed of a loose network of collagen fibrils embedded within a ground matrix. The submucosa is composed of collagen fibres that are arranged according to two main helixes, a clockwise and an anti-clockwise one, which run down the colon structure. The muscularis externa is composed by smooth muscular fibres that are distributed along longitudinal and circumferential directions. The longitudinal fibres congregate in three thick bands, as the taeniae coli, that are equally spaced around the colon structure. Between these bands, as the haustra region, the longitudinal fibres form a thin sheet. Finally, the serosa forms a thin layer composed of loose connective tissue. Because of its hierarchical and complex configuration, the colon wall shows anisotropic and strongly non-linear mechanical response, given by the sub-components organization and mechanical properties. The arrangement of fibrous elements along preferential directions entails the anisotropic behaviour (Fig. 1b-c). Rearrangement phenomena, as fibres un-crimping and alignment, develop within the tissues during loading. Such processes lead to a progressive variation of the stiffness with stretch and time, entailing non-linearity [3],[4],[5] and time-dependence of the mechanical response [6].

B. Experimental tests on tissue samples

The characterization of the tissues complex mechanical behaviour requires to develop mechanical tests according to different loading conditions. A set of uni-axial tensile tests

was performed on tissue specimens from pigs colon, with regard to both taeniae coli (TC) [4] and hasutra (HA) [5]. Samples were harvested along different directions, as 0°, 45° and 90°, with respect to the circumferential direction, for TC specimens, and 0°, 15°, 30°, 45°, 60° and 90° for HA specimens. An Instron 4464 machine was used to perform tensile tests up to failure and according to a 40%/s strain rate. A specific clamping apparatus was designed to keep the experimental sample within a glass beaker filled with physiological solution. Video image analysis techniques were adopted to monitor the shape evolution of the sample during testing, leading to the evaluation of tissue elongation and contraction in the loading and transversal directions.

C. *Inflation tests on tubular segments*

A specific experimental setup was developed to perform the inflation tests on pig colonic segments: two circumferential plates were spaced by a tube, and the sample was placed around the experimental complex and fixed to the plates by high resistance wires. Each plate had a central hole to allow gas flow within the tube. Four additional holes were circumferentially provided in the middle of the tube to allow the gas to flow from the tube to the region inside the specimen. A volumetric pump was connected to the hole of one of the plates, while a pressure transducer was connected to the opposite plate. The inflation tests were developed according to a two step procedure. The first step pertained to air in-flaw up to a prescribed top pressure and according to an almost constant pressure rate, as 3.5 mmHg/s. During the second step, the pressure was held constant to allow the development of creep phenomena. During the process, physiological saline was continuously poured onto the external surface of the samples to prevent drying. During testing, the sample was continuously video-recorded to monitor the shape evolution.

D. *Constitutive formulation and parameters identification*

A specific fiber-reinforced visco-hyperelastic model was provided to interpret the mechanical behaviour of the different colonic tissues [2],[3],[4],[5]. The structural configuration of the different tissues from the colon wall accounts for an isotropic ground matrix with one or more reinforcing fibres families. Specific hyperelastic potentials were introduced to interpret the non-linear behaviour of the specific tissue sub-components. Mucosa is characterized by almost isotropic behaviour and the specific strain energy can be defined accounting for the ground matrix terms only. Muscularis externa and taenie coli are composed by ground matrix and muscular fibres, which are mostly arranged along circumferential and longitudinal directions, respectively. It follows the transversally isotropic configuration. With regard to submucosa, two main sets of collagen fibres can be identified, leading to an overall anisotropic formulation.

E. *Parameters identification and reliability assessment*

The preliminary identification of constitutive parameters was performed by the inverse analysis of tensile tests on tissue samples [4],[5]. Accounting for the specific conformation of HA and TC specimens and the constitutive formulations of the tissues, analytical models were provided. A specific optimization algorithm was applied to minimize the discrepancy between model and experimental results, leading to preliminary sets of parameters for the different tissues. Subsequently, the reliability of parameters was improved and assessed by the analysis of inflation tests. In detail, finite element models of the tubular samples were developed, accounting for sample morphometry and tissues stratification. Numerical analyses were performed according to the experimental loading conditions.

III. Results

The micro- and macro-structural configuration of the anatomical region has been analyzed and the preliminary constitutive identification was performed by the inverse analysis of specific experimental tests on HA and TC samples. Experimental and model results are compared in Fig. 2a-b. Computational analyses of inflation tests were performed to assess the model and parameters reliability. Numerical results are reported in Fig. 3a-b together with data from the experimental tests.

IV. Conclusion

General notes have been reported about the analysis of colon tissues and structures mechanics by experimental and computational methods. The proposed procedure makes it possible to define computational models for the investigation of gastrointestinal tract mechanics. In particular, specific attention is paid to the tissues response during endoscopy or surgery, aiming to the optimal design of procedures and devices. Computational methods allow the evaluation of tissues mechanical behaviour with larger extension and detail than in experimental techniques, providing information about the strain and the stress fields. Furthermore, computational approach makes it possible the investigation of the tissues response accounting for a broad range of conditions, as different organs and tissues configuration, degenerative phenomena, different endoscopy/surgical methods and devices, different prosthetic elements and biomaterials, etc..

References

[1] E.L. Carniel, C.G. Fontanella, L. Polese, S. Merigliano, and A.N. Natali, "Computational tools for the analysis of mechanical functionality of gastrointestinal structures", *Technology and Health Care*, vol. 21, pp. 271-283, 2013.

[2] A.N. Natali, E.L. Carniel, and H. Gregersen, " Biomechanical behaviour of oesophageal tissues: material and structural configuration, experimental data and constitutive analysis", *Medical Engineering and Physics*, vol. 31, pp. 1056-62, 2009.

[3] E.L. Carniel, V. Gramigna, C.G. Fontanella, C. Stefanini, and A.N. Natali, "Constitutive formulations for the mechanical investigation of colonic tissues", *Journal of Biomedical Materials Research - Part A*, 2013b:00A: 000–000.

[4] E.L. Carniel, V. Gramigna, C.G. Fontanella, C. Stefanini, and A.N. Natali, "Analysis of the passive mechanical beahviour of taeniae coli: experimental and numerical approach", *Journal of Mechanics in Medicine and Biology*, vol. 14, 1450012, 2014.

[5] E.L. Carniel, V. Gramigna, C.G. Fontanella, A. Frigo, C. Stefanini, A. Rubini and A.N. Natali, "Characterization of the anisotropic mechanical behaviour of colon tissues: experimental activity and constitutive formulation", *Experimental Physiology*, In Press.

[6] E.L. Carniel, A. Rubini, A. Frigo, and A.N. Natali, "Analysis of the biomechanical behaviour of gastrointestinal regions adopting an experimental and computational approach", *Computer Methods and Programs in Biomedicine*, vol. 113, pp. 338-345, 2014.

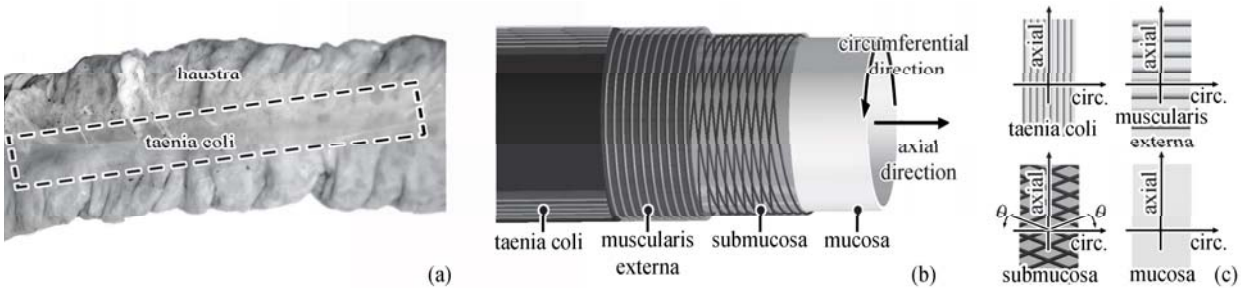

Fig. 1. Morphometrical and histological investigation of colon structures and tissues. Picture of pig colon (a) and schematic representation of colon tissues stratification (b). Definition of fibers distribution within the different colon tissues (c).

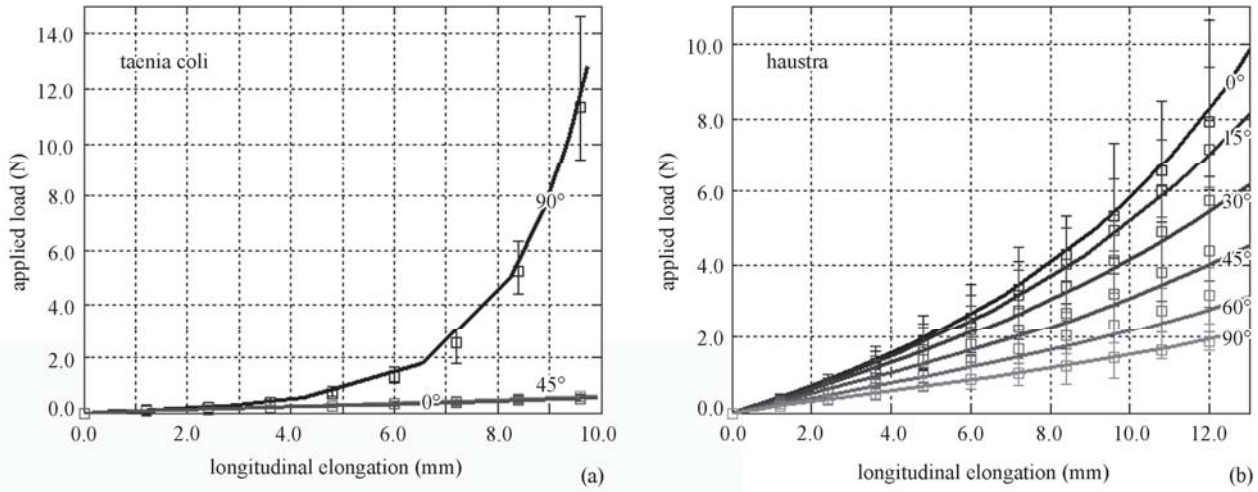

Fig. 2. Tensile tests on colon tissues samples and preliminary identification of constitutive parameters. Comparison of experimental data (empty squares) and analytical model results for tensile tests developed on taeniae coli (a) and haustra (b) samples.

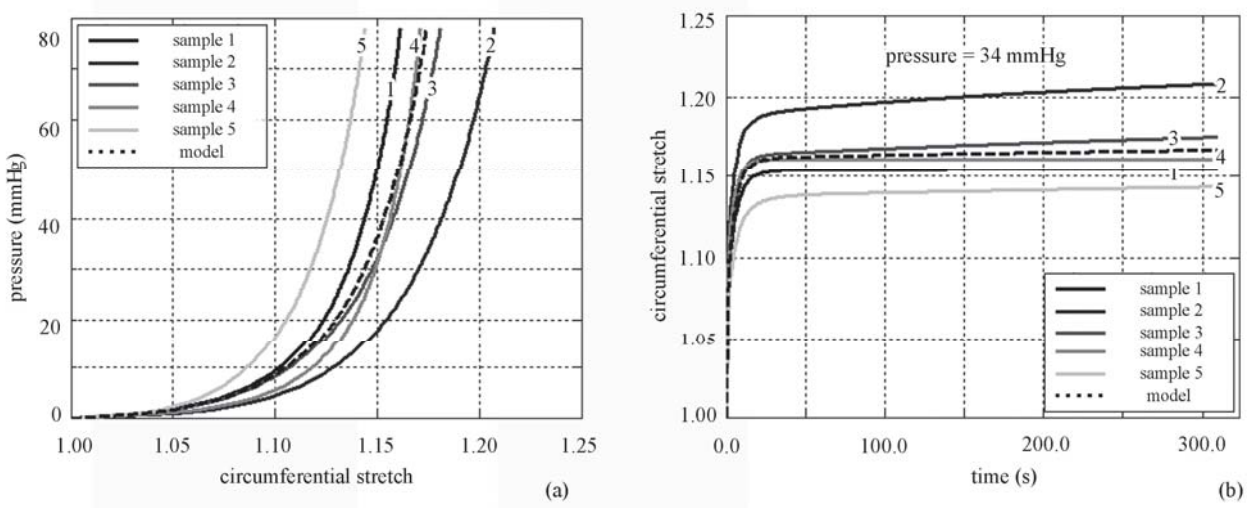

Fig. 3. Inflation tests on colon tubular segments. Comparison of experimental data form tests performed on different samples and finite element model results. Results are reported for the inflation test (a) and the creep stage at a specific pressure (b).

Identification of diabetic neuropathic patients at risk of foot ulceration through finite element models and cluster analysis

A. Guiotto[1], Z. Sawacha[1], A. Scarton[1], G. Guarneri[2], A. Avogaro[2], and C. Cobelli[1]

[1] *Dept of Information Engineering, University of Padova, Padova, 35131, Italy.*
[2] *Dept of Clinical Medicine and Metabolic Disease, University Polyclinic, Padova, 35128, Italy.*

***Abstract*—Diabetic foot is an invalidating complication of diabetes mellitus that can lead to foot ulceration and amputations. The aim of this study was to identify the neuropathic subjects at risk of ulceration with a cluster analysis classification of simulated plantar pressures and internal stresses.**

A previously developed 3D finite elements model was used and simulations were ran with gait analysis experimental data of 16 subjects (5 ulcerated) acquired 5 years prior to ulcerations. 5 ulcerated were included in one cluster with only 3 non ulcerated subjects.Longer follow up is need in order to verify if the neuropathics classified in the cluster of the ulcerated will develop ulcers.

Besides these limitations, results showed that combined FEMS and cluster analysis allowed to infer useful informations on the risk of ulceration even five years prior to the wound evolution.

***Keywords*—Diabetic foot, Gait analysis, Finite element model, Multidisciplinary approach.**

I. Introduction

DIABETIC foot is an invalidating complication of diabetes mellitus that can lead to foot ulceration and amputations. While experimental analyses are limited solely to measurements of interfacial variables, three-dimensional (3D) patient specific finite element models (FEMs) of the foot can provide both the interfacial pressures and insight into internal stresses and strains tolerated by the plantar tissue [1]. FEMs allows quantifying the loads developed in the different anatomical structures of the foot and to understand how these affect foot tissue [2].

The aim of this study was to identify the neuropathic subjects at risk of ulceration with a cluster analysis classification of simulated plantar pressures and internal stresses. Simulations were ran with gait analysis data acquired 5 years prior to ulcerations.

II. Methods

Foot biomechanical analysis was carried out as in [3] on 16 diabetic neuropathic subjects by means of a 6 cameras motion capture system (BTS, Padova), integrated and synchronized with 2 force plates (Bertec, USA), 2 plantar pressures systems (Imagortesi, Piacenza). For each patient the 3D kinematics, ground reaction forces and plantar pressures were calculated. Six of these subjects developed ulcers under metatarsals heads within 5 years after the acquisitions (ulcerated subjects (US)-age 62.3±4.1 years, BMI 26.3±2.0 kg/m^2) while the other ten did not (non US - age 63.2±6.4 years, BMI 24.3±2.9 kg/m^2).

In order to obtain the simulated stresses, a recently developed 3D FEM [4] was adopted. The MRI of the foot of a diabetic neuropathic subject was acquired, and segmented with Simpleware ScanIP (v.5.0) into 30 bones (grouped into hindfoot, midfoot, forefoot), cartilage (in the space between the bones) and the foot skin in order to get a 3D representation of the whole foot and ankle (procedure in figure 1). The model was meshed in Simpleware-scanFE with tetrahedral elements according to the literature [5] and imported into ABAQUS (Simulia,v.6.12). An horizontal rectangular element was drawn in ABAQUS under the foot to simulate the ground support. Materials properties were adopted from previous literature [6].

The simulations were run adopting the experimental kinematic and kinetics as boundary conditions as in [4]. The midstance and the push-off phases of gait were considered as they are the instants when critical loads occur in the forefoot of the diabetic subjects. The internal stresses (Von Mises and principal stresses) and the simulated plantar pressures were extracted from the simulated model (Figure 2).

K-means and hierarchical cluster analysis were performed as in [7] on simulated plantar pressures and/or internal stresses as input in order to classify the 16 subjects in 2-3-5 groups.

III. Results

TABLE I
RESULTS OF THE HIERARCHICAL CLUSTER ANALYSIS: 3 CLUSTERS (CL). DATA NORMALIZED OVER THE SUBJECT'S WEIGHT (%BW). PP=PLANTAR PRESSURE.

CL	# subject	Push-off Peak PP [%BW]	Push-off Mean PP [%BW]	Push-off Von Mises [%BW]	Mid-stance Peak PP [%BW]	Mid-stance Mean PP [%BW]	Mid-stance Von Mises [%BW]
1	0 US	42.3%	10.8%	38.1%	32.3%	8.0%	25.1%
	3 noUS	5.2%	2.3%	17.4%	2.0%	1.0%	4.4%
2	1 US	37.1%	9.7%	34.8%	27.5%	6.0%	24.5%
	4 noUS	4.1%	1.9%	5.0%	1.7%	0.7%	2.4%
3	5 US	39.0%	10.4%	37.8%	27.7%	0.06.2%	22.8%
	3 noUS	3.5%	0.7%	4.2%	2.8%	0.4%	2.1%

The best results were obtained with the hierarchical method (Ward's linkage criterion) which let to the definition of 3

clusters (Table I): 5 US were included in one cluster with only 3 non US.

IV. Conclusions

A longer follow up is needed in order to verify whether the neuropathic subjects in cluster 2 and 3 will develop ulcers. A larger dataset is needed to further validate this methodology. Besides these limitations, results showed that combined FEMS and cluster analysis allowed to infer useful informations on the risk of ulceration even five years prior to the wound evolution.

Acknowledgments

The authors thank the Imago Ortesi (Piacenza) for providing the plantar pressure systems.

References

[1] H. Yarnitzky, Z. Yizhar, A. Gefen. *Real-time subject-specific monitoring of internal deformations and stresses in the soft tissues of the foot: a new approach in gait analysis.* Journal of Biomechanics, vol.39, pp.2673-2689, 2006.

[2] P. Cavanagh, A. Erdemir, M. Petre, T. Owings, G. Botek, S. Chokhandre, R. Bafna. *Biomechanical factors in diabetic foot disease.* Journal of Foot and Ankle Research, vol.1, pp.K4, 2008.

[3] Z. Sawacha, G. Guarneri, G. Cristoferi, A. Guiotto, A. Avogaro, C. Cobelli. *Integrated kinematics-kinetics-plantar pressure data analysis: A useful tool for characterizing diabetic foot biomechanics.* Gait and Posture, vol.36, pp.20-26, 2012.

[4] A. Guiotto,Z. Sawacha, A. Scarton, G. Guarneri, A. Avogaro, C. Cobelli. *3D finite element model of the diabetic neuropathic foot: a gait analysis driven approach.* Proceedings ISB, Natal, Brasil, 2013.

[5] P. Young, TB. Beresford-West, SR. Coward, B. Notarberardino, B. Walker, A. Abdul-Aziz. *An efficient approach to converting three-dimensional image data into highly accurate computational models.* Philosophical Transactions of the Royal Society A: Mathematical, Physical and Engineering Sciences, vol.366, pp.31553173, 2008.

[6] W.-M. Chen, T. Lee, P.V.-S. Lee, J.W. Lee, S.-J. Lee. *Effects of internal stress concentrations in plantar soft-tissue–A preliminary three-dimensional finite element analysis.* Med Eng Phys, vol.32, pp.324331, 2010.

[7] Z. Sawacha, L. Laudani, A. Macaluso, G. Vannozzi. *Identifying The Association Between Physical Activity Levels And Physiological Factors Underlying mobility: a descriptive data mining approach.* Proceedings of IDAMAP, Pavia, Italy, 2012.

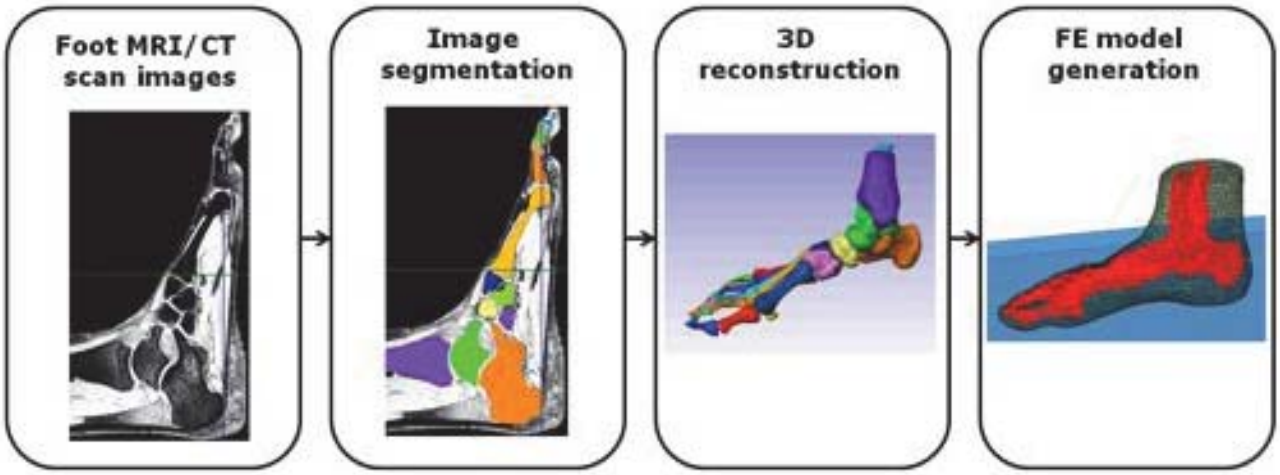

Fig. 1. Workflow of the development of an FE model of the foot.

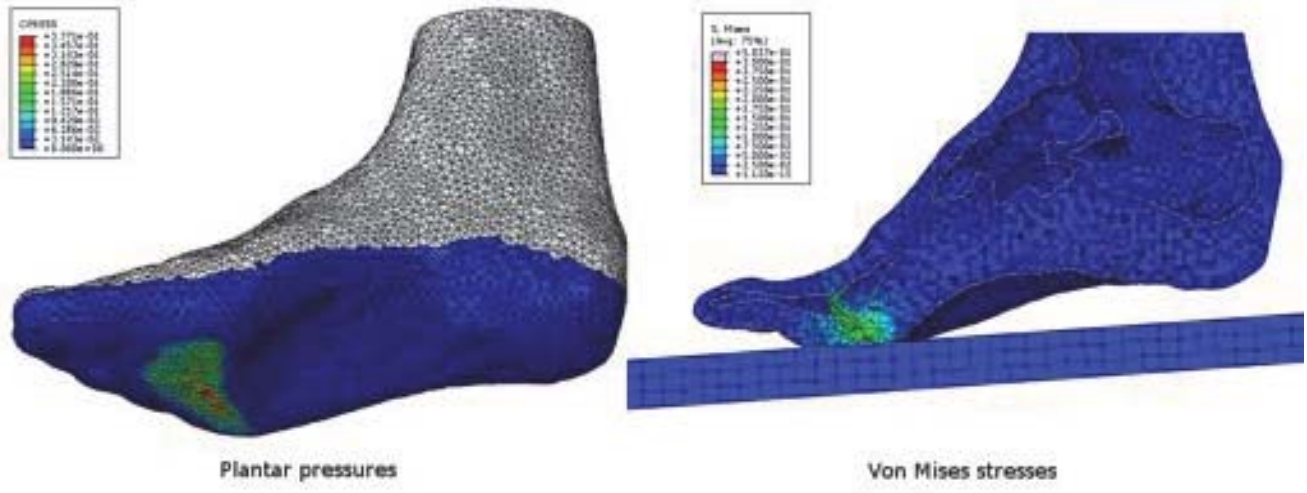

Fig. 2. Example of the results of a FEM simulation with ulcerated subject's boundary conditions: Plantar pressures (left) and Von Mises internal stresses (right).

A virtual test bench for the assessment of the flow dynamics in hemodialysis catheters

G.Isu[1], T.W. Clark[2], D. Gallo[1], P. Verdonck[3] and U. Morbiducci[1]
[1] *Department of Mechanical and Aerospace Engineering, Politecnico di Torino, Turin, Italy*
[2] *Department of Radiology, University of Pennsylvania School of Medicine, Philadelphia, Pennsylvania, USA*
[3] *Institute Biomedical Technology (IBiTech), Ghent University, De Pintelaan, Ghent, Belgium*

***Abstract*—Here we study the fluid mechanics performance of two dual lumen symmetrical tip catheters for hemodialysis by using computational fluid dynamics. A virtual test bench is set for the evaluation of those flow dynamics features inside catheter lumens impacting the outcome of dialysis therapy. The present approach, an alternative to experimental tests, is proposed as a comprehensive tool for design, characterization and optimisation of the flow-related performance of hemodialysis catheters.**

***Keywords*—CFD, hemodialysis, catheter, virtual test bench.**

I. Introduction

ALTHOUGH arteriovenous fistulae are the recommended access choice in hemodialysis, central venous catheters (CVCs) remain an important bridge to permanent access. CVCs are used to direct blood from the vena cava/right atrium to the hemodialysis machine and concurrently return it to the vena cava/right atrium. CVCs are currently the sole alternative for patients at the late stage of their renal disease or, in general, when an arteriovenous shunt is unfeasible [1],. CVCs are typically designed to work at high flow rates in order to minimize dialysis treatment time maintaining laminar flow regimes. As blood exchange devices, a paradigm in designing CVCs should be the minimization of the shear stress levels, shear-loading being a well-known promoter of mechanically-induced blood damage and of disturbed flow, which promotes thrombus formation [2]. At the same time CVCs should avoid recirculation of dialyzed blood through the inflow port of the catheter from the outflow port (a detrimental event called access recirculation, which affects hemodialysis adequacy). In the clinical practice, commercial CVC designs remain prone to thrombus formation. For this reason, it is common to reverse catheter lumen lines (reversing flow direction of the pump), in order to wash out the lumen from obstructions and/or attain more favourable dialysis pump pressures. This practice frequently produces detrimental effects on access recirculation.

In this context, among CVC designs, symmetrical dual-lumen tip dialysis catheters are currently an effective choice as a result of their low solute recirculation and their ease of positioning. It is then clear that flow dynamics largely affects the outcome of hemodialysis therapy.

In this work, we investigate in depth the flow characteristics of two different dual lumen catheter tip models (VectorFlow, a novel catheter design, and Tal Palindrome (Covidien). In detail, the hemodynamic performance of the catheters is investigated and compared by applying computational fluid dynamics (CFD). The comparison of the performance of the catheters is carried out focusing the attention on: pressure drop, shear stress luminal distribution, shear-induced blood damage potency, access recirculation and flow-related thrombogenic potency.

II. Materials and Methods

A. Computational Fluid Dynamics

Two symmetrical-tip dual lumen catheter models, which differ for the design of the central tip and for position and dimension of side holes, were considered (Fig. 1), which are typically placed into the right atrium. Here, in order to evaluate their performance, a virtual test bench was considered where catheter models were coaxially inserted into a long cylindrical conduit (diameter 18 mm, length 480 mm) modelling superior vena cava (SVC), as previously proposed to test the performance of cannulae and catheters [3]. The finite volume method was applied to solve the governing equations of the fluid motion. The general purpose CFD code Fluent (ANSYS Inc., USA) was used on mesh-grids generated using the ICEM mesh generator software (ANSYS Inc., USA): the fluid domain was divided into approximately 8,000,000 of hybrid tetrahedral/hexahedral cells. Sensitivity analysis was carried out to assure grid independence. In detail, the computational domain was made of three different sub-domains: the lumen of the conduit (SVC), the arterial lumen (corresponding to the catheter lumen where blood flows to the dialyser), and the venous lumen (where dialysed blood flows to the circulation). Blood was modelled as anisotropic, incompressible, homogeneous, Newtonian fluid, with a specific mass value equal to 1060 kg/m^3 and a dynamic viscosity equal to at 3.5 mPa s. Steady state simulations were carried out imposing the following boundary conditions (Fig. 2): constant 3 L/min flow rate was prescribed at the tube inlet section (T1, Fig. 2) in terms of flat velocity profile; reference pressure was set at the outlet section of the tube (T2); a constant flow rate of 400 mL/min [4] was prescribed at the venous inlet section (V1) in terms of flat velocity profile; a flow rate value equal to 400 mL/min was prescribed as outflow boundary condition at the arterial lumen (A2) in terms of constant mass flow. All the walls were assumed to be rigid, no slip condition was applied at the walls. In the two models under investigation, simulations were performed also in the reversed connection mode, by switching dialyzed blood from venous to arterial lumen, as

currently done in the clinical practice. To evaluate the mechanical activation of platelets and the related risk for thrombogenic events, a Lagrangian-based model of shear-induced platelet activation was applied [5]. The model takes into account the cumulative load history sustained by platelets moving along a generic fluid path to define the Platelet Activation State (PAS):

$$\mathrm{PAS} = \int_{t_0}^{t} Ca\left[\int_{t_0}^{\phi} \tau(\xi)^{b/a}\, d\xi + \frac{\mathrm{PAS}(t_0)^{1/a}}{C}\right]^{a-1} \tau(\phi)^{b/a}\, d\phi \quad (1)$$

where τ is the instantaneous shear stress values sustained by each particle along its trajectory into the flow field and a, b, and C are calibrated parameters [6]. To quantify recirculation of dialyzed blood, we ideally "labelled" blood in the venous lumen of the catheter and convection-diffusion equation was solved in order to quantify the percentage of labeled blood recirculating inside the arterial lumen.

III. Results

An example of the flow features characterizing the streaming of blood inside a dual lumen catheter is presented in Figure 3, where streamlines of blood moving into the arterial lumen (Fig. 3A) and outwards the venous lumen (Fig. 3B) of the VectorFlow catheter are depicted. As for the flow within the arterial lumen, it can be noticed that blood entering the lumen is decelerated and deflected before entering the catheter lumen. Small separation/reattachment regions can be observed downstream of the side holes (Fig. 3A), as for the venous catheter flow, a jet like structure is present downstream the venous tip, deflected outwards the axis of the SVC conduit owing to the helically shaped lumen contour, thus avoiding recirculation of dialyzed blood into the arterial lumen (Fig. 3B). Pressure drops over arterial lumen ranged from 41.8 mmHg of Palindrome to 93.8 mmHg of VectorFlow. These results are mainly affected by the fact that the greater the total area of side holes, the lower is the pressure drop, in agreement with previous results [7]. In fact, the Palindrome model is characterized by the greatest side hole area, while the VectorFlow has smaller side holes (intended to also reduce loss of interdialytic locking solution). On the other hand, smaller side hole area leads to the onset of smaller separation regions inside the lumen (Fig 3), thus reducing the thrombogenic risk within the catheter. This trade-off between pressure drop and thrombogenic risk is a key point in optimizing the design of catheters for hemodialysis, where the risk associated to thrombus formation has to be minimized. Our findings show that recirculation is negligible in both catheter models under investigation: an almost null backflow of dialyzed blood was found into the arterial lumen (both less than 0.5%). Similar values of recirculation characterize the performance of the catheter models when they operate in the reversed connection mode. Shear stress values inside the lumens give an idea of the shear-induced blood damage potency associated with the catheter design. Fig. 4 shows the presence of hot spot values for the shear stress close to the position of side holes. Moreover, both the position and the shape of the side holes is responsible for the magnitude of the hot spot values for the shear stress: the presence of smaller side holes is associated with higher local peaks in shear stress (VectorFlow). Peak values of approximately 70 Pa are reached in the Palindrome model, notwithstanding the wide area of the side hole, because of its shape, characterized by sharp angles. In general. To compare the shear-induced platelet activation potency of the catheter models under investigation, here we considered the final PAS value reached along their trajectories by platelet-like particles moving within the catheter. In detail, for each model, the PAS value averaged over all the PAS sustained by single platelet-like trajectories, was calculated. Our finding show that mean PAS values in the arterial lumen are very similar for the two catheter models, the VectorFlow being characterized by somewhat higher values (2.49×10^{-6}, compared to 1.32×10^{-6} for the Palindrome). Inside the venous lumen, platelets experience significantly higher levels of activation. This can be ascribed mainly to the high velocity jet-like structure characterizing the outflow of the catheter port. In this case, more evident differences are found: VectorFlow shows mean PAS levels at 2.77×10^{-6}, while Palindrome shows mean PAS levels at 1.23×10^{-5}, representing 440% increase over VectorFlow.

In conclusion, the comparison of the performance of the two catheter models for hemodialysis has shown that a tradeoff is needed in order to optimize the overall behavior of these blood exchange devices. Both catheters exhibited a lack of access recirculation in both forward and reversed connections. The VectorFlow produced the smallest degree of PAS in the venous lumen while similar values were observed between the catheters in the arterial lumen. In particular, it emerges that CFD analysis of recirculating dialyzed blood, thrombogenic risk and blood damage can allow for more effective and reliable catheter design.

References

[1] C.O.Stehman-Breen, D.J.Sherrard, D. Gillen, M. Caps."Determinants of type and timing of initial permanent hemodialysis vascular access". *Kidney International* 2000;57:639–45.

[2] P.L. Blackshear, G.L. Blackshear."Mechanical hemolysis. Handbook of Bioengineering".McGraw-Hill, 1987, 15.1-15.19.

[3] T.W.I. Clark, K. Van Canneyt, P. Verdonck. "Computational Flow Dynamics and Preclinical Assessment of a Novel Hemodialysis Catheter" Seminars in Dialysis 2012, 25: 574–581

[4] III-NKF-K/DOQI. Clinical practice guidelines for vascular access: update 2000. *American Journal of Kidney Disease,* 2001;37:137–81.

[5] M. Grigioni, U. Morbiducci, G. D'Avenio, G, G.D. Benedetto, Del C. Gaudio "A novel formulation for blood trauma prediction by a modified power-law mathematical model". *Biomechanics and Modeling in Mechanobiology.* 2005;4(4):249-60.

[6] M. Nobili, J.F. Sheriff, U. Morbiducci, A. Redaelli, J. Jesty, D. Bluestein. "Platelet Activation Due to Hemodynamic Shear Stresses: Damage Accumulation Model and Comparison to in vitro Measurements". *Asaio Journal* 2008;54:64-72.

[7] G. Mareels, D. S. De Wachter, and P. R. Verdonck. "Computational fluid dynamics-analysis of the Niagara hemodialysis catheter in a right heart model". *Artificial Organs*, 2004: 28(7):639–648.

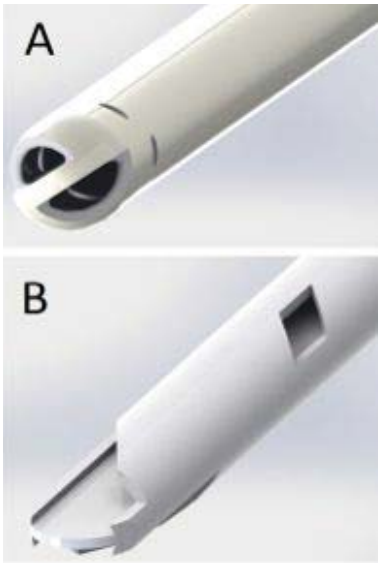

Fig. 1 Rendering of catheter geometries: VectorFlow (A), and Palindrome (B)

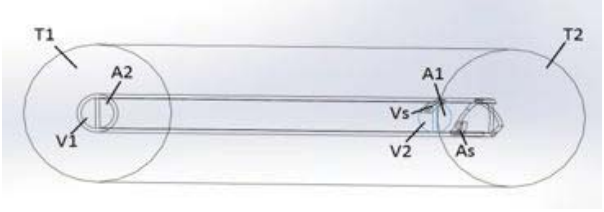

Fig. 2 Schematics of the virtual *bench test setup* for Palindrome model (representation is not in scale). T1 and T2 are tube inlet and tube outlet, V1 and V2 are the venous inlet and outlet, A2 and A1 are arterial inlet and outlet, respectively. Vs and As represent the venous and arterial side holes.

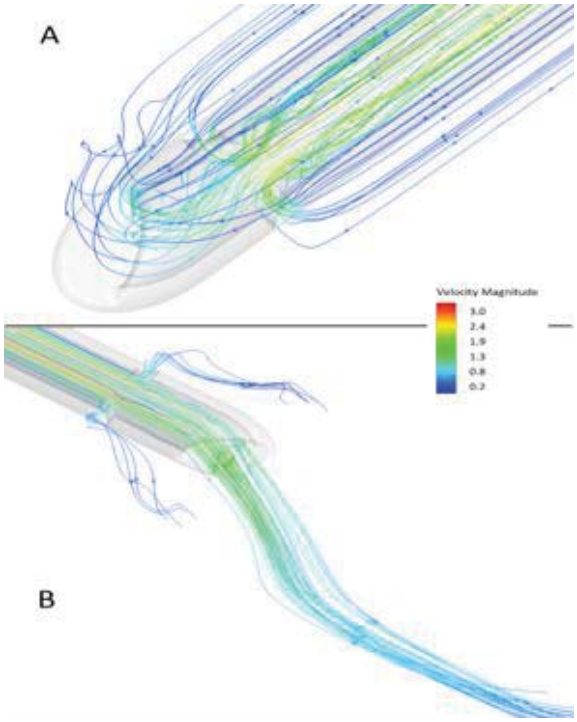

Fig. 2 VectorFlow geometry: Streamlines entering arterial lumen (A) and leaving venous lumen (B).

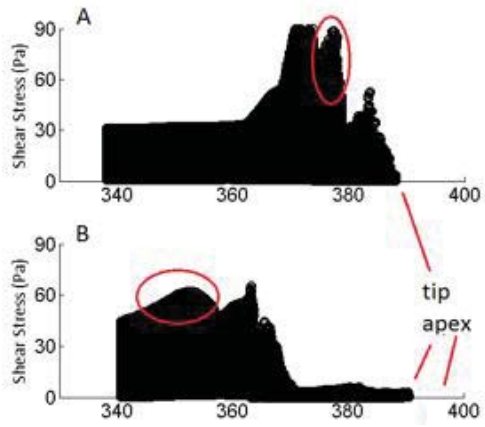

Fig. 3 Shear stress distribution along the catheter arterial lumen. VectorFlow (A) and Palindrome (B). The main direction of the flow is from right to left. Red circles indicate shear stress values in correspondence of the location of the side holes along the catheter.

Preclinical evaluation of posterior spinal fixators: a parametric FEA on international standards

Luigi La Barbera[1,2], Fabio Galbusera[2],Hans-Joachim Wilke[3] and Tomaso Villa[1,2]
[1] 1 LaBS, Department of Chemistry, Materials and Chemical Engineering "G.Natta", Politecnico di Milano, Milano, Italy
[2] IRCCS Istituto Ortopedico Galeazzi, 20161, Milano, Italy
[2] Institute of Orthopaedic Research and Biomechanics, Center of Musculoskeletal Research Ulm, Ulm University, Germany.

***Abstract*—The international standards meant to evaluate and compare the mechanical properties of posterior spinal fixators in controlled laboratory conditions are based on many simplifications. ASTM F1717 proposes a worst case vertebrectomy model, while ISO 12189 is based on an instrumented two functional spine units physiological scenario. Both standards try to mimic the clinical use of spinal devices, but the geometrical and mechanical parameters they propose are often unclear and experimental data, when available, are few. The aim of this study is to fill this gap, investigating the meaning of each parameter within the physiological range and to compare it to standard suggestions. A parametric finite element analysis was performed to investigate the relative contribution of each variable to the stress on the device and to propose a revision of the standards according to a worst case condition.**

***Keywords*—Standards, spinal fixation, ASTM F1717, ISO 12189, finite element model, spine biomechanics.**

I. Introduction

PRECLINICAL evaluation is meant to assess that a particular implant is reliable and safe enough to be implanted into a patient. This aspect is very important for orthopaedic prostheses which have to withstand an high number of loads during their clinical use.

Clinical experience demonstrated that mechanical *fatigue* is the main problem of *posterior spinal fixators* (Fig.1A), which revealed a high rate of fatigue-related failures, especially at the screw level [1-2]. Breakages were related mainly to the high number of cycles due to walking, which is the most frequent activity during everyday life [3].

International organisms periodically publish their standards or guidelines for the assessment and comparison of different implant designs in controlled simplified conditions (Fig.1B). The *American Society for Testing and Materials* (ASTM) published F1717 [4], which proposes to mimic vertebral bodies (VB) using UHMWPE blocks and assumes a worst-case vertebrectomy model. This condition is far from clinical practice since a posterior fixator is usually combined with an anterior support (e.g. bone graft, cage). The *International Standardization Society* (ISO) published the 12189 standard [5], which describes a stabilized physiological 2-functional spine units (FSUs) model that takes into account the anterior support trough three calibrated springs simulating the mechanical behaviour of the intervertebral disc (IVD) under compression.

Even if nowadays these standards are well accepted by device designers, the set of parameters (distances and angles) they suggest to describe FSU anatomy/biomechanics are often unclear. Moreover published data are few.

The principal aim of this project is to investigate the value of international standards for the preclinical evaluation of posterior spinal fixators and to propose their revision. Our aims were: the comparison between the set of values described by standards and those within the physiological range; the investigation of the influence of each parameter on the stress level in the device within this range; the determination of the physiological worst case due to the superposition of all parameters.

II. Material and Methods

A. Anatomical and mechanical parameters of interest

A total of 14 parameters were analysed (Fig. 1C).

We defined *anatomical* variables, describing the morphology of the VB or describing FSU biomechanics: the distance between screw insertion point in the pedicle and the follower-load (FL) line path (BMA); the distance between screw insertion point and the centre of rotation of the superior and inferior FSU (CoFRsup and CoFRinf respectively); screw/pedicle inclination with respect to the sagittal plane (PDIs). The range of variation for each anatomical parameter as a function of the spinal level, when available, was obtained from literature (review of 33 papers). The missing parameters (BMA and CoFR) were obtained from direct measurements on biplanar X-Ray images taken from 13 patients. We considered also some mechanical parameters (not all reported here), describing the experimental set-up and implant design, particularly the unsupported screw length (d_0). The range of variation for these variables was found among the most commonly used sizes available in commerce.

B. Parametric finite element analysis

Two parametric FEMs of the experimental set-up according to ASTM F1717 and ISO 12189 were considered. Symmetry with respect to the sagittal and transverse planes was assumed, considering only one quarter of the whole set-up. The posterior fixator design was simplified in order to keep the analysis as general as possible (Fig.1C).

A *systematic approach* was used to investigate the *local sensitivity* of each parameter on the stress calculated on the device, both beneath the screw head and on the rod (Fig.1D), assuming a reference configuration for each standard.

The *global* sensitivity of the solution was then checked combining the most important anatomical variables. Either the physiological average values for each parameters and their worst case combination were considered, as a function

of the spinal level (average and worst case, respectively).

III. Results and Discussion

The FEM approach used in this investigation has already shown good agreement with experimental measurements obtained using strain gauges technique [6].

Standards recommend a set of values which represents quite well the anatomy of an average thoracolumbar segment instrumented with a spinal fixator (Fig.2). ISO 12189 is more faithful to represent the centre of fixation to rotation (CoFR), while this is underestimated by ASTM F1717 in comparison to our measurements.

The lever arm of the applied load (BMA) has the strongest influence in increasing the stress on the fixator (Table I), so that its value was deliberately set as an overestimate by both standards. Considering that FL models the overall contribution due to muscles forces and upper body weight, assuming that its line path pass throughout the centre of the VB is right only during standing or walking [3]. Others everyday activities could not be represented.

CoFR, as well as the pedicular inclination with respect to the sagittal plane (PDIs), play an important role, but less significant than BMA (Table I).

TABLE I
Results

Parameter	*ASTM (300N)* σ_{VM}^{MAX} *increase (%)*		*ISO (2000N)* σ_{VM}^{MAX} *increase (%)*	
	Screw	Rod	*Screw*	*Rod*
BMA	7.0	6.1	12.0	8.2
CoFR	2.7	1.8	0.8	0.6
PDIs	2.2	0.8	1.4	-1.8
d_0	3.5	2.1	4.9	-5.3
Anatomical worst case (L1)	15.2	9.1	14.8	8.6

The experimental configuration suggested by ASTM F1717 and ISO 12189 standards is able to catch the state of stress of an average thoracolumbar spine in two different conditions. On one hand, considering the *worst case* vertebrectomy assumption, this may be sufficient to guarantee a high safety coefficient for a spinal fixator implanted in an average patient in the physiological population. On the other hand, assuming a physiological environment suggested by ISO, may not be safe enough to guarantee the reliability of the device.

Nevertheless the worst case combination of anatomical parameters demonstrates that a device implanted below T5 could potentially undergo higher stresses than according to standard conditions. The maximum stress increases of about 15% beneath screw head (about 9% on the rod) at L1 level for both standards.

The compressive stiffness of the springs used in ISO model to mimic the mechanical behaviour under compression of the IVD, is in good agreement with previous published data [7-8]. Spring stiffness (k) significantly influences the load sharing ratio between the device and the springs, thus changing the stress arising in the device (Fig. 3). The stress level could be artificially tuned in order to deliberately increase the load on the device and guarantee its safety. Moreover, a tunable anterior support has the advantage to allow the comparison in same conditions (i.e. stress level) between rigid and dynamic posterior fixators having very different stiffness.

IV. Conclusion

The present study quantitatively reports some important never investigated biomechanical parameters (BMA and CoFR). Moreover it reveals the anatomical/biomechanical meaning of all the parameters useful to describe the experimental set-up according to ASTM F1717 and ISO 12189 standards.

Despite not yet confirmed by an experimental study, we propose to revise both standards in order to describe the *worst case* condition we found at L1 level (BMA=43mm, CoFR=23.8mm): this will guarantee a higher reliability and safety of the implant for a wider population of patients.

In order to compensate for the lack of safety due to the physiological model proposed by ISO standard, different combinations of springs' stiffness could be used.

The main *limitation* of this study is represented by the simplified geometry assumed for the posterior spinal fixator. In order to determine if the percentage stress increase we found in the worst case condition could lead to a significant reduction in the fatigue life (number of cycles to failure) of a specific spinal fixation device, we plan to perform an experimental investigation on a commercial fixator.

References

[1] P.C. Jutte, R.M. Castelein. "Complications of pedicle screws in lumbar and lumbosacral fusions in 105 consecutive primary operations". Eur Spine J. 2002;11:594-598

[2] M.R. Farrokhi, A. Razmkon, Z. Maghami, Z. Nikoo. "Inclusion of the fracture level in short segment fixation of thoracolumbar fractures". Eur Spine J 2010;19:1651–1656.

[3] A. Rohlmann, F. Graichen, G. Bergmann, "Loads on an internal spinal fixation device during physical therapy," *Physical Therapy*, vol. 82(1), pp.44-52, 2002.

[4] ASTM Standard. F1717: "Standard test methods for spinal implant constructs in a vertebrectomy model". Ist edition in 1997 (updated on 2013).

[5] ISO Standard 12189: "Implants for surgery - Mechanical testing of implantable spinal devices - Fatigue test method for spinal implant assemblies using an anterior support". 2008.

[6] T. Villa, L. La Barbera, F. Galbusera. "Comparative analysis of international standards for the fatigue testing of posterior spinal fixation systems". Spine J, Nov 20, 2013 pii: S1529-9430(13)01479-4. doi: 10.1016/j.spinee.2013.08.032.

[7] K. Markolf. "Deformation of the thoracolumbar intervertebral joints in response to external loads. A biomechanical study using autopsy material". J Bone Joint Surg Am, Apr 01. Vol. 54(3), pp.511-533, 1972.

[8] T.S: Keller, D.M. Spengler, T.H. Hansson. "Mechanical behaviour of the human lumbar spine. I. Creep analysis during static compressive loading", J Orthop Res, vol. 5(4), pp.467-78, 1987.

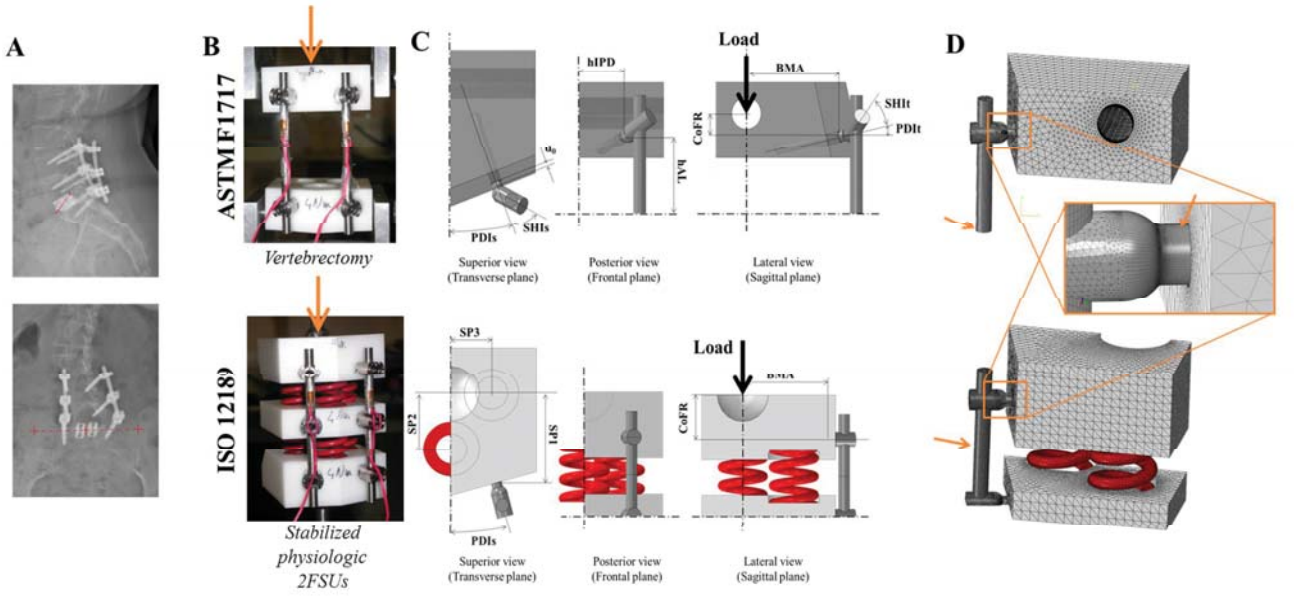

Fig.1 A: Sagittal and frontal views (upper and lower, respectively) of a patient treated using a posterior spinal fixator to stabilize the lumbosacral segment. B: Experimental set-ups used to compare and assess the mechanical properties of posterior spine fixators according to ASTM F1717 and ISO 12189 standards. C: Parametric numerical models. D: Meshed reference models.

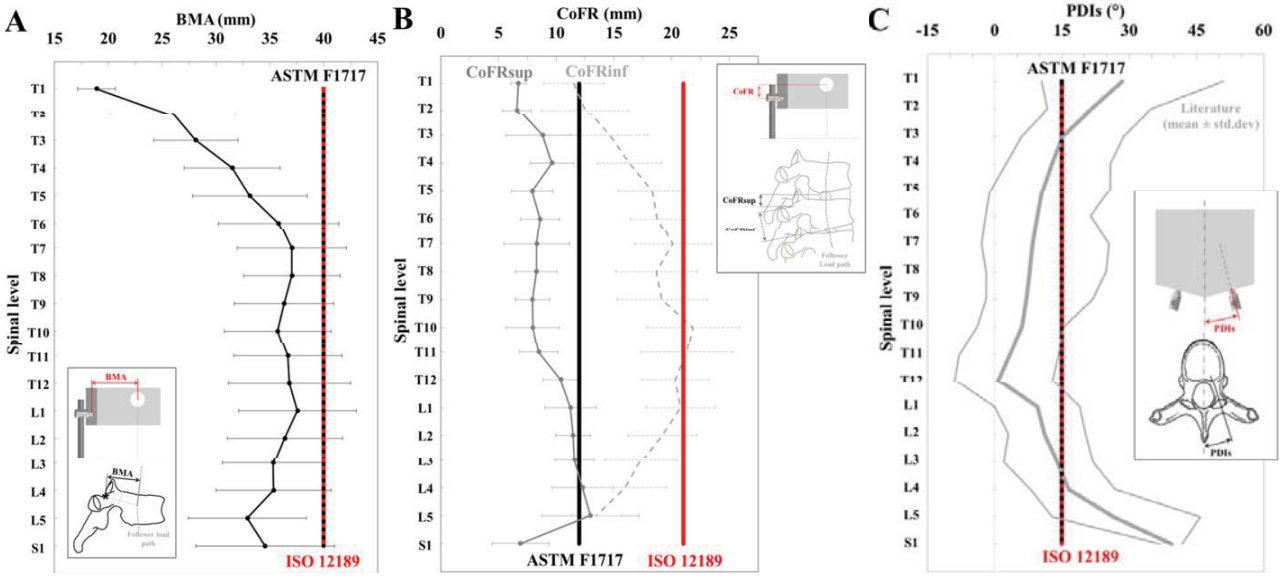

Fig.2 Block moment arm (BMA), center of fixation to rotation (CoFR) and pedicle inclination with respect to the sagittal plane (PDIs) as a function of the spinal level: comparison between the value set by standards and data from our patients data-base (A and B) or from literature (C) expressed as an average value ± standard deviation.

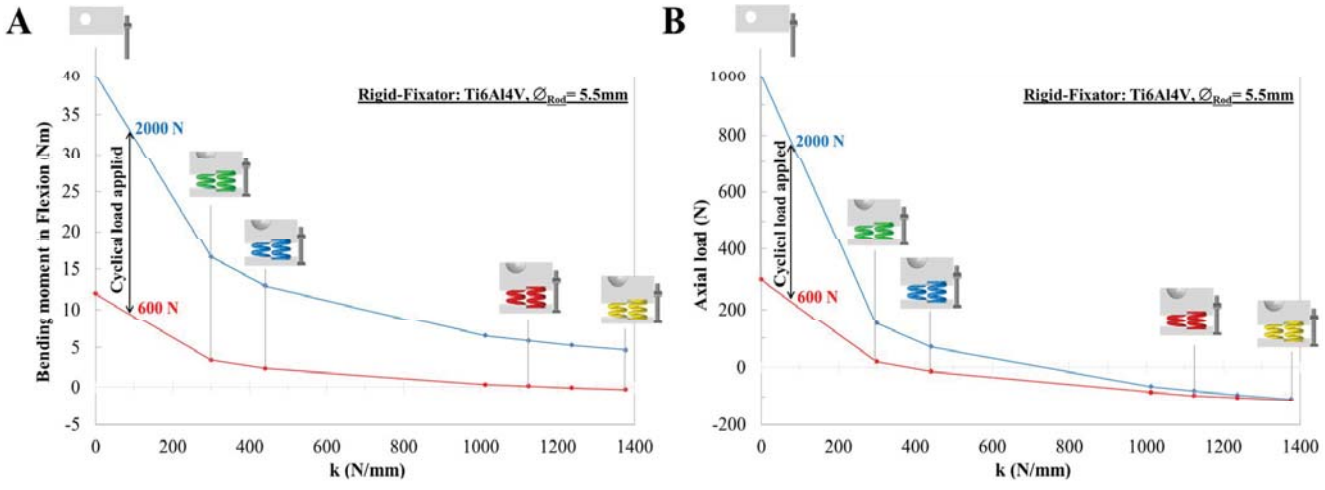

Fig.3 Internal loads applied on one half of the device as a function of spring stiffness (k). Positive values are assumed for flexion (A) and axial force (B).

Upscaling biochemical and biophysical effects in tissue mechanical modelling

Michele Marino and Giuseppe Vairo
Department of Civil Engineering and Computer Science, University of Rome "Tor Vergata", Via del Politecnico 1, 00133, Rome Italy; E-mail: m.marino@ing.uniroma2.it, vairo@ing.uniroma2.it

***Abstract*—In this paper, elasto-damage models of biostructures at different length scales are developed and integrated by means of analytical homogenization procedures. The model, based on a constrained variational formulation and established by employing convex analysis arguments, is developed within the framework of a multiscale rationale. This allows to consistently account for nanoscale mechanisms and to introduce model parameters with a clear biochemical/biophysical meaning.**

The case of collagen fibrils, the main constituents of a number of biological tissues, is investigated. A detailed description of nanoscale molecular interactions is considered, highlighting their straight influence on fibril constitutive response. The model is successfully validated by comparison with available numerical results based on molecular dynamical simulations. Moreover, proposed results proves model capability to reproduce many features of fibril response, in agreement with experimental evidence.

***Keywords*—Tissue biomechanics, collagen-rich structures, mechanobiological modelling, damage in tissues and organs.**

I. Introduction

BIOLOGICAL tissues generally share a peculiar histology, characterized by a hierarchical organization from the nano (molecules), through the micro (fibers made up of bundles of fibrils) up to the macroscale (tissues and organs, such as tendons, vessels and cornea). Hence, tissue biomechanics is strictly related with the mechanical response of tissue constituents which, in turn, depend on nanoscale properties, such as the biochemical environment in extracellular matrix and the biophysical properties of cross-linked assemblies. Therefore, several micro (e.g., mechano-regulated tissue remodeling) and macro (e.g., mechanics of joints or vessels) physio-pathological processes can be analyzed as a function of nanoscale alterations. In this field, the authors recently proposed a novel approach, namely the structural multiscale one, that opens to the effective integration of nanoscale mechanisms in macroscopic tissue biomechanical modelling, [3]–[5].

In the present work, mechanical models of collagenous biostructures at different length scales are developed and integrated by means of theoretical homogenization procedures. Elastic and inelastic mechanisms are addressed by employing the theory of standard generalized materials. Therefore, the elasto-damage response of biological structures is modelled by introducing few parameters with a clear physical meaning. A number of numerical simulations are implemented and conducted referring to the case of collagen fibrils. Obtained results allow to analyse physipathological effects as a function of altered structural features at very different length scales, opening to a special insight to the source of residual strains, hysteresis loops, strain-rate effects, brittle and softening behaviours in tissues and organs.

II. Theory

The theory of generalized standard materials, [2], is employed by introducing a suitable set $\mathcal{S}_f = \{S_f^j \text{ with } j = 1,\dots,M_f\}$ of M_f state variables for the addressed bio-structure. In order to account for inelastic mechanisms, interior forces dual to $\mathcal{S}_f$ are split in non-dissipative and dissipative contributions. State quantities and interior forces are functions of the time variable τ, although this dependence is generally implicit in the following for the sake of compactness. Time derivatives are denoted by dot superscript and $\dot{\mathcal{S}}_f$ is the set collecting the time derivatives of the state quantities.

Constitutive laws (namely, relationships among state variables and interior forces) are defined in a variational framework by suitably introducing the free-energy (depending on $\mathcal{S}_f$) and the pseudo-potential of dissipation (function of $\dot{\mathcal{S}}_f$) as convex functions, in order to satisfy *a-priori* thermodynamical consistency requirements. Derivative of the free-energy (resp., pseudo-potential of dissipation) with respect to $\mathcal{S}_f$ (resp., $\dot{\mathcal{S}}_f$) gives the non-dissipative (resp., dissipative) part of the interior forces.

By adopting a multiscale approach and introducing consistent inter-scale compatibility conditions, the elasto-damage behavior of the addressed bio-structure is described in terms of that of its nanoscale constituents. Accordingly, free-energies and pseudo-potentials of dissipation at nanoscale are introduced and suitably integrated on the basis of experimental atomic-force microscopy and atomistic computations.

Inelastic mechanisms are described by considering damage parameters as state variables, whose value is limited in beween $[0, 1]$, resulting equal to one in the undamaged case and zero in the fully-damaged case. Moreover, damage is assumed to be irreversible or not, depending on the nature of the constituent. In the former case, temporal derivative of damage parameters have to be a non-positive number. The physical restrictions on the value of damage parameters or of their evolution identify admissible convex sets. Such restrictions are enforced as internal constraints in the variational formulation, by adding indicator functions of admissibility sets and employing convex analysis arguments.

A. Model: uniaxial traction of collagen fibrils

The model is developed within an incremental framework, considering the actual value x at time t of a given state quantity as obtained from a perturbation $dx = \dot{x}d\tau$ superimposed to the reference value $\bar{x}$ relevant to the time $\bar{t} = t - d\tau$, and where $\dot{x}$ is, in agreement with the causality principle, the left-hand time derivative of x in t. The governing equations for fibril elasto-damage behavior are briefly reported in the following for the sake of completeness. For a detailed description of the model, refer to the work from the authors, [6].

Referring to a uniaxial traction case, the natural fibril strain ε_f is split in the molecular contribute e_1 and the intermolecular sliding part e_2. Thereby, the governing equations for fibril strain are:

$$F_f = \mathcal{A}_c\{\bar{\sigma}_m + E_m[(1-\alpha_1)\bar{\ell}_R de_1/\ell_{m,o} - \alpha_1\bar{\varepsilon}^e_m d\tau/\tau_o]\} = \\ = \frac{\mathcal{A}_c}{\mathcal{A}_m}\{\lambda_c[\bar{r}_c + k_c\bar{\ell}_R f_c(\bar{u}_2)de_2] + \bar{r}^e_w + k_w\bar{\ell}_R(1-\alpha_2)de_2\}\,, \tag{1a}$$

where $\mathcal{A}_c$, $\mathcal{A}_m$ are cross-sectional area measures of fibril-solid-area and molecules, λ_c is the density of covalent cross-links, k_c and k_w are respectively the stiffnesses for inter-molecular covalent cross-links and weak-bonds, and E_m is molecular tangent modulus. Moreover, $\bar{\ell}_R$ is the reference length of nanoscale assemblies, and $\bar{u}_2$ the reference molecular sliding. Furthermore, $\bar{\sigma}_m$, $\bar{r}_c$, and $\bar{r}^e_w$ are reference values of molecular stress, covalent cross-links force, and weak-bonds force, respectively. Finally, parameter τ_o, function f_c, and quantities α_1 and α_2 are defined on the basis of nanoscale behavior observed from atomistic computations, [1], [6].

Damage behavior is described in terms of damage parameters β_1 (associated to molecular inter-strand delamination) and β_2 (related to inter-molecular slip-pulse sliding mechanisms). To this aim, denote with $\bar{\mathcal{E}}_c$ (resp., $\bar{\mathcal{E}}_w$) the elastic energy stored in inter-molecular covalent-bonds (resp., weak-bonds), with c_d and w_d (resp., c_w and w_w) the inter-strand delamination (resp., slip-pulse) viscosity and threshold, and with $\Omega_{m,o}$ molecular volume. Accordingly, the governing equations of the damage behavior are:

$$\frac{c_d}{d\tau}d\check{\beta}_1 + \frac{\bar{\mathcal{E}}_c}{\Omega_{m,o}} - w_d = 0\,, \quad \frac{c_w}{d\tau}d\check{\beta}_2 + \bar{\mathcal{E}}^{el}_w - w_w = 0\,, \tag{1b}$$

where $\check{\beta}_1$, $\check{\beta}_2$ denote attempt values of damage parameters such that

$$\beta_1 = \begin{cases} \check{\beta}_1 & \text{if } \begin{cases} \check{\beta}_1 \in [0,1] \\ d\check{\beta}_1 \le 0 \end{cases} \\ \bar{\beta}_1 & \text{else} \end{cases} \qquad \beta_2 = \begin{cases} \check{\beta}_2 & \text{if } \check{\beta}_2 \in [0,1] \\ \bar{\beta}_2 & \text{else} \end{cases}. \tag{1c}$$

Equations (1) are solved by following a displacement-based approach at constant rate fibril elongation-rate $\dot{u}$ and employing a time-step $d\tau = \min(10^{-4}\ell_{m,o}/\dot{u}, 0.1\tau_o)$ as a result of a convergence analysis.

III. Results

The model reproduces with an excellent agreement available atomistic computations results proposed in [8] (see Fig. 1). Accordingly, model effectively describes the mechanics of nanoscale assemblies that, in turn, determine fibril's mechanical response.

Moreover, three cycles of a traction loading-unloading test are addressed. In agreement with experimental evidence, [7], Fig. 2 shows that hysteresis loops clearly arise in fibril constitutive response and residual strains in fibril appear at the end of each cycle.

IV. Conclusion

The mechanical behavior of biological tissues strictly depends on the biochemical environment and biophysical features of its constituents. For instance, the physiopathological behavior of a number of biological structures (e.g., tendons, ligaments, aorta, cornea) strictly depend on collagen fibrils that are here modeled by adopting a multiscale approach that allows to introduce only parameters with a clear biochemical/biophysical meaning.

Accordingly, the proposed predictive model of collagen fibrils opens to analyze physiopathological behavior of tissues and organs as a function of nanoscale structural and chemical alterations. Moreover, it can be successfully employed in tissue engineering applications, providing a useful tool for predictive studies on the quantitative tuning of fibril stiffness and strength.

Acknowledgment

The authors would like to thank Professor Franco Maceri for valuable suggestions and fruitful discussions on this paper. This research is developed in the framework of the project "Modeling of the mechanical response of biological tissues", granted by Italian Ministry of Education, University and Research (MIUR) within the Research Projects of National Interests (PRIN) framework.

References

[1] M.J. Buehler, *Atomistic and continuum modeling of mechanical properties: Elasticity, fracture, and self-assembly*, J Material Res 21:1947-1961, 2006.

[2] M. Frémond, *Non-smooth thermomechanics*, Springer-Verlag Berlin Heidelberg, 2002.

[3] F. Maceri, M. Marino, and G. Vairo, *A unified multiscale mechanical model for soft collagenous tissues with regular fiber arrangement*, J Biomech 43:355-363, 2010.

[4] F. Maceri, M. Marino, and G. Vairo, *Age-dependent arterial mechanics via a multiscale elastic approach*, Int J Comput Meth Eng Science Mech 14:141-151, 2013.

[5] M. Marino and G. Vairo, *Multiscale elastic models of collagen biostructures: From cross-linked molecules to soft tissues*. In: Gefen A, editor. Multiscale Computer Modeling in Biomechanics and Biomedical Engineering. Studies in Mechanobiology, Tissue Engineering and Biomaterials 14. Springer-Verlag, Berlin-Heidelberg, p 73-102, 2013.

[6] M. Marino and G. Vairo, *Influence of inter-molecular interactions on the elasto-damage mechanics of collagen fibrils*, Acta Biomat, 2014. Submitted.

[7] Z.L. Shen, M.R. Dodge, H. Kahn, R. Ballarini, and S.J. Eppell. *Stress-Strain Experiments on Individual Collagen Fibrils*, Biophysical J 95:3956-3963, 2008.

[8] S. Uzel and M.J. Buehler, *Molecular structure, mechanical behavior and failure mechanism of the C-terminal cross-link domain in type I collagen*, J Mech Behav Biomed Mat 4:153-161, 2011.

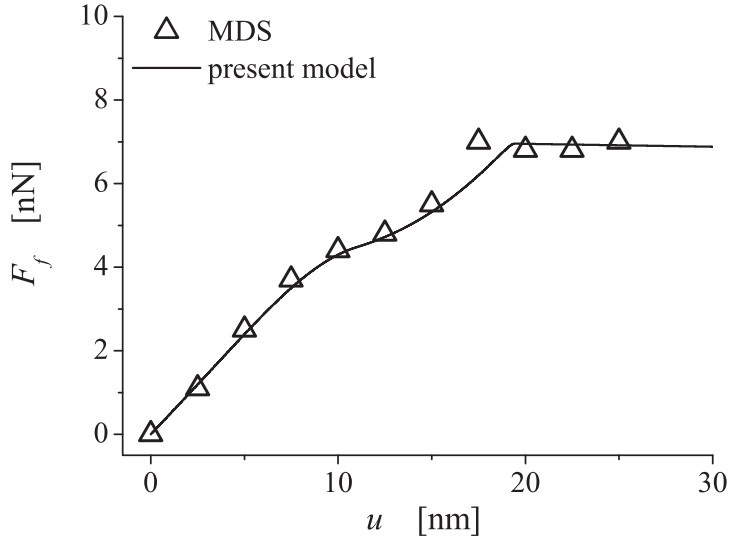

Fig. 1. Fibril force F_f vs. fibril elongation u obtained from present model and molecular dynamical simulations (MDSs) proposed in [8].

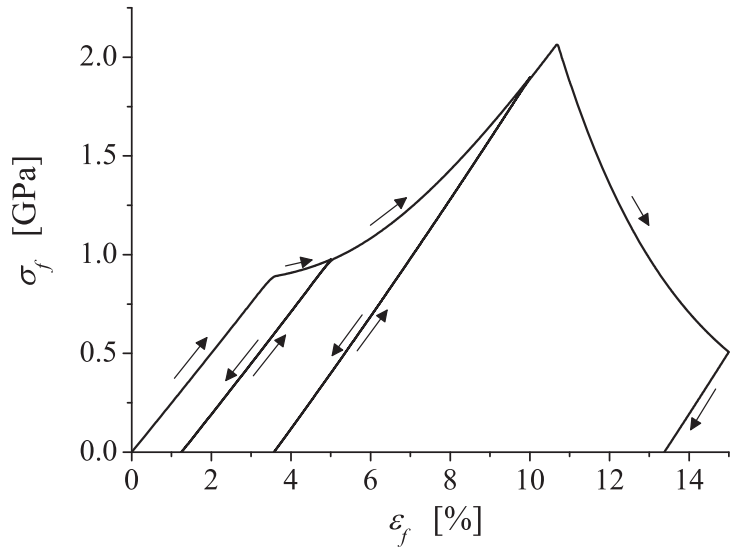

Fig. 2. Fibril stress σ_f vs. fibril natural strain ε_f obtained considering three cycles of a traction loading-unloading test.

Effects of initial exposure to upper limb robot-assisted therapy in stroke patients

S. Mazzoleni[1,2], L. Buono[1,2], P. Dario[1], and F. Posteraro[2,3]
[1] *The BioRobotics Institute, Scuola Superiore Sant'Anna, Pisa, Italy;*
[2] *Rehabilitation Bioengineering Laboratory, Auxilium Vitae Rehabilitation Centre, Volterra, Italy;*
[3] *Rehabilitation Department, Versilia Hospital -AUSL12, Lido di Camaiore, Italy*

***Abstract*—The goal of this study is to evaluate the effects of robot-assisted upper limb therapy in subacute and chronic stroke patients using a set of kinematic parameters evaluated during each of the first 15 rehabilitation sessions.**

Twenty-four stroke patients, twelve subacute and twelve chronic, participated in the study. A 2 DOFs robotic system implementing an "assist-as-needed" control strategy was used.

Kinematic parameters related to the speed measured at the robot's end-effector were computed.

Outcome clinical measures show a decrease in motor impairment at half-treatment both in chronic and subacute patients. Significant improvements in kinematic parameters within the first 15 sessions were observed in subacute patients.

***Keywords*—Rehabilitation; motor recovery; upper limb; stroke; kinematics**

I. Introduction

Several studies on robot-assisted rehabilitation treatment in subacute and chronic stroke patients have shown a reduction of upper limb impairment [1], but till now an evidence of the advantage in the use of robotic therapy compared to traditional standard treatment is not still proved [2]. Recent systematic reviews showed that upper limb robotic treatments in stroke subjects can improve short- and long-term motor control, even if impact on functional tasks is not demonstrated yet [1]-[3]. The analysis of mechanisms of recovery in subacute and chronic stroke patients, currently based on the use of clinical scales only, assumes great importance in the rehabilitation area, as it can support clinical decisions. Robotic systems allow recording kinematic variables which can be used to provide qualitative information able to provide information on changes in motor performance during the rehabilitation treatment [4]-[9].

The aim of this work is to analyse the effects of robot-assisted upper limb therapy in subacute and chronic stroke patients using clinical outcome measures and kinematic parameters evaluated during each of the first 15 rehabilitation sessions.

II. Methods

A. Participants

Twelve subacute stroke subjects, age range 49-77 (mean age 67.1±10.2) years, four men and eight women, were recruited for the study. Five had right hemiparesis . They had experienced the acute event 25±7 days prior to the study. Twelve chronic subjects, age range 31-86 (mean age 60.9±13.6) years, six men and six women, were recruited for the study. Eight had right hemiparesis. They had experienced the acute event at least one year prior to the study. The level of the upper limb impairment for each stroke patients at admission was assessed using the Stage of Arm section of the Chedoke-McMaster (CM) Stroke Assessment Scale [10]. One subacute stroke subjects received a CM value of 1, five a CM value of 2 or 3, and six a CM score of 4 or 5. Eight chronic patients received a CM value of 2 or 3 and four a CM value of 4 or 5.

B. Experimental setup

The InMotion ARM robot (Interactive Motion Technologies, Inc., Watertown, Ma, USA), designed for clinical and neurological applications, was used [11]-[13].

The 2 degrees of freedom robotic system supports the execution of reaching movements in the horizontal plane through an "assist as needed" control strategy. A monitor in front of the subject displays the exercises to be performed (Figure 1).

C. Intervention

Subacute patients performed 5 sessions per week for 6 weeks, chronic patients 5 sessions per week for 4 weeks.

Each subject was asked to perform goal-directed, planar reaching tasks, which emphasized shoulder and elbow movements, moving from the centre target to each of 8 peripheral targets (Figure 2). In each session subjects received 45 minutes of robot-mediated therapy. The robotic treatment was composed of 2 different kinds of exercises, unassisted (Record) and assisted movements (Adaptive).

In detail, each session was formed by (i) a series of 16 assisted clockwise repetitions to each robot target (training test); (ii) a series of 16 unassisted clockwise repetitions to each robot target (Record); (iii) 3 series of 320 assisted clockwise repetitions (Adaptive). At the end of each Adaptive series, the patient is asked to perform a further series of 16 unassisted clockwise movements (Record). Kinematic data were computed starting from physycal variables recorded during the Record series of each of the first 15 sessions.

D. Clinical outcome measures

Each subject underwent an upper limb evaluation by an experienced physical therapist using the following scales: 1) Stage of Arm section of the Chedoke-McMaster (CM) Stroke Assessment Scale, 2) Upper Extremity subsection of the Fugl-Meyer (FM-UE) Assessment Scale, 3) Motricity Index (MI) and 4) Passive range of motion (pROM). The clinical evaluation was performed on each patient before the first

session (Pre-treatment) and at half of the entire robot-assisted rehabilitation duration.

E. Kinematic parameters

The following kinematic parameters were computed: 1) mean velocity, 2) peak velocity and 3) normalized reaching speed. The mean speed vectors $\overline{v_x}$ and $\overline{v_y}$ are defined as follows:

$$\overline{v_x} = \frac{1}{N} \sum_{k=1}^{N} v_x[\mathrm{k}] \quad (1)$$

$$\overline{v_y} = \frac{1}{\mathrm{N}} \sum_{k=1}^{N} v_y[k] \quad (2)$$

where N represents the number of samples for each recording. In this study the v_{xy} as resultant velocity in the xy-plane was considered:

$$v_{xy} = \sqrt{v_x[\mathrm{k}])^2 + (v_y[\mathrm{k}])^2} \quad (3)$$

The mean velocity is defined as follows:

$$\overline{v_{xy}} = \frac{1}{\mathrm{N}} \sum_{k=1}^{N} v_{xy}[k] \quad (4)$$

The peak velocity ($v_{xy}max$) defined as the maximum value of v_{xy}[k] and the Normalized Reaching Speed (NRS) (Eq. 5) were computed as well.

$$\mathrm{NRS} = \frac{v_{xy}max - \overline{v_{xy}}}{v_{xy}max} \quad (5)$$

F. Statistical analysis

In order to evaluate statistical significance of the difference before and after the treatment on clinical outcomes measures, a one way repeated measures ANOVA was computed. Post-hoc comparison was carried out using the Tukey test ($p<0.05$). A one-way ANOVA was used for evaluating differences in kinematic parameters during each of the first 15 session of the treatment.

TABLE I.
PRE- AND POST-TREATMENT OUTCOME MEASURES IN SUBACUTE PATIENTS

	PRE (mean±sd)	POST (mean±sd)	Change	p
FM-UE	27.17±12.24	33.58±13.69	6.42±5.88	<0.05
MI	40.17±25.29	51.83±28.84	11.67±12.66	<0.05
pROM	747.92±123.70	786.25±109.11	38.33±31.50	<0.001

III. RESULTS AND DISCUSSION

Table I shows a significant decrease in motor impairment of subacute patients following robot-assisted treatment. In chronic patients statistically significant improvements were found in FM-UE and pROM as well (Table II). Kinematic parameters recorded in subacute patients show significant improvements (Figure 3-Figure 5). On the other hand, any significant improvements on kinematic parameters within the first 15 sessions were not observed in chronic patients (Figure 6- Figure 8).

Our preliminary results show that robotic therapy assessed at half of the entire rehabilitation duration contribute to improve upper limb motor abilities in both subacute and chronic stroke patients.

TABLE II.
PRE- AND POST-TREATMENT OUTCOME MEASURES IN CHRONIC PATIENTS

	PRE (mean±sd)	POST (mean±sd)	Change	p
FM-UE	22.75±7.48	27.33±9.46	4.58±4.34	<0.05
MI	36.83±18.77	42.17±21.12	5.33±6.70	N.S.
pROM	641.25±79.23	689.58±74.18	48.33±27.33	<0.001

The evaluation of kinematic parameters show significant improvements only in subacute patients. Chronic patients require a longer exposure to the robot-assisted therapy to achieve significant improvements [13].

ACKNOWLEDGEMENT

This work was partly funded by Regione Toscana, under the Regional Health Research Program 2009 ("Telerehabilitation and Robotics" research project) and Fondazione Cassa di Risparmio di Volterra, Italy.

REFERENCES

[1] G. Kwakkel, B. J. Kollen, and H. I. Krebs, "Effects of robot-assisted therapy on upper limb recovery after stroke: a systematic review," *Neurorehabil Neural Repair*, vol. 22, no. 2, pp. 111-21, 2008.

[2] A. C. Lo, P. D. Guarino, L. G. Richards, J. K. Haselkorn, G. F. Wittenberg, and D. G. Federman, "Robot-assisted therapy for long-term upper-limb impairment after stroke," N Engl J Med. vol. 362, no. 19, pp. 1772-83, 2010.

[3] G. B. Prange, M. J. Jannik, C. G. Groothuis-Oudshoorn, H. J. Hermens, and M. J. Ijzerman, "Systematic review of the effects of robot-aided therapy on recovery of the hemiparetic arm after stroke," *J Rehabil Res Dev*., vol. 43, no. 2, pp. 171-84, 2006

[4] S. Balasubramanian, R. Colombo, I. Sterpi, V. Sanguineti, and E. Burdet, "Robotic assessment of upper limb motor function after stroke," *Am J Phys Med Rehab*., 91:S255-S269, 2012.

[5] R. Colombo, F. Pisano, S. Micera, A. Mazzone, C. Delconte, and M. C. Carrozza, "Assessing mechanisms of recovery during robot-aided neurorehabilitation of the upper limb," Neurorehabil Neural Repair, vol. 22, pp. 50-63, 2008.

[6] H. I. Krebs, J. J. Palazzolo, L. Dipietro, M. Ferraro, J. Krol, and K. Rannekleiv, "Rehabilitation robotics: performance-based progressive robot-assisted therapy," *Auton Robot*, vol. 15, pp. 7-20, 2003.

[7] L. Zollo, E. Gallotta, E. Guglielmelli, and S.Sterzi, "Robotic technologies and rehabilitation: new tool for upper-limb therapy and assessment in chronic stroke," *Eur J Phys Rehab Med*, vol. 47, pp. 223-36, 2011.

[8] R. Colombo, I. Sterpi, A. Mazzone, F. Pisano, and C. Delconte, "Modeling upper limb clinical scales by robot-measured performance parameters," In Proc. IEEE *Int Conf Rehabil Robot*, 1-5, 2011.

[9] S. Mazzoleni, F. Posteraro, F. Forte, S. Micera, P. Dario, M. C. Carrozza, "Biomechanical assessment of reaching movements in post-stroke patients during a robot-aided rehabilitation," *Applied Bionics and Biomechanics*, vol. 8, pp. 39-54, 2011.

[10] C. Gowland, P. Stratford, M. Ward, J. Moreland, W. Torresin, S. Van Hullenaar, J. Sanford, S. Barreca, B. Vanspall, and N. Plews, "Measuring physical impairment and disability with the Chedoke-McMaster Stroke Assessment," Stroke, vol. 24, pp. 58-63, 1993.

[11] H.I. Krebs, N. Hogan, M.L. Aisen, and B.T. Volpe, "Robotaided neurorehabilitation," *IEEE Trans Rehabil Eng*, vol. 6, pp. 75-87, 1998.

[12] F. Posteraro, S. Mazzoleni, S. Aliboni, B. Cesqui, A. Battaglia, P. Dario, S. Micera, "Robot-mediated therapy for paretic upper limb of chronic patients following neurological injury", *Journal of Rehabilitation Medicine*, *vol*. 41, pp. 976-80, 2009.

[13] S. Mazzoleni, L. Puzzolante, L. Zollo, P. Dario, F. Posteraro, "Mechanisms of motor recovery in chronic and subacute stroke patients following a robot-aided training", *IEEE Transactions on Haptics* 17 Dec. 2013. http://doi.ieeecomputersociety.org/10.1109/TOH.2013.73.

Fig. 1. A stroke patient during the robot-assisted upper limb rehabilitation treatment.

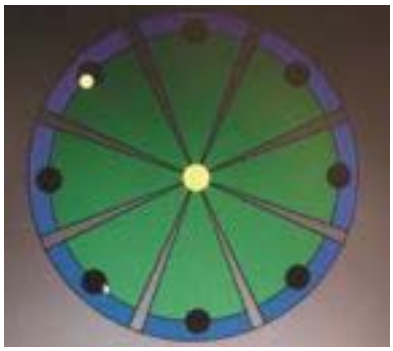

Fig. 2. The “clock-like” robot-assisted therapy scenario.

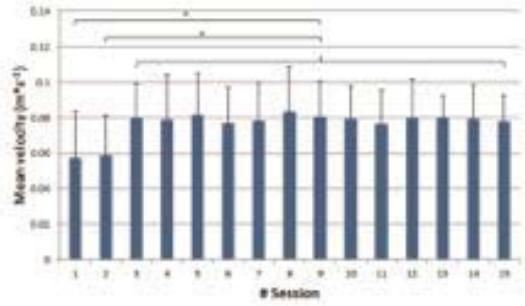

Fig. 3. Mean velocity values in subacute patients during the first 15 sessions of robot assisted training (* indicates $p<0.05$).

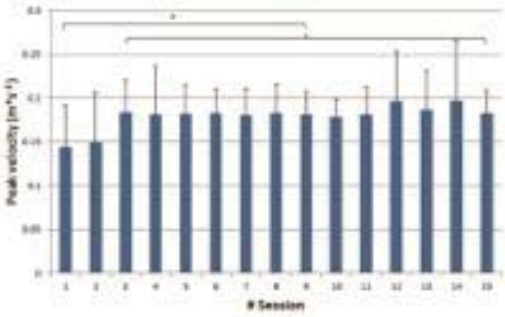

Fig. 4. Peak velocity values in subacute patients during the first 15 sessions of robot assisted training (* indicates $p<0.05$).

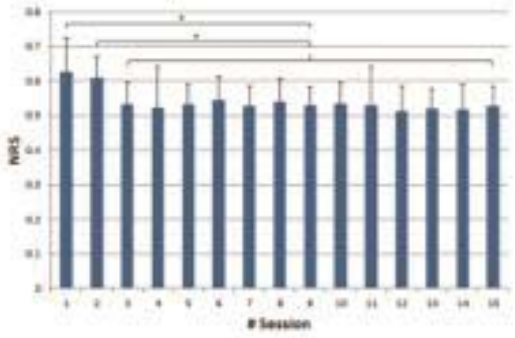

Fig. 5. NRS values in subacute patients during the first 15 sessions of robot assisted training (* indicates $p<0.05$).

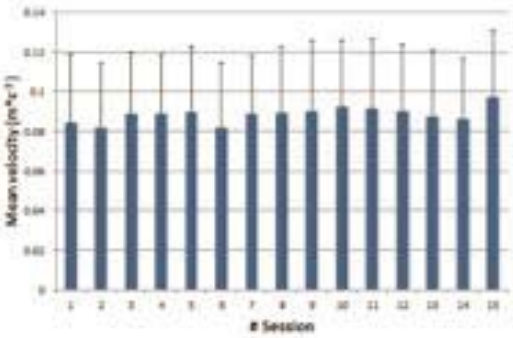

Fig. 6. Mean velocity values in chronic patients during the first 15 sessions of robot assisted training.

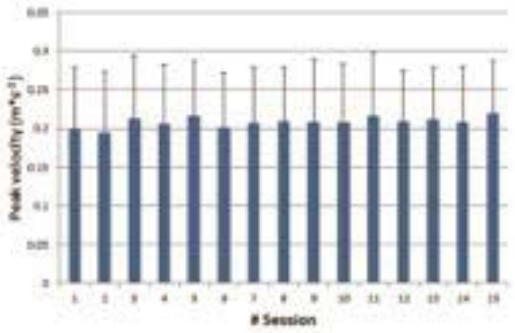

Fig. 7. Peak velocity values in chronic patients during the first 15 sessions of robot assisted training.

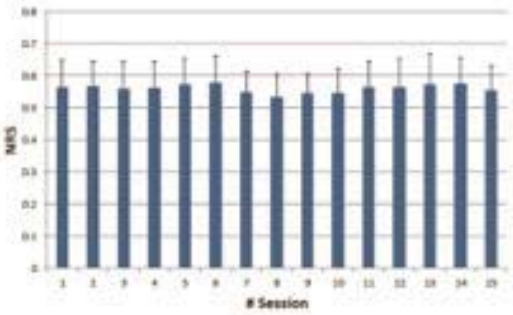

Fig. 8. NRS values in chronic patients during the first 15 sessions of robot assisted training.

Cardiac biomechanics in patient-specific multi-scale models of single ventricle circulation

A. Meoli[1], A. Baretta[1], E. Cutrì[1] G. Dubini[1], F. Migliavacca[1] and G. Pennati[1]
[1]*Politecnico di Milano, Milan, Italy*

***Abstract*—Patient-specific models of single ventricle circulation represent a powerful tool to investigate ventricular functionality. In this study, we adopt a multi-scale approach that couples a 0D circulatory model of the patient circulation to a 3D structural model of the ventricle. To investigate this particular condition a group of patients affected by hypoplastic heart syndrome have been considered.**

***Keywords*— Single ventricle heart, multi-scale patient-specific modelling, lumped parameter network, cardiac mechanics.**

I. Introduction

Single ventricle (SV) is a complex congenital heart disease characterized by underdevelopment of one ventricular chamber, which is invariably fatal during the first weeks of life without intervention. Hypoplastic left heart syndrome (HLHS) is the most common SV heart defect, occurring in approximately one in 5000 live births [1-3]. Normally, a three-stage surgical repair called the Fontan procedure is performed to obtain separated pulmonary and systemic circulations [4]. The technique involves changes in the circulatory layout, with venous return flowing passively into the lungs without a pumping chamber, and the functional SV providing systemic blood flow. Hence, SV heart is subjected to abrupt changes in the working conditions after each surgical stage in addition to an unusual high work that over time might cause ventricular dysfunction.

With the improvements in the imaging techniques, nowadays, it is easier to build patient-specific models of cardiovascular hemodynamics for both healthy and pathological patients, e.g. for the treatment of congenital heart diseases. In this regard, computational models based on clinical data represent a powerful tool to investigate different scenarios by virtually simulating the surgery or a change in the working conditions with the goal of evaluating ventricular functionality. In particular, 3D finite element models have proved to be a valid tool to assess regional information (e.g. stress and strain) in the normal and abnormal heart in patient-specific cases that cannot be directly measured in the patient [5-7].

The aim of this study is the assessment of SV heart functionality by means of patient-specific multi-scale 3D-0D models. The approach consists in obtaining a computational solution coupling a patient-specific lumped-parameter network (LPN) of the entire circulatory system with a 3D structural model of the SV. The interface conditions of pressures are mutually exchanged by the LPN and 3D models. Iterations of this multi-scale solution allow the prediction of local information of ventricular function (i.e. stress and wall kinematics), as well as global parameters such as pressure-volume (PV) loops and cardiac performance (i.e. cardiac output and ejection fraction). A group of patients from different surgical stages and pathologies (right or left SV hearts) have been considered.

II. Materials and Methods

A multi-scale 3D-0D patient-specific model of SV is mainly composed of four components: i) a closed-loop circulatory model; ii) an anatomical model of the SV; iii) a passive constitutive law; iv) an active dynamic model.

A. Closed loop LPN model

Patient-specific closed-loop 0D models of the circulatory network were developed to apply proper hemodynamic boundary conditions (preload and afterload) to the 3D models. The basic circulatory layout is comprised of four RLCRCR blocks to account for upper body, lower body, right and left pulmonary branches. The proper connection of the four blocks allows the description of SV circulations for different stages.

To estimate the LPN parameters, the loop is closed with two time-varying elastances, representing the single atrium and the SV, as well as atrio-ventricular (AV) and aortic valves, described by non-linear diodes [8].

Patient right and left pulmonary vascular resistances (RPVR, LPVR) and upper and lower body systemic vascular resistances (UBSVR, LBSVR) were calculated on the basis of mean values of pressures and flows [9].

Associated pathologies such as atrio-ventricular (AV) valve regurgitation were also considered and modeled when observed clinically in patients.

Once LPN parameters are estimated, the SV elastance block is substituted with the 3D structural model to perform multiple beats simulations.

B. Anatomical model

Hexahedral cubic-Hermite finite element mesh of the ventricular geometry is constructed based on the clinical image data. Endocardial and epicardial contours of the SV

heart at end-diastole were manually segmented from cardiac magnetic resonance images. Then an initial template of a SV was fitted to the reconstructed geometry in order to match the patient anatomy. Fibre architecture is assumed as in physiological ventricles since information for SV hearts are lacking.

C. Passive model

The resting material properties of the myocardium were described using the transversely-isotropic form of the constitutive model developed by Holzapfel and Ogden [10]. In this model, the anisotropy of the myocardium in the fibre and cross-fibre directions is modelled using a separate exponential term with different exponents. Parameters of the model were fitted in order to match the biaxial tests of Yin et al. [11] and the shear tests of Dokos et al. [12] of ex-vivo canine myocardial tissue. These default parameters resulted in extremely stiff stress–strain relations in the patient-specific models. Hence, the pressure scaling parameters were adjusted uniformly to match the patient available data (e.g. pressure and volume tracings).

D. Active model

After SV geometry and passive material parameters were obtained, the contractile parameters were determined to match the measured peak left ventricular pressures and end-systolic volumes. To adjust the parameters of the Lumens et al. [13] active contraction model, the 3D model was contracted iso-volumically by activating the fibres. Active stress scaling coefficient (SfAct), activation rise time (t_R), and activation decay time (t_D), were adjusted in order to match the simulated pressure trace with the measured catheter pressures in the patient.

III. Results and Discussion

0D models of the whole circulation reproduced the main hemodynamic features recorded clinically, such as pulmonary/systemic flow distribution, right/left pulmonary flow split, upper/lower body flow repartition and cardiac output. A comprehensive good performance was shown by the ventricular PV loop, which was well positioned matching clinical end-systolic and end-diastolic volumes (Fig. 1), thus suggesting a good arterial-ventricular coupling. When present, AV valve regurgitant flow well matched the clinical one.

The patient-specific 3D-0D model allows the simulation of several cardiac cycles. To reduce computation time, initial conditions for the multi-scale model were determined by solving the 0D model. Thus, to obtain a steady solution from the coupled model only few cycles are required. Once the steady solution is obtained, the comparison with the clinical available data showed good capacity of the multi-scale model in reproducing global results (pressure, volumes and flows). Figure 2 shows the strain distribution in the fibre direction in a patient with AV valve regurgitation at different instants of the cardiac cycle.

Simulations of virtual surgery changing the layout of the circulatory model or including specific associated pathologies (i.e. AV valve regurgitation or coarctation) have been successfully perfomed depending on the specific patient case.

IV. Conclusion

In this work, we adopted a patient-specific multi-scale approach to study the cardiac biomechanics in patients affected by SV malformations. The model consists in the coupling of a 0D model of the circulation to a 3D model of the functional ventricle. The circulatory model provides proper boundary conditions to the 3D model, which showed good capability in reproducing hemodynamics of different patients affected by SV defects.

Acknowledgement

This study was supported by a grant from the Fondation Leducq, Paris, France.

References

[1] Bardo DM, Frankel DG, Applegate KE, Murphy DJ and Saneto RP (2001) Hypoplastic left heart syndrome. Radiographics 21:705–717.

[2] Khairy P, Poirier N and Mercier LA (2007) Univentricular heart. Circulation 115:800–812.

[3] Muthurangu V, Taylor AM, Hegde SR, Johnson R, Tulloh R, Simpson JM, Qureshi S, Rosenthal E, Baker E, Anderson D and Razavi R (2005) Cardiac magnetic resonance imaging after stage I Norwood operation for hypoplastic left heart syndrome. Circulation 112:3256–3263.

[4] de Leval, MR and Deanfield, JE 2010 Four decades of Fontan palliation. Nat. Rev. Cardiol. 7:520–527.

[5] Kerckhoffs RCP, McCulloch AD, Omens JH and Mulligan LJ (2009) Effects of biventricular pacing and scar size in a computational model of the failing heart with left bundle branch block. Med Image Anal 13:362-369.

[6] Aguado-Sierra A, Krishnamurthy A, Villongco C, Chuang J, Howard E, Gonzales MJ, Omens J, Krummen DE, Narayan S, Kerckhoffs RCP, and McCulloch AD (2011) Patient-specific modeling of dyssynchronous heart failure: A case study. Prog Biophys Mol Bio. 107:147-155.

[7] Krishnamurthy A, Villongco CT, Chuang J, Frank LR, Nigam V, Belez-zuoli E, Stark P, Krummen DE, Narayan S, Omens JH, McCulloch AD, Kerckhoffs RCP (2013) Patient-specific models of cardiac biomechanics. J Comput Phys. 244:4-21.

[8] Migliavacca F, Pennati G, Dubini G, Fumero R, Pietrabissa R, Urcelay G, Bove EL, Hsia, TY and de Leval MR (2001) Modeling of the Norwood circulation: effects of shunt size, vascular resistances, and heart rate. Am. J. Physiol. Heart Circ. Physiol. 280:2076–2086.

[9] Baretta A, Corsini C, Yang W, Vignon-Clementel IE, Marsden AL, Feinstein JA, Hsia TY, Dubini G, Migliavacca F, Pennati G and The Modeling of Congenital Hearts Alliance (MOCHA) Investigators (2011) Virtual surgeries in patients with congenital heart disease: a multi-scale modelling test case. Philos T R Soc A. 369:4316-4330.

[10] Holzapfel G and Ogden R (2009) Constitutive modelling of passive myocardium: a structurally based framework for material characterization. Philos T R Soc A. 367:3445-3475.

[11] Yin F, Strumpf R, Chew P and Zeger S (1987) Quantification of the mechanical properties of noncontracting canine myocardium under simutaneous biaxial loading. J Biomech. 20(6):577-589.

[12] Dokos S, Smaill B, Young A and LeGrice I (2002) Shear properties of passive ventricular myocardium. Am. J. Physiol. Heart Circ. Physiol. 283(6):2650-2659.

[13] Lumens J, Delhaas T, Kirn B and Arts T (2009) Three-wall segment (TriSeg) model describing mechanics and hemodynamics of ventricular interaction. Ann Biomed Eng. 37 11:2234–2255.

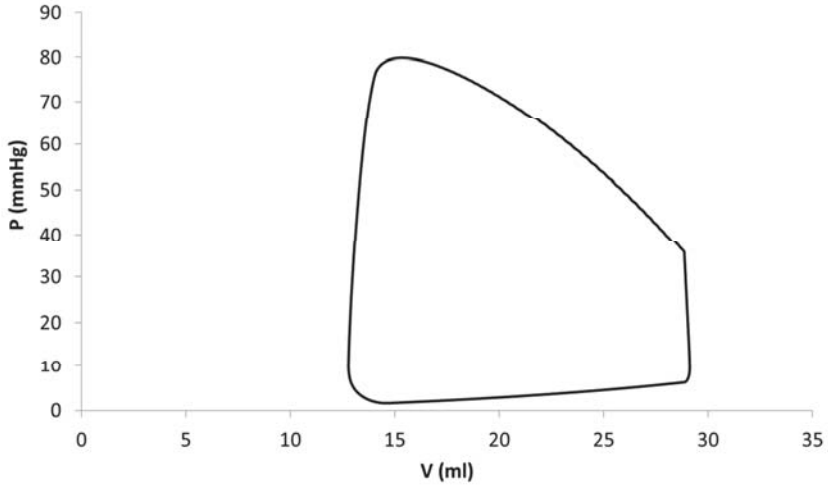

Fig. 1: Ventricular PV loop resulting from the 0D model of a SV patient circulation. Slopes in the isovolumic phases are due to the presence of AV valve regurgitation present in this patient. End-systolic and end-diastolic volumes obtained by the model match the measured ones (12.8 and 29.0 ml vs. 12.0 and 29.0 ml respectively).

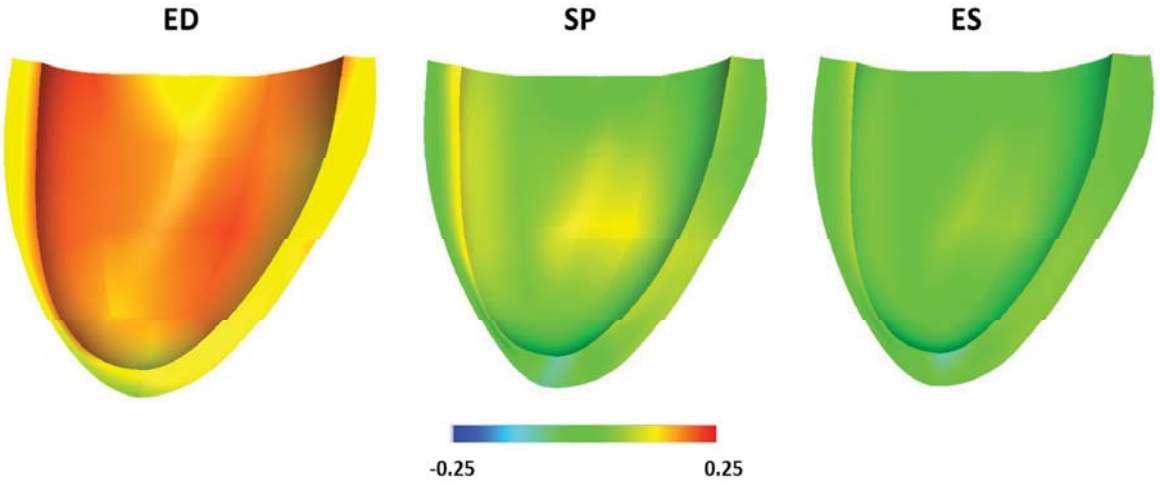

Fig. 2: Strain distribution in the fibre direction at different points of the cardiac cycle: ED (End Diastole); SP (Systolic Peak); ES (End Systole).

Investigation of TAVI outcomes through patient-specific finite element analysis: two clinical cases

S. Morganti[1], F. Auricchio[2], M. Conti[2], A. Reali[2] and M. Aiello[3]
[1] *Dip. di Ingegneria Industriale e dell'Informazione (DIII), Università di Pavia, Via Ferrata 3, Pavia, Italy*
[2] *Dip. di Ingegneria Civile e Architettura (DICAr), Università di Pavia, Via Ferrata 3, Pavia, Italy*
[3] *Dip. Cardiotoracovascolare, Divisione di Cardiochirurgia, IRCCS Policlinico S. Matteo, Viale Golgi 19, Pavia, Italy*

***Abstract*— Transcatheter aortic valve implantation (TAVI) is a minimally-invasive procedure introduced to treat aortic valve stenosis in elder patients. Its clinical outcomes are strictly related to patient selection, operator skills, and dedicated pre-procedural planning based on accurate medical imaging analysis. The goal of this work is to define a finite element framework to realistically reproduce TAVI and evaluate the impact of aortic root anatomy on procedure outcomes through a comparative study based on two real patient datasets. A patient-specific aortic root model including native leaflets, calcific plaques extracted from medical images, and an accurate stent geometry based on micro-CT reconstruction are innovative aspects included in the present study. Through the proposed simulation strategy we observed that, in both patients, stent apposition significantly induces anatomical configuration changes, while it leads to different stress distributions on the aortic wall. Moreover, for one patient, a possible risk of paravalvular leakage has been found in agreement with post-operative clinical data, which have been analyzed to prove reliability of the performed simulations.**

***Keywords*—aortic valve, finite element analysis, patient-specific modelling, TAVI.**

I. Introduction

The first percutaneous transcatheter implantation of an aortic valve prosthesis in humans was described more than 10 years ago, in 2002, by Cribier [1]. Since then, such a minimally-invasive procedure to restore valve functionality in case of calcific stenosis has become a routine approach for high-risk or even inoperable patients [2].

However, a high percentage of treated patients have shown moderate to severe perivalvular aortic regurgitation which is one of the most frequent complications associated with TAVI which correlates with an increased rate of mortality [3]. Incomplete prosthesis apposition due to calcifications or annular eccentricity, undersizing of the device, and malpositioning of the valve are the most common determinants of paravalvular leakage [3]. As a direct consequence, appropriate annular measurements, a correct evaluation of calcifications and of how they can affect prosthesis placement, as well as the optimal selection of prosthetic valve size are ``of utmost importance" [4].

Given such considerations, advanced computational tools integrating patient-specific information and accurate device data can be used to support pre-operative planning.

In this context, the present work proposes a systematic approach to realistically simulate TAVI, tailored to the clinical practice; in particular, we propose a study, based on the analysis of pre-operative medical images of two real patients who underwent TAVI, with the final goal of predicting the post-operative performance of the prosthesis with respect to the specific anatomical features. The present work includes different issues which make it an original contribution, presenting the capabilities of an advanced tool for clinical support. In particular, i) the aortic valve model is complete of both the aortic sinuses and the native valve leaflets and the considered material model is calibrated on human data, ii) the calcific plaque is included within the model on the basis of imaging records, iii) the geometry of the prosthetic stent is very accurate, being obtained from micro-CT reconstruction.

Last but not least, post-operative data collected by physicians for patients' follow-up are used to validate the obtained results. Validation of TAVI simulation is a critical issue since it is usually difficult to obtain good quality post-operative data and images from the medical team. Additionally, postoperative CT is not included in the routine protocol of transcatheter aortic valve implantation either to not overload renal activity of often critical patients with the use of contrast die, or to avoid high radiation doses for the patient. Instead, the operation outcome is generally evaluated by intraoperative angiography as well as by follow-up ultrasound. In the present paper, on the basis of such routinely obtained data, we try to address a comparison between the real procedure outcomes and the simulation results.

II. Materials and Methods

Two patients were recruited for the present study, both with severe symptomatic aortic stenosis. For both patients the Edwards SAPIEN XT size 26 was selected by physicians as the optimal device for implantation.

The overall strategy we developed to obtain predictive outcomes of transcatheter aortic valve implantation through advanced computational tools can be roughly divided into four main stages:

- processing of medical images;
- creation of analysis-suitable models;
- analyses to reproduce the clinical procedure;
- post-processing and comparison with follow-up data.

In the following we present a brief description of each procedural step.

A. Medical image processing

The native aortic valve geometry, including aortic sinuses and leaflets, as well as position and dimensions of

calcifications are extracted as STL representations from CT images using OsiriX software.

B. Analysis-suitable models

Starting from the STL file, an *ad-hoc* code implemented in Matlab (Mathworks Inc., Natick, USA) leads to a quasi-automatic generation of meshed geometry of the aortic root. Native leaflets are constructed within the obtained aortic root model integrating CT data and ultrasound information. Calcium properties, in terms of material properties and thickness, are assigned to the elements of the aortic valve overlapping the plaque deposits extracted from CT.

A faithful geometrical model of the implanted device is finally generated on the basis of a high-resolution micro-CT scan (Skyscan 1172 with a resolution of 0.17 micron) of a real device sample.

In dealing with the adopted material models: an hyperelastic nearly-incompressible Yeoh model calibrated on human experimental data [5] is used to describe the aortic root and leaflet behaviour. Calcification are modelled according to [6], while the prosthetic device is modelled as follows: a von Mises-Hill plasticity model with isotropic hardening is used for the stent, while an isotropic hyperelastic model is used for the prosthetic leaflets made of bovine pericardium [7].

C. Finite element analyses

TAVI is a complex intervention composed of several steps; to realistically reproduce the whole procedure, we set-up a simulation strategy consisting in the following two main stages [8]:

[a.] stent crimping and deployment: in this step, the prosthesis stent model is crimped to achieve the catheter diameter which, for a transapical approach, is usually 24 French (8 mm); then, the prosthetic stent is expanded within the patient-specific aortic root to reproduce the implantation due to balloon expansion;

[b.] valve mapping and closure: the prosthetic leaflets are mapped onto the implanted stent and a physiological pressure is applied to virtually recreate the diastolic behavior of the prosthetic device.

In Fig. 1 the principal phases of the TAVI simulation strategy are shown. All the numerical analyses are non-linear problems involving large deformation and contact performed using Abaqus Explicit solver v6.10.

III. Results

The obtained results can be classified into two main groups: (i) from the simulation of stent expansion we can evaluate the impact of the metallic frame of the stent on the native calcified aortic valve; (ii) after performing prosthetic valve mapping, from the simulation of valve closure, we can predict the post-operative device performance.

Geometric changes of the aortic root after TAVI may have important clinical implications during follow-up management of the patient. For this reason, computational simulations can be used to compute the variation of the annulus dimensions, as well as the impact of the prosthesis on the aortic root and the related stress distribution along the vessel wall (as shown in Fig. 2). The uniform stress distribution of Patient-2 suggests a more homogeneous interaction between the stent and the aortic tissue than for Patient-1, where two areas of stress concentration indicate on one side a better anchoring of the stent onto the aortic wall, on the other side, weak points prone to tissue degeneration and, eventually, aortic rupture.

Another very important aspect we can evaluate and measure from the analysis results is paravalvular leakage, i.e., a retrograde blood flow which may occur after TAVI. In Fig. 3 (left column) a measure of paravalvular leakage in terms of distance between the implanted stent and the aortic tissue is represented. Results show a more critical condition for Patient-2, which is in agreement with postoperative data collected from Echo-doppler evaluations: Patient-2 shows greater retrograde blood flow than Patient-1 (see Fig. 3).

Finally, also the coaptation between the prosthetic leaflets can be measured from simulation outcomes, that is a parameter which directly correlates with intravalvular leakage. Also in this case, the comparison between Patient-1 and Patient-2 highlights a good qualitative agreement with postoperative medical images.

IV. Conclusions

As extensively highlighted by medical papers, optimal prosthesis sizing with an accurate evaluation of the effects of calcifications represents a critical issue for TAVI procedure. In this study, we have investigated through structural finite element analysis the impact of patient-specific anatomical features of the aortic root on the post-operative performance of implanted TAVI device in two real cases. The numerical results underline the importance of an adequate adherence of the prosthesis stent to the aortic wall to reduce the risk of paravalvular leakage and the positive link between an appropriate apposition and the uniform distribution of the wall stress. The comparison between analysis results and routinely performed postoperative examinations demonstrates that the proposed simulation strategy can offer a reliable and useful tool to evaluate several clinically relevant aspects of TAVI, thus improving the efficacy of the operation technique and supporting device optimization.

References

[1] A. Cribier, *Percutaneous transcatheter implantation of an aortic valve prosthesis for calcific aortic stenosis: First human case description*, Circulation, 2002, vol. 106, pp. 3006–3008.

[2] C.R. Smith et al., *Transcatheter versus surgical aortic-valve replacement in high-risk patients*, New England Journal of Medicine, 2011, vol. 364, pp. 2187-2198.

[3] P. Generaux et al., *Paravalvular leak after transcatheter aortic valve replacement.* JACC, 2013, vol. 61, pp. 1125-1136

[4] R. Gurvitch et al., *Transcatheter aortic valve implantation: Lessons from the learning curve of the first 270 high-risk patients*, Catheterization and Cardiovascular Interventions, 2011, vol. 78, pp. 977-984

[5] C. Martin et al., *Significant differences in the material properties between aged human and porcine aortic tissues*, EJCTS, 2011, vol. 40, pp. 28-34.

[6] C. Capelli et al., *Patient-specific simulations of transcatheter aortic valve stent implantation*, Medical and Biological Engineering and Computing, 2012, vol. 368, pp. 183-192.

[7] F.L. Xiong et al., *Finite element investigation of stentless pericardial aortic valves: Relevance of leaflet geometry*. Annals of Biomedical Engineering, 38, 1908-1918.

[8] F. Auricchio et al., *Simulation of transcatheter aortic valve implantation: a patient-specific finite element approach*, Computer Meth. in Biomech. and Biomed. Eng.,2013, DOI: 10.1080/10255842.2012.746676

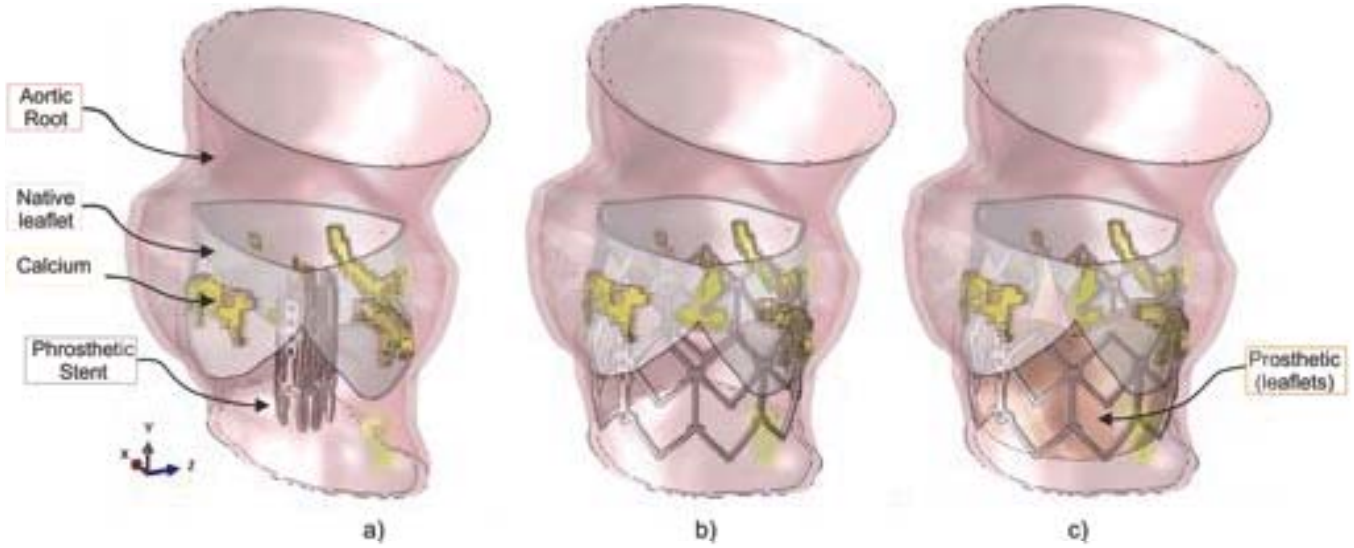

Fig. 1. Procedural steps of TAVI reproduced through a computer-based simulation strategy: a) the crimped stent is properly placed inside the aortic root model which is composed of the native leaflets (white), the native sinuses and surrounding aortic tissues (pink), and calcifications (yellow); b) the stent is expanded within the patient-specific aortic root; c) prosthetic leaflet closure is reproduced to evaluate postoperative performance.

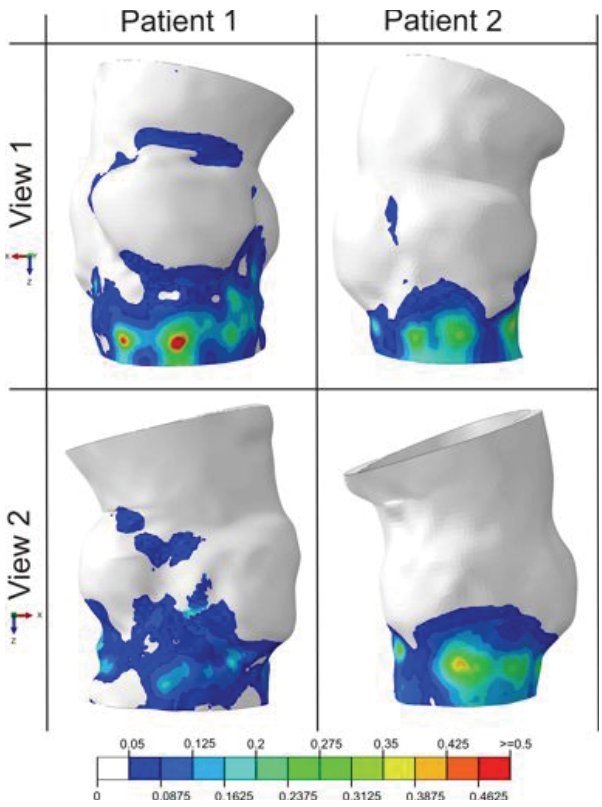

Fig. 2. Impact of the prosthesis implant on the aortic root: von Mises stress [MPa] distribution along the vessel is reported to evaluate the interaction between the prosthetic stent and the aortic root wall. The more uniform stress distribution of Patient-2 suggests a more homogeneous interaction between the stent and the aortic tissue than for Patient-1, where two areas of stress concentration indicate on one side a better anchoring of the stent onto the aortic wall, on the other side, weak points prone to tissue degeneration and, eventually, aortic rupture.

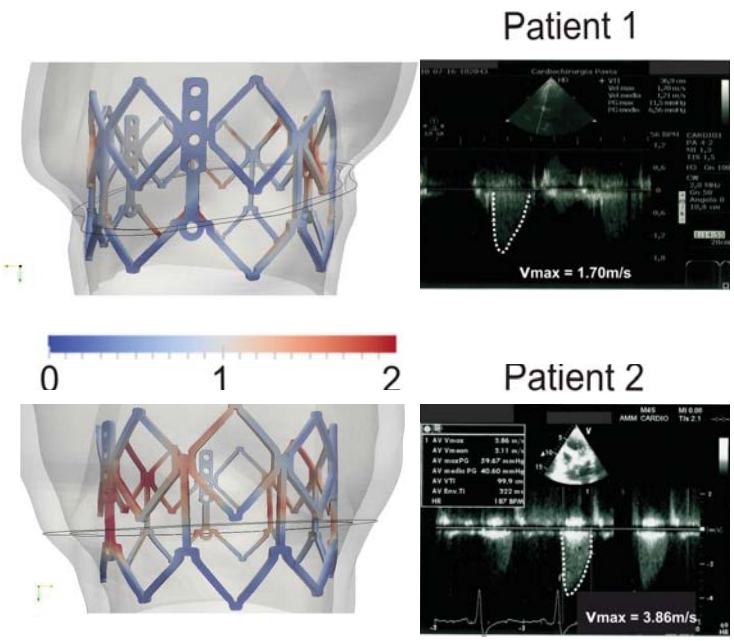

Fig. 3. Evaluation of the degree of apposition between the prosthesis stent and the patient-specific aortic root anatomy: a contour plot of the distance [mm] between the aortic wall and the prosthetic stent is represented. Correspondent postoperative ultrasound images for the two considered patients are shown highlighting a greater retrograde blood flow for Patient-2 than for Patient-1.

Synthetic three-dimensional niches to control mesenchymal stromal cell colonization in vitro

M.M Nava[1], M.T. Raimondi[1], G. Cerullo[3] and R. Osellame[2,3]
[1]*Department of Chemistry, Materials and Chemical Engineering "Giulio Natta", Politecnico di Milano, Milan*
[2]*Istituto di Fotonica e Nanotecnologie – Consiglio Nazionale delle Ricerche (IFN-CNR), Milan, Italy,*
[3] *Department of Physics, Politecnico di Milano, Milan, Italy*

***Abstract*—The ultimate clinical success of stem cell therapies lies entirely in the ability to efficiently control and manipulate stem cell fate. Towards this goal, researchers have explored the use of advanced culture substrates called "synthetic niches". These are polymeric systems mimicking individual aspects of the stem cell aspects of the stem cell interaction with the extra-cellular microenvironment of the native niche, such as material properties and spatiotemporal variations of specific bioactive agents. We used two-photon laser polymerization to fabricate synthetic niches arranged in complex patterns, to study the effect of mechano-topological parameters on morphology, renewal and differentiation of rat mesenchymal stromal cells.**

We observed that niches directed cell homing, aggregate formation. They also provided an increased and truly three-dimensional space for stem cell to adhere and renew.

***Keywords*— Mesenchymal stem cell, synthetic niches, colonization, differentiation**

I. Introduction

Recent developments towards control over stem cell response have explored the use of the advanced culture substrates called "synthetic niches" [1]. These are polymeric systems aiming to mimic aspects of the interaction between stem cells (SCs) and the surrounding environment. Within this context, mechanical cues have been proved to be potent enough to guide cell response [2]. To study the effect of micro-geometry on SC behaviour, we developed a niche system composed of microstructures fabricated by two-photon laser polymerization (2PP) [3]. We used this model system to elucidate aspects of the effects of 3D mechano-topological features on SC response, including colonization and differentiation.

II. Materials and Methods

We used Irgacure-based SZ2080 photoresist as a material for scaffold fabrication. The niche geometry was prismatic of size 90 μm×90 μm×30 μm (Fig. 1A). They were formed by an internal lattice with graded pores (10-30 μm) surrounded by an external confinement grid with horizontal beams spaced by 2 μm. Seven micro-scaffolds arranged in a hexagonal pattern, six at the vertexes and one at the centre, were laser written onto standard coverslip glasses (Fig. 1B). Rat mesenchymal stromal cells (rMSCs) were seeded on the niches and cultured for 21 days. We evaluated cell and nuclear morphology via phase contrast microscopy and scanning electron microscopy (SEM), proliferation and differentiation via cell count and immunofluorescence.

III. Results

The synthetic niches were structurally stable after 3 weeks of culture. The low photoresist autofluorescence enabled the visualization of the fluorescence emission of the markers used for biological staining. At 3 weeks of expansion in the niches, cell density increased by almost 10-fold and resulted 67% greater than in monolayer culture. Lineage commitment was observed in monolayer culture surrounding the structural niches (2D culture conditions) and within cell aggregates, but not inside the niches (3D culture conditions). Furthermore, niches directed cell homing, and were able to guide cell colonization and aggregate formation (Fig. 2 C), likely providing increased surface-to-volume ratios and space for stem cells to adhere and renew, respectively (Fig. 2 A, B).

IV. Conclusion

Altering adhesive condition from 2D to 3D affects MSC commitment: an isotropic cytoskeletal tension and the resulting rounded nuclear shape observed in cells within niches might explain cell self-renewal and pluripotency maintenance. Conversely, spontaneous lineage commitment observed on flat surfaces (2D) might be related to cell polarization. Additional quantitative characterization is ongoing to further demonstrate the significance of our findings.

Acknowledgements

This research is supported by the grant: "3D Micro-structuring and Functionalisation of Polymeric Materials for Scaffolds in Regenerative Medicine" (Fondazione Cariplo,

2010).

.

REFERENCES

[1] M.T. Raimondi, S.M. Eaton, M. Laganà, V. Aprile, M.M. Nava, G. Cerullo and R. Osellame, "Three-dimensional structural niches engineered via two-photon laser polymerization promote stem cell homing," *Acta Biomaterialia*, vol. 9, number 1, pp. 4579–4584, 2013.

[2] M.M. Nava, M.T. Raimondi and R. Pietrabissa, "Controlling self-renewal and differentiation of stem cells via mechanical cues," *Journal of Biomedicine and Biotechnology*, vol. 2012, pp. 1-12, 2012.

[3] M.T. Raimondi, S.M.Eaton, M.M. Nava, M. Laganà, G. Cerullo and R. Osellame, "Two-photon laser polymerization: from fundamentals to biomedical application in tissue engineering and regenerative medicine," *Journal of Applied Biomaterials and Functional Materials*, vol. 10, number 1, pp. 56-66, 2012.

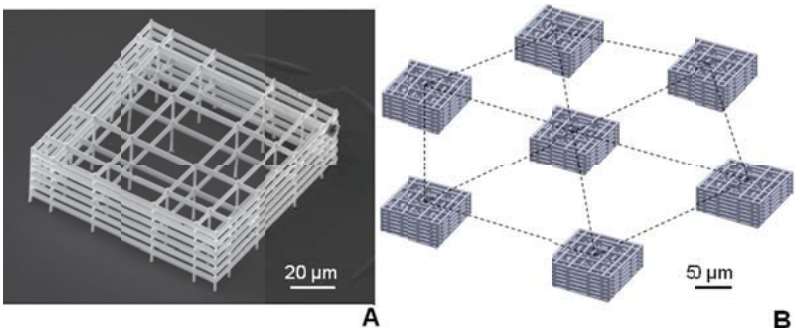

Fig. 1. Configuration of the structural niche system, laser-written on glass coverslips by two-photon laser polymerization. The material used is the SZ2080 with Irg photoinitiator. A) SEM of the structural niche, allowing easy penetration of the cells from the larger central pores and a higher surface-to-volume ratio at the borders of the scaffold, where the external walls confine the cells. B) On each coverglass, 7 structural niches were arranged in a hexagonal pattern.

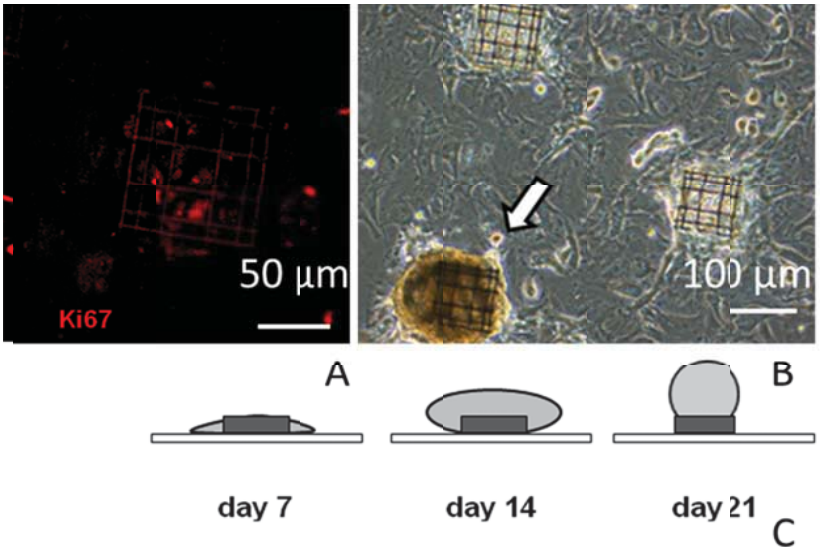

Fig. 2. A) Results of proliferation analysis using immunostaining for the Ki67 antigen. Within niches, proliferating cells are preferentially located in the central regions of the niches. B) Phase contrast images acquired on MSC-seeded niche systems at an inter-niche distance of 400 µm, Colonies form on top of each niche (arrows) C) Scheme of cell aggregate development: from culture day 7, colonies spontaneously forming on glass raise up from the flat surface and progressively form spherical cell aggregates

2-Dimensional foot FE models for clinical application in gait analysis

Alessandra Scarton[1], Annamaria Guiotto[1], Zimi Sawacha[1], Gabriella Guarneri[2], Angelo Avogaro[2], Claudio Cobelli[1]

[1] *Department of Information Engineering, University of Padova, Padova, 35131, Italy*

[2] *Department of Clinical Medicine and Metabolic Disease, University Polyclinic, Padova, 35131, Italy*

***Abstract*— Foot ulcerations are one of the most common and invalidating complications that affect the diabetic patients [1]-[2]. Several two-dimensional (2D) finite element (FE) models of the foot have been developed in the last decades in order to understand what are the causes and to decrease their progress [3]–[4]-[5]. The aim of this work was to create four 2D FE models of an healthy and of a diabetic neuropathic subject integrating kinematic, kinetic and pressure data and to validate them by means of a comparison between experimental and simulated pressure values. These models could be a useful and fast application for the clinicians to prevent the development of the diabetic ulcers.**

***Keywords*—Gait Analysis, Finite Element Models, Diabetic Foot, Foot Ulcers.**

I. Introduction

The diabetic foot is determined by the simultaneous presence of both peripheral neuropathy and vasculopathy that alter the biomechanics of the foot with the formation of callosity and ulcerations. The social and economic burden of the diabetic foot can be reduced through a prompt diagnosis and treatment. FE analysis allows to characterise and quantify the loads developed in the different anatomical structures and to understand how these affect foot tissue in dynamic conditions [2]. In this study 8 experimentally kinematics-kinetics based FE models of the hindfoot of a healthy and of a diabetic neuropathic subject were developed in order to define more efficient subject specific computational model of the hindfoot that accounts for in-vivo kinematics, kinetics and plantar pressure data together with foot magnetic resonance images (MRI) data.

.

II. Material and Methods

A. Experimental Procedure

The biomechanical analysis of the foot was carried out as in [6]–[8] on 10 healthy (HS) (age 58.7±10 years, BMI 24.5±2.6 kg/m^2) and 10 diabetic subjects with neuropathy (NS) (age 63.2±6.4 years, BMI 24.3±2.9 kg/m^2). The experimental setup included a 6 cameras stereophotogrammetric system (60-120 Hz BTS S.r.l, Padova), 2 force plates (FP4060-10, Bertec Corporation, USA) and 2 plantar pressure systems (Imagortesi, Piacenza). The signals coming from all systems were synchronized in post processing as in [6]. For each patient's foot the hindfoot, midfoot, forefoot and tibia subsegments 3-dimensional (3D) kinematic was calculated together with hindfoot, midfoot, forefoot 3D ground reaction forces and plantar pressure.

B. Finite Element Models

The MRI of the foot of a healthy subject and of a diabetic neuropathic subject was acquired with 1.5T devices (Philips Achieva and Siemens Avanto, Spacing between slides: 0.6-0.7mm, Slice thickness: 1.2-1.5mm). MRI images were then segmented with Simpleware ScanIP-ScanFE (v.5.0) in order to get four slice of the foot from which four 2D FE models of the foot were developed both for the healthy and the diabetic subjects (Fig. 1 and Fig. 2). The modeled section were chosen as typical areas of development of ulcers and according to the position of the marker in the gait analysis protocol: the slice passing through the first and the fifth metatarsal heads, the slice passing through the malleoli, the slice passing through the calcaneus and the second metatarsal head and the slice passing through the calcaneus and the first metatarsal head.

Finally the slices were imported into ABAQUS (Simulia, v.6.12) and meshed with quadrilateral elements according to the literature [9]. An horizontal rectangular element was drawn in ABAQUS under the heel slice to simulate the ground support. It was meshed with 8 mm side quadratic elements with the aim to obtain contact pressures values comparable with the experimental ones (according to plantar pressure system sensors dimension). The skin was represented by an homogeneous isotropic soft tissue model with an hyperelastic material formulation in first order Ogden form and coefficients from [10]. Both the floor and the bones were modelled as homogeneous isotropic linear elastic materials [5]- [9]. The foot-floor interface was modelled using contact surfaces with a coefficient of friction of 0.6 [11]. The bones were tied to the soft tissues.

The displacements of the markers determined from the gait analysis data for each patient in four instances of the stance phase of gait (initial contact, loading response, midstance and push-off) were used as input for the simulations. Also the position of the foot with respect to the floor was considered, matching the FE model angles to the experimental one obtained from the kinematic data. FE simulations were run with the kinematics and kinetics data of 10 HS and of 10 NS included the 2 subjects whose MRIs were used for defining the FE models geometry.

III. Results

The validations of the models have been performed computing the RMSE between the experimental and the simulated plantar pressures in percentage of the experimental peak value. Results for the diabetic subjects are shown in Table I. For the healthy subject the values are comparable

and shown in Table II.

TABLE I
RMSE BETWEEN THE EXPERIMENTAL AND THE SIMULATED PLANTAR PRESSURES IN PERCENTAGE OF THE EXPERIMENTAL PEAK VALUE, IN FOUR INSTANCES OF THE STANCE PHASE OF GAIT AND FOR THE FOUR MODEL OF THE DIABETIC SUBJECT.

	Initial contact	*Loading response*	*Midstance*	*Push-off*
1st metatarsal -calcaneus model	25.08	20.43	33.26	24.69
2st metatarsal - calcaneus model	22.20	24.68	37.82	41.67
1st-5th metatarsal head model	-	45.77	46.34	46.25
Through malleoli model	35.36	42.12	46.58	-

TABLE II
RMSE BETWEEN THE EXPERIMENTAL AND THE SIMULATED PLANTAR PRESSURES IN PERCENTAGE OF THE EXPERIMENTAL PEAK VALUE, IN FOUR INSTANCES OF THE STANCE PHASE OF GAIT AND FOR THE FOUR MODEL OF THE HEALTHY SUBJECT.

	Initial contact	*Loading response*	*Midstance*	*Push-off*
1st metatarsal -calcaneus model	17.08	27.57	27.76	22.07
2st metatarsal - calcaneus model	43.62	28.62	55.59	26.05
1st-5th metatarsal head model	-	30.47	45.06	24.83
Through malleoli model	16.78	18.10	15.18	-

IV. CONCLUSION

In general, model predicted plantar pressures were in good agreement with those measured during the considered sub-phases of the stance phase of gait.

Even under the restrictive assumptions of 2D representation, which is clearly inadequate for a complete model of the complex mechanics of the foot, it is possible to run fast computational simulations that provide useful information for the clinicians towards a prevention of plantar ulcer formation.

This information may provide new insight into planning preventive treatment by including pressure relief insoles in the simulation. In conclusion, our research indicated that using the subject specific in-vivo measured biomechanical data for the simulation of the FE foot model can provide more realistic results on the soft tissue plantar pad pressure distributions and deformations.

REFERENCES

[1] A. J. Boulton, L. Vileikyte, G. Ragnarson-Tennvall, and J. Apelqvist, "The global burden of diabetic foot disease", *The Lancet*, vol. 366, n. 9498, pp. 1719–1724, 2005.

[2] P. Cavanagh, A. Erdemir, M. Petre, T. Owings, G. Botek, S. Chokhandre, and R. Bafna, "Biomechanical factors in diabetic foot disease", *J. Foot Ankle Res.*, vol. 1, n. Suppl 1, pag. K4, 2008.

[3] L. Wu, "Nonlinear finite element analysis for musculoskeletal biomechanics of medial and lateral plantar longitudinal arch of Virtual Chinese Human after plantar ligamentous structure failures", *Clin. Biomech.*, vol. 22, n. 2, pp. 221–229, Feb. 2007.

[4] A. Scarton, A. Guiotto, Z. Sawacha, G. Guarneri, A. Avogaro, and C. Cobelli, "Gait analysis driven 2d finite element model of the neuropathic hindfoot", in *Proceedings ISB 2013*, Natal, Brasil.

[5] A. Gefen, M. Megido-Ravid, Y. Itzchak, and M. Arcan, "Biomechanical analysis of the three-dimensional foot structure during gait: a basic tool for clinical applications", *J. Biomech. Eng.*, vol. 122, n. 6, pp. 630–639, Dec. 2000.

[6] Z. Sawacha, G. Cristoferi, G. Guarneri, S. Corazza, G. Donà, P. Denti, A. Facchinetti, A. Avogaro, and C. Cobelli, "Characterizing multisegment foot kinematics during gait in diabetic foot patients", *J. NeuroEngineering Rehabil.*, vol. 6, pp. 37–37, Oct. 2009.

[7] Z. Sawacha, A. Guiotto, G. Boso, G. Sciumè, G. Guarneri, A. Scarton, A. Avogaro, and C. Cobelli, "Development of a foot multiscale model for diabetic foot prevention", in *Proceedings International Society of Biomechanics (ISB)*, Natal, Brasil, 2013.

[8] Z. Sawacha, F. Spolaor, G. Guarneri, P. Contessa, E. Carraro, A. Venturin, A. Avogaro, and C. Cobelli, "Abnormal muscle activation during gait in diabetes patients with and without neuropathy", *Gait Posture*, vol. 35, n. 1, pp. 101–105, Jan. 2012.

[9] S. Goske, A. Erdemir, M. Petre, S. Budhabhatti, and P. R. Cavanagh, "Reduction of plantar heel pressures: Insole design using finite element analysis", *J. Biomech.*, vol. 39, n. 13, pp. 2363–2370, Jan. 2006.

[10] W.-M. Chen, T. Lee, P. V.-S. Lee, J. W. Lee, and S.-J. Lee, "Effects of internal stress concentrations in plantar soft-tissue--A preliminary three-dimensional finite element analysis", *Med. Eng. Phys.*, vol. 32, n. 4, pp. 324–331, May 2010.

[11] J. T.-M. Cheung and M. Zhang, "A 3-dimensional finite element model of the human foot and ankle for insole design", *Arch. Phys. Med. Rehabil.*, vol. 86, n. 2, pp. 353–358, Feb. 2005.

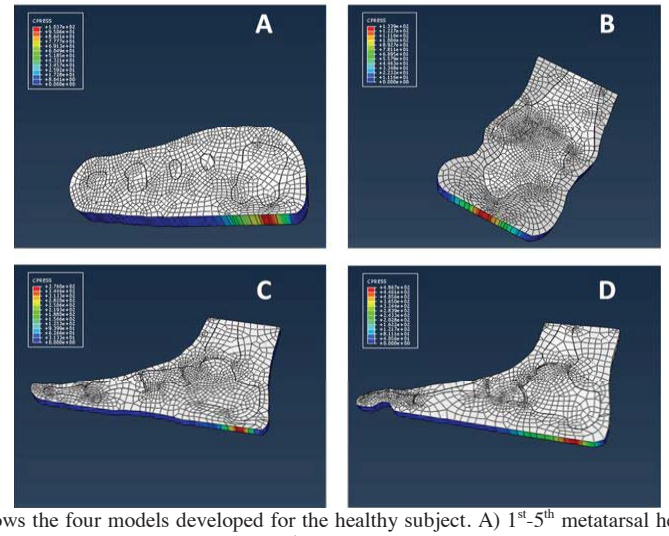

Fig. 1. The figure shows the four models developed for the healthy subject. A) 1st-5th metatarsal head model; B) Through malleoli model; C) 1st metatarsal -calcaneus model; D) 2st metatarsal -calcaneus model.

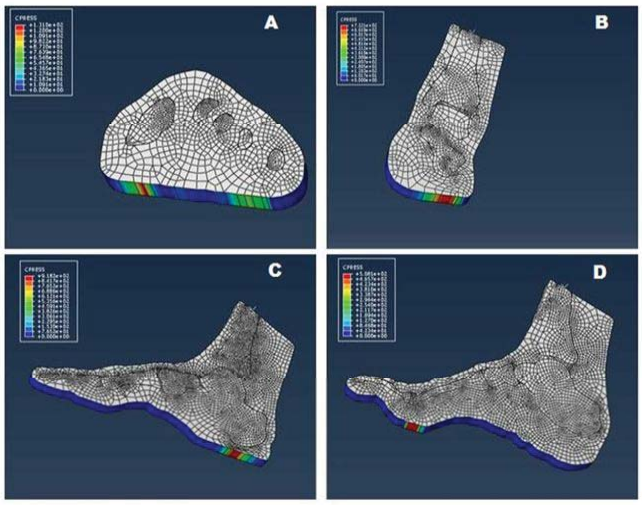

Fig. 2. The figure shows the four models developed for the diabetic subject. A) 1st-5th metatarsal head model; B) Through malleoli model; C) 1st metatarsal -calcaneus model; D) 2st metatarsal -calcaneus model.

The Influence of Cardiac Trabeculae on Ventricular Mechanics

M. Serrani[1], M. Mariani[1], R. Fumero[1] and M.L. Costantino[1]
[1] *LaBS, Department of Chemistry, Materials and Chemical Engineering, Politecnico di Milano, Milan, Italy*

***Abstract*— Cardiac trabeculae are cylindrical structures characterized by an axially orientation of myocytes which cover the ventricles endocardium. They are preferably oriented in the apico-basal direction, and represent a significant percentage of the ventricular mass (from 12% to 17%). The aim of the project is to study the influence of the trabecular mass on ventricular performances by comparing different finite-element models (with or without trabeculae) of the left ventricle, keeping constant the total muscular mass and the intra-ventricular volume. The ventricle was simplified as a truncated ellipsoid and the trabeculae as cylindrical strands laying onto the endocardium oriented along the ventricular axis. The cardiac tissue was modelled by an hyperelastic anisotropic law, and the cardiac fibers oriented according to literature data. Physiologic atrial pressure was set during the ventricular filling phase, while an RCR model was coupled to the ventricle to simulate the systemic circulation. The results show a significant role of trabeculae on ventricular hemodynamics: the presence of trabecular mass increases the ventricular filling, allowing a remarkably higher ventricular cardiac output to be developed.**

***Keywords*—trabeculae, cardiac mechanics, computational modelling.**

I. Introduction

In the adult heart, cardiac trabeculae appear as cylindrical structures which cover the endocardial surfaces of both ventricles. They are characterized by an axial orientation of cardiac fibres and are arranged in a complex shape, preferably arising from the free wall and insert into the atrio-ventricular ring. The trabecular mass represents a significant percentage of the ventricular total mass; in healthy subjects, this percentage has been estimated to vary from 12 to 17% of the total ventricular muscular mass [1,2].

Left ventricular trabeculae are frequently seen during echocardiographic examinations, and even if there is not a universally accepted criteria, a value of trabecular mass higher than 20% of ventricular mass is considered an index of left ventricular non compaction, a primary cardiomyopathy of genetic origin that can lead to heart failure, trombo-embolism and arrhythmia. Despite these findings, the literature lacks of studies about the role of trabecular mass on heart behaviour.
The aim of this work is to understand the influence of ventricular trabeculae on cardiac performances.

II. Materials and Methods

To understand the influence of cardiac trabeculae on heart mechanics, a finite element model of the left ventricle was developed within the finite element framework provided by Abaqus (Abaqus®, SIMULIA, Dessault Systémes).
In particular, the purpose is to compare the ventricular behaviour in the presence or the absence of the trabecular non-compact layer. Thus, different geometrical models, with or without trabeculae, were designed keeping both the total ventricular muscular mass and the intraventricular volume constant. Further, different trabeculae diameters and mass were implemented to investigate the influence of these parameters on the model outcomes.

A. Geometrical model

Two different types of geometry were implemented: a "smooth" and a trabeculated model. In both cases, the left ventricle was simplified as a truncated ellipsoid. The undeformed configuration of the smooth ellipsoid is characterized by a major axis of 57 mm, a minor axis of 14 mm and a constant wall thickness of 9 mm; thus, the ventricular volume at zero pressure is 43 ml, according to previous works [3]. To design the trabeculated geometries, a percentage of the total muscle mass was changed from compact layer to trabeculae at the endocardium, keeping constant the intraventricular volume. The trabeculae were described as cylindrical strands oriented along the ventricular axis direction, laying onto the endocardium (Fig.1). Thus, the wall thickness is not uniform in the trabeculated models: at the trabeculae the wall thickness increases, while in the inter-trabecular spaces the wall thickness is lower with respect to the smooth model. The reference trabeculated model is characterized by a trabecular mass equal to the 15% of the ventricular mass, and a trabeculae diameter of 4 mm. Two additional trabecular mass were implemented, in particular the 7% and the 22%. Further, trabeculae diameter of 3.4 mm and 5.2 mm were considered at a constant trabeculated mass of the 15%. All the models were discretized by 8-node hexahedral elements; a different number of elements was required for each model, but this number was always higher for the trabeculated models, due to their geometrical complexity (Fig.1). In particular, the smooth model was discretized in about 18000 elements, while 61000 elements were required for the reference trabeculated model.

B. Cardiac tissue modelling

The left ventricular wall is composed of discrete layers of parallel myocytes with a variable orientation through the wall thickness: in the compact layer, the preferential fibres direction is about -80° near the epicardium, rotates to 0° at the midwall and reaches +80° at the endocardium with respect to circumferential direction [4]; in the non-compact layer the fibres follow the trabecular axial direction. To replicate this fibre arrangement, a custom MATLAB routine (MATLAB®, The MathWorks, Inc) was developed (Fig.1). To model the cardiac tissue behaviour, both the passive and

active behaviour of the cardiac fibres have to be modelled. About the passive material properties, a hyperelastic anisotropic constitutive model was chosen (Eq.1-3) [5];

$$\Psi = C_{10}(\bar{I}_1 - 3) + \frac{k_1}{2k_2}(\exp(k_2(\bar{I}_4 - 1)^2) - 1) \quad (1)$$

$$\overline{I_1} = tr(\overline{\boldsymbol{C}}); \qquad \overline{I_4} = \boldsymbol{A_\alpha} \cdot \overline{\boldsymbol{C}} \cdot \boldsymbol{A_\alpha} \quad (2,3)$$

The cardiac fibres direction is defined by the unit vector $\boldsymbol{A_\alpha}$. This form of the constitutive law is valid for a single family of perfectly aligned fibres. The material parameters (C_{10}, k_1, k_2) were chosen such that the diastolic pressure-volume (PV) relationship of the reference trabeculated model fitted a physiological one [6]. The active behaviour of myocytes was implemented by increasing the material stiffness during systole according to the contraction curve of a cardiac fibre [7]. The maximum parameters values (Table I) were chosen to obtain a physiologic ventricular torsion peak in the reference model. Indeed the ventricular torsion, which is the rotational movement of the ventricular apex with respect to the base, reflects the synergic interaction between myocardial constitutive components; a physiologic value of torsion is fundamental for a realistic ventricular kinematics [8].

TABLE I. MATERIAL PARAMETERS VALUES

Parameter	*Diastolic Value [kPa]*	*Maximum systolic value [kPa]*
C10	0.2	6
k1	1	150
k2	2	2

C. Boundary conditions

The models boundary conditions included: kinematic constraints to avoid rigid motions of the structure; the implementation of a pre and an afterload circuit for the ventricle. About the kinematic boundary conditions, to constrain the model, all the displacements of the ventricular base were prevented. The preload circuit consist of a resistance placed between a single node, representing the left atrium (LA), and the ventricle. The diastolic phase is simulated by applying a constant pressure of 5.25 mmHg at the atrium. Instead, the afterload circuit was simulated by an RCR model, according to a previous work [8] (Fig. 2). Briefly, the circuits resistances were set by imposing a piecewise linear Δp-Q relationship between the nodes upstream and downstream to the resistance of interest. Thus, the backward flows, e.g. from the ventricle to the atrium, were prevented by imposing zero-flow at a negative pressure difference. Since a hydraulic compliance is not implemented in Abaqus, a sphere composed of shell elements was designed to guarantee a compliant element which can simulate the systemic circulation compliance. To reach the steady state of the system, a minimum of five cardiac cycles were simulated for each model.

III. RESULTS

The results of the simulations are first shown in terms of ventricular PV loop. In Fig. 3 the comparison between the smooth and the reference trabeculated model is presented. The trabeculated model is characterized by an higher compliance with respect to the smooth: the end-diastolic volume (EDV) is significantly higher (+30%) if the trabeculae are present, as well as the stroke volume (SV) (+20%). Hence, the cardiac output (CO) at 75 bpm is 5 l/min for the trabeculated ventricle and 4 l/min for the smooth ventricle. Further, the EDV increases as the trabecular mass increase; the results highlight a non-linear relationship of the EDV (and SV) against the spongy layer mass (Fig. 4). Thus, the mere presence of a trabeculated mass is more relevant than the progressive growth of the spongy mass in terms of ventricular filling. Furthermore, the trabeculae diameter influences the fibre stress distribution across the ventricular wall. Indeed, a lower diameter is responsible for a more uniform fibre stress between the trabeculae and the inter-trabecular spaces (Fig. 5).

IV. CONCLUSION

In this work a dependence of the ventricular filling from the presence of an endocardial spongy layer was assessed. The ventricular filling is a fundamental parameter in determining the heart performances; more than the 50% of the patients suffering of heart failure symptoms show a normal ejection fraction and are referred to as diastolic heart failure patients. In this context, the trabeculae play a fundamental role, since they can significantly contribute to the achievement of a physiologic EDV and CO. Moreover, the computational approach adopted in this work allowed a parametric study to be performed, which revealed a more homogeneous stress distribution in the ventricular wall as the trabeculae diameter reduces. This finding can explain the preferentially presence of fine trabeculations at the endocardium. Indeed, the stress distribution uniformity is important for a homogeneous energetic consumption of the cardiac cells and, consequently, of a uniform myocytes work and oxygen demand.

REFERENCES

[1] Jacquier A, Thuny F et al., "Measurement of trabeculated left ventricular mass using cardiac magnetic resonance imaging in the diagnosis of left ventricular non-compaction," *Eur Heart J* 2010;9:1098-104.

[2] Fernández-Golfín C, Pachón M et al., "Left ventricular trabeculae: Quantification in different cardiac diseases and impact on left ventricular morphological and functional parameters assessed with cardiac magnetic resonance," *J Cardiovasc Med*, 2009;10:827-833.

[3] R. C. P. Kerckhoffs, P. H. M. Bovendeerd, J. C. S. Kotte, F. W. Prinzen, K. Smits, and T. Arts, "Homogeneity of Cardiac Contraction Despite Physiological Asynchrony of Depolarization: A Model Study," *Ann. Biomed. Eng.*, 2003;31(5):536–547.

[4] D. D. Streeter, H. M. Spotnitz, D. et al., "Fiber Orientation in the Canine Left Ventricle during Diastole and Systole," *Circulation Research*, 1969;24:339-347.

[5] T. C. Gasser, R. W. Ogden, and G. a Holzapfel, "Hyperelastic modelling of arterial layers with distributed collagen fibre orientations.," *J. R. Soc. Interface*, 2006;3(6):15–35.

[6] Westermann D, Kasner M et al., Role of left ventricular stiffness in heart failure with normal ejection fraction. *Circulation* 2008;117:2051-60.

[7] Backs PH, Gao WD et al., The Relationship between contractile force and intracellular [Ca2+] in intact rat cardiac trabeculae. *J Gen Physiol* 1995;105:1-19.

[8] Bagnoli P, Malagutti N et al., Computational finite element model of cardiac torsion. *Int J Artif Organs*, 2011;34:44-53.

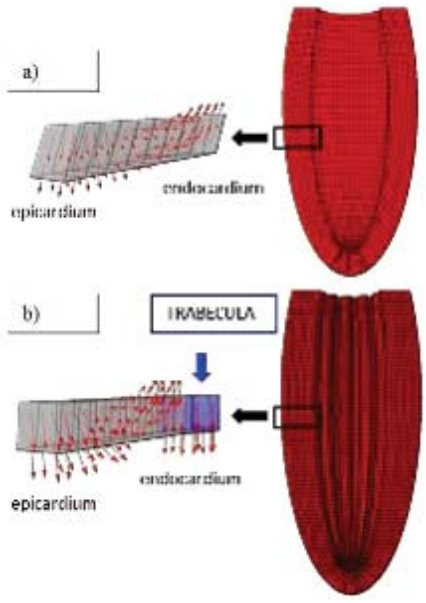

Fig. 1. Geometrical model and fiber distribution from epicardium to endocardium in (a) the smooth model and (b) the reference trabeculated model. The trabecula, with an axial fiber orientation, is highlighted in blue.

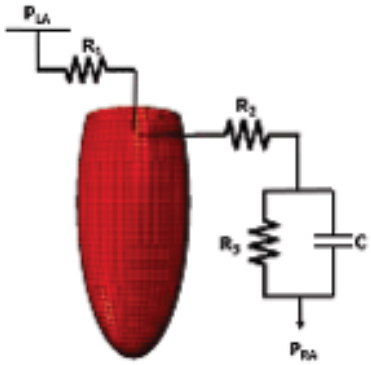

Fig. 2. Ventricular pre-load and after-load circuits (P_{LA}=left atrium pressure; R_1=0.2 mmHg/(l/min); R_2=0.325 mmHg/(l/min); R_3=22.72 mmHg/(l/min); C=8*10-5 l/mmHg, P_{RA}=right atrium pressure).

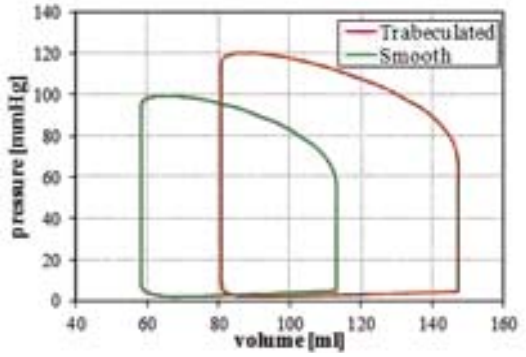

Fig. 3. PV loop of the smooth and the trabeculated model.

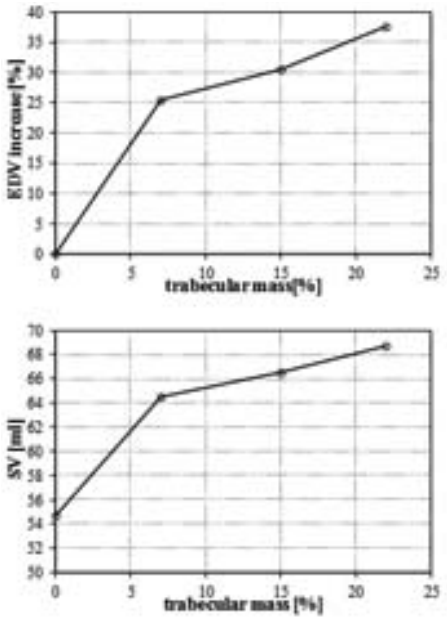

Fig. 4. EDV (top) and SV (bottom) values against the trabecular mass variation for the different models. A trabecular mass of 0% represents the smooth case.

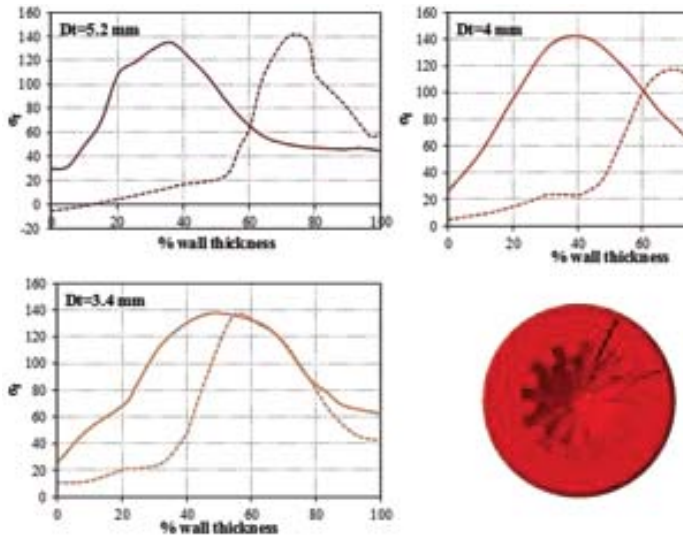

Fig. 5. Stress distribution at the systolic pressure peak along the wall thickness for different trabeculae diameters (D_t) (0% of wall thickness is the endocardium, 100% represents the epicardium).

Optical, mechanical and biochemical characterization of trabecular bone

G. Spatafora[1], I. Bargigia[2], M. Malo[3], F. Tortelli[4], M. Shahgholi[5], M. Domenicucci[7], M. Agnoletto[7], P. Vena[6], G.M. Peretti[6,7], J.A. Hubbell[4], J. Jurvelin[3], A. Pifferi[2], P. Taroni[2], F. Boschetti[1,7]

[1] *LaBS, Dipartimento di Chimica, Materiali e Ingegneria Chimica "Giulio Natta", Politecnico di Milano, Milan, Italy*
[2] *Dipartimento di Fisica, Politecnico di Milano*
[3] *Department of Applied Physics, University of Eastern Finland, Kuopio, Finland*
[4] *EPFL SV IBI, Laboratory for Regenerative Medicine and Pharmacobiology (LMRP), Lausanne, Switzerland*
[5] *Dipartimento di Elettronica, Informatica e Bioingegneria, Politecnico di Milano, Milan, Italy*
[6] *Dipartimento di Scienze Biomediche per la salute, Università di Milano*
[7] *IRCCS Istituto Ortopedico Galeazzi, Milan, Italy*

***Abstract*—The evaluation of bone quality in the early stage of the disease is important both in terms of costs and quality of life. This work aims at providing novel information about optical, biochemical and mechanical properties in trabecular bone with a special goal to increase our understanding of the capability of diffuse optical spectroscopy (DOS) in the detection of bone structure and composition. Pathological human and healthy bovine samples were characterized both optically and mechanically using several techniques (Raman spectroscopy, µCT, DOS, permeability tests, mechanical tests at meso and nano scale, and biochemical compositional analysis). Results from all techniques were compared and statistical correlations were investigated revealing relationships between the structure, the composition and the mechanical properties of trabecular bone, some of which are novel, such as those between bone permeability and DOS spectra parameters. This study represents the first step in the development of DOS methodology as a non-invasive diagnostic tool to detect osteoporosis in the early stage.**

***Keywords* — DOS, optical characterization, mechanical characterization, trabecular bone.**

I. Introduction

Efforts in clinical research have led to important progress in medical diagnostics. On one side, this induces an improvement in quality of life and, in particular, a lengthening of the active life of the population; on the other side, it exposes each person to the risk of undergoing pathologies typical of the elderly (*e.g.* osteoarthritis and fractures as a consequence of the reduction of bone mass).

At present, the diagnosis of osteoporosis is related to the quantitative assessment of bone mineral density (BMD), often assessed by densitometry techniques like DXA. The research is moving towards the development of new techniques able to non-invasively assess, with reduced costs, the conditions of bone and to detect changes in composition and/or structure in the very early phase of the pathology development.

This work aims at providing novel information about optical, biochemical and mechanical properties in trabecular bone with a special goal to increase our understanding of the capability of Diffuse Optical Spectroscopy (DOS) for the evaluation of bone quality and for the detection of osteoporosis in an earlier stage than DXA.

II. Materials and Methods

Three optical methods were used: µCT to analyze the microstructure, Raman spectroscopy to assess local changes in the composition related to the level of mineralization and cristallinity, and diffuse optical spectroscopy (DOS) to define the bulk structure and composition at the same time. The mechanical behavior was defined using unconfined compression tests, permeability measurements, nanoindentation. The collagen amount was derived from the hydroxyproline content.

Human and bovine trabecular bone cylindrical samples from the femoral neck and head were characterized. Specifically, 10 bovine samples from five healthy 30-months-old animals (Ø=11.9±0.1mm, height=17.4±3.5mm) and 57 human specimens from 12 patients (Ø=11.1±0.6mm, height=11.8±2.9mm) who underwent arthoplasty of the hip at the I.R.C.C.S Orthopedic Institute Galeazzi in Milan were analysed.

The Raman measurements (Senterra 200LX, Brucer Optics GmbH, Ettingen, Germany) were performed on different trabeculae of each sample. The OPUS software (v 6.5, Bruker Optics GmbH, Ettlingen, Germany) was used to locate the Raman measurement points and spectra analysis was done using a custom-made MatLab (MatLab 7.6.0, The MathWorks. Inc.) routine (Turunen et al, 2011 and 2012). Parameters evaluated were the full width high maximum of $1/\nu_1$, related to the cristallinity, and the peak height and area of $\nu_1/\text{Amide}_\text{I}$, $\nu_1/\text{Amide}_\text{III}$, $\nu_3/\text{Amide}_\text{I}$, $\nu_3/\text{Amide}_\text{III}$ and ν_3/ν_1 that are mineral to matrix ratios, related to the mineralization.

µCT images were acquired (SkyScan 1172, Aartselaar, Belgium) with an isotropic voxel size of 15 µm, and the SkyScan 1172 nRecon software and the Skyscan CT Analyzer (CTAn) software were used for the images reconstruction and the morphometric indices calculation respectively.

Time domain DOS analysis was performed with a home built instrument on each clean sample by acquisitions repeated ten times between 600 and 1300 nm with a step of 5 nm and then averaged. The scattering spectra are interpolated using a power law (Mie theory) where the amplitude is related to the tissue density and the exponent to the equivalent size of the scattering centers. The absorption coefficient spectrum is fitted (Beer's law) using the spectra of

the tissue components, minimizing the gap between experimental data and mathematical model.

The hydraulic permeability was evaluated for all of the samples using a custom made device. Different levels of flow rate were imposed through the bone samples using a centrifugal pump (Medtronic, BIO-MEDICUS® - 550 BIOCONSOLE®) and the resulting pressure drops across the samples were measured. The permeability was then evaluated by the Darcy law.

To evaluate the mechanical properties at the nanoscale, one sample from each patient and one from each animal (11 human and 5 bovine samples), were embedded in resin (EpoFix, Struers), polished (Buehler EcoMet) and subjected to multi load creep tests (Nanotest Platform 3, MicroMaterials®). The reduced Young modulus E_r was measured for each sample. The remaining of the samples was tested at the mesoscale, under unconfined compression configuration (MTS 858 Mini-Bionix, S/N 1015457, MTS, Minneapolis, MN). Each sample underwent 6 cycles of load-unload in the linear field at compression rates of 0.01mm/s and 0.1mm/s, before being loaded to failure at a compression rate of 0.1mm/s. For each sample, the apparent stiffness (E_{app}), the yield and the ultimate stresses (σ_y and σ_u) and strains (ε_y and ε_u) were derived from the stress-strain data.

The bone collagen content was evaluated using a hydroxyproline (HYP) assay kit (Hydroxyproline Assay kit, Sigma –Aldrich 3050 Spruce Street, St. Louis, MO 63103 USA), from the absorbance at 560nm of each hydrolysed sample.

Results from the experimental tests and from the computational analyses were compared looking for correlations (qualitative and quantitative) between different methodologies. The correlations were evaluated using a parametric or non-parametric test depending on the data distribution. Pearson or Spearman coefficients were evaluated (α=0.05). The collagen amounts resulting from DOS and biochemical analyses were compared using a Mann-Whitney test (α=0.05).

III. Results

Results from Raman spectroscopy, μCT, DOS, and unconfined compression tests are summarized in Tables I, II, III, and IV.

TABLE I
RAMAN RESULTS (AVG±STD DEV)

	1/v1 FWHM	*v1/amideI PH*	*v1/amideIII PH*	*v3/amideI PH*
Human	*3.5E-2±1E-3*	*7.7±0.8*	*4.2±0.9*	*2.2±0.4*
Bovine	*3.6E-2±8E-4*	*7.9±0.4*	*5±0.7*	*1.9±0.1*
	v3/v1 PH	*v1/amideI PA*	*v3/amideI PA*	*v3/v1 PA*
Human	*0.3±5.8E-2*	*5±0.4*	*0.7±8.5E-2*	*0.1±1.3E-2*
Bovine	*2.4±1.5E-2*	*5.4±1.6*	*0.8±0.3*	*0.1±2.5E-2*

TABLE II
μCT MORPHOMETRIC PARAMETERS (AVG±STD DEV)

	BV/TV %	*BS/BV[mm-1]*	*Tb.Th[mm]*	*Tb.Sp[mm]*
Human	*21.3±3.4*	*14.2±1.1*	*0.2±0.02*	*0.9±0.2*
Bovine	*28.9±7.2*	*13.5±2.6*	*0.24±0.05*	*0.8±0.1*
	Tb.N[mm]	*Tb.Pf[mm]*	*SMI [-]*	*DA [-]*
Human	*0.9±0.15*	*3.3±1.2*	*1.6±0.5*	*0.5±0.08*
Bovine	*1.2±0.2*	*1.5±2.4*	*1.01±1*	*0.6±0.16*

TABLE III
COMPOSITION FROM DOS (AVG±STD DEV)

	Collagen [mg/cm3]	*Hydroxyapatite [mg/cm3]*	*Hydroxyapatite/Collagen [-]*
Human	*174.4±31.6*	*250.8±42.6*	*1.83±0.93*
Bovine	*259.0±62.2*	*318.5±167*	*1.29±0.65*
DOS SCATTERING PARAMETERS (AVG±STD DEV)			
		a [-]	*b [-]*
Human		*9.52±1.4*	*0.17±0.07*
Bovine		*11.8±3.7*	*0.35±0.1*

TABLE IV
MECHANICAL PARAMETERS @ MESOSCALE (AVG±STD DEV)

	E_{app}*[MPa]*	σ_y*[MPa]*	σ_u*[MPa]*	ε_y*[-]*	ε_u*[-]*
Human	*189±54*	*-2.7±1.3*	*-3.8±1.6*	*-0.02±0.01*	*-0.05±-0.02*
Bovine	*425±219*	*-8.2±-5.6*	*-12.5±6.7*	*-0.02±0.01*	*-0.08±-0.06*

Figures 1 and 2 respectively show the permeability values and the reduced Young modulus values.

Among the several correlations between samples features (*e.g.* age, sex), experimental and computational parameters that resulted statistically significant (p-value<0.05), we underline the novel ones regarding the relationships between DOS and mechanical and chemical parameters. Density evaluated by DOS has a statistical significant correlation with failure stress (R^2=0.54 and p-value=0.006) and yield stresses (R^2=0.59 and p-value=0.004). The permeability is correlated to collagen content (R^2=0.44 and p-value=0.02) and to hydroxyapatite to collagen ratio (R^2=0.66 and p-value=0.001). The collagen content measured by DOS for each sample is statistically equal to the content measured by standard biochemical techniques (Mann-Whitney tests), results are compared in Figure 3.

IV. Discussion

Our results are in general in agreement with the literature. The pathological conditions of our samples are reflected by an increase in Raman parameters related to the mineralization content with respect to healthy femoral bone [1]. The higher values of the reduced moduli with respect to literature [2] can also be attributed to the higher mineral content of our pathological samples. Degradation of the solid matrix is reflected by our values of permeability, higher than those evaluated for healthy bone [3].

As far as we know, this is the first systematic study to reveal the potential of DOS as a non-invasive diagnostic tool for early detection of osteoporosis.

References

[1] McCreadie BR, Morris MD, Chen TC, Sudhaker Rao D, Finney WF, Widjaja E, Goldstein SA, "Bone tissue compositional differences in women with and without osteoporotic fracture," *Bone* vol. 39(6), pp. 1190-11955, 2006.

[2] Zysset PK, Guo XE, Hoffler CE, Moore KE and Goldstein SA, "Elastic modulus and hardness of cortical and trabecular bone lamellae measured by nanoindentation in the human femur," *J Biomech.* Vol. 32(10), pp. 1005-1012, 1999.

[3] Nauman EA, Fong KE, Keaveny TM, "Dependence of intertrabecular permeability on flow direction and anatomic site," *Ann Biomed Eng.* Vol: 27(4), pp. 517-524, 1999.

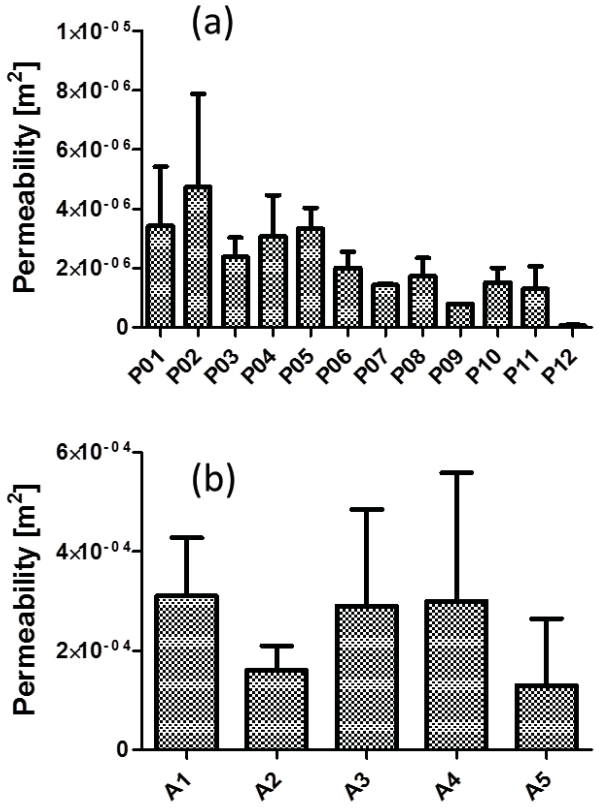

Figure. 1. Permeability values for *a)* human trabecular bone samples and *b)* bovine trabecular samples.

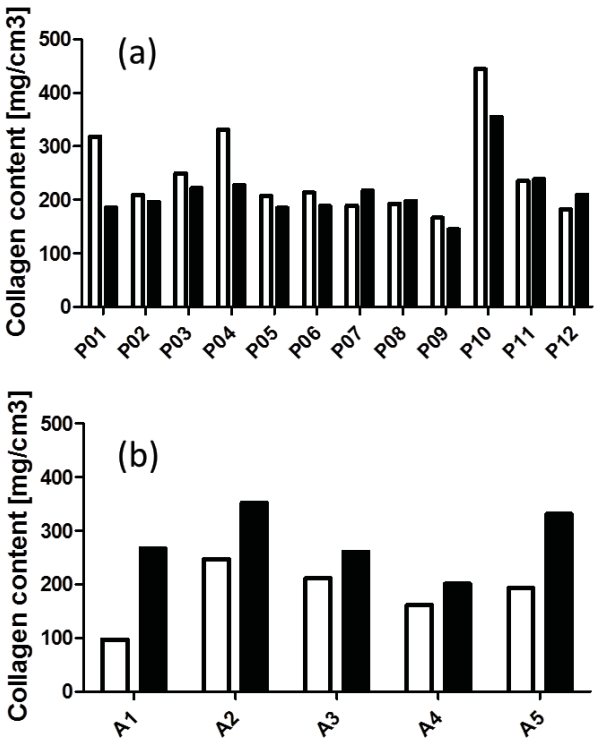

Figure 3. Comparison between the collagen content evaluated by DOS (black bars) and hydroxyproline (white bars) for *a)* human samples, and *b)* bovine samples

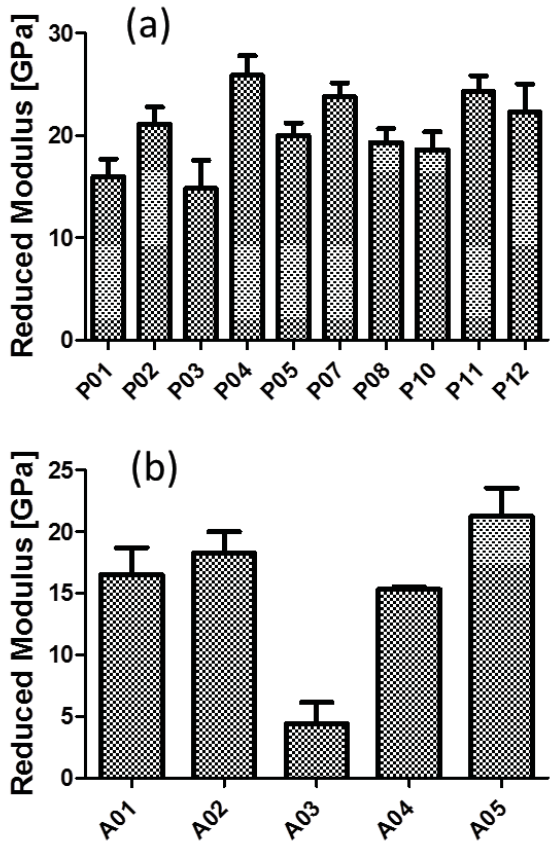

Figure 2. Reduced Young moduli evaluated from multi-load nanoindentation creep tests *a)* human samples, and *b)* bovine samples

Influence of cell removal treatment on dermis mechanical behaviour

M. Terzini[1], C. Bignardi[1], C. Castagnoli[2], E.M. Zanetti[3] and A.L. Audenino[1]
[1] *Department of Mechanical and Aerospace Engineering – Politecnico di Torino, ITALY*
[2] *Skin Bank – Trauma Center, Torino, ITALY*
[3] *Department of Industrial Engineering – Università di Perugia, ITALY*

***Abstract*—The knowledge of the mechanical behaviour of the skin is required by various medical disciplines such as dermatology, surgery and traumatology. More specifically, this work has been focused on one specific skin layer: the dermis. The aim was to verify the influence of the decellularization treatment on its properties.**

The specimens were subjected to uniaxial static tests performed with Bose Electroforce® 3200 and experimental data were represented with engineering and real time stress-strain curves. Descriptive parameters were identified from stress vs. strain curves, and they were subsequently compared through multivariate analysis of variance to determine the influence of the specimen cut orientation and of the decellularization treatment duration. The dermis which had been decellularized for 5 to 6 weeks, has exhibited mechanical properties comparable with native dermis ones. The ultimate tensile strength and the maximum Young's modulus were shown to be considerably higher in real time curves than in engineering ones: real time curves should therefore be used when modelling dermis behaviour, while engineering curves should be confined to comparative analysis, where they are able to provide indications with a higher repeatability and a simpler experimental set up.

***Keywords*—human dermis, static mechanical tests, decellularization treatment.**

I. Introduction

THE skin is the largest organ of the body; it works as a barrier to the environment and it controls thermal regulation and hydration retention. Engineered skin substitutes have a significant medical practice in relation to patients with extensive burn wounds. Up to now, the engineered tissue cannot faithfully replicate the mechanical properties of normal skin although advances in tissues engineering let foresee that skin substitutes will be indistinguishable from the normal skin in a near future. Alloplastic material and skin allografts are the most suitable replacement integumentary for reconstructive surgery [1]. In fact, they maintain the peculiar architectural structure of the dermis and, at the same time, the decellularized human reticular dermis is a not an immunogenic product when transplanted in the patient.

The tensile test is the most widely used mechanical test performed on ex vivo skin (epidermis, dermis, and hypodermis) specimens: using this method, the anisotropic, non-linear and viscoelastic behaviours of skin have been explored, as well as its failure behaviour [2]. In general the dermis gives a major contribution to the overall mechanical characteristics of the skin because of its main constituents: collagen and elastin fibrils allow for high levels of deformation and flexibility, as the fibrils stretch and re-orientate [3].

II. Materials and Methods

A. Specimens

Specimens of skin tissue have been collected from a single donor back to decrease the number of factors that could bias results; they were dissected along craniocaudal (CC) or mediolateral (ML) directions and decellularized in NaOH culture (Fig. 1). They were either non-chemically treated or incubated from 1 to 7 weeks; all specimens were preserved in glycerol at 85%.

B. Photographic set-up

Two different photographic set-ups have been developed in order to assess the size of the specimens:

Set-up 1: Finalized to measure the specimens' dimension at rest. It included a full-frame digital camera (Canon EOS 5D Mark II), with an autofocus lens for macro photography (Canon EF 100mm f/2.8 Macro USM), a camera stand with two light stands, and a tripod.

Set-up 2: Finalized to follow rupture tests in real time. It included the previously described digital camera, a second digital single-lens reflex camera (Canon EOS 400D), a tripod and remote capture software (DSLR Remote Pro).

Before testing, specimen pictures were taken from the top and from the side (Fig. 2). Width and thickness of the middle zone were measured using the image analysis software ImageJ (as an average of five different measures), obtaining a 0.01 mm/pixel measurement resolution from a 21.0 MP image (5616x3744 pixels).

C. Mechanical Tests

The specimens were washed in physiological solution to eliminate all the glycerol and were successively subjected to uniaxial tests in order to assess their mechanical properties; test parameters were selected according to natural tissue properties and Bose Electroforce® features. Each failure tensile test was performed in displacement control at a strain rate of 0.032 s^{-1} (0.16 mm/s).

D. Elaboration Data

In this work, the results of failure tests have been reported following two different representations:

- 'Engineering' stress/strain curves [4]: stress and strain calculated from load and displacement, referring to the initial specimen cross section and length, respectively.
- 'Real time' stress/strain curves [5]: specimen cross section and length measured in real time.

Some descriptive parameters have been identified in both curves: ultimate tensile strength (UTS) and maximum Young's modulus (E). The normality of the statistical distribution of both parameters has been tested by Lillie test function in Matlab R2010a and multivariate analysis of variance (ANOVA) has been performed in order to assess the influence of specimen cut orientation and duration of cell removal treatment. Significance levels for these tests were set to $p<0.05$. ANOVA was followed by the Tukey–Kramer *post-hoc* test to compare the averages of two reference groups (non-chemically treated specimens cut along two directions) with the averages of each combination of duration treatment and specimen orientation.

III. Results and Discussions

The results of uniaxial experimental tests were compared assuming a perfectly uniaxial loading condition, homogeneous stress-strain fields and a uniform distribution of collagen fibers. A softening trend of stress-strain curves (both "engineering" and "real-time" ones) was observed as well as a nonlinear elastic anisotropic behaviour of the tissue. Furthermore, the decellularization treatment has proven to reduce dermal mechanical properties, considering all incubation times. An incubation period between 5 and 6 weeks makes an exception since, in this case, the mechanical properties are partially recovered (Fig. 3).

The influence of specimen orientations and treatment duration was evaluated applying statistical tests (ANOVA) to the results obtained from the engineering curves. This type of analysis turned out to be only qualitative because engineering curves were based on a simplified hypothesis that could not be considered adequate for soft tissue. ANOVA demonstrated how both specimen cut orientation and treatment duration have significant influence on UTS and E. Multiple comparison demonstrated how specimens cut along ML direction and decellularized for 5 and 6 weeks were not significantly different from 'untreated' ones, both considering UTS and E, with a confidence level of 95% and 97% respectively. On the contrary, all specimens cut along craniocaudal direction, for whatever treatment duration, were significantly different from the reference native group.

Also real time curves were considered since the dermis has exhibited large deformations during tests. The trend of real time curves has remained similar to the engineering ones, but UTS and E values have resulted to be considerably higher: 3-4 times and up to 7 times respectively for UTS and E (Fig. 4).

IV. Conclusion

This work is part of a project focused on the mechanical characterization of acellular human dermal matrix. The measurement of the fundamental mechanical properties of the decellularized excised human skin is mandatory in order to be able to develop engineered materials for skin reconstruction, and to compare their performances with those of native skin. This work was focused on failure tests and was aimed to the assessment of the impact of different durations of cell removal treatment on specimen's structural performance or material behaviour. Specimen orientation has been taken into consideration because of tissue anisotropy.

As a result, the authors were able to prove how the human excised dermal matrix tissue, when decellularized under incubation culture in NaOH for 5–6 weeks, exhibits mechanical properties, which are comparable to the native one. Besides, the mechanical behaviour of specimens cut along the mediolateral direction was systematically higher than those cut along the craniocaudal one.

From a quantitative point of view, the values of ultimate tensile strength and maximum Young's modulus can be greatly underestimated whenever a tissue undergoes large deformations and engineering stress/strain curves are considered; therefore real time stress/strain curves have also been measured in order to achieve the best estimate of these parameters, as needed to set up and validate skin computational models, such as those based on finite elements.

On the whole, indications about the optimal decellularization treatment duration have been given together with refined mechanical properties of the tissue.

References

[1] D. J. Wong and H.Y. Chang, *Skin tissue engineering*, StemBook, ed. The Stem Cell Research Community, StemBook, 2009.

[2] B. P. Pereira, P. W. Lucas and S.H. Teoh, "Ranking the fracture toughness of thin mammalian soft tissue using the scissor cutting test," *Journal of Biomechanics*, vol. 30(1), pp. 91–94, 1997.

[3] R. Sanders, "Torsional elasticity of human skin in vivo," *Pflügers Archiv European Journal of Physiology*, vol. 342, pp. 255-260, 1973.

[4] A. N. Annaidh, K. Bruyère, M. Destrade, M. D. Gilchrist and M. Otténio, "Characterization of the anisotropic mechanical properties of excised human skin," *Journal of the Mechanical Behaviour of Biomedical Materials*, vol. 5(1), pp. 139-148, 2012.

[5] J.H. Yoder and D.M. Elliott, "Non linear and anisotropic tensile properties of graft materials used in soft tissue applications," *Clinical biomechanics*, vol. 25(4), pp. 378-382, 2010.

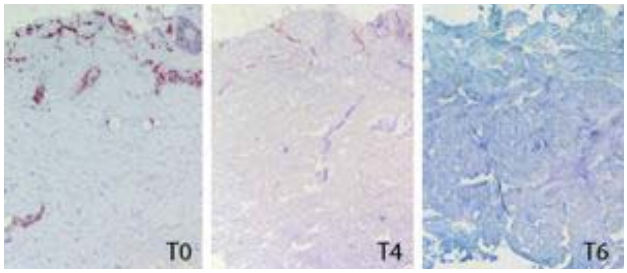

Fig. 1. Immunohistochemistry: staining with anti-HLA II (human major histocompatibility complex class II) before the treatment and after 4 and 6 weeks of incubation in NaOH.

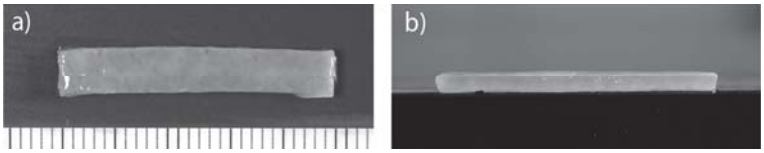

Fig. 2. Specimen sizing: a) top view; b) lateral view.

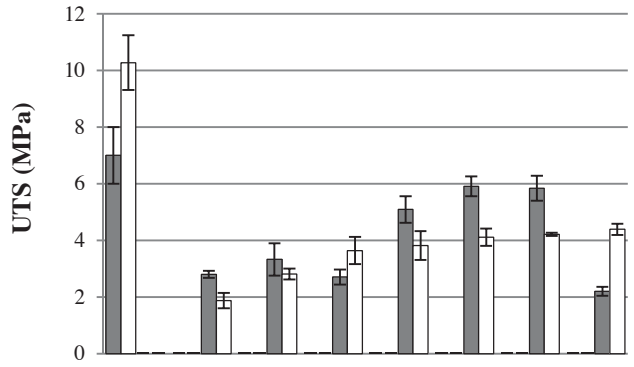

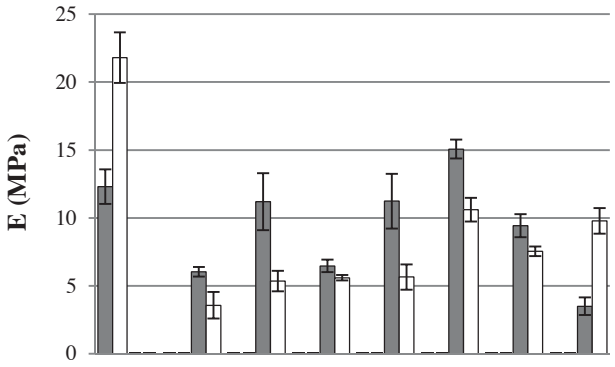

	Untreated	T1	T2	T3	T4	T5	T6	T7	Untreated	T1	T2	T3	T4	T5	T6	T7
ML	7,01 ±1,00	2,81 ±0,13	3,33 ±0,13	2,71 ±0,27	5,10 ±0,47	5,92 ±0,35	5,85 ±0,44	2,21 ±0,16	12,31 ±1,27	6,04 ±0,35	11,19 ±2,09	6,47 ±0,46	11,27 ±2,01	15,07 ±0,69	9,44 ±0,85	3,50 ±0,65
CC	10,28 ±0,96	1,88 ±0,27	2,82 ±0,19	3,65 ±0,48	3,83 ±0,51	4,12 ±0,30	4,22 ±0,06	4,40 ±0,20	21,79 ±1,86	3,58 ±0,98	5,36 ±0,74	5,60 ±0,19	5,66 ±0,94	10,62 ±0,88	7,55 ±0,35	9,79 ±0,94

Fig. 3. a) Engineering ultimate tensile strength (UTS) and b) engineering maximum Young's Modulus (E) with relative standard deviations in function of the treatment length (the number following T represents the number of treatment weeks) for specimens cut along craniocaudal (CC) and mediolateral (ML) directions respectively.

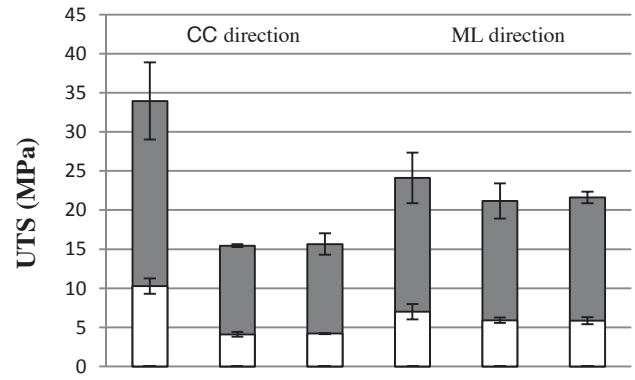

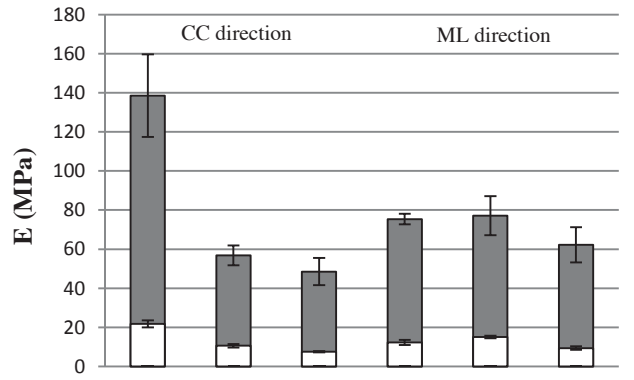

	Untreated	T5	T6	Untreated	T5	T6	Untreated	T5	T6	Untreated	T5	T6
Engineering	10,28 ±0,96	4,12 ±0,30	4,22 ±0,06	7,01 ±1,00	5,92 ±0,35	5,85 ±0,44	21,8 ±1,86	10,62 ±0,88	7,55 ±0,35	12,31 ±1,27	15,07 ±0,69	9,44 ±0,85
Real time	33,95 ±4,94	15,45 ±0,18	15,66 ±1,38	24,12 ±3,24	21,17 ±2,24	21,62 ±0,74	138,52 ±21,08	56,79 ±5,11	48,52 ±6,93	75,41 ±2,74	77,19 ±9,99	62,29 ±9,02

Fig. 4. a) Comparison between ultimate tensile strength (UTS) values and b) maximum Young's modulus (E) values obtained for engineering and real time curves, with relative standard deviations, in function of treatment length (the number following T represents the number of treatment weeks) for specimens cut along craniocaudal (CC) and mediolateral (ML) directions respectively.

Experimental set-up for the study of dental implant retrieval

M. Terzini[1], A. R. Ciccola[1], G. Menicucci[2], C. Manzella[2], S. Carossa[2], E.M. Zanetti[3], C. Bignardi[1], A.L. Audenino[1]

[1] *Department of Mechanical and Aerospace Engineering – Politecnico di Torino, ITALY*

[2] *Dental School – Università di Torino, ITALY*

[3] *Department of Industrial Engineering – Università di Perugia, ITALY*

***Abstract*—The purpose of this study was to design an experimental set-up for an in-depth analysis of dental implant retrieval. As a benchmark, a comparison has been made between two different tools: CORONAflex® and a sliding hammer crown-remover.**

Six operators have tested both tools with 40 replications; results were subsequently compared through multivariate analysis of variance (ANOVA) to determine the magnitude of the experimental error and to assess the influence of both factors (the tool and the operator) and of their interaction.

Both CORONAflex® and the manual sliding hammer crown-remover performances have resulted to be affected by the operator and by the specific device being used; however CORONAflex® data have shown a higher repeatability. Moreover, while the peak removal force for CORONAflex® belongs to a range between 374 N and 490 N, the range of variation of the same peak force is between 99 N and 316 N for the sliding hammer crown-remover.

***Keywords*—coronaflex, crown-remover, implant retrievability**

I. Introduction

Dental implants have a high success rate and have significantly improved both in terms of function and aesthetics [1], nonetheless there are still complications which may lead to the need of removal of the implant due to complications or implant failure in the medium-to long-term. Clinical methods to retrieve an implant-supported crown make use of devices with a high modulus and short duration impact force. However, there is no guideline for the clinician as to the best practice for crown removal: many low-force impacts or one single shot? Furthermore, it is unclear which kind of removal device, cement and cement application technique is useful to achieve an adequate retention, while still maintaining retrievability [2]. This study is aimed to provide some more insight into this subject, having designed an apposite experimental set-up, able to provide quantitative and reproducible data. The comparison between two different implant retrieval tools is used as a benchmark; these tools are CORONAflex® and a sliding hammer crown-remover; both tools are currently sold on the market.

II. Materials and Methods

The plan of experiments considered six tools (three different CORONAflex® and three sliding hammer crown-remover), and six operators: three dental practitioners, and three inexperienced operators. Each experiment was identified by the respective tool and operator, and was replicated 40 times at regular intervals lasting 3 seconds. On the whole, 1440 tests have been performed.

A. CORONAflex® tool

CORONAflex® is a device manufactured by Kaltenbach&Voigt GmbH, distributed by KaVo Dental GmbH and intended solely for procedures in the dental medicine (fig. 1). In the intention of its designer, it allows performing rapid, effective and secure dentures and crowns extractions; in most cases, the prosthesis remains intact after removal and can therefore be re-used. The energy source is compressed air, with an operating pressure ranging from 3 to 5 bar, which pushes a plunger towards the extractor tip. This pulse fractures the cement, and allows the prosthesis removal [3]. This article refers to the extraction of dental crowns using a loop (fig. 1) which is introduced under the bridge, as close as possible to one of its pillars. It is then secured by a special loop holder, where the impact force is applied. The same operations are then repeated next to each pillar, and the whole procedure is repeated until the complete removal of the bridge is obtained.

B. Sliding hammer crown-remover

The sliding hammer crown-remover (fig. 1) belongs to the category of manual instruments. It is made of a steel rod, and a concentric mobile mass, whose shape and weight can vary from a hammer to another one; various tips can be attached to the rod end. The hammer tip is positioned between two crowns and the moving mass is then repeatedly thrown along its guide, producing small strokes, in a short period of time.

C. Instrumentation

The experimental set-up employed a screw bearing a diametric hole (fig. 2) which the loop holder passed through. The screw has been attached to a force transducer (Brüel&Kjær, type 8201). The loop holder arm has been kept perpendicular to the transducer axis, through a special fixture. Several preliminary tests have been performed in order to test if this experimental set-up could faithfully reproduce the actual procedure, despite having simplified real working conditions.

Preliminary tests have also demonstrated that the input pressure is not influent on the amplitude of the signal produced by CORONAflex®. This pressure has therefore been kept equal to 4 bar in all experiments.

D. Signal analysis

The force signal produced by CORONAflex® has shown a higher repeatability, as it could be expected since this signal is produced automatically. The force pattern is made of two components (fig. 3): the pulse itself, which is the object of this inquiry, and an extinguishing oscillating response due to

the dynamic response of the load cell; these two signals overlap in the first phase, and this is the reason why the peak is not symmetric and its amplitude might be wrongly estimated. The following procedure has been therefore implemented: the pulse peak has been identified and the signal has been made symmetric with respect to this point. The so generated curve (fig. 3) has been interpolated with a 6th degree polynomial and the peak width has been so established.

E. Statistical analysis

Two null hypotheses have been formulated with reference to the significance of the operator and of the removal tool on the peak removal force. The analyses of variance (ANOVA) have been performed both considering each tool singularly, and all data together (Table I): in the last case, results obtained with different tools of the same kind (CORONAflex® or the slider hammer crown-remover) have been considered as replications of the same experiment.

TABLE I
ANALYSIS OF VARIANCE

	Factors	*SS [N²]*	*dof*	*MS [N²]*	$F_{experim}$	*Significance*
ANOVA for CORONAflex®	Coronaflex	41262	2	20631	36.46	<1E-3
	Operator	326733	5	65347	115.48	<1E-3
	Interaction	272788	10	27279	48.21	<1E-3
	Error	397227	702	566		
	TOTAL	1038011	719			
	Factors	*SS [N²]*	*dof*	*MS [N²]*	$F_{experim}$	*Significance*
ANOVA for the sliding hammer crown-remover	Sliding Hammer	222573	2	111286	60.99	<1E-3
	Operator	1477681	5	295536	61.97	<1E-3
	Interaction	938018	10	93801	51.41	<1E-3
	Error	1280865	702	1825		
	TOTAL	3919137	719			
	Factors	*SS [N²]*	*dof*	*MS [N²]*	$F_{experim}$	*Significance*
ANOVA for the kind of tool and the operator	Kind of Tool	495569	1	495569	322.62	<1E-3
	Operator	5738	5	1148	0.75	0.596
	Interaction	39372	5	7874	5.13	2.00E-03
	Error	36866	24	1536		
	TOTAL	577545	35			

III. Results and Discussion

A. Results repeatability

The replication of tests has proven that the peak amplitude of forces reached by CORONAflex® is much more repeatable compared to the slider hammer crown-remover: a coefficient of variation (i.e. the ratio of the standard deviation to the mean) of 22% has been measured, against 31% measured employing the sliding hammer crown-remover.

B. Operator influence

The operator has resulted to play a significant influence, and this assertion remains true also considering each tool singularly (Table I). However, with reference to CORONAflex® tool, changing operator produces a coefficient of variation up to 9.8%, while it rises up to 43.3% with reference to the sliding hammer crown remover.
Images of signals obtained by different operators have been reported in figure 4: even when the peak amplitude is the most similar, the pattern of the signal can be very different in the case of the sliding hammer crown-remover.

C. Tool influence

The employed tool has resulted to play a significant influence and this assertion remains true also considering CORONAflex® or the sliding hammer crown-remover singularly (Table I). However, with reference to CORONAflex® tool, changing the tool produces a percentage variation equal to 8.8%, while it rises up to 37.5% with reference to the sliding hammer crown remover. Figure 5 allows to visually appreciating the impact of employing different tools on the final signal shape.

D. Tool-operator interaction

The interaction between the tool and the operator is indeed significant: certain operators have produced much more repeatable results in spite of using different tools, compared to other operators (Table II).

TABLE II
AVERAGE REMOVAL FORCES OBTAINED FOR DIFFERENT TOOL/OPERATOR COUPLES [N]

	CORONAflex® 1	*CORONAflex® 2*	*CORONAflex® 3*
Operator 1	438	441	470
Operator 2	423	411	398
Operator 3	436	457	490
Operator 4	446	395	453
Operator 5	373	444	393
Operator 6	418	391	429
	Sliding hammer 1	*Sliding hammer 2*	*Sliding hammer 3*
Operator 1	170	124	112
Operator 2	177	187	279
Operator 3	118	198	99
Operator 4	187	185	186
Operator 5	163	316	297
Operator 6	198	243	243

IV. Conclusion

The analysis carried out in this study could lead to the wrong conclusion that both removal devices produce a significant variability in the procedure; however it should be considered that a 15% variation can be considered a reasonable condition of work; in relation to this limit, CORONAflex® has certainly performed well: changing both the operator and the device, the peak removal force stays in the range from 374 N to 490 N. On the contrary, the range of variation of the same peak force when using the sliding hammer crown-remover is very wide, being between 99 N and 316 N.
The experimental set-up has proved to allow the study of dental implant retrieval, providing force pattern versus time with good repeatability, and well simulating real working conditions.

References

[1] K. Pavel, M. Seydlova, T. Dostalova, V. Zdenek, K. Chleborad, Z. Jana, J. Feberova and H. Radek, "Dental implants and improvement of oral health-related of life," *Community Dent Oral Epidemiol*, vol.40 (Suppl. 1), pp. 66–71, February 2012.
[2] C. Mehl, S. Harder, M. Wolfart, M. Kern and S. Wolfart, "Retrievability of implant-retained crowns following cementation," *Clinical Oral Implants Research*, vol. 19, pp. 1304–1311, December 2008.
[3] CORONAflex® datasheet.

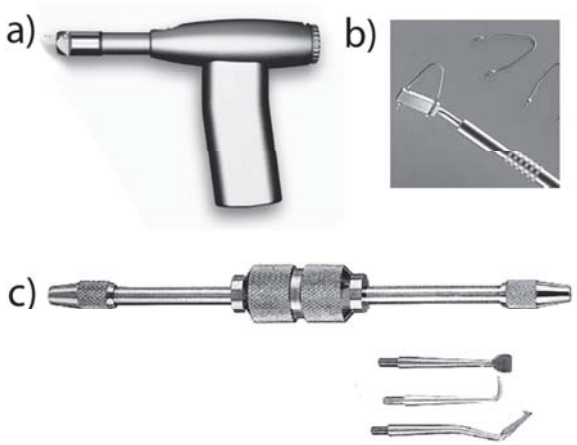

Fig. 1. CORONAflex® (a), its loop for the extraction of dental crowns (b) and the sliding hammer crown-remover (c).

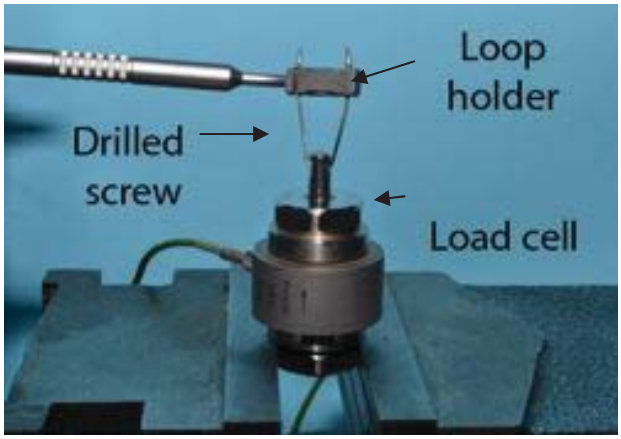

Fig. 2. The experimental set-up.

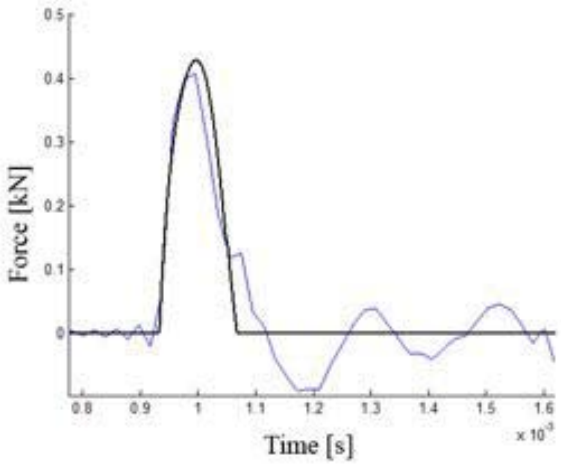

Fig. 3. Signal interpolation for the estimation of peak amplitude.

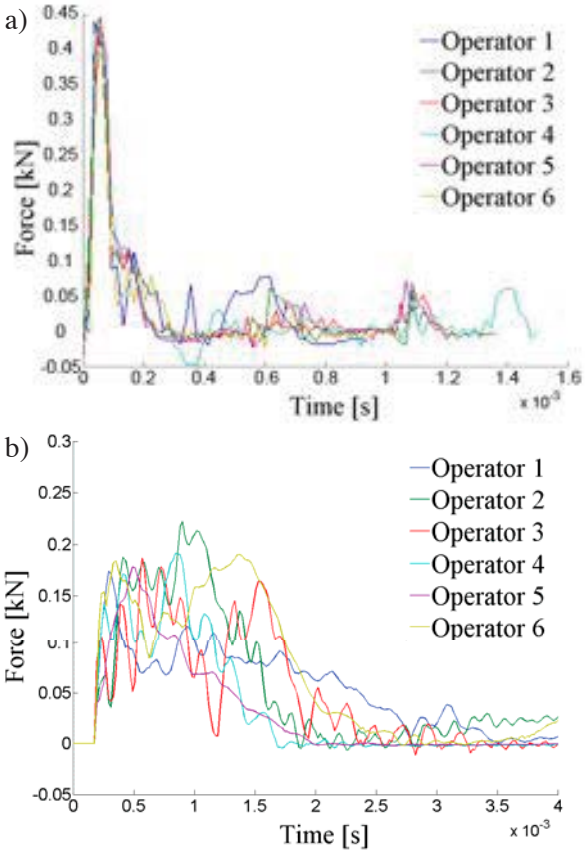

Fig. 4. Force pattern vs. time, produced by different operators in the case of CORONAflex® tool (a) or of the sliding hammer crown-remover

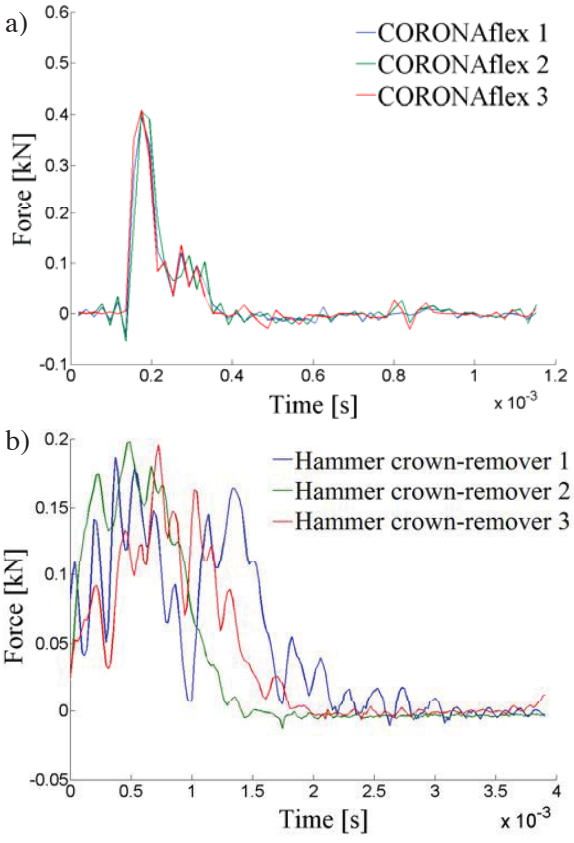

Fig. 5. Force pattern vs. time, produced by different tools in the case of CORONAflex® tool (a) or of the sliding hammer crown-remover (b).

Neuroprotective effect of mesenchymal stromal cells in a 3D model of Parkinson's disease

M. Tunesi[1,2], M.M. Nava[1], F. Caterina[3], C. Giordano[1,2], D. Albani[3], M.T. Raimondi[1]
[1] *Department of Chemistry, Materials and Chemical Engineering "G.Natta", Politecnico di Milano, Milan*
[2] *Unità di Ricerca Consorzio INSTM, Politecnico di Milano, Milan*
[3] *Department of Neuroscience, IRCCS-Istituto di Ricerche Farmacologiche "Mario Negri", Milan*

***Abstract*—We have adapted a miniaturized and optically accessible bioreactor to study the neuroprotective effect of mesenchymal stromal cells on neuronal-like cells in a 3D model of Parkinson's disease. Both stromal and neuronal-like cells were seeded on polystyrene scaffolds, then the neuronal-like cells were exposed to 6-hydroxydopamine. Finally, both cell types were moved to the bioreactor, where the medium conditioned by the stromal cells was used to culture the neuronal-like cells. Our data indicate a neuroprotective effect of stromal cells in the conditions tested, suggesting that this bioreactor might be a suitable co-culture platform to be exploited for the study of cell therapies against neurodegeneration.**

***Keywords*—perfusion bioreactor, microfluidic testing, neuroprotection, Parkinson's disease.**

I. Introduction

Perfusion bioreactors have been extensively used in tissue engineering to provide reliable models of tissue growth in controlled conditions.

In particular, a miniaturized and optically accessible bioreactor for interstitial perfusion of 3D cell-seeded scaffolds was recently developed to systematically study the effect of several parameters on engineered tissue growth using non-destructive analysis, such as viable staining and standard fluorescence microscope [1]. The advantage of this culture system, that is composed of three independent chambers, is the possibility to follow the evolution of the growing tissue on the same construct.

In this work, we have adapted this bioreactor and culture conditions to investigate the ability of mesenchymal stromal cells (MSCs) to protect neuronal-like cells against the effects of the catecholaminergic neurotoxin 6-hydroxydopamine (6-OHDA) in a dynamic co-culture model of Parkinson's disease.

II. Materials and Methods

A. Cell culture

Human neuroblastoma SH-SY5Y cells (American Type Culture Collection® code CRL-2266™) and MSCs from rat bone marrow were cultured in Dulbecco's Modified Eagle Medium supplemented with 10% (v/v) fetal bovine serum, 2 mM L-glutamine, 100 U/mL of penicillin and 100 μg/mL streptomycin (Invitrogen Corporation, Carlsbad, CA, USA). Cells were kept at 37 °C in 5% CO_2.

B. Scaffolds and cell seeding

Both SH-SY5Y and MSCs were seeded on cell culture treated-polystyrene scaffolds (3D Biotek, North Brunswick, NJ, USA). These scaffolds were optically transparent and showed a highly defined architecture. Their fibers were 100 μm in diameter with a pore size of 300 μm and stacked in an offset cross-hatch geometry (four flats, each one shifted 150 μm in respect of the adjacent flat), as reported in Fig.1. The following day, SH-SY5Y cells were challenged with 6-OHDA and their viability was assessed by trypan blue (Sigma-Aldrich, St. Louis, MO, USA) staining and 3-(4,5-dimethylthiazol-2-yl)-5-(3-carboxymethoxyphenyl)-2-(4-sulfophenyl)-2H-tetrazolium (MTS, CellTiter 96® Aqueous One solution Cell Proliferation assay, Promega Corporation, Madison, WI, USA) assay.

C. Microfluidic testing of the neuroprotective effect of MSCs on SH-SY5Y cells

To investigate the ability of MSCs to improve the survival of SH-SY5Y cells, the scaffolds were moved to the miniaturized and optically accessible bioreactor. Thanks to a bypass (Fig. 2), the chamber with MSCs was connected to that with SH-SY5Y cells, so that the medium enriched by MSCs was used to condition the neuronal-like cells. The third chamber was independent from the others and was used as a non-conditioned control for SH-SY5Y cells. After 24 h, the viability of SH-SY5Y cells was assessed, as previously described. The experiment was also repeated in static conditions.

D. Statistical analysis

Statistical analysis was performed with the software GraphPad Prism® (GraphPad Software Corporation, La Jolla, CA, USA). The significance level was set at $p < 0.05$.

III. Results and Discussion

A. Cell viability after seeding

Both trypan blue staining and MTS assay have shown that 6-OHDA reduced the viability of SH-SY5Y cells with respect to untreated controls. In particular, after 24 h of incubation with 25, 50 and 75 μM 6-OHDA, SH-SY5Y cell viability was reduced of about 25%, 50% and 75%, respectively. One-way analysis of variance (ANOVA) followed by Dunnett's multiple comparison test has indicated that for the first condition $p < 0.05$, while for the remaining $p < 0.001$.

B. Microfluidic testing of the neuroprotective effect of MSCs on SH-SY5Y cells

MSCs have improved the survival of SH-SY5Y cells in

static conditions (as already reported in literature for neural cultures [2]), but also in dynamic conditions. In particular, the better performances were achieved with the bioreactor, suggesting that the applied bioreactor and its modification are suitable to study the proposed biological issue.

IV. Conclusion

The applied bioreactor and its modification have allowed to achieve better performances than standard cell culture techniques.

Future works will focus on the study of the molecules released by MSCs in the culture medium. Aiming at developing a co-culture platform to investigate the suitability of cell therapies for neurodegenerative disorders, future studies will also focus on the possibility to further adapt the bioreactor to perform the whole experimental activity in dynamic conditions.

Acknowledgement

The authors are grateful to Fondazione Cariplo (Grant no: 2011-0335) for financial support. They also thank Ilaria Pazzola for helping with experimental activities.

References

[1] L. Laganà and M. T. Raimondi, “A miniaturized, optically accessible bioreactor for systematic 3D tissue engineering research,” *Biomed Microdevices*, vol. 14, pp. 225-234, February 2012.

[2] L. Cova, P. Bossolasco, M. Armentero, V. Diana, E. Zennaro *et al.*, “Neuroprotective effects of human mesenchymal stem cells on neural cultures exposed to 6-hydroxydopmaine: implications for reparative therapy in Parkinson's disease,” *Apoptosis*, vol. 17, pp. 289-204, March 2012.

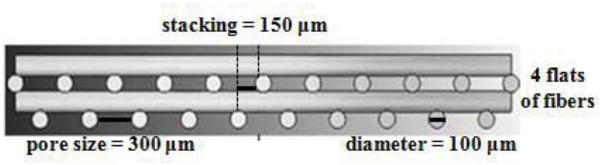

Fig. 1. Polystyrene scaffolds for cell seeding (6 mm x 3 mm x 0.4 mm).

Fig. 2. The optically accessible and miniaturized bioreactor used in this work. The picture shows the bypass, that connects the outlet of the first chamber to the inlet of the second chamber. The third chamber was independent from the others.

Biomechanical behaviour of tibio-talar joint in stance and push-off configuration with degraded articular cartilage

C. Venturato[1,2], P.G. Pavan[1,2], A. Forestiero[1,2], E.L. Carniel[1,2] and A.N. Natali[1,2]
[1] *Department of Industrial Engineering, University of Padova, Padova, Italy*
[2] *Centre for Mechanics of Biological Materials, University of Padova, Padova, Italy*

***Abstract* - Osteoarthritis is a degenerative pathology that can affect joints invalidating human movements, with relevant effects from social and economic point of view. The mechanical behaviour of articular cartilage, in particular, is of high interest when considering the biomechanics of osteoarthritic joint. The aim of this work is to develop a finite element model of the tibio-talar joint, suitable to evaluate the effects of osteoarthritic degradation on cartilage, under different loading condition as stance and push-off. Particular attention is paid to obtain a detailed numerical model of the joint, representing the complex morphology of the anatomical region. The numerical analyses interpret correctly the mechanical changes that occur in OA cartilages and the consequent effects on the biomechanical response of the joint under application of physiological loads.**

Keywords - Tibio-talar joint, osteoarthritic cartilage, constitutive modelling, numerical modelling.

I. Introduction

OSTEOARTHRITIS (OA) is a leading cause of disability in population. It is often more painful in weight bearing joints, such as the knee, hip and ankle [1]. This degenerative pathology can be related to different causes such as overuse, trauma or the degeneration of the joint cartilage that takes place with aging. Joints that are used extensively in work or sports may show signs of osteoarthritis and other disorders, such as obesity, may induce the pathology. Osteoarthritic joint first degrades the smooth cartilage lining that allows for low friction and pain-free weight bearing. In advanced phase, the pathology changes overall cartilage mechanical response, determining various degrees of pain. Radiographic analyses show of joint space narrowing, subchondral sclerosis and osteophyte formation. All these phenomena have important effects on the mechanical state of cartilage and on the biomechanical behavior of the joint [2].

Because of the complex morphology of the tibio-talar joint, a precise evaluation of the mechanical conditions acting on the different tissues is difficult. The use of finite element analyses is helpful to overcome these limits, since it is possible to evaluate mechanical quantities that, otherwise, could be roughly estimated. With this motivation, the aim is to develop a numerical model to investigate the tibio-talar joint capable of representing the biomechanical response under different loading conditions and states of the articular cartilages.

II. Material and methods

A. Cartilage constitutive model and parameters fitting

Articular cartilage is a multiple layer tissue organized into four zones: the superficial zone, the transitional zone, the middle zone and the calcified cartilage zone. The superficial zone is about 20% of the thickness of articular cartilage and gives a frictionless surface, providing also the most important mechanical response in compression and shear resistance. This zone is rich in collagen and presents closely packed fibres aligned parallel to articular surface.

The mechanical response of cartilage is described by assuming a fibre-reinforced and almost-incompressible hyperelastic constitutive model. This constitutive formulation takes into account large strains, elastic non-linear behaviour and anisotropic response due to collagen fibres [3]. The constitutive model is capable to describe the mechanical response of articular cartilage in healthy or OA conditions by assuming specific values for the constitutive parameters. At this purpose, a finite element model of a cartilage disk sample is investigated providing a result comparison with reference to experimental indentation test of healthy and OA cartilages [4], [5]. Since the aim of this work is to consider physiological strain rate corresponding to normal walking speed. In the literature there is a limited number of experimental data about OA cartilage that refer to this condition, the following procedure is adopted. The different mechanical response of OA tissue with respect to healthy condition deduced by *in-vitro* indentation tests performed on healthy and OA cartilage at strain rate of 10%/s, evaluating the percentage difference in stress between OA and healthy cartilage, at the same level of strain [4]. The estimated difference is the basis to define the compressive response of OA cartilage from experimental data obtained on healthy cartilage by *in-vitro* unconfined compression tests at strain rate of 28%/s [5], a value close to the strain rate expected in the main cartilages of the hindfoot at normal walking speed. The optimum sets of parameters for healthy and OA cartilages are estimated by means of a combined stochastic-deterministic optimization procedure to minimize the discrepancy between experimental and numerical results [6]. The constitutive parameters defined for healthy and OA cartilages are adopted in the constitutive model that is included in the numerical model of tibio-talar joint.

B. Finite Element Model

The solid model of the foot is developed taking into account for the real morphology of the joint. Foot bones, ligaments, cartilages and synovial capsules are included. Bony segments are developed from CT images [3], while cartilages and synovial capsules are obtained on the basis of MRI data. These data are verified to be in agreement with the literature [7]. The finite element model is obtained by

meshing the solid regions with tetrahedral elements, using local refinements of the mesh within specific regions in order to have suitable accuracy. The interaction between cartilage surfaces is modelled by using appropriate frictionless contact strategy [8]. Specific constitutive formulations are adopted for each tissue of the hindfoot. An orthotropic and linearly elastic model is assumed to describe bony segments, a fibre-reinforced visco-hyperelastic model is adopted for ligaments [9], while the synovial capsule is modelled by a linear elastic and incompressible material, with shear modulus of 2 MPa [10]. Cartilaginous tissues are modelled by using the fibre-reinforced hyperelastic constitutive model described in the previous section. The constitutive models are implemented in the general-purpose finite element software ABAQUS® (Dassault Systèmes, France) that is adopted for the non linear static analyses developed.

C. Loading conditions

To evaluate the loads applied to the ankle joint during the gait cycle OpenSim 2.2 (National Center for Simulation in Rehabilitation Research – NCSRR, Stanford, CA) is adopted. Experimental data of a subject walking in bare condition at speed of 1.3 m/s are considered and processed by means of dynamic analysis. Joints angles, articular moment and ground reaction force are used to obtain the compressive force acting on the tibia by imposing the equilibrium at ankle joint. In Fig. 1 external moment and dorsiflexion angle on the ankle from stance to push-off phase are reported as evaluated by means of OpenSim. The maximum dorsiflexion of 14° corresponds to the push-off phase. Data obtained are in agreement with the literature [11].

The compressive force in the stance phase of the gait cycle corresponds to a load of 765 N imposed on the proximal end of the tibia segment and along its proximal-distal axis. This configuration corresponds to the maximum measured ground reaction force when it is aligned with the tibial axis and the dorsiflexion angle is close to 0. In the push-off configuration, the load is obtained by considering a dorsiflexion with angle of 14° [11]. In this condition, an axial compressive load of 2600 N acting on the tibia is the resulting load transmitted by leg bones to the foot.

III. Results

The sagittal section of tibio-talar joint (Fig. 2) highlights the structure of the tibio-talar joint, with articular cartilage layer on each bone head and the synovial capsule. The detail shows the minimum principal strain field in correspondence of the peak value region for healthy and OA cartilage. This result is reported to evidence the high strain on the overall region in contact: a peak of 22% for the case of OA cartilage and 17% for healthy cartilage is found. These values are in agreement with the level of compressive strain estimated from *in-vivo* tests [12].

Fig. 3 shows the minimum principal strain field of OA cartilage surface for stance and push-off phase of the gait cycle. Position and values of the maximum compressive strain in antero-medial region for stance configuration are consistent with *in-vivo* results reported in the literature [11]. The comparison of stance and push-off configuration evidences the variation of strain values and spatial distribution. Local peaks of compressive strain of about 36% are placed anteriorly in push-off, again in accordance with data from the literature [13].

IV. Conclusion

The results confirm the reliability of the model in describing the physiological loading conditions considered, with limit given by the possible comparison to experimental data. The procedure adopted is suitable to describe the mechanical states within tibio-talar joint, also when considering OA cartilage.

Additional analyses can be planned in order to study other foot configurations that are proved to be correlated to OA, due to overuse of ankle joint.

It is also of interest the investigation of the biomechanical behaviour of substitutes commonly adopted in cartilage surgical reconstruction. This activity is already in progress with regard to polymeric hydrogels substitutes (i.e. PVA cryogel) that have faster recovery time and less surgical trauma. The success rate of PVA plugs implants is affected by surgical insertion methods, dimension and number of plugs used to remove cartilage defects. These aspects can be evaluated with effectiveness by the numerical approach proposed, both with regard to local mechanical interaction and to overall biomechanical response.

References

[1] J.W.J. Bijlsma, F. Berenbaum, F.P.J.G Lafeber, “Osteoarthritis: an update with relevance for clinical practice”, *The Lancet*, vol. 377(9783), pp. 2115-2126, 2011.

[2] N. Kanzaki et al., “Osteoarthritis of the talo navicular joint with pseudarthrosis of the navicular bone: a case report”, *J Med Case Rep*, vol 5, pp 547-552, 2011.

[3] C. Venturato, P.G. Pavan, A. Forestiero, E.L. Carniel, A.N. Natali, “Investigation of the biomechanical behaviour of articular cartilage in hindfoot joints”, *Acta Bioeng and Biomech*, vol. 16(2), 2014.

[4] C. P. Brown, R. W. Crawford, A. Oloyede, “Indentation stiffness does not discriminate between normal and degraded articular cartilage”, *Clin Biomech*, vol. 22(7), pp. 843-848, 2007.

[5] S. Park, C.T. Hung, G.A. Ateshian, “Mechanical response of bovine articular cartilage under dynamic unconfined compression loading at physiological stress levels”, *Osteoarthr Cart*, vol. 12(1), pp. 65-73, 2004 .

[6] A.N. Natali, A. Forestiero, E.L. Carniel, P.G. Pavan, C. Dal Zovo, “Investigation of foot plantar pressure: experimental and numerical analysis”, *Med Biol Eng Comput*, vol. 48, pp.1167-1174, 2010.

[7] D. Al-Ali, H. Graichen, S. Faber, K.H. Englmeier, M. Reiser, F. Eckstein, “Quantitative cartilage imaging of the human hind foot: precision and inter-subject variability”, *J Orthop Res*, vol. 20(2), pp. 249-256, 2002.

[8] S.L. Bevill, A. Thambyah, N.D. Broom, “New insights into the role of the superficial tangential zone in influencing the microstructural response of articular cartilage to compression”, *Osteoarthr Cart*, vol. 18(10), pp. 1310-1318, 2010.

[9] A. Forestiero, E.L. Carniel, C. Venturato, A.N. Natali, “Investigation of the biomechanical behaviour of hindfoot ligaments”, *Proc Inst Mech Eng Part H: J Eng In Med*, vol. 227(6), pp. 683-692, 2013.

[10] H. Fam, J.T. Bryant, M. Kontopoulou, “Rheological properties of synovial fluids”, *Biorheol*, vol. 44(1-2), pp. 59-74, 2007.

[11] A. Roaas, G.B. Andersson, “Normal range of motion of the hip, knee and ankle joints in male subjects, 30-40 years of age”, *Acta Orthop Scand*, vol. 53(2), pp. 205-208, 1982.

[12] L. Wan, R.J. de Asla, H.E. Rubash, G. Li,“Determination of in-vivo articular cartilage contact areas of human talocrural joint under weight-bearing condition”, *Osteoarthr Cart*, vol. 14(12), pp. 1294-1301, 2006.

[13] H.B. Kitaoka, Z.P. Luo, K.N. An, “Contact features of the talo navicular joint of the foot”, *Clin Orthop Relat Res*, vol. 325, pp. 290-295, 1996.

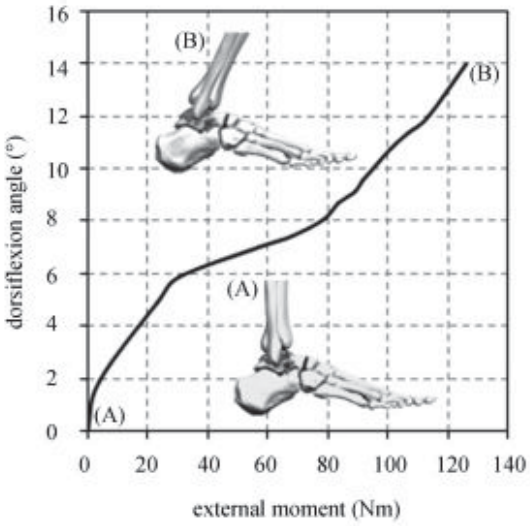

Fig. 1. Dorsiflexion angle and corresponding external moment M_{ext} as obtained by means of inverse dynamic analysis.

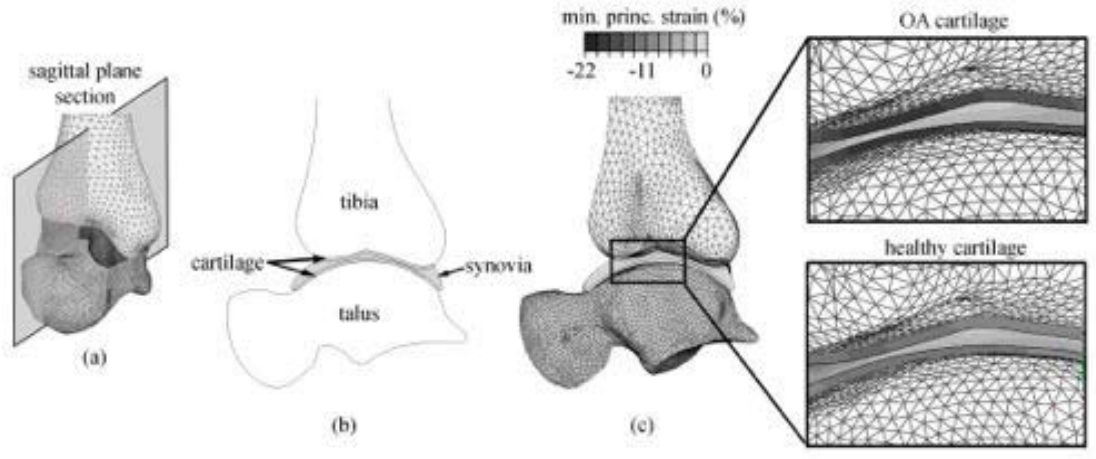

Fig. 2. Sagittal plane section (a) of the tibio-talar joint with synovia and cartilage layers (b) for stance configuration with details of the minimum principal strain on the antero-medial peaks area in OA and Healthy cartilage (c).

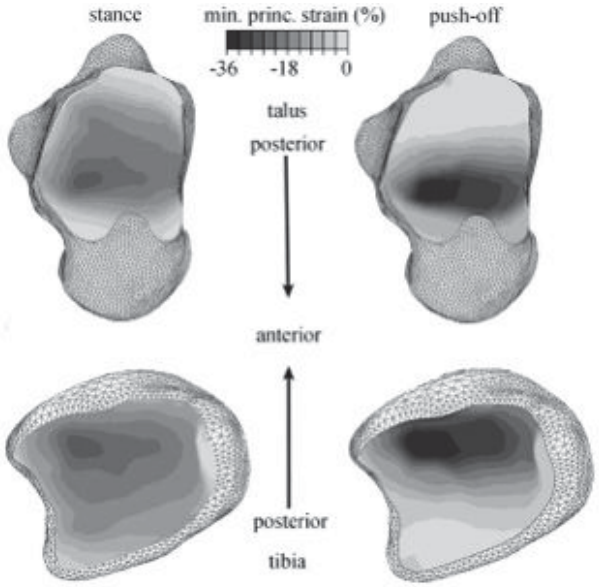

Fig. 3. Minimum principal strain field (%) on talus and tibia cartilage surfaces for stance configuration (on the left) and push-off configuration (on the right).